The study of vesicle phoresis in a concentration gradient

A thesis submitted to the University College London in accordance with the requirements for the degree of Doctor of Philosophy

SAFA ALI ALMADHI

SUPERVISOR: PROF. GIUSEPPE BATTAGLIA

FACULTY OF MATHEMATICAL AND PHYSICAL SCIENCES
Department of Chemistry, UCL, London UK
February 2022

TO MY FAMILY

Declaration

I, Safa Ali Almadhi, confirm that the work presented in this thesis is my own, unless explicitly stated otherwise. Where information has been derived from other sources, I confirm that this has been indicated in this thesis.

SAFA ALI ALMADHI
Department of Chemistry
University College London
London, UK
February 2022

The study of vesicle phoresis in a concentration gradient
Safa Ali Almadhi
University College London
February 2022

IMPACT STATEMENT

Brain diseases and disorders are major public health problems. In the UK, 45 million brain disorders were diagnosed in 2010 alone, with an estimated cost of £ 112 billion.[1] Despite the significant advancements in medicine over the past decade, the brain remains a challenging organ to treat. This is attributed to the protective barrier that restricts access of most known therapeutics. In fact, this protective barrier hinders the treatment of most central nervous system (CNS) diseases, i.e., diseases in the brain and spinal cord. The limited access of therapeutics to the brain from the circulating blood is met with an increase in the administered drug dose, often leading to undesirable side effects that substantially impact the patient's quality of life. These side effects are attributed to the unwanted interactions of the drug with other organs or active sites in the body. Hence there is a need for drugs that can (i) be delivered directly to the brain hence limiting its interactions with other organs, tissues and cells and (ii) that can cross the protective barrier to enter the brain. The latter can be achieved by using nanovesicles, these are nanosized carriers capable of encapsulating medications and, when modified, effectively cross the protective barriers releasing the therapeutics only to the intended organ. However, the former is a challenging task, in fact, no known medication has achieved direct delivery to the target site. This is due to the complex journey of the drug in the body, which facilitates many possible unwanted interactions with multiple active sites that resemble the target site. The work in this thesis focuses on creating a new generation of nanovesicles (active nanovesicles) that can autonomously swim and navigate in the blood vessels to reach only the target site.

The idea is to exploit the natural glucose gradient of the brain to drive and direct the swimming nanovesicles to it. The brain consumes about 60 % of the glucose in the body. This metabolic demand is sustained by creating gradients across the protective barrier. The findings in this thesis show the directional motion of two types of nanovesicles towards glucose in a gradient. I show that these nanovesicles swim at a speed of 3-6 times their size in length, making this the first and most accurate measurement yet.

In addition, this work reports other phenomena that induce movement in nanovesicles when in a gradient. The movement of passive nanovesicles by the shear interaction of their surface with the glucose gradient (diffusiophoresis) and the movement of the fluid by the mere addition of nanovesicles into the gradient (diffusioosmosis) are shown. Diffusiophoresis highlights the influence of gradients in governing the motion of nanovesicles. In the body, physiological gradients are constantly varying and usually exist simultaneously. Thus, the impact of this work extends beyond controlling the movement of nanovesicles in glucose gradients but also scratches the surface to possibly understanding the motion of other passive particles like nutrients, proteins, DNA and even viruses in a non-equilibrium state i.e., a real-life environment.

ABSTRACT

The targeted delivery of drugs to specific diseased sites within the body is one of the major issues in the development of drug delivery today. This is particularly relevant in addressing central nervous system (CNS) disorders and diseases, diseases localised in the brain and spinal cord, where the delivery of the therapeutics is limited by the brain barriers. Consequently, the design of drug delivery systems able to independently navigate within the body to specifically deliver the cargo into the brain is desirable. Inspired by nature, scientists have created artificial self-propelling micro and nanoparticles, known as micro- or nano- swimmers. This thesis focuses on the self-assembly and migration of vesicular nanoparticles within a glucose gradient as potential nanoswimmers. Two types of nanoparticles are explored: a) bi-component PMPC-PDPA:PEO-PBO polymersomes and b) α-hemolysine-porated liposomes. First, a methodology to self-assemble the PMPC-PDPA:PEO-PBO polymersomes is optimised to attain a monodisperse, vesicular sample. This was followed by the incorporation of glucose oxidase enzyme into both the polymersomes and liposomes with an average of 6 and 16 enzymes per nanoparticle respectively.

The diffusioosmotic drift and the background convection of the fluid within the glucose gradient in presence of the nanoparticles was then investigated. It is found that velocities of the fluid significantly vary by the mere introduction of a nanoparticle into the gradient. Velocity profiles of each nanoparticle in the glucose gradient were developed isolating the diffusioosmotic drifts. Finally, the diffusiophoretic and chemotactic components of the nanoparticles were quantified and isolated. It was found that the polymersomes experience higher mean-square displacement with directed self-propulsion velocities towards the region of higher glucose concentration. The liposomes experience a strong diffusioosmotic drift away from the glucose gradient, nevertheless, a slight reduction in these velocities was observed suggesting self-propulsion of the active liposomes towards the glucose incapable of overcoming the diffusioosmotic drift.

ACKNOWLEDGEMENTS

Primarily, I would like to express my sincere gratitude to my supervisor Prof Giuseppe Battaglia, for his guidance, continues support, inexhaustible patience, and astute criticism during the past four years. Working alongside such an esteemed and honoured academic has immensely impacted me and continues to inspire me to be a better scientist. My gratitude extends to Dr. Giorgio Volpe for being my secondary supervisor.

The work presented in this thesis would also not have been possible without Dr. Laura Rodriguez-Arco, Dr. Lorena Ruiz-Perez, Dr. Joe Forth and Dr. Ian Williams who require particular acknowledgement and whom I consider my mentors. I am deeply grateful to Dr. Laura Rodriguez-Arco for her guidance and unwavering support, particularly at the start of this thesis, which was very influential in shaping my experimental skills. My sincere gratitude goes out to Dr. Lorena Ruiz-Perez for her guidance on TEM imaging and constant encouragement during challenging times. A big thank you to Dr Joe Forth for his invaluable insights, tireless patience and accommodating help, especially throughout the pandemic. I am extremely thankful to Dr. Ian Williams who has been invaluable to this PhD journey. His knowledge, guidance and encouragement over the past three years have expanded my interests and imparted on me the skills needed to conduct higher quality research. He has definitely had immense patience while introducing me to everything I now know about conducting diffusioosmotic/diffusiophoretic experiments and particle tracking.

Additionally, I would like to particularly thank Ian and Joe for being supportive during these past pandemic years, as well as for helping with the preparation of this thesis, from proof-reading to providing invaluable comments, which have certainly made finishing it a less challenging task.

I would like to express my gratitude to Dr Alessandro Poma and Dr Aroa Duro-Castaño for providing the polymers used in this work. Thanks is due to Gabriel Ing for imaging the liposomes samples.

I am thankful to all members of the Molecular Bionics Lab for all the shared knowledge, memories, and friendships. I would particularly like to acknowledge Dr Diana Lourenco Matias, Dr Virginia Gouveia, Dr Diana Moreira Leite, and Dr Edoardo Scarpa who have always been a source of encouragement and mindful discussions. I must also thank Dr Carlos Nobel Jesus, Miss Barbara Ibarzo Yus, Miss Chiara Cursi, Mr Miko Sipin, Mrs. Maryam Al-Ghandi, Mr Valentino Barbieri and Miss Melis Pisiren, it is their kind and joyful presence that made my study and work in the laboratory a wonderful time. Special acknowledgements go out to Dr Belen Sola who have shared this PhD journey with me and has made this adventure enjoyable.

These acknowledgments would certainly not be complete without thanking the ones who have been with me through it all, my parents. They deserve a great deal of thanks for their endless love, support, and belief in me which has always been the source of my motivation in everything I do. My sisters, whom I love so dearly, and who have made my life full of joy since they entered it. It has been a blessing to experiencing the student life in the UK alongside both of them and I am grateful to their tremendous encouragement, support and understanding. Finally, my grandfather who wanted to see me submit this thesis.

Publications & Presentations

Publications

The minimal chemotactic cell

Azzurra Apriceno, Safa Almadhi, Ian Williams, Amatullah Akhtar, Lorena Ruiz-Pérez and Giuseppe Battaglia

In preparation

Self-digestive biodegradable polymersomes for glucose-responsive insulin delivery

Safa Almadhi, Joe Forth, Laura Rodríguez-Arco , Giuseppe Battaglia

In preparation

Interaction potential characterisation of nanovesicles in a glucose gradient.

Safa Almadhi, Ian Williams, Joe Forth, Laura Rodríguez-Arco, Giuseppe Battaglia

In preparation

Isolation of diffusiophoresis of nanovesicles: Towards accurate measurements of chemotaxis.

Safa Almadhi, Ian Williams, Joe Forth, Laura Rodríguez-Arco, Giuseppe Battaglia

In preparation

Presentations

Enzyme-driven chemotactic synthetic vesicles and applications in blood-brain barrier crossing

12th International Symposium on Polymer Therapeutics: From Laboratory to Clinical Practice, Valencia, Spain (May 2018)
Oral presentation and poster presentation

Deliver me

3MT: Three-minute thesis (May 2019)
Oral presentation

Chemotactic synthesis vesicles

3rd meeting of the UCL Cross-Disciplinary Network on Soft Materials, UCL, UK (June 2019)
Poster presentation

Side courses

SPERO DISCOVER: Entrepreneurial skills for PhD and doctoral students
UCL BaseKX, London, UK (January 2018)

SPERO ADVANCED: Advanced entrepreneurship skills for PhD Students-Part 1
UCL BaseKX, London, UK (February 2019)

SPERO ADVANCED: Advanced entrepreneurship skills for PhD Students-Part 2
UCL BaseKX, London, UK (June 2019)

TABLE OF CONTENTS

INTRODUCTION & OUTLINE

NANOMEDICINE AND ACTIVE MATTER FOR BRAIN DRUG DELIVERY

GLUCOSE OXIDASE LOADED NANOVESICLES

OVERCOMING DENSITY DRIVEN CONVECTION TO MEASURE CHEMOTAXIS AT THE NANOSCALE

NANOVESICLE INFLUENCED DIFFUSIOOSMOTIC FLOW IN A GLUCOSE CONCENTRATION GRADIENT

CHEMOTAXIS & DIFFUSIOPHORESIS OF VESICLES AT THE NANOSCALE

LIST OF ABBREVIATIONS

ATRP	Atom transfer radical polymerization
BBB	Blood-Brain Barrier
Cryo-TEM	Cryogenic transmission electron microscopy
DLS	Dynamic light scattering
DMSO	Dimethyl sulfoxide
DO	Diffusioosmosis
DP	Diffusiophoresis
GOX	Glucose oxidase enzyme
H_2O_2	Hydrogen peroxide
L_N	Loading efficiency
LRP1	Lipoprotein receptor-related protein 1
MSD	Mean square displacement
NTA	Nanoparticle tracking analysis
PBO	Poly(oxybutylene)
PBS	Phosphate buffered saline
PDPA	poly(2- diisopropylamino) ethyl methacrylate)
PEG	Polyethylene glycol
PEO	Poly(oxyethylene)
PMPC	Poly(2-(methacryloyloxy) ethyl phosphorylcholine)
PTA	Phophotungstic acid
rcf	Relative centrifugal force
Re	Reynolds number
RP-HPLC	Reverse Phase - High Performance Liquid Chromatography
SEC	Size exclusion chromatography
TEM	Transmission electron microscopy
UK	United Kingdom

LIST OF FIGURES

LIST OF TABLES

CHAPTER ONE

INTRODUCTION & OUTLINE

1.1 Introduction

This thesis is concerned with designing therapeutics that can navigate within the body towards diseased areas. The particular focus is on targeting the brain to address central nervous system (CNS) disorders and diseases, diseases localised in the brain and spinal cord.[1] This idea is explored by engineering nano-sized carriers that can move in response to glucose gradients. 60% of our body's glucose is consumed and converted into energy by our brain.[2, 3] Our body has developed several ways to maintain such a metabolic demand by creating gradients across the brain barriers.[4-6] In between meals the concentration of glucose in blood is 4-6 mM while 1-2 mM is the concentration in the brain interstitium. This gradient is maintained by the uptake of glucose into the astrocytes and neurons as well as the glucose metabolic degradation in cells. [5, 6] Hence engineering nanocarriers able to sense and exploit glucose gradients will allow for more efficient delivery of the therapeutic payload to the brain. This is the premise of this thesis.

Novel modified nanocarriers are produced that show superior phoretic motion towards glucose.[7] In particular, the chemotactic propulsion of these carriers was experimentally observed and quantified. Two minimal criteria are required to design self-propelling nanocarriers: (i) breaking the membrane symmetry by incorporating a patch or a pore and (ii) the chemical sensing of the nanocarriers to glucose by using enzymes.[8]

To successfully attain these chemotactic nanocarriers, their preparation methods were optimised to improve uniformity in size and shape as well as sample reproducibility. In addition, a method to characterise the interactions between non-ionic molecules in solution and polymer or lipid-coated surfaces by measuring fluid flows was developed.

1.2 Thesis structure and outline

This thesis is organised as outlined below. The background information and motivation are covered in chapter 2. This chapter is split into three main sections. Sections 2.1 and 2.2 introduce nanocarrier-assisted delivery systems and describe the rationale behind the development and design of these systems. Nanovesicles, a class of nanocarriers, are introduced, and their journey within the body is described, highlighting the benefits and challenges of nanovesicles such as liposomes and polymersomes. The second section, Section 2.3, describes the fundamental physical laws of motion at the micro and nanoscale and discusses their relevance in a series of examples. This is followed by highlighting examples of natural and artificial systems that move at this length scale, focusing on the design and the different mechanisms used to achieve them.

The final section, Section 2.4, introduces the concept of phoretic behaviour and its origins. The possibilities and challenges in creating biologically compatible active nanoswimmers are discussed. It highlights the practical nanovesicles to use (such as polymersomes and liposomes) and the sensible propulsion mechanisms which utilise available gradients in the body. This chapter is concluded by providing a description and rational design of the proposed nanovesicles to be engineered in this work as potentially autonomously propelling units.

Chapter 3 details the specifications of the materials and methods used in this thesis. These include the nanovesicle preparation, physicochemical characterisation protocols as well as the experimental procedures to characterise nanovesicle migration.

The experimental results are covered in chapters 4 to 8. This thesis explores two types of nanovesicles, either assembled from block copolymers (polymersomes) or lipids (liposomes). A picture illustrating these is drawn in Figure 1. The main focus of chapter 4 is the preparation of these nanovesicles. Section 4.1 focuses on the bicomponent polymersomes preparation, which is optimised to attain a monodispersed, vesicular sample. The liposome's preparation is the focus of section 4.2, the preparation of pristine liposomes is described first as previously reported in the literature.[9] These are then modified post-assembly by the insertion of α-hemolysin, a cytotoxic protein capable of binding to the membrane of eukaryotic cells, to form nano-sized pores. These membrane modifications break the symmetry of the spherical nanovesicles. This is an important criterion to allow the vesicle to sense the direction of a concentration gradient.

Another essential criterion that fuels the motion towards the sensed gradient is the need for an enzyme that effectively act as the engine. Hence, both the polymersomes and liposomes are then loaded with glucose oxidase enzyme, in chapter 5. Once the enzymes were successfully encapsulated, the sensitivity of the polymersome system towards the presence of glucose, the enzyme substrate that fuels the motion, in the surrounding environment was explored next. This was monitored over time, thus, validating the responsiveness of the glucose oxidase loaded polymersomes towards the glucose.

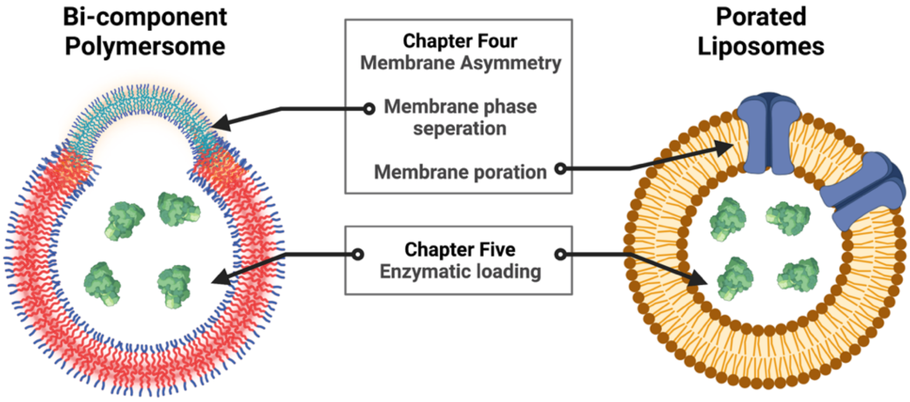

Figure 1. A schematic illustrating the two types of nanovesicles explored in this thesis. (left) Bi-component polymersomes consisting of a PMPC-PDPA (red and blue) and PEO-PBO (green and purple) copolymers loaded with glucose oxidase enzyme (green) within the aqueous core. (Right) Porated liposome formed by a phospholipid membrane (yellow and brown) which is porated with α-hemolysin (purple pore) and encapsulated with glucose oxidase enzyme (green). The membrane modifications in polymersomes and liposomes are the focus of Chapter 4. The enzymatic loading of glucose oxidase of both the nanovesicle systems is the focus of Chapter 5. Not drawn to scale. Drawn in Biorender® with permission to publish.

Once the vesicular systems were prepared and responsiveness to glucose validated, the migration behaviour of these in a glucose gradient was investigated. Chapter 6 looks at the previously used experimental setup by Joseph et al.[8], to evaluate the migration of polymersomes. This highlighted the formation of a background convective flow that overshadow any autonomous nanovesicle movement, thus indicating the inefficiencies of this setup to characterise motion at the nanoscale.

To overcome and suppress the underlying convective flows, another experimental setup based on previously reported microfluidic chambers by Williams et al. [10] was used. Chapter 7 firstly introduces the fluid flows in such a setup. The influence of the nanovesicles on this fluid flow was explored next, with a particular focus on the measurements of velocity profiles. Comparing these velocity profiles with theoretical flow profiles reported by Williams et al. This setup was also used to develop a method to characterise the nature of the glucose-nanovesicle interactions based on fluid flow measurements.

Chapter 8 uses the identical experimental setups established in Chapter 7 to investigate the behaviour of the modified bicomponent polymersomes and porated liposomes themselves within a glucose concentration gradient. Successful detection and isolation of chemotactic motion of liposomes and polymersomes are reported. This is the first and most accurate measurement of chemotactic motion in nanovesicles to date.

The thesis is concluded with Chapter 9 that summarizes the main findings of this thesis and describes the opportunities for future work to progress these systems into biological applications.

CHAPTER TWO

NANOMEDICINE AND ACTIVE MATTER FOR BRAIN DRUG DELIVERY

2.1 Brain Drug Delivery

Brain diseases and disorders are a major public health problem, affecting 1.5 billion people and accounting for 9 million deaths worldwide in 2016 alone.[11] A study conducted in Europe by the UN World Health Organisation (WHO) estimated that in 2004 the annual economic cost of such diseases was about € 139 billion (£ 116 billion) and projected to rise.[12] While advancements in the treatment and prevention have led to a substantial decrease in mortality of cardiovascular diseases (decreased by 70% since 1950) and cancer, decreased by 16% since 1950[13], the same cannot be said about brain disorders. For example, mortality from Alzheimer's disease (AD) has increased by 68% in the past decade, and the total expected prevalence by 2050 is to be 13.8 million cases.[14] The estimated total cost of care for AD alone in the US in 2012 alone was over $ 200 billion (£ 146.2 billion) and is projected to rise to $1.2 trillion (£ 0.9 trillion) in the next 40 years.[14] A similar trend in economical cost and progression of disease is evident in other brain diseases such as Parkinson's disease,[15] Huntington's disease[16] and certain types of multiple sclerosis.[17]

One of the most challenging tasks in oncology is the treatment of brain tumours.[18] The most frequent and lethal brain tumour is Glioma arising from the uncontrolled proliferation of glial cells.[19] Depending on the speed and the degree of infiltration to nearby brain tissues, glioma can be classed as low-grade (I and II) or high grade (III and IV).[20] High-grade Gliomas are more aggressive due to their rapid proliferation towards healthy brain tissues. Current treatment options include radiation, surgery, chemotherapy or their combination.[21] Despite these therapies, the median survival time for patients (14.6 months) has not significantly changed for 30 years.[20, 22] While the same treatments have decreased the mortality rates in most cancers,[23] the same trend is not conserved for brain tumours. The main hindrance is the impermeability of the brain to most drugs. This is due to the protective Blood-Brain Barrier (BBB), which shields the brain by restricting access of harmful compounds or substances from the circulating blood.[24]

The BBB is used to describe the unique physiological properties of the endothelial cells that vascularize the CNS.[25] The BBB is very selective and strictly regulates the movement of ions, molecules and cells across the brain.[26] BBB endothelial cells adhere among each other forming protein complexes called tight junctions. This blocks the passage of most molecules across the BBB and restricts the passage of only small molecules such as H_2O, O_2 and CO_2 by diffusion through the lipid membranes.[4, 26] Essential nutrients such as glucose, lactate, amino acids, and fatty acids access the brain through specific transport systems, known as solute transporters.[27] Another type of these transport systems acts to exclude potentially harmful compounds from the brain and back into the blood, known as efflux transporters.[28] Larger hydrophobic molecules like peptides and proteins are typically transferred by specific receptor-mediated transcytosis.[29] Transcytosis is a process in which large molecules are transported from one side of a cell to the other. Here the macromolecules are entrapped into a vesicle (endosome) on one side of the cell, which is then drawn across and ejected at the other side. These properties, ranging from passive and active features, make the BBB highly selective towards the substances that can enter the brain.[30, 31] This selectivity means that the BBB also restricts the entry of therapeutics, which makes the treatment of brain cancer a difficult task.

As a consequence of the relatively poor accessibility of therapeutics to brain tumours, therapeutic drugs are administered at a significantly higher dose. This inevitably elevates the toxicity in healthy cells.[32] Particularly in the case of chemotherapeutic drugs, the administration of higher doses leads to fatal damage to healthy cells.[33] This results from the non-selectivity of the chemotherapeutic agents, which preferentially destroy proliferating cells.[34] While this is a sound strategy to eliminate cancer, which is a disease involving the uncontrolled cell proliferative growth that attack and multiply onto nearby cells and tissues of the body, the non-selectivity of the agents also results in damage of healthy normal proliferating cells. These severe adverse effects caused by chemotherapeutic drugs on normal healthy tissues and organs are a major reason behind the high mortality rate in cancer patients.[23]

The BBB is a hurdle, not only in the treatment of brain cancer but in the treatment of most central nervous system (CNS) diseases.[35] In fact, the BBB restricts more than 98% of known drugs from entering the CNS from blood circulation.[35] Therefore, there is a need for CNS drugs that can (i) be delivered to the brain but have limited interactions with other cells, tissues and organs (ii) that can access the brain, i.e., transport across the BBB to reach the required therapeutic site. Achieving this would reduce side effects and toxicity while improving therapeutic efficacy.

The concept of targeting drugs to their site of action was first introduced by Paul Ehrlich and popularised as the “magic bullet”. The idea of this concept is to selectively target and kill microbes (such as bacteria) without harming the body.[36] Ehrlich approached this concept in two steps, the first being screening for drugs toxic to the pathogen, and the second is modifying these to be more specific and less toxic to the host.[37, 38]

About 50 years later, Nobel physicist Richard P. Feynman proposed in his 1959 talk “There’s Plenty of Room at the Bottom”, an approach where individual atoms, molecules or microscopic components could be manipulated using precise tools which build and operate even smaller-scale machine tools and so on all the way to the atomic level.[39] Feynman proposed that a small machine could be built using this approach. When in the body, it could roam inside the blood vessel and travel to a specific diseased location within the body to carry out surgery. [39] Other potential medical applications of this technology are using these small machines to deliver drugs to cure diseases.[40]

Since then, and for more than a century, these ideas have fascinated many researchers to investigate further and led to the discovery of different nanometre-scale drug delivery devices (called nanomedicine).[41] The field of nanomedicine is the application of nanotechnology in medicine.[42] This area of studies aims to overcome drug-associated problems such as targeted delivery into cells, delivery of poorly water-soluble drugs, co-delivery of multiple drugs for combination therapy and in *vivo* efficacy readings of a therapeutic agent in real-time. [43, 44]

2.2 Vesicles for drug delivery

Some well-known nanometre-scale delivery systems include DNA-drug complexes,[45] liposomes,[46] polymer-drug conjugates,[47] polymer-protein conjugates,[48] micelles and polymeric particles.[49] Few of these have made it to the clinic with about 50 products based on liposomes.[50] The most recognized pharmaceuticals of liposomes are based on pegylated doxorubicin liposomes, known as Doxil®, which are used for the treatment of cancer.[51] Liposomes are vesicles formed by the self-assembly of amphiphilic molecules known as phospholipid into a phospholipid bilayer membrane entrapping an aqueous core. The phospholipid membrane consists of a hydrophobic bilayer surrounded by hydrophilic head groups, allowing these vesicles to encapsulate both hydrophobic drugs in the membrane and hydrophilic drugs in the core, Figure 2.

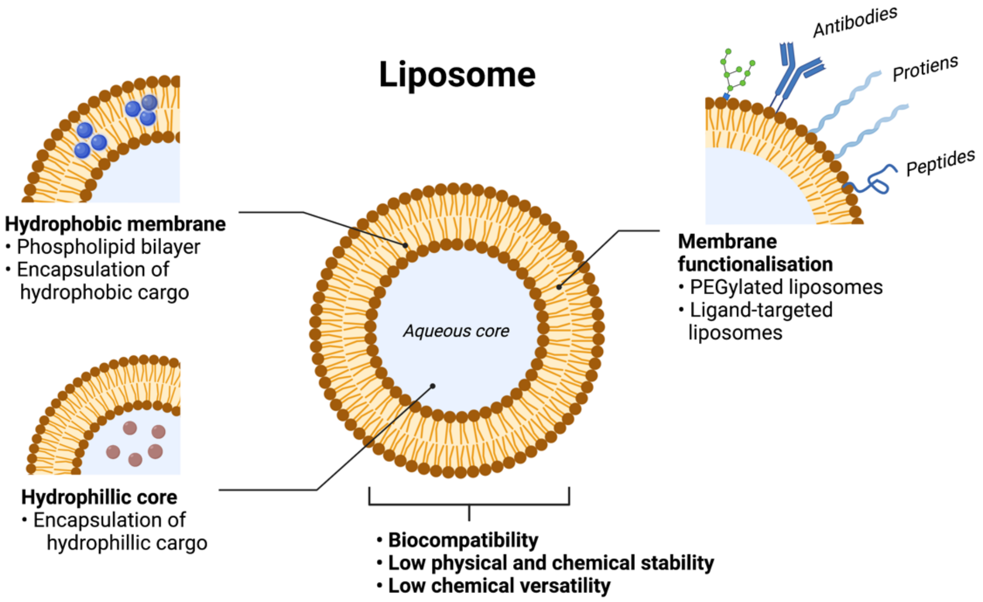

Figure 2. Schematic representation of the compartmental architecture of liposomes for drug delivery.

Despite these benefits, liposomes possess low physical and chemical stability.[52, 53] Consequently, interest in amphiphilic diblock copolymer assemblies has grown due to their superior chemical and physical stability,[54] as well as chemical versatility.[55] Amphiphilic block copolymers are able to self-assemble into different structures, one of which is the vesicle structure, known as polymersomes.[56] Polymersomes resemble the liposomal structure with an aqueous core entrapped within a bilayer membrane comprising of hydrophobic polymer chains, stabilized by the surrounding hydrophilic polymer brushes, Figure 3. This structural resemblance contributes to the liposomal structural advantages of polymersomes whilst maintaining the stability and versatile chemical properties of the block copolymer.[55,57]

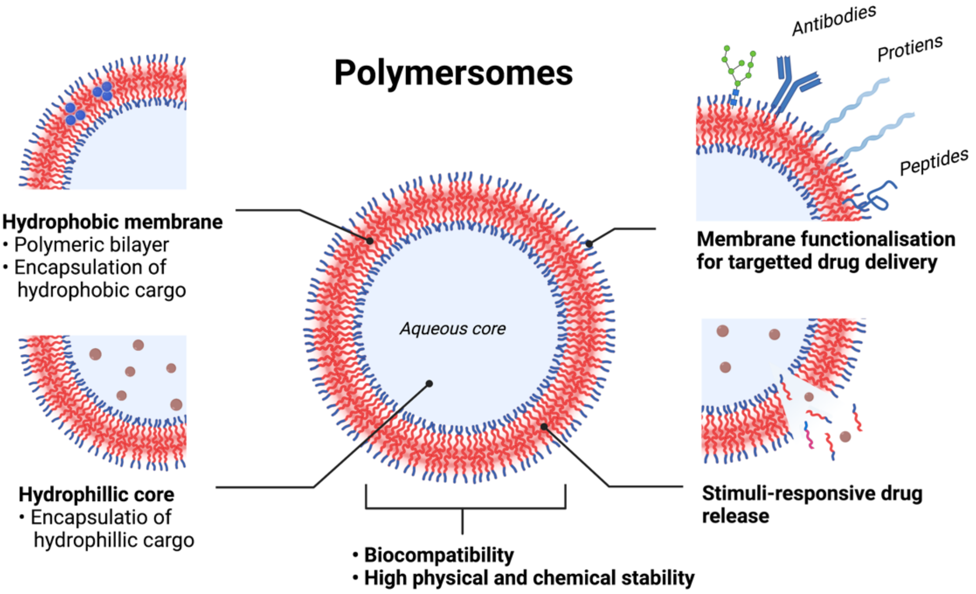

Figure 3. Illustration of the compartmental architecture of polymersomes (that resemble liposomes) and the strategies employed to improve the drug delivery.

Recent advancements of liposomes and polymersomes as drug delivery systems are highlighted in a number of fields such as medicine, pharmacy and biotechnology because of their ability to encapsulate a variety of therapeutic molecules such as hydrophilic and hydrophobic drugs,[58] proteins and peptides,[59] DNA and RNA fragments[60,61] and combinatorial drug loading.[62] Therefore, a lot of work has been directed to developing nanovesicles capable of targeted delivery, particularly the development of stimuli-responsive polymersomes to control the release of drugs. To date, biocompatible and/or stimuli-responsive polymersomes are prepared using block copolymers that are responsive to pH, temperature, redox conditions, light, magnetic field, and ionic strength.[63]

To further enhance the specific target delivery, targeting moieties such as antibodies can be introduced to the surface of liposomes and polymersomes to act as guiding agents to allow for interaction with specific cells.[64] On arriving at the target site, the therapeutics are released in response to an external stimulus, hence enhancing the therapeutic efficacy and minimizing side effects.[60] Figure 3 summarises the strategies employed to improve the polymersome delivery system.[65]

Both liposomes and polymersomes have been studied as brain drug delivery systems. What makes these nanovesicles specifically attractive for targeted delivery to the brain is the ease of surface modifications. In which they can be covalently linked to specific targeting agents that allow the nanovesicles to exploit natural transport pathways for the passage across the BBB. The most common example are receptors that mediate the crossing of macromolecules like transferrin and insulin receptors or low-density related protein 1 (LRP-1) receptors.[66] These modifications also entail the incorporation of ligands on the surface that may also serve to direct the nanovesicles to specific diseased cells within the CNS such as tumours[67] or even protein aggregates in the case of senile plaques in AD.[68] Recently, ligand surface-modified polymersomes with dual-targeting properties were developed. These use angiopep-2-conjugated polymersomes encapsulating doxorubicin and are able to exploit the transport of the nanovesicle by LRP-1 receptors, which are overexpressed in both the BBB and glioma cells. This makes these systems able to cross the BBB and internalize into glioma cells by the conjugation of a single, short peptide.[69, 70]

Surface modifications by polyethylene glycol (PEG), also known as PEGylation, have been shown to make these nanovesicles resistant to immune systems and increase circulation time in the blood.[71] This is due to the stealth characteristics of the PEG hydrophilic block, which minimize the interfacial free energy by introducing steric repulsion on the surface.[72]

Focusing on the most recent advancements, biocompatible and biodegradable polymersomes based on the poly[(2-methacryloyl)ethyl phosphorylcholine]–poly[2-(diisopropylamino)ethyl methacrylate] (PMPC-PDPA) block copolymers have been developed.[73, 74] These offer the dual-targeting properties for delivery to the brain and glioma cells while benefiting from a stimuli-responsive release of the encapsulated therapeutics within the glioma cells (pH-sensitive drug release).[56]

These nanovesicles are potentially very useful and fulfil many traits of Ehrlich's "magic bullet". Nevertheless, an important missing trait is that the drugs should move straight to the target site in the body and only interact with the target cells or molecules.[75] This is not the case for nanovesicles, in fact, this is not the case for any known drug. When in the body, all drugs (or nanovesicles) pass through a complex pathway and encounter many contacts during their journey to the target site. The possible interactions of the drug with multiple sites in the body results in undesirable side effects. These interactions can result from the expression of potential active sites that resemble the targeted site.[76] For example, in the case of the ligand-conjugated nanovesicles to the brain, the receptor of interest that the ligand would interact with to mediate the crossing into the BBB can be present in other organs leading to the unwanted internalization of the nanovesicles into these organs resulting in side effects.

Unfortunately, there is no drug or nanomedicine that have the ability to directly reach the target and bypass these undesirable pathway interactions.[75] In an attempt to limit the interference of nanovesicles with serval targets and consequently interact with a single target, a handful of researchers have attempted the task of developing nanovesicles that can autonomously move (or swim) in the blood vessels to reach a single, predetermined targeted site. This is not a straightforward task as these nanovesicles would need to overcome stringent constrictions imposed by the physics at the nano and microscopic scale.

2.3 Active matter

The engineering of artificial autonomously moving nanovesicles for drug delivery is a major challenge in nanomedicine.[77] In general, autonomous motion and activity are fundamental in living systems from bacteria to sheep. Organisms adopt different methods of locomotion (i.e. movement, taxis) to search for food, orient towards light, avoid toxins, coordinate virulence and synchronize collective behaviour.[78] However, the physical laws of motion needs to adapt to the small scale to understand the movement of these systems.

The current interest towards understanding these systems and engineering artificial variants have stimulated the relatively new field “Active matter”.[79] This field focuses on the physical aspects of propulsion mechanisms and motility-induced collective behaviours ranging from people, birds, fish to cells and micro and nanomotors.[80] Mostly active matter examples are biological in origin, however, the growing interest in designing artificial active systems is rapid.[81]

2.3.1 Fundamentals of motion at the nano and micro-scale

The differences in movement strategies of fishes and bacteria were first investigated in 1951 by Sir Geoffrey Taylor[82] and followed by Edward Mills Purcell in 1977 in the famous and illustrative article "Life at low Reynolds number"[83].

2.3.1.1 Reynolds Number and The Scallop Theorem

Reynolds number (Re) characterizes the ratio of inertial to viscous forces governing motion at the macro-, micro- and nano-scales. It is a dimensionless parameter defined as,

$$Re = \frac{Inertial\ forces}{Viscous\ forces} = \frac{\rho v L}{\eta} \qquad (1)$$

where ρ is the fluid density, η is viscosity, v is velocity, and L is the length of the organism/object. The motion in the macroscopic world is governed by inertial forces; the Re number is high. For smaller objects, both velocity and length of the object are small, hence small Re number (<<1). The inertial forces contribution is insignificant while viscous forces dominate motion, this applies to micro and nano systems (natural or synthetic).[83] For example, the Re of bacteria is in the order of $10^{-6,}$ and spermatozoa is 10^{-2}.[84]

To a micro and nanoscopic object water can feel like a very viscous liquid creating resistance to movement of the object. This could be visualized as the resistance a swimmer would face trying to swim in a pool of almost solid molasses.[83] Because of this resistance, swimming strategies at the macroscale fail at the micro and nanoscopic scale. This is a result of two main challenges imposed by the low

Reynolds number regime which need to be taken to account when designing nanovesicles with nanoscale-appropriate swimming strategies.

The first relates to the fact that contributions of inertia to motion effectively disappear; hence constant supply of energy is required to maintain motion. In other words, to sustain motion at low Reynolds number a constant force must be applied, this can be chemical, magnetic, electric, or even acoustic. This means that macroscopic propulsion mechanisms like recoil from chemically produced bubbles, in which the force (recoil force) is applied only at the moment bubbles are released, i.e., not constant supply of force, are ineffective in generating motion at the nanoscale.

First challenge:

To maintain motion, a constant supply of energy is required.

The second obstacle to achieving motion at this realm is that movement of the object be non-reciprocal. This is a big difference between the design of nanoscale propellers/swimmers. To clarify this, Purcell framed the well-known Scallop Theorem.[83]. Scallops are animals that can swim in seawater by a simple swimming mechanism, Figure 4. It involves the repeated opening and closing of their two shells, using one degree of freedom. Now, if we imagine this scallop swimming in a low Re number setting, i.e., the absence of inertial forces, the scallop will not be able to cover any distance. This is to do with the reversibility at low Re numbers, in which the opening motion of the shells will cause fluid to move, when the shells close the exact opposite fluid motion occurs, i.e., time reversal. A way for the scallop to move without inertia, is by breaking the time-reversal symmetry. This can be achieved through non-reciprocal motion (each motion leading to a different flow of fluid), like through motors that have more than one degree of freedom.

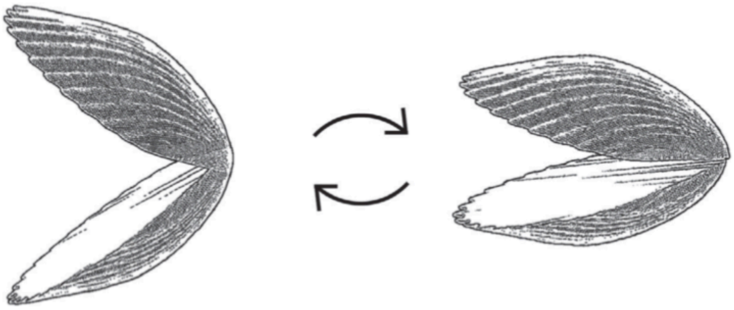

Figure 4. The scallop theorem: Schematic of the reciprocal motion of a scallop. This motion consists of cycles of closing and opening its two shells. With each cycle, the scallop returns to its original shape with little net displacement. The scallop theorem states that in low Reynolds numbers (i.e., viscous fluid), this reciprocal motion will not result in any propulsion or net displacement. Reprinted from ref 85 and 83.

For example, bacteria such as Escherichia coli (E.coli) have filamentous appendage known as flagellum, which protrudes from the body of the bacteria into the external medium. The flagellum facilitates the motion in the low Re number realm by a series of non-reciprocal movements, which enable the bacteria to create a propulsion motion.[78] Sperm cells also move due to the back and forth rhythmical longitudinal movement of the flagellum.[86] Neutrophil motion, on the other hand, is facilitated by the polarised intercellular response to the chemical gradient, which allows the cell to undergo morphological changes. The cell polarisation leads to an asymmetric distribution of the intercellular structure allowing for directional movement.[87]

Scientists have studied and successfully replicated many of these natural mechanical motions. Such as the artificial nanoparticles that mimic bacteria by propelling using rotating or beating flagella, known as flagellar propulsion, which have been explored extensively in the literature.[88] More interesting is work by Qie et al., which reported the capability of a micro-scallop system, which is a single-hinge micro sized scallop, that can achieve propulsion at low-Reynolds numbers provided the activation is asymmetric (no propulsion when it is symmetric).[85] In this case, this asymmetry was achieved by breaking the time-reversal symmetry in which the motion of the scallop consists of a cycle of slow-open and fast-close. In general, in order to induce motion at this realm and break symmetry either by controlled shape changes or even surface reactions.[89]

Second challenge:
To cover distance, asymmetry needs to be incorporated into the design of the nanovesicles.

2.3.1.2 Brownian motion

Another challenge to achieving motion for nanoobjects has less to do with low Re number limits and more a consequence of the small size of these objects. Brownian diffusivity is the main contributor to the nanoparticle motion in the absence of turbulence. Brownian motion is the random motion of a particle in a fluid due to the continuous collisions with the medium molecules. The impact of these collisions significantly increases as the size of the objects decreases. The randomness of this process interferes with the directionality of motion, and nano-sized objects appear to diffuse randomly.

The randomness allows only probabilities to be predicted in which the nanoparticle is prone to move with equal probability in any direction, and the direction of the moved steps should in no way correlate to the direction of the subsequent step. The mean square displacement (MSD),$\langle x^2(t)\rangle$, can be used as a characteristic quantity for such systems. It describes the mean value of the square of the net displacement, x, after n steps, which corresponds to time t=nτ, where τ is the time between subsequent steps. The mean square displacement in N dimensions is given b

$$\langle x^2(t)\rangle = 2ND_Tt \qquad (2)$$

where D_T is the translational diffusion coefficient. For a single spherical particle of radius R_p , in a homogenous environment (in absence of physical barriers or other particles, and in a constant distribution of energy source), the D_T is given by:

$$D_T = \frac{k_B T}{6\pi\eta R_p} \qquad (3)$$

where k_B denotes the Boltzmann constant, T is the temperature and η the fluid viscosity. The Brownian effect is linearly related to the thermal energy and inversely related to the particles size, i.e., it increases with decrease in particle size. In addition to translational diffusion, particles also undergo rotational diffusion which happens within a characteristic time scale, τ_R, that is the inverse of the particle's rotational diffusion coefficient.

$$D_R = \tau_R^{-1} = \frac{k_B T}{8\pi\eta R_p^3}\,. \qquad (4)$$

The rotational diffusion is linearly related to the volume of the particle (R_p^3). This shows that as the particle size decreases from 1μm to 100 nm, the translation diffusion would increase by one order of magnitude, but the rotational diffusion would increase by three orders of magnitude. Hence it is essential to take Brownian effects into consideration when designing of nanovesicles that can propel in fluid, as they can interfere with the directional motion by causing their constant reorientation.

Third challenge:

Nanoscopic particles encounter significant randomization by Brownian effect.

2.3.2 Active motion in natural and artificial systems

The movement of a particle is active when energy from the surrounding (chemical, magnetic, acoustic) is converted to mechanical energy (generation of motion). This can be achieved at the micro and nanoscale by overcoming the previously stated limitations.

Active motion is abundant in nature. Over all the length scales, living organisms are typical examples of active particles. They convert chemical energy from metabolized nutrients to kinetic energy resulting in movement. On large length scales, fish move by repeatedly flexing their elastic body and birds flap their wings. On the micron scale, bacteria, algae and cells are great examples. We have seen how bacteria uses its non-reciprocal flagellar motion for directional movement. Another common example is eukaryotic cells such as Dictyostelium discoidum which typically crawl on other cells and tissues by protrusion and retraction facilitated by the transformation of their cytoskeleton.

Actively moving biological cells have overcome the low Re number limitations and Brownian fluctuations giving them the advantage of being autonomous *in vivo*, interacting selectively with targeted sites and inhibiting growth of diseased sites. However, safety and performance concerns have been raised such as undesirable inflammatory response and cell mutation over time, [84, 90] further supporting the need of artificial active particles.

Initial efforts by scientists to develop artificially propelling particles have focused on the microscopic scale, yielding a variety of propulsion mechanisms. Some of which are bio-inspired like the flexible or helical propellers that mimic the bacterial flagellar propulsion, Figure 5A and B. Others achieve micropropulsion by exploiting physical mechanisms that are not biological in origin such as catalytic Janus particles, Figure 5D. An important class of active particles based on physical mechanism are self-phoretic particles, which propel as a result of a local generated chemical gradients (self-diffusiophoresis), electric potentials (self-electrophoresis) or thermal gradients (self-thermophoresis).

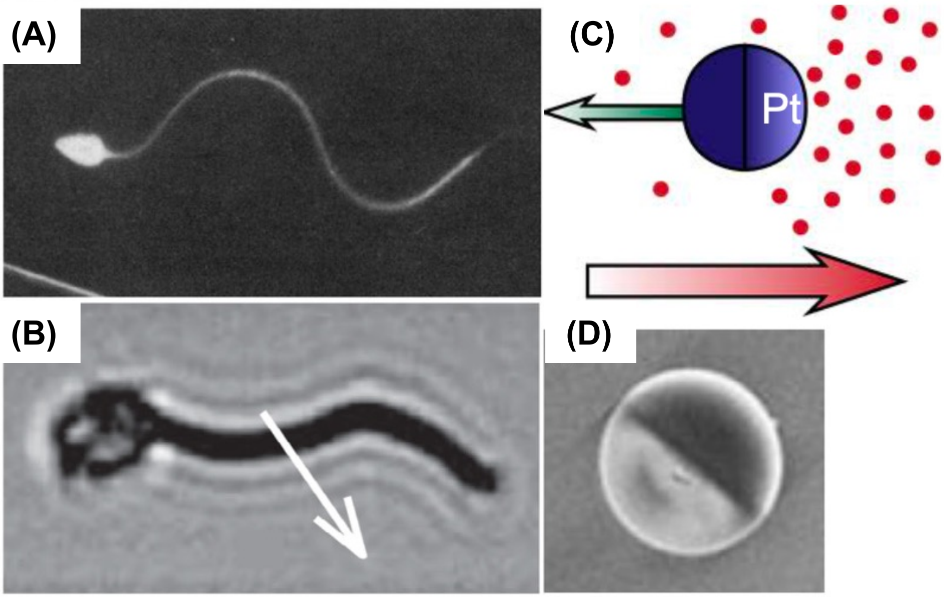

Figure 5. The different propulsion mechanisms employed by (A) A sea-urchin spermatozoon with planar flagellar beating. (B) A bacterium (V. alginolyticus) propelling with a rotating helical flagellum. (C) A Janus (PtSiO2) catalytic motor propelling (green arrow direction of propulsion) by generating the local gradients of chemical concentration due to asymmetric surface chemistry (red arrow indicated the direction of increase in gradient concentration), and (D) its TEM micrograph. Reproduced from ref 84.

2.4 Phoretic forces

As stated in section 2.3.1.1, the second fundamental challenge to achieve self-propulsion at the micro and nanoscale is breaking symmetry. The most instinctive ways, adapted from biological systems, are employing helical propellers mimicking beating bacterial flagella which yield non-reciprocal motion. However, the symmetry break can be also obtained without the need of such complicated geometries. This alternative relies instead on an asymmetry in physical properties of the surrounding medium. This was initially observed in the phoretic force experienced by spherical colloids within a heterogenous distribution of physical or chemical properties of a fluid. The particle motion can be triggered by the phoretic force such as a result of either temperature or chemical gradients, known as thermophoresis and diffusiophoresis respectively. The design of particles that can generate these gradients locally themselves promoting their own directional motion are referred to as self-propelling phoretic particles.

To explain this, I start this chapter by introducing the basic features of phoretic forces, and their origin. I will start by describing the first discovered phoretic motion which is electrophoresis. This was then followed by the findings related to phoresies in uncharged solutions by either chemical or temperature gradients, diffusiophoresis and thermophoresis.

The second subsection delves into the self-propelling phoretic particles with major emphases on chemical gradients (self-diffusiophoresis) describing how they demonstrate their own local gradients and how they achieve this propulsion. Finally, a few examples of enzyme powered micro and nano particles that achieve chemotactic like behaviour by controlling phoretic effects.

2.4.1 The origins of phoretic forces

This phenomenon is exclusive to the micro and nanoscopic world, in which objects of this length scale tend to drift up or down physical or chemical gradients. Unlike the motion of magnetic particles in the presence of an external field, movement due to phoresis is solely a non-equilibrium effect.[91]

This phenomena was first reported by Ferdinand Frederic Reuss in 1807, who observed that floating clay particles in water moved in response to a constant electric field.[92] These clay particles were not subjected to an external force and the motion was caused by the mere reorganization of water ions, known as electrophoresis. Since then, scientists have developed a variety of applications of electrophoresis. One of the most known is using electrophoresis to separate proteins or DNA and RNA mixtures by size and mobility.[93]

Later this movement was also reported to occur in uncharged heterogenous solutions both in experimental work and using computational simulations.[94, 95] This phenomena was observed in gradients of non-electrolytes and is known as diffusiophoresis or chemophoresis.[96] More recently, the motion of particles has been shown not to be confined with a heterogenous solution of charged or uncharged solutes, but also homogenous solutions in the presence of temperature gradients, termed thermophoresis. This was first observed by the influence of temperature gradients on the diffusion of salt by Carl Ludwig.[97] This phenomenon is not to be confused with thermal convection, which is the movement of fluid in a temperature gradient, this is the movement of micro and nano-sized particles themselves in a temperature gradient. A theoretical explanation of thermophoresis was attempted in 1879 by Carles Soret, and despite all the efforts that followed a predictive model is still lacking .[98]

All these phoretic migrations presented above are all a result of non-equilibrium effects and strong interfacial phenomena. I draw your attention to the main focus of this thesis which is diffusiophoresis as a potential mechanism to drive drug delivery in nanovesicles. Thus, the focus from here on is on diffusiophoretic forces that drive migration of particles. For further information on electrophoresis and thermophoresis and the fields that drive their migration, the reader is referred to read these comprehensive reviews.[99-101]

Phoretic motion is fundamentally very different from any other force-driven motion. In that, force is not applied on to the particles to drive this motion and the motion is driven purely by an interfacial phenomenon, known as diffusioosmosis (DO). Generally speaking, most of the interfaces between particle and the solute are considered insignificant to the motion of the particle. Thus no-slip boundary condition is commonly applied to simplify solving mathematical and numerical fluid dynamic equations.[102] However, in the case of phoresis, the interfacial particle surface-solute interactions become important. To understand diffusiophoresis migration let us first have a look at the principal of diffusioosmosis.

2.4.2 Diffusioosmosis fluid flow

Diffusioosmosis is the generation of a fluid flow due to the interactions of an externally imposed concentration gradient with a surface. These interactions happen within a small distance, typically a few nanometres, from the surface. The main type of interaction between the neutral solute and the surface are van der Waals forces and steric interactions.[103] These interactions can be attractive or repulsive i.e., the solute molecules “like” or “do not like” the particles surface, respectively. This region where interactions happen is known as the interfacial layer, Figure 6.[104] The potential (U) of these interactions decays further away from the particles surface and disappear beyond the interfacial layer.

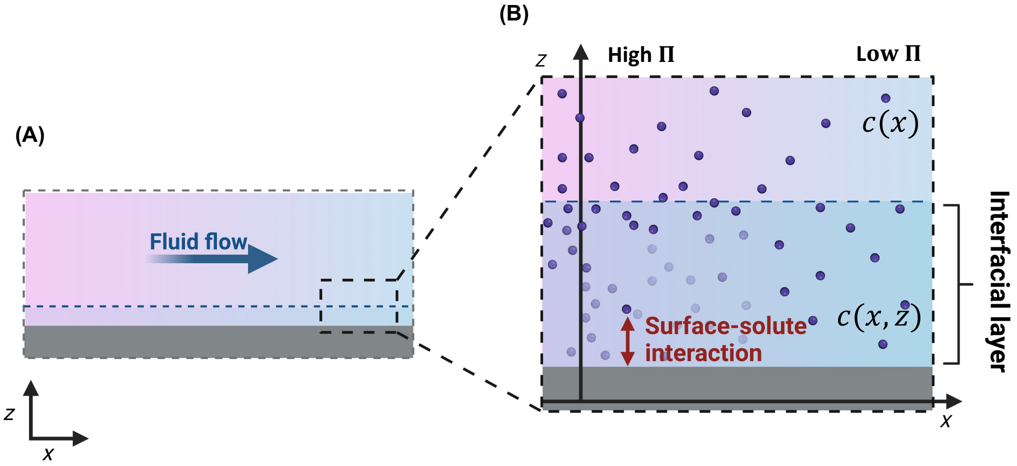

Figure 6. Schematic illustration of the (A) the fluid flow generated outside the interfacial region due to diffusioosmosis. The slip velocity of this flow is characterized by the osmotic pressure (Π) gradient which increases linearly with solute concentration (high in pink and low in blue) and the slip coefficient which is related to the concentration close to the surface $c(x,z)$ *and that far from the surface* $c(x)$*.*

The generated flow exhibits a gradient of velocity limited within the interfacial region. Beyond this region, the velocity of the flow is quantified by the slip velocity (v_s),

$$v_s = \Gamma_{DO}\left(\frac{d\Pi}{dx}\right), \tag{5}$$

where Π is the osmotic pressure generated far from the wall, and Γ_{DO} is the slip coefficient given as

$$\Gamma_{DO} = -\frac{1}{\eta}\int_0^{\infty} z\left[\left(\frac{c(x,z)}{c(x)}\right) - 1\right] dz. \tag{6}$$

In which $c(x)$ is the concentration at position x far from the surface, and $c(x,z)$ is the position near the surface at height z, Figure 6.[91, 105-107]

In the case of an attractive solute-surface interaction, the solute molecules experience a negative potential energy profile, exemplified by the dotted surface interaction potential profile, Figure 7. The interaction potential U is strong near the walls and vanishes beyond the diffusive interfacial layer. This potential well leads to an excess of solute within the interfacial layer, thus a slip coefficient ($\Gamma_{DO} < 0$). Additionally, the presence of solute at the walls induces an osmotic pressure, which is proportional to the solute's concentration. As a result of the solute gradient an osmotic pressure gradient occurs within the diffusive interfacial layer close to the surface. Hence driving the slip velocity (v_s), towards the low concentration.

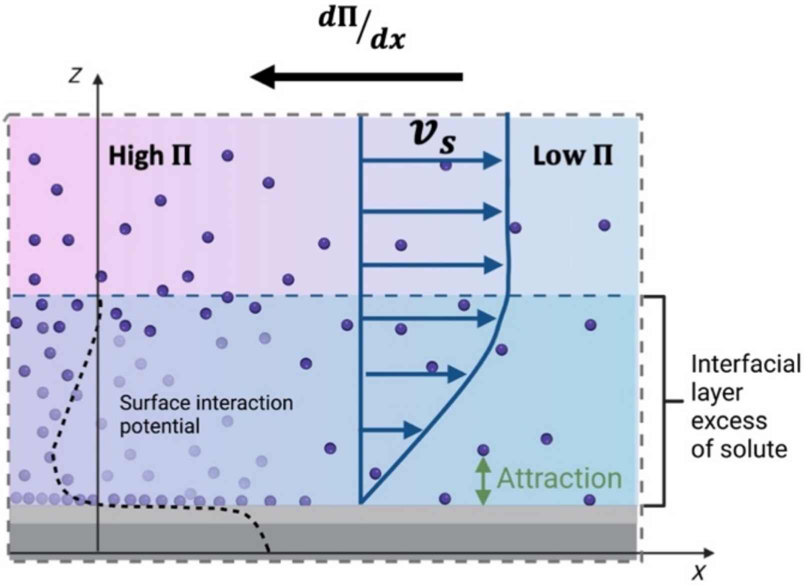

Figure 7. An illustration of the attractive solute-surface interaction facilitating diffusioosmotic fluid flow. The solute (purple sphere) gradient is shown with a maximum concentration (pink region) and minimum concentration of (blue region). The interactions between the solute and the walls happen within the diffusive interfacial layer which is the region near the surface. In this region the solute undergoes a negative interaction potential $U(z)$(the dotted black curve). This potential well, attracts the solute to the walls of the channel leading to an excess of solute in this layer. The solute concentration gradient at the walls leads to an osmotic pressure gradient that drives the fluid flow towards low glucose concentrations.

In the case of a strong repulsive interaction potential U between the wall and the solute, a depletion in the solute concentration within the interfacial layer occurs, Figure 8. The slip coefficient ($\Gamma_{DO} > 0$), generates an osmotic pressure gradient caused by the asymmetric distribution in solute concentration, which in turn drives an interfacial fluid flow towards the high concentration.

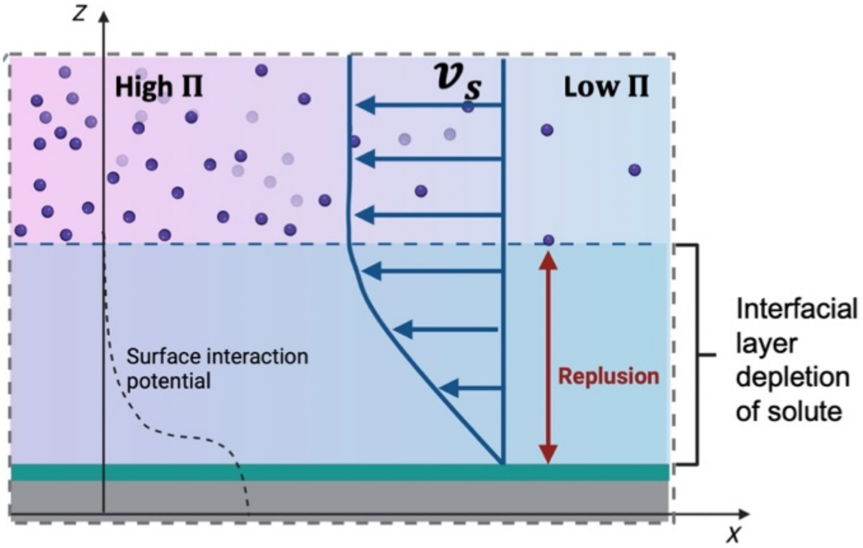

Figure 8. An illustration of the repulsive solute-surface facilitating diffusioosmotic fluid flow. The solute (purple sphere) gradient is shown with a maximum concentration (pink region) and minimum concentration of (blue region). The interactions between the solute and the walls happen within the diffusive interfacial layer which is the region near the surface. The solute undergoes a positive interaction potential $U(z)$*(The dotted black curve). This repeals the solute leading to the depletion of the interfacial layer. This in conjugation with the osmotic pressure gradient (*$^{d\Pi}/_{dx}$*) drives the fluid flow towards high solute concentrations*

2.4.3 Diffusiophoresis

These diffusioosmotic fluid flows arise when the surface experiencing this asymmetric solute gradient is anchored, hence the flow that starts inside the interfacial layer also extends outside this region since a continuity of the pressure must be fulfilled, Figure 9. However, if the surface experiencing the asymmetric solute distribution is a surface of a particle that is "floating" in the solute, the generated flow within the interfacial layer is balanced by the movement of the whole particle i.e., particle phoresis. The particle moves towards the favourite regions to balance out the osmotic pressure and swiftly decaying the fluid flow to zero outside.

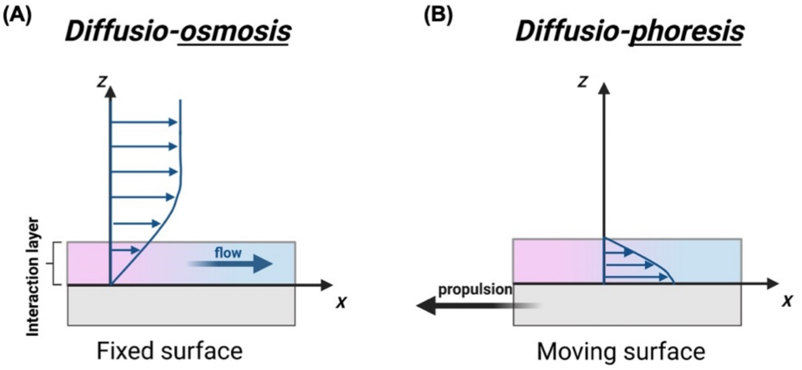

Figure 9. Illustration of the generated fluid flow during (A) diffusioosmosis and (B) diffusiophoresis as a result of the asymmetric interactions at the interfacial layer.

In a homogenous medium, the mean force acting on the spherical particle due to the surface-solute interactions would sum to zero because of isotropy. However, when the particles surface experiences an asymmetric distribution of solute (imposed by the gradient) a gradient in the normal force is generated on the surrounding fluid within the interfacial layer, in turn generating an osmotic pressure gradient around the particle. To balance this an interfacial flow of fluid (identical to that formed by diffusioosmosis) is generated which causes the particle to propel in the opposite direction, Figure 10.[108]

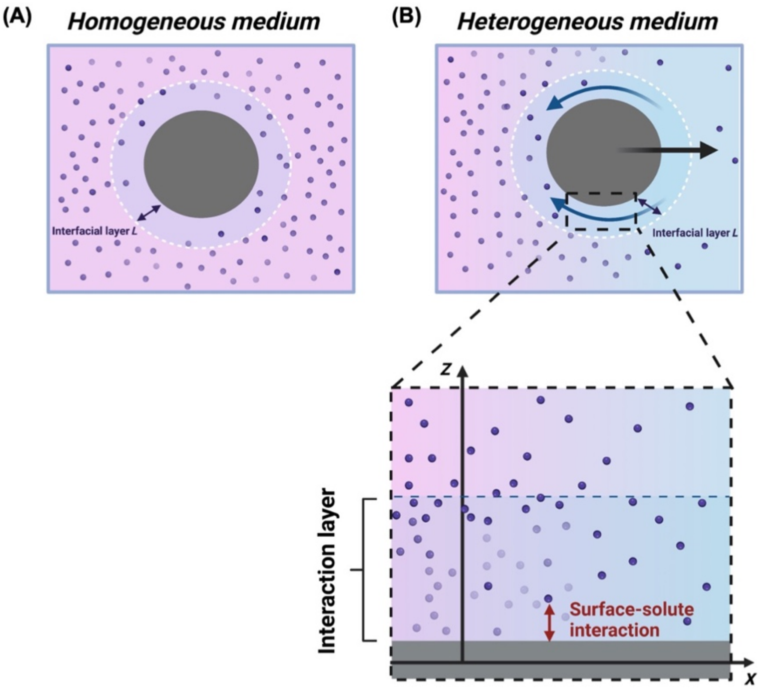

Figure 10. A schematic representation of a spherical colloidal particle in a (a) homogeneous medium (i.e., homogeneous distribution of solute around it), due to isotopy the surface-solute interactions are identical around the particle with no net force experienced by the particle. (B) When this particle is placed in a heterogenous medium (i.e., within a gradient of solute, pink being high and blue is low) the asymmetric distribution of solutes around the particle generates an osmotic pressure gradient, that is balanced by a fluid flow within the interfacial layer which pushes the particle in the opposite direction.

In the case that the solute-surface of the particle have an attractive interaction, based on Eqn. (5)&(6), an interfacial fluid flow is generated towards the low solute concentration, Figure 11. This will in turn propel the particle in the opposite direction (towards the high glucose). The opposite is true in the case of a repulsive solute-particle surface interaction. Both Figure 9 and Figure 10 display the movement of the interfacial flow around the moving particle from the reference frame of the fluid (lab frame).

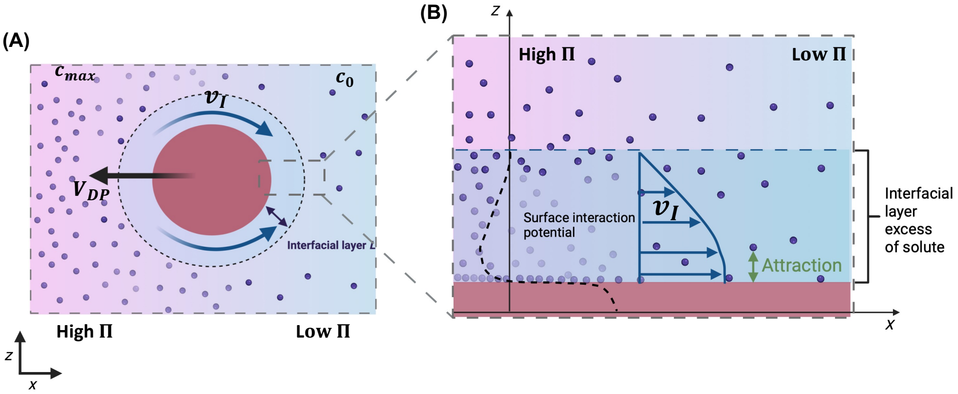

Figure 11. Illustration of diffusiophoretic motion of particles due to an attractive surface potential with solute. (A) The particle (red circle) suspended in a solute gradient can move towards high solute concentration at a velocity V_{DP} due to the fluid movement at the surface (slip velocity, v_S). (B) This interfacial fluid flow v_I, is driven by osmotic pressure gradient generated at the interfacial layer due to the attractive interaction potential at the interfacial layer which leads to an excess of solute (purple circles) at that layer.

2.4.4 Phoretic self-propulsion

As described in diffusiophoresis, when a colloid particle is in a non-uniform environment, phoretic forces act on the particle due to the surface-particle interaction to effectively drive directional motion. Hence despite the fact that no external forces induces this motion, the mere breaking of symmetry by a solute concentration gradient is sufficient to get directional migration at the micro and nanoworld.

By exploiting this, scientists have developed particles able to move and navigate at low Re numbers, known as self-propelled phoretic swimmers. For a particle to be "self-propelling" it needs to have the ability to independently manage and modify its propulsion by locally altering the properties of the fluid around it, also known as self-phoresis. Compared to the situation of diffusiophoretic motion, where an external concentration gradient drives the particles, self-propelling particles can generate their own local gradient to facilitate its movement, Figure 12.

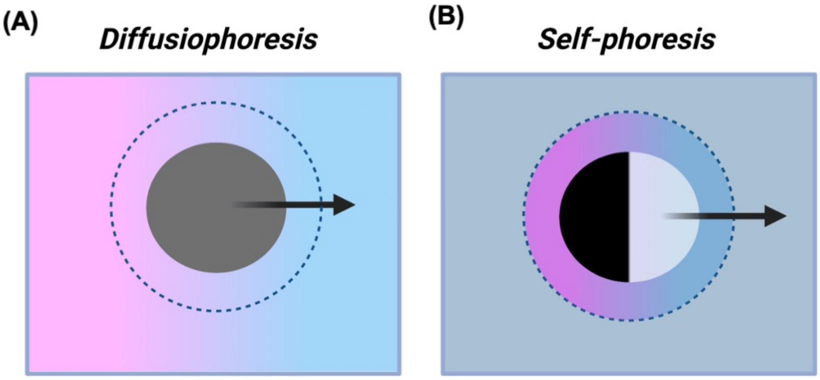

Figure 12. Sketch illustrating the difference between (A) diffusiophoresis and (B) self-phoresis (self-diffusiophoresis). The main difference is that in diffusiophoresis particles move due to an externally imposed chemical gradient while in self-phoresies particles can independently manage their movement by generating a local chemical gradient around it.

For a particle to create local gradients it must have a surface asymmetry that will interact differently with the solute molecules at different parts of the particles, i.e., generating a differential interaction. Particles can create local gradients of temperature (self-thermophoresis), charged ions (self-electrophoresis), or uncharged chemical gradients (self-diffusiophoresis). In this thesis we focus on self-diffusiophoresis.

A very interesting theoretical example was put forth by Golestanian and coworkers, where they modelled a hypothetical self-propelling particle.[109] This particle is made of a colloid which has an enzymatic patch, shown in Figure 13. The enzymatic patch is expected to promote a chemical reaction which in turn leads to an excess of reaction products in its vicinity, as shown by the small blue circles in Figure 13. This leads to an asymmetric distribution of reaction products, generating a gradient of product molecules around the particles, with the high concentration at the enzymatic site. This gradient induces an osmotic pressure gradient which in turn leads to phoretic motion of the particle.

In line with Golestanian's model, a variety of micro and nano-sized particles have been developed that possess spotted surfaces, known as patchy particles able to perform self-phoresis. Additionally, particles in which the patch covers half of the surface are known as Janus particles which have also been reported to display self-propulsive motion.[110] The motion of these self-diffusiophoretic particles is random and directionless. Unlike diffusiophoresis, no external gradient is present, in fact the gradient is produced locally by the particle which leads to the constant randomization of the orientation and can be detected as an enhancement of diffusion over longer time scales (typically longer $\tau_R = 1/D_R$).[7] The orientation of the particle can be affected by an externally imposed gradient of substrate molecules. One mechanism to do so is chemotaxis.

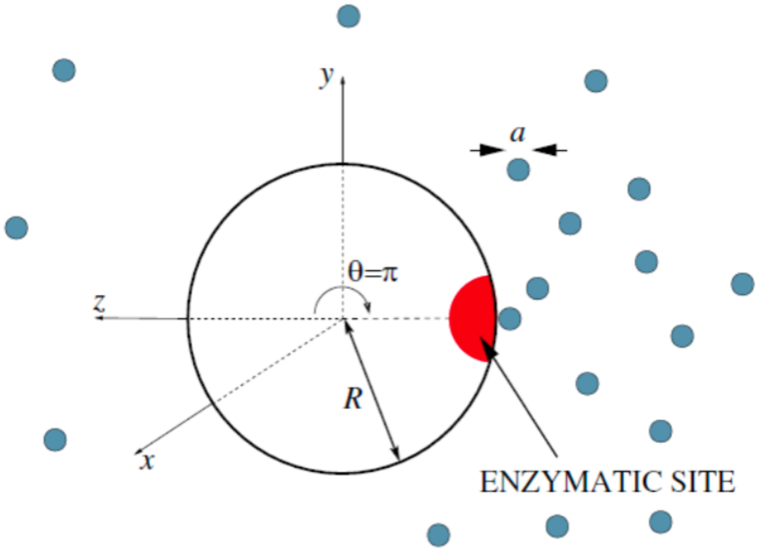

Figure 13. The model of the self-diffusiophoretic particle proposed by Golestanian and cowork. Reproduced from ref 109.

2.4.5 Chemotactic behaviour by self-phoresis

This directed motion towards or away from a chemical can be seen in nature. In unicellular organisms, chemotaxis allows for movement in response to long-range chemical stimuli several orders of magnitude larger than the organism itself.[77] For instance, bacteria are able to swim, using rotating flagellum, towards glucose (positive chemotaxis) and away from acidic environments (negative chemotaxis).[111] Similarly, in multicellular organisms, cells use chemotaxis in critical processes like reproduction (movement of sperm cells towards the eggs during fertilization), tissue development, immune and inflammatory responses (movement of leukocytes because of an injury or infection).[112] In these processes, the presence of a specific signalling molecule gradient is sensed by the cell using intracellular signalling routes and converted into mechanical energy.

The directional motion of the cell is determined by the signalling molecules and is maintained as long as the gradient is present, however, the mechanism of motion is different from one cell type to another. Neutrophil motion, for example, is facilitated by the polarised intercellular response to the chemical gradient which allows the cell to undergo morphological changes. The cell polarisation leads to an asymmetric distribution of the intercellular structure allowing for directional movement.[87] In the same way, self-diffusiophoresis can be used to promote chemotactic like behaviour in artificial particles by applying a chemical gradient to resist the consistent Brownian reorientation hence allowing the particles to “sense” the gradient (selectively move towards or away from the chemical) .

In the previous cases we have seen the motion of particles due to the interaction of the surface with an externally applied substrate gradient (diffusiophoresis) or by the interaction of the surface with a local gradient of product generated by a catalytic activity of the particle (Self-diffusiophoresis). In chemotaxis, the motion of the particle is a result of the coupling of both of these phenomena, Figure 14. Here the particle’s surface experiences an interaction with the externally applied substrate gradient which is also used to generate a local gradient of product. The presence of both of these gradients contributes to superior phoretic motion of these particles.

In the case of diffusiophoresis, the particle responds to an externally applied chemical gradient, shown in Figure 14A by the purple (high concentration) to white colour (low concentration) gradient. The particle surface interacts with the gradient molecules (purple circles) which induce a slip velocity governed by slip coefficient ($\mathit{\Gamma}_{DO}$), Figure 14B. In the case of an attractive interaction between the particle and the molecules, a resultant fluid flow propels the particle up the gradient. This movement is directional with fluctuations due to influence of Brownian collisions.

On the other hand, self-diffusiophoresis of a particle in a homogenous environment (no external gradient) of substrate is a result of the transformation of the substrate to a product by the catalyst coated hemisphere of the particle. This leads to the generation of a local gradient of product as illustrated in Figure 14C and D, here the uniform substrate environment (solid purple colour) is used by the catalytic hemisphere and converted to a product (green circles). A gradient of product is generated around the particle (green gradient around particle), leading to an osmotic pressure gradient. This pressure is balanced by a fluid flow which propels the particle in the opposite direction. In the case of a positive interaction of the surface and the product (i.e., $\Gamma_{DO} < 0$), the particle propels towards the high concentration. The direction of the high product concentration is determined by the orientation of the particle itself. Due to the randomized orientation of the particles (D_R is high), their alignment is consistently changing and hence the direction of the local product gradient consistently changes. Thus, the motion of the particles is non-directional and appears as an enhancement in diffusivity.

Chemotactic motion is a combination of enhanced diffusivity (by self-diffusiophoresis) and the directionality produced by the application of an external gradient (diffusiophoresis). Here the active particle experiences an external substrate gradient and a local generated product gradient which projects the particle. The interaction of the surface of the particle with both the substrate and product drives the motion. However, the external applied substrate gradient dictates the directionality of the motion of the particle as it constantly realigns the particle despite its randomized orientation. This type of motion involving the consecutive realignment of the particle followed by a directional propulsion of the particle is known as the run-and-tumble and is illustrated in Figure 14E. The translational velocity (v_c) of this chemotactic behaviour can be expressed as

$$v_c = V_o(s)\hat{n} - \alpha_0 \nabla \mathrm{s} - \alpha_1 \hat{n}\hat{n} \cdot \nabla s + \sqrt{2D} f_\alpha^r(t) \qquad (7)$$

where $V_o(s)$ denotes the self-diffusiophoretic component, $\hat{n}$ the symmetry axis of the Janus particle (the direction the particle moves are determined by $\hat{n}$), α_0 the phoretic drift component, $\nabla \mathrm{s}$ the change in substrate concentration, α_1 corresponds to the anisotropic drift and f_α^r the white noise term. In this context four contributions influence the translational velocity of the particles.

Firstly, the self-diffusiophoretic component ($V_o(s)\hat{n}$), which represents the propulsion of the particle in response to the local product gradient and is along the $\hat{n}$. The second is the phoretic drift of the particle due to the externally applied substrate gradient ($\nabla \mathrm{s}$). The direction of this drift is along the substrate gradient and governed by the slip coefficient Γ_{DO}. The third is an isotropic drift that instantaneously acts at $\hat{n}$ but results in a net movement along the substrate gradient despite the rotational noise acting on $\hat{n}$. The final contributor are the thermal and active fluctuations due to Brownian motion.

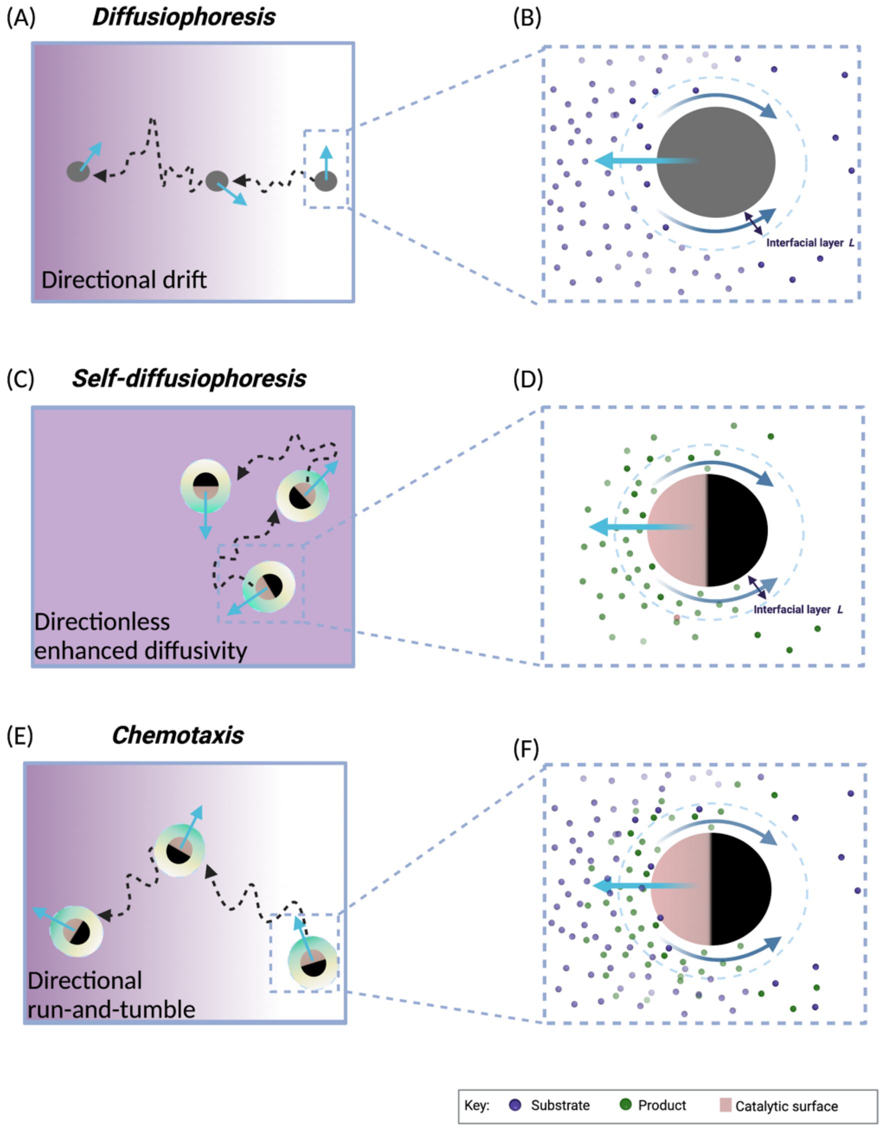

Figure 14. The three different phoretic driven particle migrations are illustrated, for each three consecutive snapshots at equivalent time intervals are illustrated with the connecting trajectories (dashed lines). (A) Diffusiophoretic driven particles (grey circles) in an externally applied chemical gradient (purple high concentration and white low concentration) which displays a net directional drift of the particle. (B) This motion is a result of the uneven distribution of molecules (purple circles) around the particle which generate a fluid flow down the gradient propelling the particle towards the high concentration. In self-diffusiophoresis (C) the particle is suspended in a uniform concentration of substrate which is used to generate a local concentration gradient of product (green high concentration, white low concentration). (D) This is achieved by the catalytic coated hemisphere of the particle (pink surface) which results in an uneven distribution of the product (green circles), resulting

in a particle motion towards the high product concentration, assuming an attractive interaction. The motion is directionless and appears as an enhancement in diffusivity. (E) Chemotactic motion is the response of the particle to both the external substrate gradient and the local product gradient. The movement of the particle is directional and can be described as a run-and-tumble motion. Here (F) the surface of the particle interacts with both the substrate (purple) and product (green), assuming an attractive interaction, the particle moves up the substrate gradient.

2.4.6 Examples of self-phoretic particles

Most of the developed self-phoretic particles are based on self-diffusiophoresis, which have been reported to display enhanced diffusivity. The most exploited chemical reaction used to make micro-propelling devices is the catalytic decomposition of hydrogen peroxide. This chemical reaction has proven to be an effective propulsion mechanism to particles of different shapes, sizes and coatings.[113, 114] The simplest is the Janus Pt coated spherical colloids (colloids which are half-coated with Pt) when suspended in a dilute aqueous solution of hydrogen peroxide (H_2O_2), the chemical reaction catalyzed by the Pt is;

$$2H_2O_2 \overset{Pt}{\rightarrow} 2H_2O + O_2$$

The chemical reaction constantly consumes H_2O_2 from the surrounding medium and continuously produces O_2. Since half of the surface of the colloid is coated with Pt, over time and due to diffusion, an uneven distribution of reactant and product around the colloid leads to the generation of an osmotic pressure gradient which in turn propels the particle.[114] These particles were reported to exhibit enhanced diffusivity in a dilute solution of hydrogen peroxide.

Following Golestanian's model, I now present micro and nanoparticles that are powered by an enzymatic patch. The most prevalent examples of enzyme asymmetry are the spherical Janus particle that involve coating half of the particle with enzyme. This method has successfully demonstrated propulsion of micro and nanoparticles by Ma *et al*. [115, 116] Here Janus mesoporous silica particles ranging in size of 90 nm, 390 nm and 2µm are half coated with catalase, Figure 15.

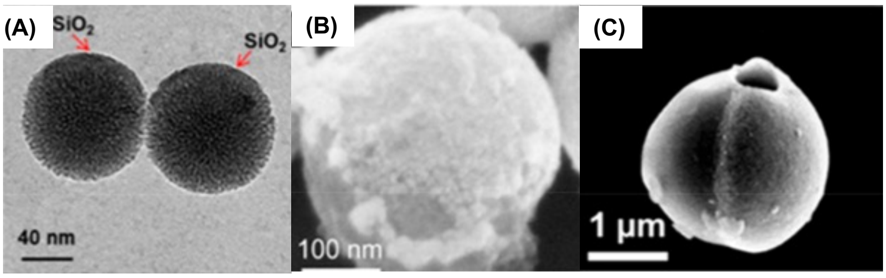

Figure 15. Micrographs of Janus catalase/ mesoporous silia self-propelling particles (A) 90nm, (B) 390 nm and (c) 2 µm. Reproduced from ref 115 and 116.

Catalase is predominantly the most widely used enzyme to fuel micro and nano-propelling particles, which was first reported by S. Sanchez *et al*.[117] This enzymatic reaction evolves the decomposition of H_2O_2 into oxygen and water,

$$2H_2O_2 \rightarrow 2H_2O + O_2.$$

This propulsion mechanism has also been used to generate propulsion in micro and nano-jets which are based on tubular shaped self-propelling swimmers. The nano-sized catalase/ mesoporous silica particles have been reported to display an enhancement of diffusivity. [115, 116] As an increase in the diffusion coefficient from 0.75 µm^2/s (of the non-active particle) to about 1.25 µm^2/s for self-phoretic particles in the presence of hydrogen peroxide.

Another example involves using the use of urease enzymes to functionalize the surface of polystyrene microparticles. [118] Subsequently, these enzymes act by facilitating the phoresis of these particles in presence of a urea. Urease catalysis the hydrolysis of urea to carbon dioxide and ammonia

$$(NH_2)\ _2\mathrm{CO} + \ 2H_2O \rightarrow CO_2 + NH_3 + \ H_2O.$$

It has been reported to promote self-propulsion in Janus polystyrene microparticles[7] and Janus hollow mesoporous silica microparticles[119, 120].

Nevertheless, none of these examples investigate chemotactic motion (directed) of particles, in fact only a handful of scientists have studied this. Work by Baraban *et al.*[121] have reported chemotactic motion of microsized Janus particles composed of silica colloids coated with Pt. These were suspended in a hydrogen peroxide concentration gradient, in which the chemotactic motion was found to depend on the concentration of this chemoattractant. This project aims to study the chemotactic motion of nanovesicles. In particular, the aim of developing these chemotactic nanovesicles is for potential use as brain drug delivery. The translation of self-phoresing particles into biologically compatible systems also comes with its set of challenges.

2.4.7 Translating towards biological suitable self-propulsion

The translation to biologically functioning self-propelling particles remains a problematic task for most of the developed particles. One of the main issues is the use of enzymes externally (in a patch or hemisphere) which when in the body would be subject to protein corona and degraded by protease, enzymes capable of hydrolyzing proteins.[122] Recently, another technique exploited is the entrapment of enzymes within micro/nanoparticles (i.e., compartmentalized) to cause the propulsion, while protecting the enzymes themselves. Wilson and coworkers encapsulate glucose oxidase and catalase into 500 nm asymmetric polymer vesicles called stomatocytes, in which glucose is the signalling chemical which is converted to gluconic acid and hydrogen peroxide by glucose oxidase. The catalase then converts hydrogen peroxide into oxygen and water. The bubbling of the oxygen gas through a very small opening in the structure propels the vesicle, Figure 16.[123] Nevertheless, this method is highly undesirable for biological applications as oxygen bubbles inside the blood vessels can have serious health implications.

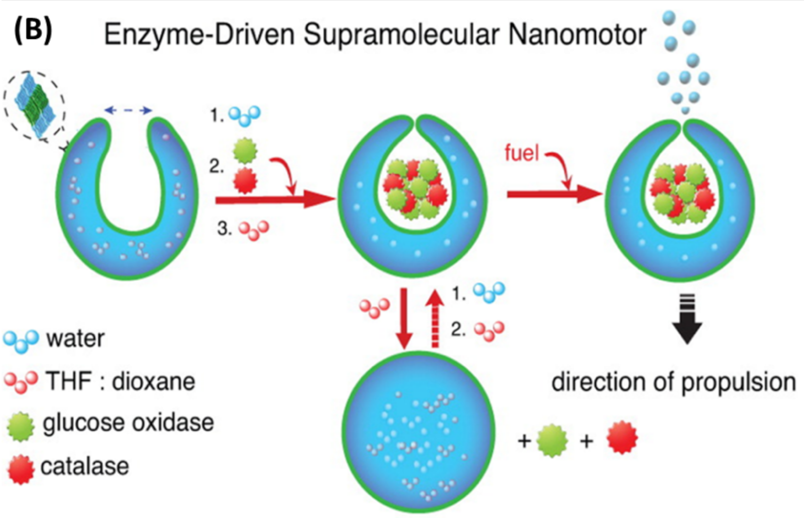

Figure 16. Diagrammatic representation of the self-propulsion of stomatocytes encapsulating glucose oxidase and catalase. Reproduced from ref. 123.

Another challenge that lies in the face of translating moving particles to be used for biological applications is associated with size, in which microscopic particles can lead to blood clotting as they are unable to flow through small capillaries which range from 8 to 10 microns in diameter.[124] In addition, nano-sized particles are more effective in penetrating in tissue systems which facilitate easy uptake of drugs into cells. It has been observed experimentally that the uptake of nano-sized particles is much higher than their larger micro-sized counterparts ranging between 1 to 10 µm.[65, 125] Thus, improving efficacy of therapeutics. Unfortunately, the majority of developed self-propelling particles are micro-sized., this is because the smaller nano-sized particles experience faster rotational diffusion hence making it more difficult to overcome Brownian motion.

Another important factor to consider is the choice of enzyme. It is necessary to have an enzyme that (i) is reactively powerful enough to facilitate movement of the particle, (ii) uses a physiologically available substrate while (iii) avoiding any toxicity to the body.

Work conducted by Joseph *et al*, has reported chemotactic polymersomes.[8] These systems use the previously introduced type of nanovesicles, in section 2.2, known as polymersomes and modify them by incorporation of a patch and enzymes to attain self-diffusiophoresis.

In this system, the enzyme was entrapped within the aqueous core of the nanovesicle and the spherical polymersome were modified by phase separation technique to fabricate a patch on their surface. The patch was introduced to the topology of the block copolymer bilayer by using a combination of 90% poly[(2-methacryloyl)ethyl phosphorylcholine]–poly[2-(diisopropylamino)ethyl methacrylate] (PMPC-PDPA) or poly[oligo(ethylene glycol) methyl methacrylate] (POEGMA)–PDPA and 10% poly(ethylene oxide) poly(butylene oxide) (PEO-PBO) copolymers, to form two distinct domains, Figure 17. This asymmetry of the topology is essential to form the uneven distribution of products around the swimmer as discussed for self-diffusiophoresis.

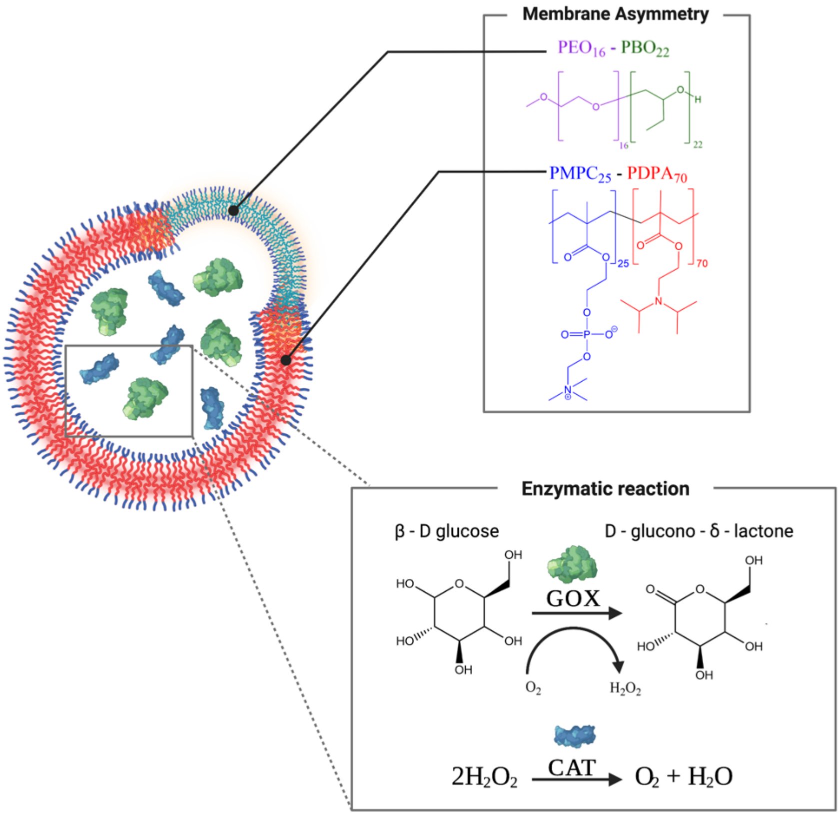

Figure 17. Schematic of the conditions employed to promote chemotaxis of polymersomes.

To achieve self-propulsion, by an enzymatic patch as stated by Golestanian's model, this patchy polymersome was then coupled with the encapsulation of glucose oxidase (GOX.) alone or in combination with catalase (CAT.) in the aqueous core of the polymersomes acting as enzymatic patch in the presence of the substrate, glucose. The enzymatic reaction that drives the polymersomes, as seen previously for the stomatocytes, is the conversion of glucose into D-glucono-δ-lactone and hydrogen peroxide by glucose oxidase, which is then converted to water and oxygen by catalase. Nevertheless, no oxygen gas is released by these systems, as opposed to the stomatocyte microparticles, the oxygen produced is in low concentrations and is used up by the glucose oxidase within the vesicle.

Finally, in order to obtain a chemotactic-like directional motion, a substrate gradient (glucose) needs to be maintained and acting as a signalling chemical. The strategy adopted to promote chemotactic motion in polymersomes is summarised in, Figure 17.

As mentioned above, the membrane topology was designed to enable an asymmetric distribution of domains of different permeability within the polymersome surface. The most permeable domain being the PEO-PBO and the least being PMPC-PDPA. Once the glucose entered the polymersomes and underwent the catalyzed reaction, the products (D-glucono-δ-lactone and water) were locally expelled from the most permeable domain. This localization promoted the chemotactic motion up an applied glucose gradient (chemoattraction-like motion), Figure 18.

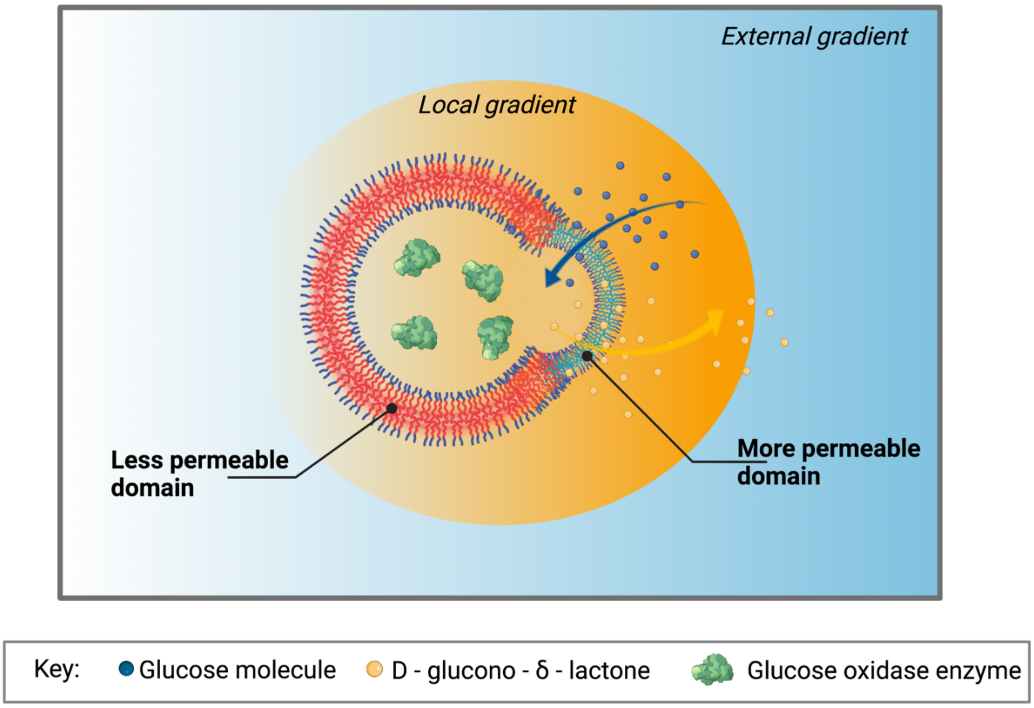

Figure 18. Illustration of the effects of the asymmetric domain distribution on the orientation of the polymersomes up the substrate gradient. Here the PEO-PBO domain (green and purple) is more permeable to the substrate, i.e., glucose molecules (blue circles) and the enzymatic product, i.e., D-glucono-δ-lactone (yellow circles) than the PMPC-PDPA domain (red and blue). This results in a localized gradient of product (yellow to white gradient) within the externally applied glucose gradient (blue to white gradient).

Since the brain is the highest glucose consuming organ in the body,[126] the glucose gradient in the body is directed towards it. Consequently, *in vivo* experiments of Angiopep-2 (LA) conjugated chemotactic polymersomes ,LA is a peptide for brain targeting, demonstrated a fourfold increase in blood brain barrier crossing compared to non-chemotactic LA conjugated polymersomes.[8]

2.5 Project Aim and Experimental rationale

As mentioned in the previous subsection, the work conducted by Joseph *et al.* has reported the ability of modified polymersomes to propel up glucose gradients[8], as I will show in the experimental section, explicitly in Chapter 5 and 6, that this is not a straightforward endeavour. Other phenomena such as diffusiophoresis or fluid turbulence can mask or disturb self-diffusiophoresis migration of nano-sized particles. Expanding on previous work, this research aims to isolate chemotaxis migration from other particle drifts (such as diffusiophoresis or convective fluid flows). In an attempt to better contribute towards a nanovesicle drug delivery system based on chemotactic propulsion.

To do so, I investigate two nanovesicle systems based on the Golestanian's model, the first is the polymersome system previously reported by Joseph *et al*[8], in which GOX enzyme is encapsulated into the aqueous core of a patchy polymersome. The second is based on liposome system with involves the encapsulation of the GOX enzyme in the aqueous core. The asymmetry of on the liposomes surface is introduced by a pore which creates a small opening in the membrane, Figure 1. These systems will be;

1- Prepared by self-assembly and methods optimized when needed.
    a. Fabrication of the asymmetric surfaces
    b. Encapsulation of the glucose oxidase (GOX) enzyme
2- Chemotactic studies are then conducted on these nanovesicles in the presence of a glucose gradient:
    a. The identification and suppression of background particle drifts in a glucose gradient (such as fluid convection and diffusiophoresis)
    b. Chemotactic movement assessed, and velocity of nanovesicles migration measured. Making this the first and most accurate measurement so far of chemotactic motion in nanovesicles.

CHAPTER THREE

MATERIAL & METHODS

3.1 Block copolymers

The block copolymers used to prepare the polymersomes were poly(2-(methacryloyloxy) ethyl phosphorylcholine)- block- poly(2- diisopropylamino) ethyl methacrylate ($PMPC_{25}$-$PDPA_{70}$) and poly(oxyethylene) -block-poly(oxybutylene) (PEO_{16}-PBO_{22}). The PEO-PBO block copolymer is shown in Figure 19. It is a commercially available copolymer and was purchased from Advanced Polymers Material Inc., (Canada). It is made of two blocks, the hydrophilic PEO and hydrophobic PBO blocks. The PEO block is also known as poly(ethyleneglycol), PEG, for short. The PEO block is highly hydrophilic due to the presence of ether groups which form hydrogen bonds with water molecules leading to the incorporation of 2-3 molecules of water per monomer.[127] PEO is non-immunogenic, non-antigenic and non-toxic which is FDA approved for medical and cosmetics hence making it a good candidate for biomedical applications. The hydrophobicity of the PBO block makes this copolymer very attractive for polymeric assembly in water.

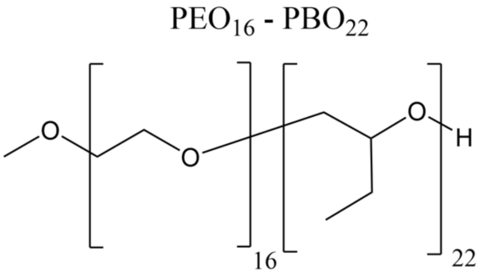

Figure 19. The PEO_{16}-PBO_{22} amphiphilic block copolymer structure. The PEO is the hydrophilic parts and the PBO the hydrophobic parts.

The PMPC-PDPA is a pH sensitive, amphiphilic block co-polymer, formed from the hydrophilic PMPC and hydrophobic PDPA blocks. The PMPC is a highly water soluble zwitterionic block, presenting a positively charged amine group and a negatively charged phosphate group making the net monomer charge neutral.[128] This block is biocompatible, and hence commonly used to coat medical devices such as contact lenses and stent implants.[129] The PDPA block on the other hand, is a hydrophobic polymer which consists of a tertiary amino group enabling the pH sensitive properties of the copolymer. The acid dissociation constant at logarithmic scale (pKa) of the tertiary amino group in water is 6.4, Figure 20. Therefore, the hydrophobicity of the PDPA block can be tuned by variations in pH, shifting from the hydrophobic deprotonated state at physiological pH (pH 7.4) to the hydrophilic protonated state in mildly acidic environments (pH < 6.4). The acquired water solubility at pH lower than 6.4 is a result of the positively charged amine group once protonated. In this case, the copolymer is no longer amphiphilic with both its blocks hydrophilic and hence is well dispersed in water with no aggregation formation, Figure 20. This in turn allows for the possible switch on/off PMPC-PDPA assembly by altering pH.

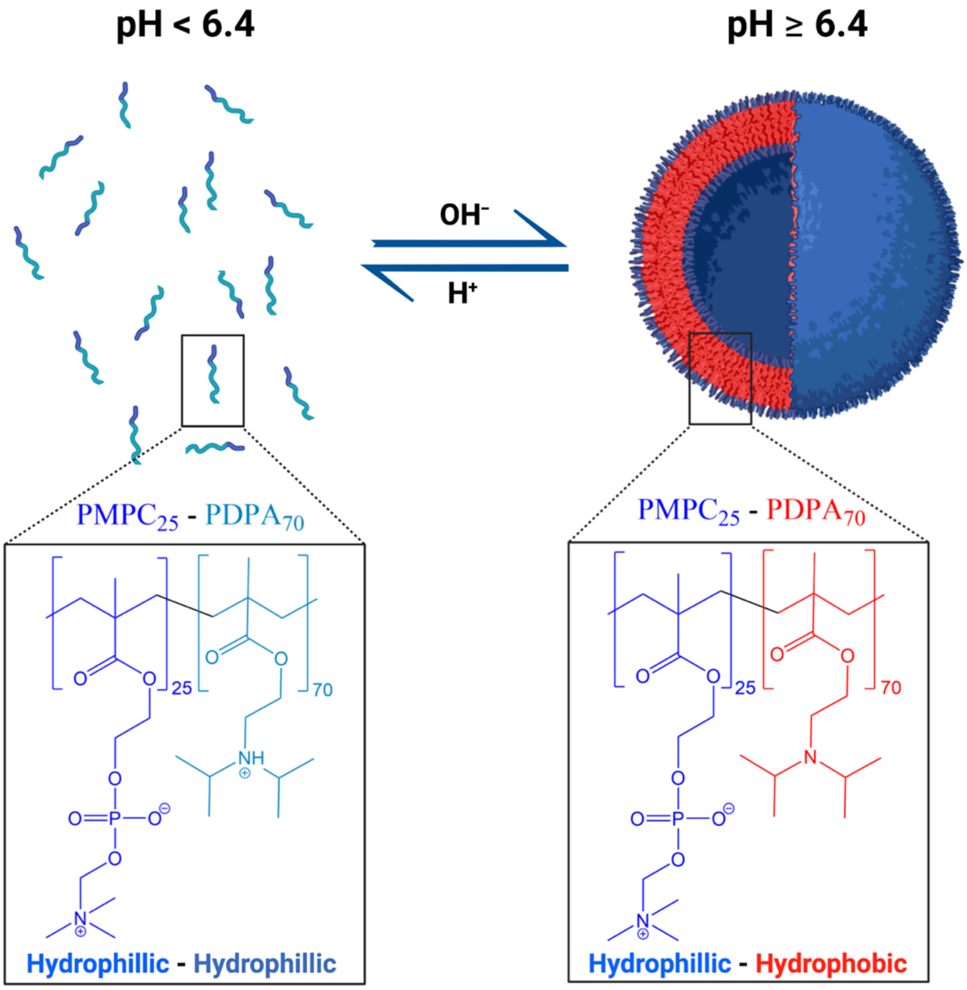

Figure 20. Schematic of the PMPC-PDPA pH sensitivity characterised by the protonation of the amino group at pH < 6.4 leading to the solubilising of the co-polymer in water and deprotonation at pH ≥ 6.4 which leads to the assembly of the co-polymer to form aggregated structures.

The PMPC-PDPA was synthesised by the Battaglia group using the Atom Transfer Radical Polymerisation (ATRP) method.[130] Briefly, in a Schlenk flask 2-(Methacryloyoxy)ethyl phosphorylcholine (5 g, 17 mM, 25 equivalents, Biocompatibles, UK) and 2-(N-morpholino)ethyl 2-bromo-2-methylpropanoate initiator (0.2 g, 0.68 mM, 1 equivalent, synthesized as previously recorded)[130] were dissolved in anhydrous ethanol, and the mixture was purged under nitrogen at 20°C for 30 minutes. To this, both copper (I) bromide catalyst (0.1 g, 0.68 mM, 1 equivalent, Sigma-Aldrich, UK) and 2,2'bipyridyl ligand (0.21 g, 1.4 mM, 2 equivalents, Sigma-Aldrich, UK) were added. After one hour, a solution of deoxygenated 2-(dissopropylamino) ethyl methacrylate (10 g, 47 mM, 70 equivalents, Scientific Polymer Products, USA) in methanol (7 ml, Sigma-Aldrich, UK) was added to the flask. After two hours, ethanol was added to dilute the solution, which was then purified by removing the copper catalyst using a silica column (grade silica gel 60, E. Merck, UK). The organic solvents were removed using dialysis in water and freeze-drying.

3.2 PMPC-PDPA Polymersome preparation

Amphiphilic block copolymers have the ability to interact and arrange themselves into structures, known as self-assembly. The most well-known self-assembly process in nature is the formation of membranes. These are made by the arrangement of phospholipids in water into supermolecular assemblies, compartmentalising and protecting the interior of cells. Like phospholipids, amphiphilic block copolymers can arrange themselves in water. This self-assembly is driven by the hydrophilic interactions and hydrophobic repulsion of the copolymer blocks in water, to minimise the free energy of the system and form the most thermodynamically stable structures.

A number of methods have been utilised to prepare PMPC-PDPA polymersomes by the self-assembly process. The most frequently used are (1) the film rehydration method (top-down approach), and (2) the solvent switch method (bottom-up approach). The top-down approach involves the preparation of a thin copolymer film which when hydrated breaks apart into aggregates [73]

The solvent switch method involves dissolving the copolymers in an organic solvent and the gradual addition of water drives the aggregation of the copolymers. In the bottom-up approach, the copolymers are fully solubilized in organic solution, the amphiphiles assemble upon the gradual exchange of the organic solvent with water. The underlying mechanism for the bottom-up self-assembly process of PMPC-PDPA involves the evolution of the suspended copolymers to form micelles, which further grow to form vesicles and final high-genus vesicles, Figure 21. While the top-down method involves the breaking down of a larger polymeric film leading to larger aggregates, Figure 21. It has been shown that the aggregates formed are affected by the method of self-assembly.[131] Hence these two methods are explored for the preparation of the single component PMPC-PDPA and the bicomponent PMPC-PDPA + PEO-PBO polymersomes to obtain mono-dispersed single/bicomponent spherical polymersomes of 50 nm.

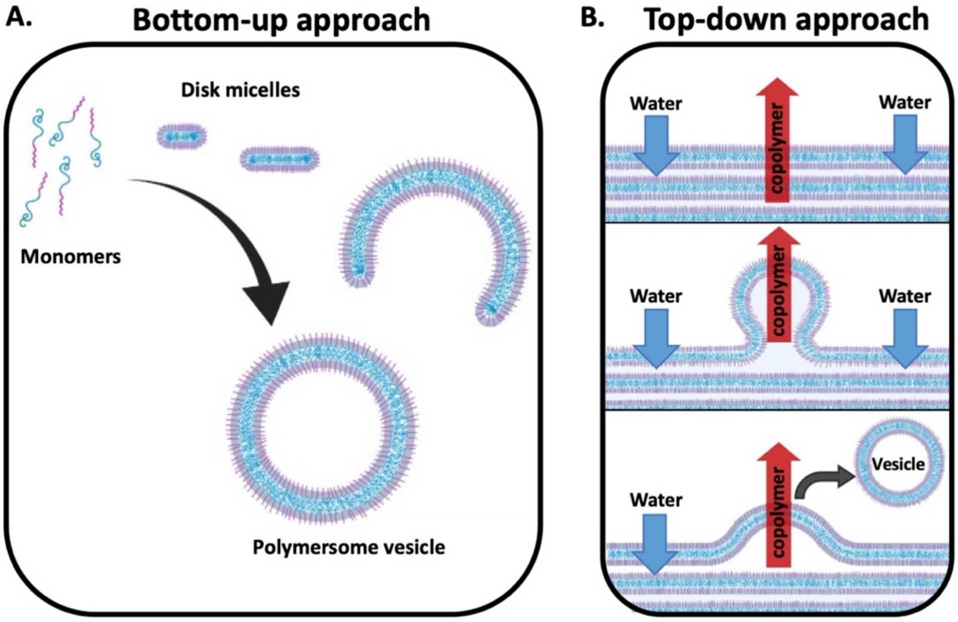

Figure 21. Processes of the self-assembly of polymersomes. (A) The bottom-up approach (e.g., Solvent switch) which involves the evolution of the polymersome vesicles from the co-polymer monomers suspended in an organic solvent. (B) The top-down approach (e.g., Film rehydration method) which involves the hydration of a polymeric thin film, which in turn swells and breakdown to form vesicles.

3.2.1 Film rehydration: Top-down approach

The film rehydration method was used to prepare the nano-sized polymersomes, as illustrated in Figure 22.[132] For this purpose, the block copolymers were dissolved in a 2:1 (v/v) chloroform/methanol mixture at a total concentration of 5 mg/ml . For the preparation of the symmetric polymersomes, 10 mg of the $PMPC_{25}$-$PDPA_{70}$ was dissolved in 2 mL solution of 2:1 (v/v) chloroform/methanol. The asymmetric polymersomes were prepared by mixing 90% $PMPC_{25}$-$PDPA_{70}$ and 10% PEO_{16}-PBO_{22} in molar ratio of the overall block copolymer concentration of 5 mg/ml. Hence 9.89 mg of $PMPC_{25}$-$PDPA_{70}$ and 0.11 mg PEO_{16}-PBO_{22} were dissolved in 2 mL solution of 2:1 (v/v) chloroform/ methanol. Fluorescently labelled polymersomes were made by adding Rhodamine B octadecyl ester perchlorate (fluorescent dye) at a concentration of 100 μg/ml to the organic solution of PMPC-PDPA.

The solutions were dried in a vacuum oven (VACUTHERM vacuum oven, Thermo scientific, United States) at 60 °C for 48 hours to allow for the formation of a thin film of polymer. Once the solvent was completely evaporated, the film was rehydrated using phosphate buffer saline, PBS, (1 mL, 0.1 M, pH 7.4) which was previously filtered with 0.22 µm PES syringe driven filter (Milex ™ GP, Millipore, Ireland). The rehydrated film was stirred for 8 weeks at room temperature (magnetic stirring at 200 rpm). This time allowed for the vesicle formation and detachment, as well as for phase separation of the membrane in the asymmetric polymersomes to give rise to differentiated PMPC$_{25}$-PDPA$_{70}$ and PEO$_{16}$-PBO$_{22}$ domains.

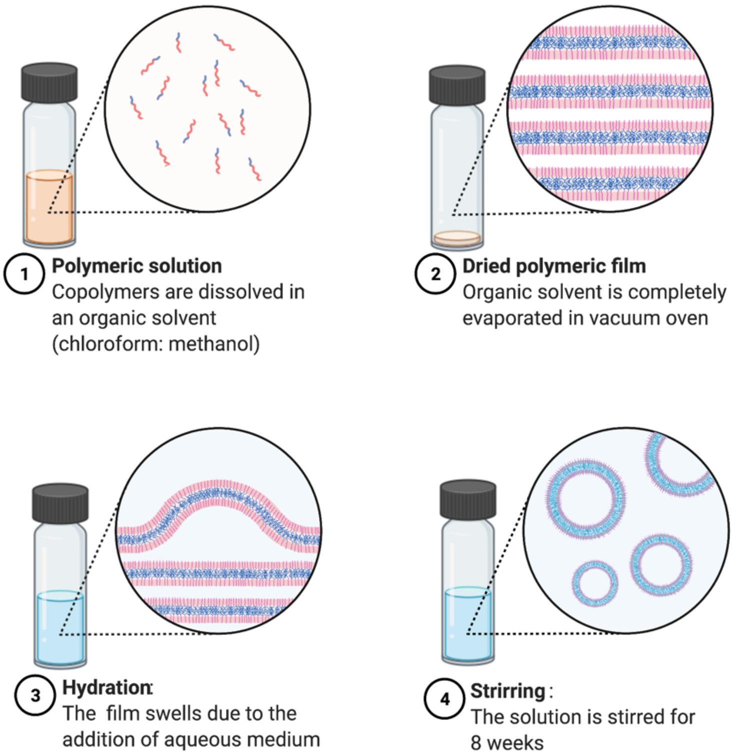

Figure 22. The preparation setup for PMPC-PDPA polymersomes by film rehydration method. The process involves the (1) solubilising the PMPC-PDPA copolymer in a chloroform: methanol organic solution then (2) the solvent is evaporated in a vacuum oven to produce a thin film which is then (3) hydrated and (4) stirred for 8 weeks.

3.2.1.1 Density gradient purification rehydration

The polymersome suspension prepared using film rehydration contains a mixture of different self-assembled structures, due to the ability of amphiphilic block copolymers to form different polymer aggregate structures (small tubes, vesicles, Genus structures) ranging from 100-5000 nm. In order to obtain a monodispersed polymersome system, density gradient centrifugation (DGC) was performed.[133] The process is based on the difference in density between the different structures, in which the non-spherical structures have a larger density compared to spherical ones due to their larger polymer:water ratio. Different concentrations of sucrose solutions were layered delicately to maintain the discontinuity between the layers in a 1.5 mL microcentrifuge tube (Eppendorf Ltd, Germany). The layers contained the following concentrations from bottom to top: 25%, 20%, 15%, 10% and 5% w/v sucrose in PBS, 200 µl each. Finally, 150 µl of sample was added on top of the upper layer and centrifuged (centrifuge 5424, Eppendorf, Germany) for 2 hours at 20,000 relative centrifugal force (rcf). This led to the separation of the structures of different shape in the different layers, with large Genus structures (highest polymer: water ratio) at the bottom (25% fraction) and the polymersomes were collected from the 10% fraction.

3.2.2 Solvent switch: Bottom-up approach

Another well-established method for the self-assembly of polymersomes is known as solvent switch,[134] this was used to induce the self-assembly of bicomponent polymersomes. As illustrated in Figure 23, this process involves four main steps the first being the dissolution of both the PMPC-PDPA alone (20 mg) or in combination with PEO-PBO at a 90:10 mol% (19.7 mg PMPC:PDPA and 0.3 mg of PEO-PBO) in a common organic solvent capable of dissolving all the blocks, in this case 0.5 mL MeOH: THF (3:1 v/v, Sigma-Aldrich, UK) was used. To this organic polymeric solution, 1.15 mL of water or phosphate buffered saline (PBS) was slowly added at a rate of 2 (results section 4.1.2.1) or 1 µl/min (results in section 4.1.2.2) while under mechanical stirring at 40 °C. Water or PBS acts as a selective solvent favoring the PMPC and/or PEO block while it is incompatible with the hydrophobic PDPA and/or PBO block. The water used was obtained via reverse osmosis and had a resistivity of 18.0 mΩcm. In this aqueous phase the hydrophobic PDPA and/or PBO assembles together to form the membrane while the PMPC and/or PEO are solvated and form the exterior of the membrane. The self-assembled structures are quenched by the instantaneous addition of 1.35 mL of water which arrests the unimer exchange between the bulk and the formed membrane. Finally, the organic solvent is removed by dialysis (3.5 KDa cut-off dialysis bag) against water for 3 days (changes a minimum of 4 hours apart) under stirring to finally yield an aqueous polymersome solution. Two conditions have been reported, the first is by solubilizing the polymers into a 3:1 (v/v) MeOH:THF and hydrating at a rate of 2 μl/min, and the second is by hydrating at a rate of 1 μl/min.

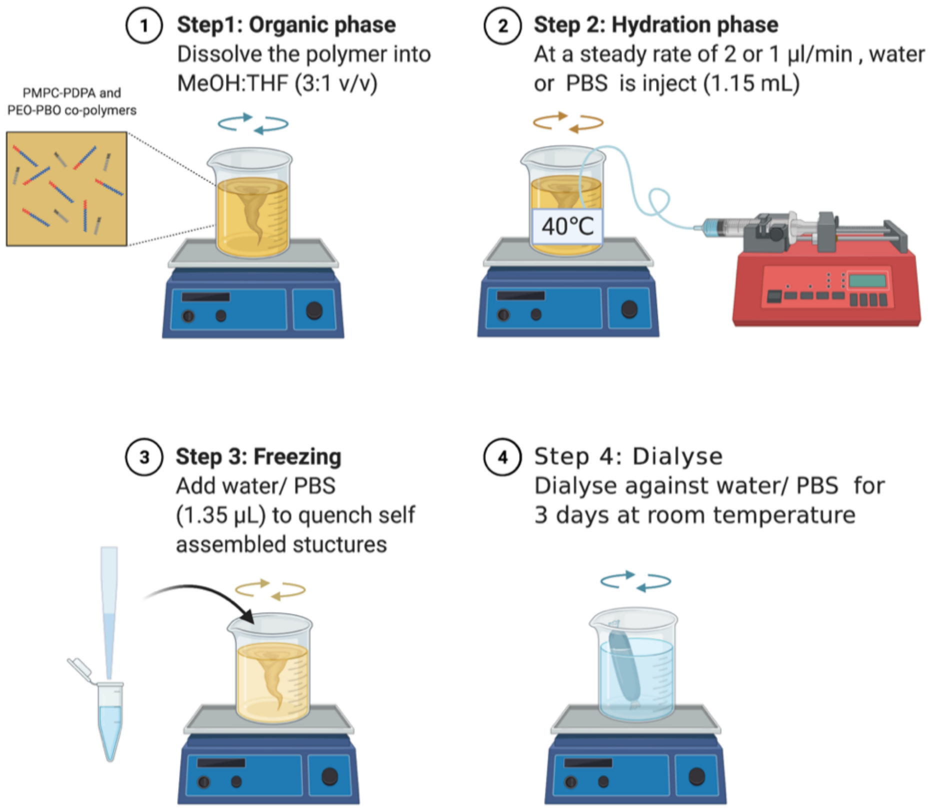

Figure 23. The solvent switch setup for PMPC-PDPA: PEO-PBO polymersomes in water. Both the block co-polymers are first completely dissolved in methanol:THF (3:1 v/v) organic solution. To this, water or PBS water is injected at a steady rate using a syringe pump (at a rate of 2 or 1 µl/min), these self-assembled structures are then quenched by the quick addition of water or PBS and dialysed for 3 days.

3.3 PEO-PBO polymersome preparation

PEO-PBO polymersomes were prepared by the film rehydration method. Poly(oxyethylene) -block- poly(oxybutylene) (PEO$_{16}$-PBO$_{22}$) copolymer and Rhodamine B octadecyl ester perchlorate, as a fluorescent dye (Sigma Aldrich, UK), were dissolved in chloroform: methanol (2:1 v/v, Sigma-Aldrich, UK). The organic solvent was evaporated in a vacuum oven overnight. This was then hydrated with water at a total copolymer concentration of 5 mg/ml and a fluorescent dye concentration of 100 µg/ml. The copolymer suspension was sonicated for 10 minutes and extruded by using an Avanti Mini Extruder™ . The PEO-PBO aggregated solution was passed 21 times through a polycarbonate membrane with a pore size of 100 nm.

3.4 Liposome preparation

3.4.1 Liposome self-assembly

As illustrated in Figure 24, liposomes were prepared by the film rehydration method, in which L-α- phosphatidylcholine from soy (Avanti Polar Lipids Inc., United States), and Rhodamine B octadecyl ester perchlorate, as a fluorescent dye (Sigma Aldrich, UK), were dissolved in chloroform: methanol (2:1 v/v, Sigma-Aldrich, UK). This organic solvent was evaporated in a vacuum oven overnight to obtain a thin lipid film. The film was hydrated with water at a total lipid concentration of 5 mg/ml and a fluorescent dye concentration of 50 μg/ml. The lipid suspension was stirred for 1 hour at 4°C and sonicated for 10 minutes. This was followed by the extrusion of the liposome solution by using an Avanti Mini Extruder™. The liposome solution was passed 21 times through a polycarbonate membrane with a pore size of 100 nm.

3.4.2 Liposome poration

The liposome membrane was porated by the membrane-active protein α-hemolysin, a cytotoxic protein capable of binding to membrane of eukaryotic cells. The α-hemolysin unimers bind to the lipid membrane and assemble to form a heptameric nanopore.[135, 136] This nanopore has been demonstrated to allow the passage of molecules smaller than 3 kDa.[137] This was performed by the addition 1 ml of α-hemolysin (0.5 mg/ml, from Staphylococcus aureus, Sigma Aldrich, UK) to 1 ml of the previously prepared 100 nm liposome suspension at a α-hemolysin/ liposome ratio of 0.1 (mass/mass). The sample was incubated for 1 hour at 25°C, as illustrated in Figure 24.

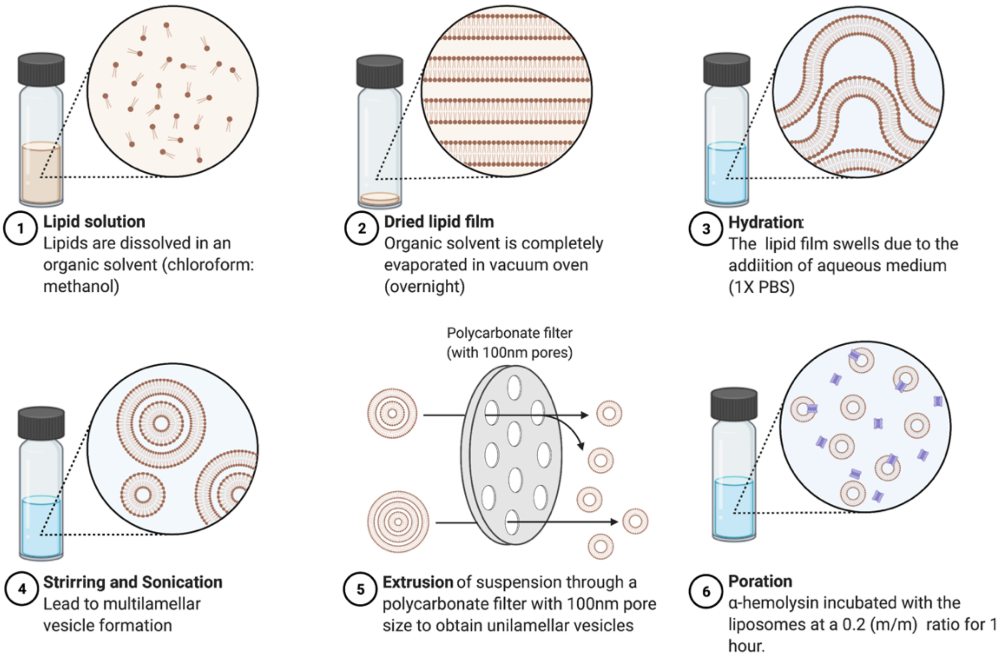

Figure 24. The preparation setup for L-α- phosphatidylcholine liposome self-assembly. Firstly, multilamellar vesicles were prepared by the film rehydration process which involves (1) solubilising the lipids in a chloroform: methanol organic solution then (2) the solvent is evaporated overnight in a vacuum oven to produce a thin lipid film which is then (3) hydrated and (4) broken down by stirring and sonication to yield large vesicles. Nanosized vesicles are prepared by (5) extrusion through a polycarbonate filter. (6) Finally, the liposomes are porated by incubation with α-hemolysin monomer.

3.5 Morphological characterisation of nanoparticles

The morphology and size distribution of the prepared liposomes and polymersomes were characterised by Dynamic Light Scattering (DLS) and Transmission Electron Microscopy (TEM).

3.5.1 Dynamic Light Scattering (DLS)

Dynamic light scattering is one of the most common light scattering techniques used to study the size distribution of particles in suspension because of its capability to resolve particles down to 1 nm in diameter. To do so, the particles are assumed to exhibit Brownian motion and are assumed to be spherical in shape.

The DLS instrument shines a laser through the sample creating an oscillating dipole moment in the particles which scatters light. The intensity of the scattered light is detected by a fast photon detector at a fixed angle known as the scattering angle θ. As a result of the constant and random Brownian motion of the particles in solution, the intensity of the scattered light fluctuates and is measured as a function of time. The detected intensity is related to the particle size, refractive index, laser wavelength, and detection angle. The smaller the particles, the faster is their diffusion, and the more rapid are the scattered light fluctuations, Figure 25B. The particle size distribution is characterised by computing the time correlation function obtained from the fluctuations of the scattering intensity. For a sample with a large number of monodisperse particles the correlation function (G) is an exponentially decaying function of the correlator time delay τ:

$$G(\tau) = A\,[1 + B^{(-2\Gamma\tau)}] \tag{8}$$

$$\Gamma = Dq^2 \tag{9}$$

$$q = \left(\frac{4\pi n}{\lambda_o}\right) \sin\left(\frac{\theta}{2}\right) \tag{10}$$

where A and B are the baseline and the y-intercept of the correlation function respectively. D is the translational diffusion coefficient, n the refractive index of the dispersant, λ_o the wavelength of the laser and θ is the scattering angle. The correlation function contains the translational diffusion coefficient (D) information which is related to the particle hydrodynamic diameter (D_H), in the case of spherical particles, by the Stokes-Einstein equation below

$$D_H = \frac{kT}{3\pi\eta D} \tag{11}$$

where k, T, η are the Boltzmann's constant, absolute temperature, and viscosity respectively. D_H represents the diameter of a solid sphere that diffuses at the same rate of the particle scattering light. This diameter comprises of the core particle and surface bound ions or adsorbed polymers.

These diffusion coefficients are obtained by fitting the correlation function using different algorithms either by implementing a single exponential fitting also known as the cumulants analysis (outlined in international standards ISO13321 (1996) and ISO22412 (2008))[138] or fitting of multiple exponentials to the correlation function, known as the distribution analysis. The former provides information on the mean size (z-average diameter) and an estimate of the polydispersity index. The time at which the autocorrelation function starts to decay indicates the mean size of the particles wherein the larger the particle, the slower is its Brownian diffusion and slower is the intensity-time autocorrelation function decay, Figure 25C. The gradient of the decay indicates the polydispersity which is used to compute polydispersity index (PDI). PDI is a dimensionless value ranging from 0.0 to 1.0. This index is used to determine the dispersity (non-uniformity) of the measured particle size, with 0.0 for the ideal monodispersed system and values greater than 0.7 indicate a very broad size distribution i.e., polydisperse sample.[139]

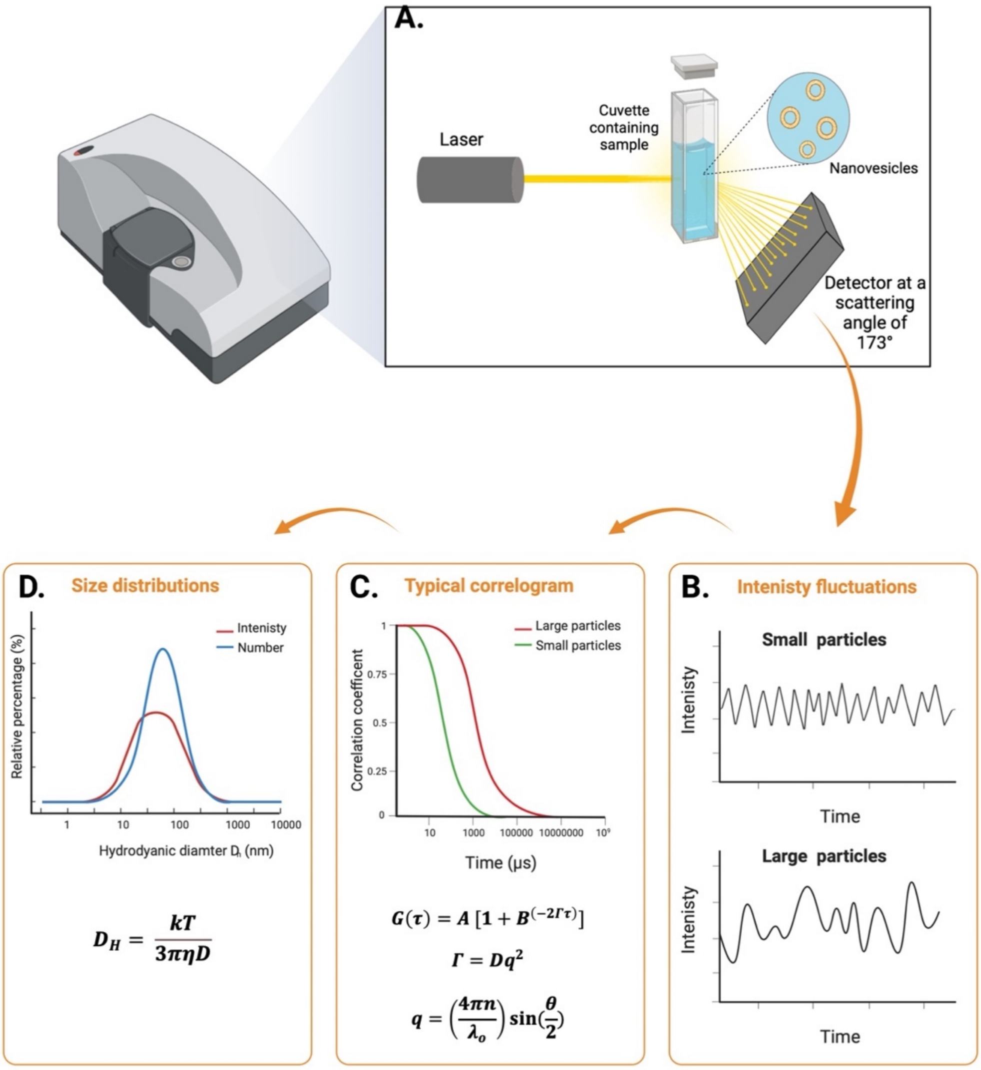

Figure 25. For the Dynamic light scattering (DLS), (A) a schematic representation of a typical apparatus setup used to characterise nanovesicles. (B-D) Analysis process of the DLS measurement (B) the light scattering intensity as a function of time showing faster fluctuations for smaller particles than larger ones due to faster Brownian motion. (C) the intensity-time autocorrelation function generated, exemplifying an earlier and steeper decay for smaller, more homogenous samples, from which the translational diffusion coefficient (D) is extracted as expressed in equation (1-3). (D) From the diffusion coefficient the hydrodynamic radius is obtained using the Stokes-Einstein equation (4) to obtain an intensity size distribution which can also be expressed as a number size distribution.

To study the scattering of a distribution of uncharged spherical particles Rayleigh and Mie approximations are used.

The primary size distribution obtained is a plot of the intensity of scattered light from each of the size classes in the sample and is here forth known as the intensity size distribution. This plot is sensitive to larger particles compared to smaller ones, as expressed in Rayleigh approximation which states that for small particles, typically less than $d = \lambda/10$ which in the case of a 633 nm laser is 60 nm particles, the scattered light by this particle due to the illumination from a vertically polarised laser could be considered isotropic. The Rayleigh approximation The Rayleigh approximation tells us that that for smaller particles, whose diameter is less than 1/10th of the laser wavelength, the intensity of the scattered light is proportional to the d^6 ($I \propto d^6$). This states that a 50 nm particle will scatter 10^6 times that a 5 nm particle. Hence, while the intensity size distribution can be used to characterise the presence of larger aggregates in the samples, nanoparticles scattering signal can be swamped by the scattering intensity of larger aggregates.

This is corrected for by applying the Mie theory which is an exact description of how spherical particles of all sizes and optical properties scatter light. This theory describes the difference in scattering as a function of the wavelength of the laser, in which particles roughly equivalent to or greater than the wavelength of the laser scatter light in a complex function of maxima and minima with respect to angle. Mie theory correctly correlates the maxima and minima in the plot intensity with angle to convert intensity size distribution into number size distribution. This distribution provides an estimate of the relative amount of particles in separate peaks.

The DLS instrument used is the Malvern Nano Zetasizer (United Kingdom) with a 120-mW He-Ne laser with a wavelength 633 nm at 25°C. The scattered light was detected at a scattering angle of 173°. For the measurements, the sample was diluted to 0.2 mg/ml using filtered PBS (pH 7.4) in a 500 μL polystyrene cuvette.

3.5.2 Transmission electron microscopy (TEM)

Transmission electron microscopy (TEM) is a popular method for imaging nanoparticle samples due to its high resolution compared to light microscopy. This is because, unlike light microscopy, TEM uses a focused high energy beam (100 keV) of electrons with a smaller de Broglie wavelength (~ 2 Å) allowing for a superior resolution. When the electron beam interacts with the sample an image is formed which is detected.

3.5.2.1 Image acquisition

TEM imaging was performed using the JOEL 2100 instrument operating at 200 kV equipped with a CDD Orius SC2001 camera from Gatan. The polymersomes were stained with 0.75% (w/v) phosphotungstic acid (PTA). The solution was prepared by dissolving 37.5 mg of PTA (10% w/v, Sigma-Aldrich, UK) in distilled water (5 ml) while maintaining a pH 7.4 by adding few drops of 5 M NaOH while stirring. The PTA solution is then filtered through a 0.2 μm filter. 400 mesh Copper grids were glow-discharged for 40 s, and the sample was adsorbed onto the now hydrophilic grid by depositing 5 μL of sample onto the grid. This was followed by staining with PTA solution for 4 s. The grid was finally blotted with filter paper and dried under vacuum for 1 min.

For the bicomponent PMPC-PDPA + PEO-PBO samples, a differential staining method of the two copolymers is used. [140] The PTA reacts with carboxylic ester groups,[141] which are present in the PMPC-PDPA co-polymer but not the PEO-PBO, this allows for selective staining of the PMPC-PDPA. When imaged the now electron dense PMPC-PDPA, appears as the darker domains while the PEO-PBO as the lighter unstained domains. The TEM imaging was used to visually characterise the morphologies of the nano-objects as well as the size distribution in dry state by measuring the diameter of the nanoparticles (Dry state diameter D_D). This was measured (1) manually or (2) automated, these methods are described below.

3.5.2.2 Manual micrographs analysis

TEM micrographs were analysed manually using Image J. The micrographs contain polymersomes with all the membrane visible and a few with compromised representation, such as polymersomes towards the borders of the image. The compromised polymersomes have been omitted from these measurements when the diameter of the polymersomes is not visible within the image. A total of 30 polymersomes were counted and diameters measured. The diameter of each polymersome was measured as the distance between the stained membranes, corresponding to the minima in the intensity plots, as shown in Figure 26. The measurements were performed in triplicate and averaged to attain the diameter of each polymersome. This method was performed in samples containing different aggregate morphologies (other than spherical polymersomes).

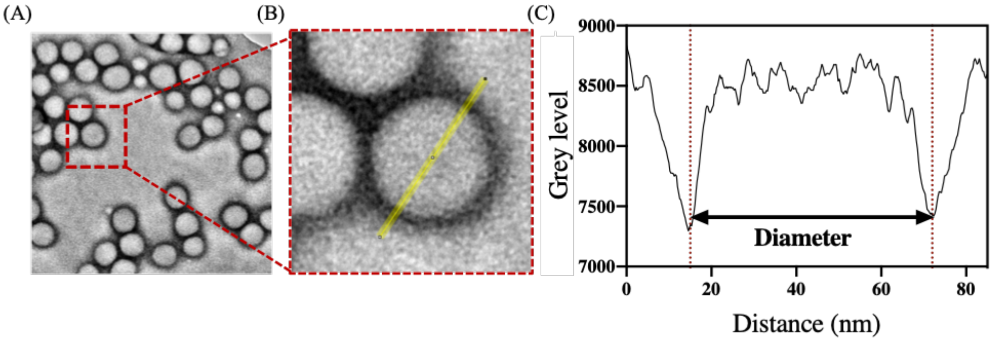

Figure 26. The polymersome diameter measurements as the distance between the minima in the intensity plot. (A) The raw TEM micrograph and the (B) zoomed in polymersomes with the highlighted region (yellow) corresponding to the (C) intensity plot. The distance between the two minima of the intensity plot is measured as the diameter of the polymersome i.e., the distance between the stained membrane.

3.5.2.3 Automated image analysis

In the case of samples with highly mono-dispersed spherical polymersomes with no presence of more complex aggregate morphologies, the D_D was measured using computational aid. Figure 27 presents a simplified flow diagram of the algorithm and demonstrates an example of the outputs of every implemented step. Detailed descriptions of the algorithm are introduced below.

3.5.2.3.1 Pre-processing

The pre-processing steps can be split into contrast enhancement and de-noising. The micrographs contain polymersomes with weak luminance, hence the contrast of these polymersomes was enhanced by the Contrast Limited Adaptive Histogram Equalization (CLAHE) method.[142] Firstly the image is split into 8*8 tiles, and the local intensity histogram of each tile is computed. Before the histogram equalization, and to limit the over-amplification of noise, the local histogram is clipped at a predefined value T. The portion of the local histogram that exceeds T is redistributed along the histogram bins to maintain the area of the histogram. The histogram equalization then uses the transformation of the local histogram to transform all the pixels in the tile and improve local contrast. Finally, all the contrast enhanced tiles are combined by applying the interpolation to eliminate block effects. Figure 27B shows the CLAHE output in which the polymersomes with low intensity have predominantly enhanced contrast.

Additionally, the salt and pepper noise was removed by performing a convolution of the image with a Gaussian kernel of default size

$$2\lceil 2 \times \sigma + 1\rceil \qquad (12)$$

where σ is the user defined standard deviation. This attenuates noise and smooths the image, as shown in Figure 27B. A further mean filter was optionally applied to noisy micrographs.

3.5.2.3.2 Image segmentation

The most common approach to segmentation is thresholding, this method applies a threshold to a greyscale image where all intensity values lower than the threshold are replaced by a value of 0 (black) while the rest are replaced with a value of 255 (white), hence converting to a binary image. The threshold is adaptively chosen based on the Otsu's method, where it is selected to minimize the intraclass variance between the thresholded black and white pixels.[143]

3.5.2.3.3 Round object detection

After the implementation of the image thresholding, the binary resulting image contains regions of high intensity areas in white, as shown in Figure 27B. The centroid, eccentricity and the bounding boxes of each detected region can then be identified. The objects with an eccentricity of zero (i.e., perfect circle) are discarded. The remaining regions are contained within bounding boxes which represent the smallest possible box that can enclose the region. The area of the bounding boxes is computed for those with a user-defined difference in main dimensions. In this case, the range of difference in the main dimensions, represented as a ratio of the width and height of the bounding boxes, is set between 0.8 and 1.2 corresponding to the difference in dimensions of a round object and accounting for deformities on drying the polymersomes. Another parameter to be included into the round object detection is a range of the areas corresponding to polymersomes. Finally, the diameters of each polymersome detected with the defined range of areas are computed and converted to appropriate length-scales by providing the pixel to length scale factor.

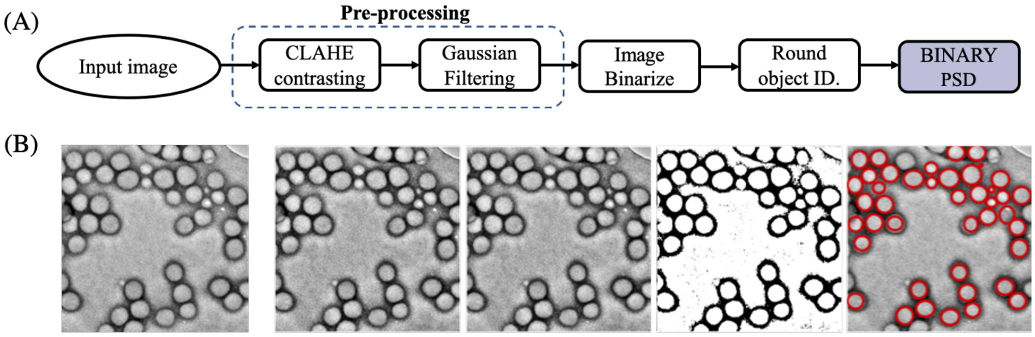

Figure 27. The (A) flowchart of the algorithm which involves a two-step pre-processing followed by an image binarization and a round object identification. (B) The corresponding images (from left to right) of the original raw inputted image, the output of the contrast enhancement, denoising, binarization, round object identification respectively.

3.6 Enzymatic encapsulation

3.6.1 PMPC-PDPA Polymersomes

Both the symmetric and asymmetric PMPC-PDPA polymersomes were loaded with glucose oxidase (Sigma-Aldrich, UK) by electroporation. The polymersomes were subjected to a temporary external electric field, which causes the copolymers within the membrane bilayer to rearrange, subsequently forming hydrophilic nano-sized pores in the bilayer membrane. These pores allow the diffusion of the proteins dispersed in the external solution into the vesicles and subsequent encapsulation once the pore is closed. The protocol has been previously optimised for the encapsulation of proteins into polymersomes and it was demonstrated that variation in the applied AC voltage, number of pulses and duration of each pulse has an effect on the loading efficiency.[144] A voltage of 2500 V was applied in 10 pulses to a mixture of glucose oxidase enzyme (1 mg/ml) and empty polymersomes (5 mg/ml) in water or PBS. Disposable electroporation cuvettes were used (2.0 mm gap size, VWR, United Kingdom) and loaded into the Eppendorf 2510 electroporator.

3.6.2 PEO-PBO POLYMERSOMES

In the case of PEO-PBO polymersomes, the glucose oxidase was encapsulated during the formulation process by preparing a dry film of PEO-PBO as mentioned in section 3.3. The film is rehydrated with glucose oxidase in water solution (0.5 mg/ml) to a final polymer concentration of 5 mg/ml and fluorescent dye concentration of 100 μg/ml. The suspension was sonicated for 10 minutes and extruded using the Avanti Mini Extruder™ , by passing the solution 21 times through a polycarbonate membrane with a pore size of 100 nm.

3.6.3 Liposomes

The glucose oxidase loaded liposomes were prepared using the film rehydration method by dissolving L-α- phosphatidylcholine from soy (Avanti Polar Lipids Inc., United States), and Rhodamine B octadecyl ester perchlorate (Sigma Aldrich, UK), in chloroform: methanol (2:1 v/v, Sigma-Aldrich, UK). This organic solvent was evaporated in a vacuum oven overnight to obtain a thin lipid film, as illustrated in Figure 24 . The film was hydrated with glucose oxidase solution (0.5 mg/ml) to a final lipid concentration of 5 mg/ml and a fluorescent dye concentration of 50 μg/ml. The lipid suspension was stirred for 1 hour at 4°C and sonicated for 10 minutes. This was followed by the extrusion of the liposome solution by using the Avanti Mini Extruder™. The liposome solution was passed 21 times through a polycarbonate membrane with a pore size of 100 nm, this forms the pristine liposomes loaded with GOX. A portion of this sample is then incubated with α-Hemolysin for 1 hour to form the porated liposomes loaded with GOX.

3.7 Size exclusion chromatography (SEC)

Once the nanovesicles are loaded by electroporation or during the film rehydration process the nanovesicle suspensions were purified. These suspensions can contain some free, non-encapsulated enzyme, which can be separated based on their size using size exclusion chromatography (SEC). This was performed using a column containing a gel of porous agarose beads (Sepharose 4B, Sigma-Aldrich, UK). The sample was introduced on the top of the column and eluted using PBS buffer (0.1 M, pH 7.4). The proteins, due to their smaller size, spend longer time in the stationary phase (agarose beads) since they can access the intra-particle pores, hence increasing their retention time. On the other hand, the larger polymersomes pass through the column faster and hence can be collected in earlier aliquots at the outlet of the column.

3.8 Polymer and Enzyme quantification

3.8.1 Quantification by Reversed-phase HPLC

Reversed-phase HPLC (RP-HPLC) was performed to quantify the components within the polymersome suspensions. This type of chromatography column, like typical chromatography apparatuses, absorbs the sample that was dissolved in the solvents of the mobile phase into the stationary phase of the column. The elutes (polar and apolar) of the mobile phase are changed over the experiment causing the different components of the sample to dispense from the column at different retention times according to their affinity with the two mobile phases. The detection of the dispensed peaks allows for the identification and quantification of the mixture of elements within the sample mixture. Hence, this technique was used to quantify the $PMPC_{25}$-$PDPA_{70}$ copolymer of a polymersome suspension, by first breaking the polymersomes to reveal the encapsulated protein using acidic PBS (50% v/v, pH 2). RP-HPLC was performed with the Phenomenex Jupiter C18 (5 µm, 300 Å, 4.60 mm x 250 mm column), at 1 mL min^{-}

^{1} constant flow. The mobile phase was a mixture of 0.05% v/v of trifluoroacetic acid solutions in CH_3OH and milliQ water. The $PMPC_{25}$-$PDPA_{70}$ absorbance peak was detected at 220 nm while the proteins were detected in the fluorescent mode (λ_{ex}= 270 nm and λ_{em}= 354 nm).

3.8.2 Quantification of GOX by BCA assay

Glucose oxidase enzyme encapsulated within the nanoparticles was quantified by using Micro BCA Protein Assay Kit (Thermo Scientific). Both the liposomes and the polymersomes, are disassembled first to expose the glucose oxidase enzyme for quantification. To a NaOH solution (0.05M, Sigma), 4% (v/v) sodium dodecyl sulphate (SDS) solution is added. This was then mixed with Dimethyl sulfoxide (DMSO) at a ratio of 5:1 v/v. This mixing solution was then added in equal volume to the nanoparticle sample (50 µl each) and mixed gently with the pipette to ensure the breaking of the nanoparticles. The glucose oxidase standard curve was prepared by a 2-fold serial dilution using the mixing solution as the dilutant. In a separate Eppendorf, the working reagent was prepared by mixing 50 parts of Micro BCA MA, 46 parts of the Micro MB and 4 parts of the Micro BCA MC solution. 100 µl of the working solution was added to the samples and the standard solutions and mixed thoroughly by pipette or on a plate shaker for 30 seconds and incubation at 60^{o}C for 1 hour. About 150 µl of each sample and standard solution was transferred into a 96-well plate, and the absorbance at 570 nm was measured using a Varioscan plate reader (Thermo Scientific). Two control samples were performed, first was the blank (mixing solution + working reagents 1:1 v/v) as well as the pristine nanoparticles to evaluate the degree of nanoparticle interference. The absorbance of the blank was subtracted from all the standard solutions and the nanoparticle samples. The standards were used to prepare a calibration curve Fig. showing the average absorbance readings for corresponding glucose oxidase concentrations. This was then used to identify the concentration of the glucose oxidase in the nanoparticle sample from the absorbance measurements.

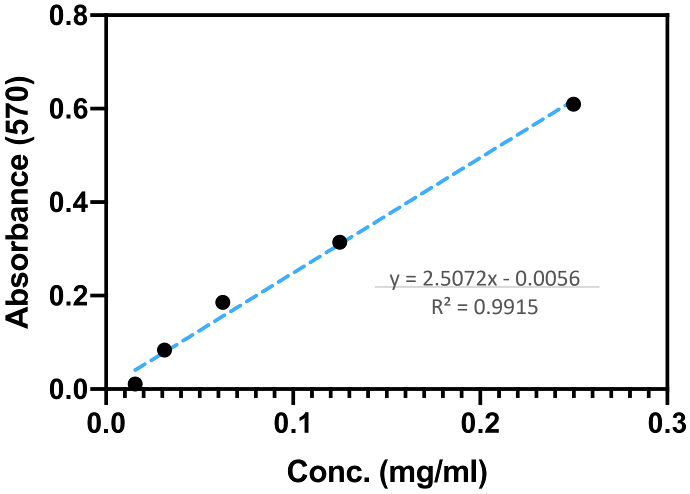

Figure 28. BCA assay glucose oxidase calibration curve showing absorbance (at 570 nm) as a function of glucose oxidase concentration (mg/ml).

3.8.3 Loading efficiency

The HPLC, BCA and DLS data were used to quantify the amount of polymersomes produced and the average number of enzymes encapsulated per polymersome (loading efficiency), as detailed by Wang *et al.*[144] The loading efficiency is defined as,

$$L_N = \frac{N_b}{N_p}$$

where N_b is the number of protein molecules in solution after purification by SEC and N_p is the total number of polymersomes in the sample. N_b was quantified as follows,

$$N_b = \frac{M_b}{M_{wb}} \times N_A = \frac{C_b \times V_s}{M_{wb}} \times N_A$$

where M_b is the mass of protein after purification by SEC (expressed as the protein concentration after SEC purification, C_b, times the volume of the solution after SEC purification, V_s), M_{wb} the molecular weight of the protein and N_A Avogadro number. N_p was calculated as the sum of all the number of polymersomes of each size population N_p^i.

$$N_p = \sum_{1}^{n} N_p^i$$

The number of polymersomes in each size population, N_p^i, was calculated as follows,

$$N_p^i = \frac{M_c}{M_{wc}} \times N_A \times R^i \times N_a^I = \frac{C_C \times V_s}{M_{wc}} \times N_A \times R^i \times N_a^i$$

where M_c is the mass of polymersomes after SEC purification, M_{wc} is the polymer molecular weight, R^i is the number of polymersomes for each population obtained from the DLS, C_C and V_s are the concentration and volume of the copolymer respectively and the N_a^i is the aggregation number of the amphiphilic copolymer population which is defined as,

$$N_a^i = \frac{4}{3}\pi \frac{(R - l_b)^3 - (R - l_b - t_m)^3}{V_{pdpa}}$$

in which l_b is the length of the hydrophilic PMPC brush, t_m is the thickness of the PDPA bilayer membrane, and V_{pdpa} is the molecular volume of a single PDPA chain.

3.9 Chemotaxis characterisation

The phoretic behaviour of the previously synthesised and encapsulated nanovesicles are explored next. Two methods were used to study this behaviour (i) Nanoparticle Tracking Analysis (NTA) and (ii) Ibidi chemotaxis microfluidic slides imaged by confocal microscopy. The detailed experimental methodology of each is presented in the next sections.

3.10 Nanoparticle tracking analysis (NTA)

NTA was executed using the NanoSight LM14 instrument (Malvern Panalytical LTD, United Kingdom) to track the movement of the nanovesicles in real-time. The NanoSight, is a device designed to characterise nanoparticles size and concentration in a liquid suspension. Like DLS, the NanoSight focuses a laser beam on the sample causing the particles to scatter light in all directions. In the NanoSight the sample is loaded into a crescent-shaped chamber of thickness 900 µm. The chamber is located on a plate under a microscope to track the light scattered by the particles, Figure 29. The laser is produced by a single mode diode with a wavelength of 405 nm and a focus of 80 µm, which crosses the sample causing the particles to scatter light in all directions. The microscope is connected to a CCD camera operating at 30 frames/second.

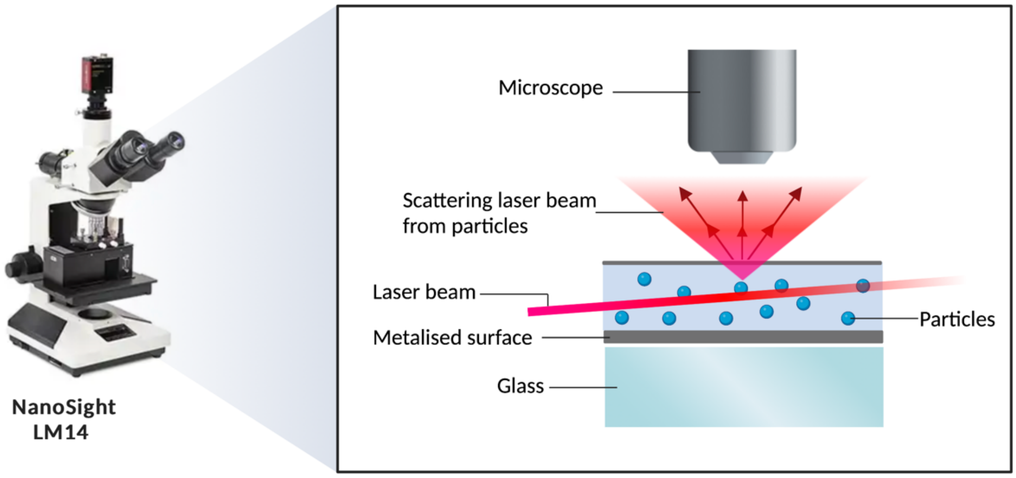

Figure 29. Schematic that illustrates how nanoparticles are imaged using the Nanosight LM14. This is done by shining a laser beam into the particle's suspension. The particles scatter the laser under a microscope to visualize the particles. Videos are recorded at different time intervals.

This method has been previously reported as a tool to evaluate the motion of particles in a gradient.[8] To do this a glucose gradient was established in the sample chamber. First the nanovesicle sample was injected through the inlet of the chamber (1 ml, 100 particles/ml). Both the inlet and the outlet ports were plugged with two tubes each connected to a syringe pump. Glucose solution (1M) was injected through the inlet by the first syringe pump and at the same time an equal amount of solution was withdrawn by the second syringe pump, to not alter the system. 100 μL was injected or withdrawn at a rate of 100 μL/min. Videos of the behaviour of the particles were recorded for 60 seconds at 5, 10, 15, 20, 25 and 30 minutes after injection. Figure 30, shows the NanoSight chamber indicating (i) the inlet for the injection of the sample and the substrate and outlet (ii) and the frame of the video recordings of the scattered light from the polymersomes. The particles were tracked using a built-in nanoparticle tracking analysis software and then analysed using Matlab®. The mean square displacement was calculated as reported in Volpe *et al.*[145] for 1 second, with an average of 2,000 - 10,000 tracks per sample.

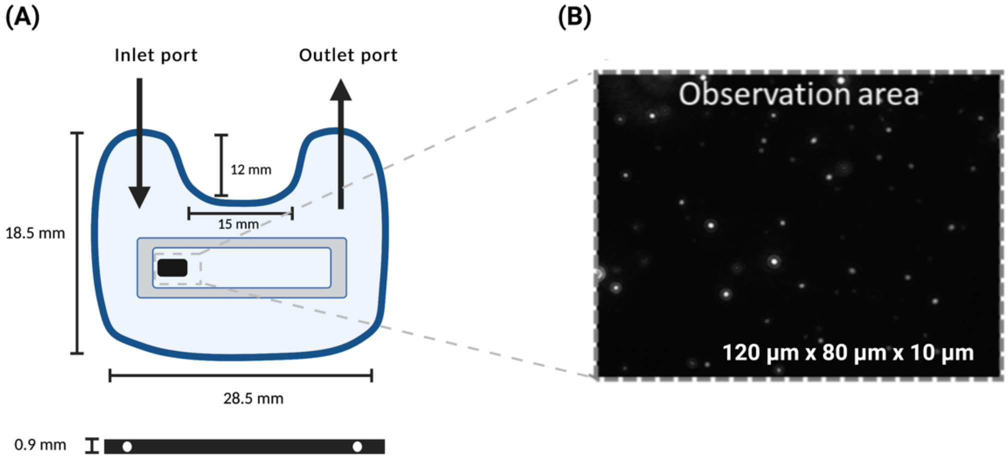

Figure 30. (A) The NanoSight sample chamber and (B) a video frame showing the scattering light from the nanoparticles.

3.11 Ibidi chemotaxis microfluidic slides

These experiments were conducted by establishing a glucose gradient within the commercially available ibidi µslide chemotaxis chambers, Figure 31. They consist of two reservoirs connected by a channel. These reservoirs are triangular with a depth of 1mm and are filled with high and low glucose concentration solutions. The gradient between them is established within the connective channel, which is 1mm in length (L), i.e., the distance between the two reservoirs, and has a depth of 70 µm and a width (W) of 2 mm. The channel walls are coated with a hydrophilic polymer ibiTreat coating. Using micropipettes, the chamber is loaded with the nanoparticle sample and unloaded through six inlets, two are located at each reservoir and two on either end of the channel. The channels are filled in carefully to prevent entrapping of bubbles and allow exit of air through the inlets. Once the channel is filled the inlets are sealed with plastic stoppers (no flow in channel). The x direction is defined along L, between the reservoirs from high to low glucose concentration. Gravitational pull acts in the negative z direction of the channel.

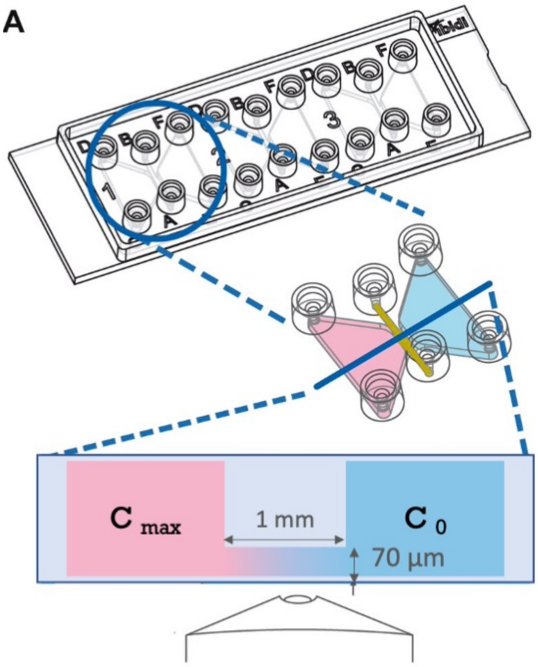

Figure 31. Graphic illustration of the ibidi µslide chemotaxis chambers used. The illustration of the device shows the six inlets used to load the triangular reservoirs with the high glucose solution (c_{max}*, pink) and low concentration (*c_0*, blue). The top view schematic of the sample chamber shows the channel connecting the two reservoirs and the gradient established between them. Figure reproduced from Ref.*[146]

3.11.1 Fluid flow characterisation setup

The experimental setup is established by first preparing a solution of glucose (Sigma-Aldrich) in PBS water at a concentration of 0 M (pure water), 0.5 M and 1 M. The 4 µL of the fluorescently labelled amine-modified polystyrene beads suspension at ~ 2.5% solids (Sigma-Aldrich, diameter = 1 µm) is added to 1 mL of the prepared glucose solutions (0, 0.5 and 1 M). The ibidi µslide chemotaxis chambers are loaded by first filling and sealing the low concentration reservoir with 0 M glucose concentration. This is then repeated for the high glucose concentration reservoir (either 0.5 or 1 M glucose solution). The chamber is now completely sealed, and a 5-minute waiting time is allowed for the gradient to establish before data collection. The diffusive mixing in this setup that would eventually lead to a uniform concentration within the chamber happens at significantly larger time scales than the experimental time of 5 to 60 minutes.[10]

3.11.2 Nanovesicle phoresis characterisation setup

To conduct the phoresis characterisation, the previously prepared nanovesicle solutions are diluted to a stock solution of 1 mg/ml. 60 µL of this stock solution is dissolved in 1 mL of the glucose solutions (0 and 0.5 M). The ibidi µslide chemotaxis chambers are loaded by first filling and sealing the low concentration reservoir followed by filling and sealing the high glucose concentration reservoir (0.5 M nanovesicle containing glucose solution). The chamber is now completely sealed, and a 5-minute waiting time is allowed for the gradient to establish before data collection.

3.11.3 Confocal microscopy

After allowing for the glucose gradient to establish, confocal imaging was performed using the Leica TCS SP8 inverted laser scanning confocal microscope. Laser scanning confocal microscopy is a special type of fluorescent microscopy known for its high resolution and contrast. Fluorescence is excited by illuminating a small section of the sample with a tightly focused laser beam and collecting fluorescence emission using a photomultiplier tube (PMT). A pinhole located at the conjugate focal (confocal) plane of the objective ensures only perfectly focused light is collected. By raster scanning the laser illumination spot a 2D image of the sample is acquired in an asynchronous manner. The fluorophores in the sample are excited and emit light which is filtered by a dichroic mirror and then passes through a second pinhole at the focal plane which allows only the light coming from the targeted point of the sample to be detected by the objective. The sample can be moved horizontally and vertically providing 2D or 3D images of the sample with good spatial resolution.

For this experiment, resonance scanning was used which utilises advanced resonant scanning mirrors to enable faster scanning across the specimen up to 30 frames per second. The Leica SP8 confocal microscope used is equipped with diode 405, Argon, DPSS 561 and HeN633 lasers. In the case of the fluorescently labelled polystyrene beads, and rhodamine labelled nanovesicles where illuminated by the Argon ion laser at a wavelength of 514 nm. The emission was detected using the HyD3 detector at 550-650 nm. The pinholeAiry of 1AU was set for the beads and 3.5 AU for the nanovesicles.

3.11.4 Data acquisition

Two types of data acquisition protocols were used, the XYtZ protocol to generate velocity profiles and the XYt protocol to generate velocity as a function of time plots.

3.11.4.1 XYtZ protocol

In this method, a 2D video is recorded in the middle of the gradient (x and y axis) at 7 different heights separated by 10 μm along the height of the 70 μm deep channel from bottom to the top. At each height, z, a 400-frame video is recorded in resonant mode at a rate of 14 frames per second. The 63x oil objective (HC PL APD CS2/63X/1.40oil) was used to give a 2D image size of 512 x 512 μm. The acquisition of the whole stack of videos takes approximately 3.5 minutes. Hence within an experiment there is a time delay between the recordings at the bottom and the top of the channel.

3.11.4.2 XYt protocol

Here 2D videos are recorded at different times at the same height (z= 35 μm) of the channel. The x and y direction are taken half way along the channel maintaining the position at the middle of the gradient. Making this position at the middle of the channel along x, y and z axis. The videos are recorded at 5-minute intervals up to 20 minutes from the establishment of the gradient. At each time, a 400-frame video is recorded in resonant mode at a rate of 14 frames per second, using the 63x objective. Each 2D frame is 258 x 258 μm.

3.11.5 Particle tracking analysis

From the recorded 2D videos, particle trajectories are obtained using standard particle-tracking algorithms written in R programming language by Dr. Ian Williams.[10, 147] In which the mean displacement along the x-direction, the direction of the concentration gradient, was computed from all displacements of all the tracked particles. The displacements are calculated between consecutive frames all the way up to 1 second. The slope of the displacement plot is used to attain the velocity of the particles. This is repeated at the different heights of the channel to develop a velocity profile, i.e., the velocity of the particles (be beads or nanovesicles) at different heights of the channel. Hence each point in the velocity profile corresponds to a spatial average over the 258 μm square at the middle of the gradient (x and y axis) and at a time average over approximately 30 seconds of video acquisition at each height. Each velocity profile is an average of six independent experiments. The videos attained through the XYtZ protocol are also analysed in the same way and velocities at different experimental time is collected to develop a velocity vs time plot. Hence each point in this profile represents a spatial average over the 258 μm square at the middle of the gradient along x, y and z (z=35 μm) and at a time average over approximately 30 seconds of video acquisition at different times along the experiment (5, 10, 15 and 20 minutes after the gradient is established).

CHAPTER FOUR

NANOVESICLES SELF-ASSEMBLY

In this chapter I describe the fabrication of asymmetric PMPC-PDPA polymersomes and liposomes. I investigate the formulation and characterisation of the physicochemical properties of the nanovesicle systems and report detailed characterisation by examining the size distribution, morphology, and membrane topology by DLS and TEM.

4.1 PMPC-PDPA polymersomes

This section of the chapter focuses on the introduction of a more permeable PEO-PBO domain into the membrane of a PMPC-PDPA polymersome, as shown in Figure 32. The self-assembly is optimised to attain a monodisperse, spherical polymersome sample suitable for future chemotactic experiments.

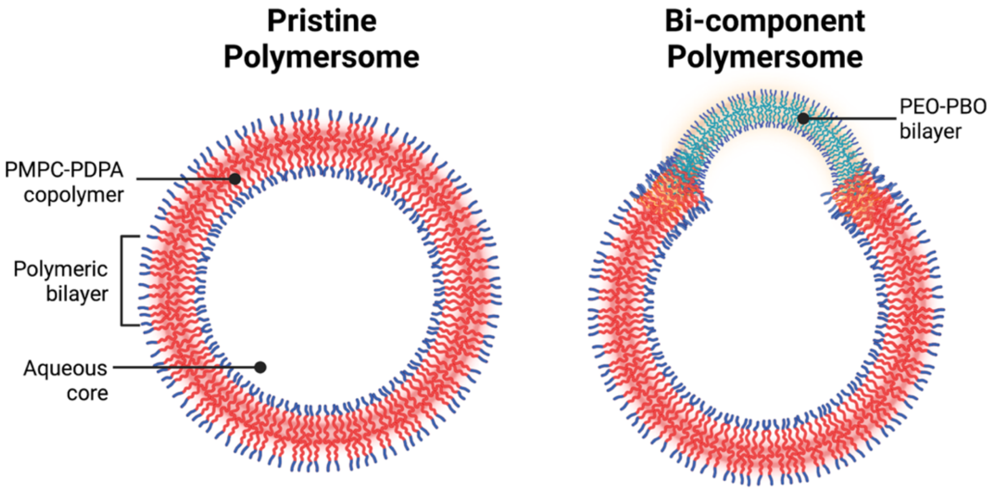

Figure 32. A schematic illustrating the pristine, single component PMPC-PDPA and the modified bicomponent PMPC-PDPA + PEO-PBO polymersomes in which the two copolymers phase separate to form an asymmetry on the membrane. The PMPC, PDPA, PEO and PBO polymer blocks are in red, blue, light green and purple respectively.

Polymersomes can be prepared by direct dispersion of block copolymers film in aqueous solution by film rehydration (the solvent free technique).[148] Alternatively, they can also be prepared by the phase inversion technique (solvent switch method), in which block copolymers are dissolved in an organic solvent suitable for all blocks, followed by the addition of water that is a poor solvent for the hydrophobic block.[149, 150] It has been demonstrated that the method of preparation affects the size and morphologies of the final vesicles.[131]

Consequently, I explore each of these methods by firstly defining a protocol of self-assembly and post-preparation purification to prepare pristine PMPC-PDPA polymersomes with an average diameter of 50-100 nm, and of a spherical, vesicular morphology. This is then advanced to prepare vesicular bicomponent PMPC-PDPA + PEO-PBO polymersomes of similar size, with phase separated PEO-PBO domains on the membrane. The physiochemical properties of the self-organised block copolymers in water were investigated with dynamic light scattering and transmission electron microscopy.

4.1.1 Film rehydration

To prepare the $PMPC_{25}$-$PDPA_{70}$ polymersomes, the film is hydrated and stirred for 8 weeks, which facilitates the lamellae swelling and complete unbinding while giving the necessary time for the most stable structures to evolve.[74]

4.1.1.1 PRISTINE polymersomes

I begin by confirming the self-assembly of the PMPC-PDPA block copolymer by film rehydration. The appearance of the block copolymer changes during the self-assembly process, Figure 33. When the copolymer is dissolved in organic solvent, the solution is clear indicating the complete solubilisation of the copolymer. After the organic solvents are evaporated under vacuum, the polymeric film is formed. Upon the hydration of the film by the addition of water, the solution starts to become translucent. Which when stirred for 8 weeks, becomes opaque and milky. This change in turbidity is associated with the aggregation of the copolymers driven by the hydrophobicity of the PDPA block in the presence of water.

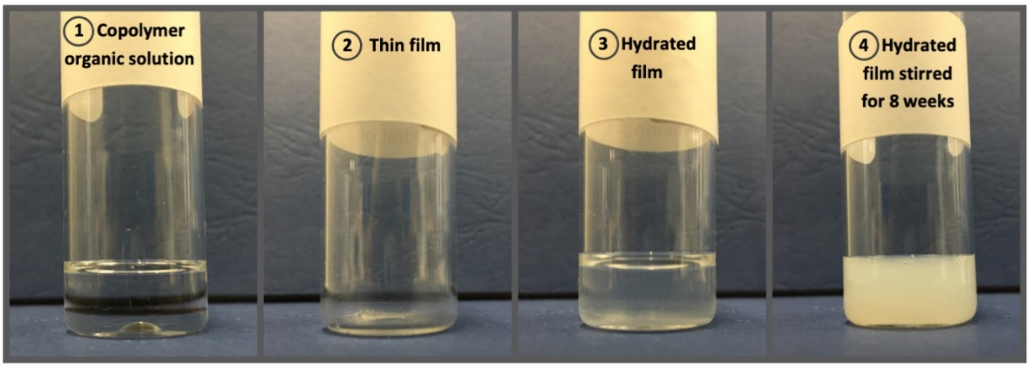

Figure 33. Images of the sample during the film rehydration self-assembly of PMPC-PDPA. In which (1) the copolymer is dissolved in an organic mixture of chloroform and methanol, displaying a clear solution. The organic solvents are evaporated to produce a (2) thin film, upon the (3) hydration of the sample, the film swells. (4) After stirring for 8 weeks, the sample becomes turbid indicating the formation of self-assembled aggregates.

TEM micrographs of this sample are shown in Figure 34. The vesicular morphologies are identified by the spherically shaped structures, outlined by a thick stained membrane representing the PTA-stained PMPC-PDPA membrane of the polymersomes, Figure 34D. The spherical polymersomes have an average dry-phase diameter (D_D) of 122.4 ± 80.3 nm (n=30). Among spherical polymersomes, deformed vesicles can also be observed, these are slightly elongated forming short tubes. These tubular polymersomes vary in length as shown in Figure 34C.

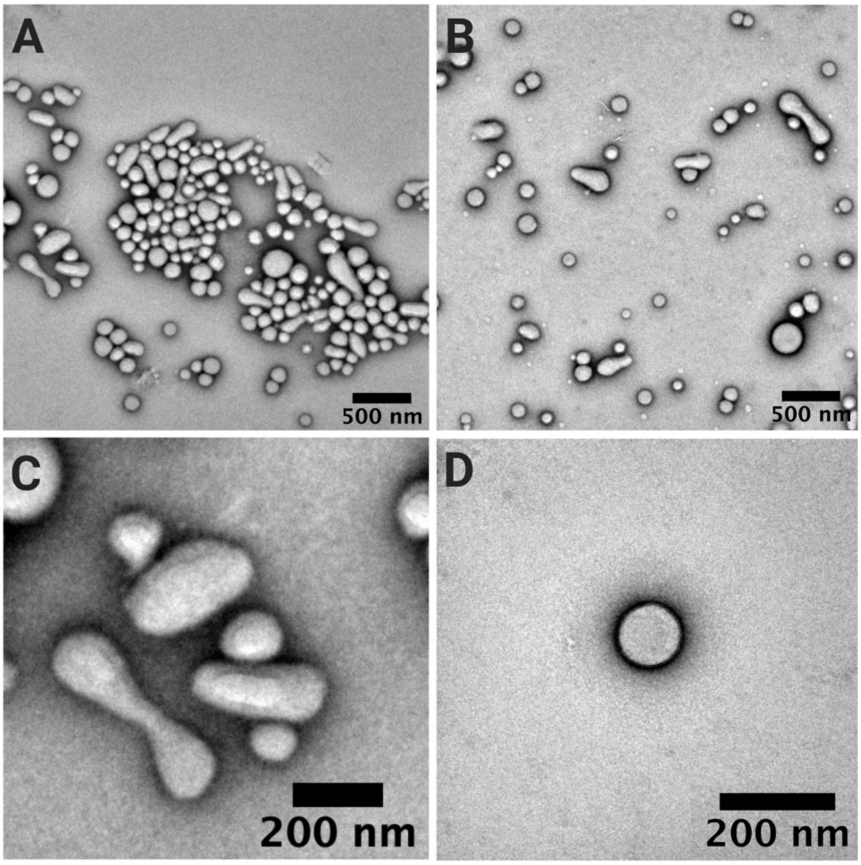

Figure 34. TEM micrographs of PMPC-PDPA vesicles formed by film rehydration after 8 weeks of stirring, (A, B) low magnification capturing the dispersity of the sample containing both spherical and tubular polymersomes. (C) high magnification of tubular and (D) spherical polymersome in the sample. Scale bars presented in black at the bottom right of images.

The tubular vesicles are intermediate states that form during the rehydration of the polymeric film, and the presence of both spherical and tubular polymersomes indicates the incomplete transformation of tubes to spheres.[151, 152]

During this process the addition of water to the thin film causes the layers of the copolymer to swell and wrinkle, following a sub-diffusional growth.[153] This swelling is dominated by the diffusion of water into the copolymer and the copolymer into water. The diffusion of water into the amphiphilic membranes (lamellae) occurs at a faster rate than the diffusion of the copolymer out.[153] This leads to a decrease in polymer concentration, effectively altering the hydrophobic and hydrophilic interactions of the copolymers blocks and water which lead to a molecular-level arrangement of the lamellae, known as collective diffusion.[154] This arrangements leads to the formation of the disordered bicontinuous membrane (sponge phase) which consists of finger instabilities and holes in the film which grows leading to the development of the characteristic rims.[155] When they detach from the film, the polymer concentration decreases further, hence changing the attractive and repulsive forces between the hydrophobic and hydrophilic blocks of the copolymer with water. These are balanced by “breaking” the tubular “finger-like” structures into spherical vesicles through a process of budding and pearling.[156]

Robertson et al. has demonstrated that the during the initial stages of the film rehydration of PMPC-PDPA lyotropic structures make the high percentage of the detached particles. With time and constant stirring the number of tubular and spherical polymersomes increases. The tubular polymersomes reach maximum abundance after 4 weeks of stirring. These decrease over time as the amount of spherical polymersomes increases. The maximum concentration of spherical polymersomes is reached after 8 weeks of stirring.[152]

Despite the linearity of this process, the continuous unbinding of swollen film into solution means that at any point in time multiple phases coexist. This is as observed by the TEM micrographs of this sample, in which both spherical and tubular polymersome coexist. I next aim to isolate only the spherical polymersomes from this sample to improve homogeneity and purify the sample from the tubular polymersomes and other larger aggregates.

4.1.1.1.1 Purification of spherical polymersomes

Although the self-assembly produces spherical polymersomes, the presence of tubular polymersomes is disadvantageous for our preparation of patchy polymersomes for chemotactic applications. This is important as the motion of an object is highly affected by its shape. For this reason, I evaluate here the purification of the prepared sample in the aim of attaining a sample consisting mainly of spherical polymersomes.

A possible way to improve the homogeneity of the sample is by applying mechanical force to breakdown and re-form the vesicles. Extrusion is a common method used to prepare liposomes[157] and some polymersomes[158]. In this method, phospholipid/polymeric self-assembled solutions are passed through a polycarbonate filter several times, breaking up larger structures and narrowing the size distribution. Nevertheless, high molecular weight polymers used to make polymersomes (like PMPC-PDPA) introduce a mechanical resistance which would require substantial force to break the tough polymeric membrane.[159] Therefore extrusion is inappropriate for PMPC-PDPA polymersomes. Another method to improve the homogeneity of the sample is by separating the polymersomes based on the aggregates size and shape, known as density gradient centrifugation method.[160]

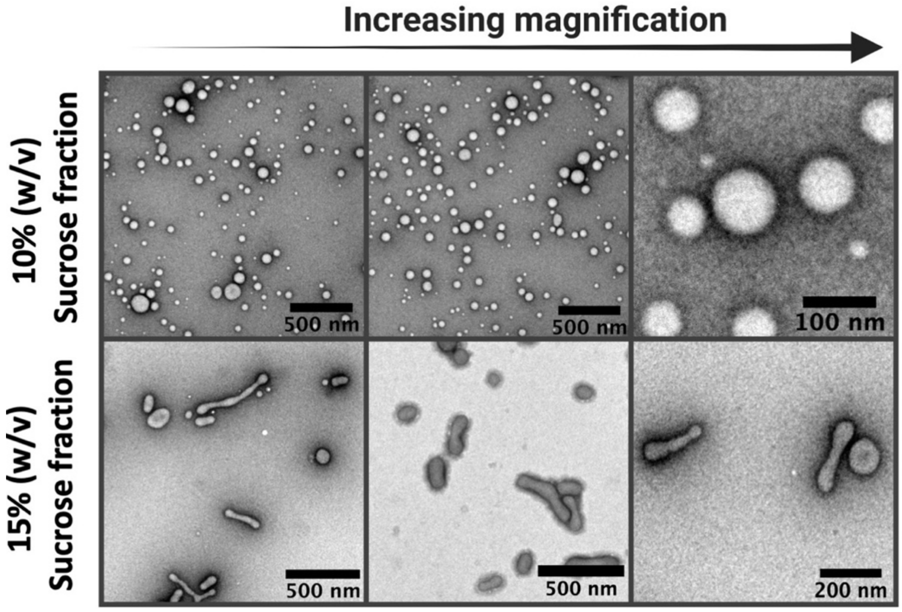

Figure 35. TEM micrographs of pristine PMPC-PDPA samples after density gradient centrifugation purification isolated from the (A) 10% (B) 15 % (w/v) sucrose fractions with increasing magnification from left to right. The low magnification images (column 1 and 2) show the population of the self-assembled structures in the samples (scale bar of 500 nm). The high magnification images (right column) show the spherical and tubular polymersomes isolated (scale bar of 200nm).

Figure 35 shows the TEM micrographs of the polymersomes isolated from the 10% and 15% (w/v) sucrose fractions. For the 10% fraction, the low magnification images signify the abundance of spherical polymersomes. These exhibit a vesicular morphology with an average D_D of 80.3 ± 20.3 (n=30). On the other hand, the 15% fraction displays a combination of both tubular and vesicular morphologies indicative of the presence of tubular and some spherical polymersomes. While some spherical polymersomes are lost in fraction 15%, fraction 10% (w/v) contains spherical polymersomes with an improvement in the homogeneity compared to that before purification.

This difference in populations can also be observed by DLS, Figure 36. Both the autocorrelation functions follow an exponential decay, while the 10% fraction decays at a slightly shorter time than that of the 15 % fraction suggesting a smaller size in the 10% fraction. This is a result of the faster Brownian motion experienced by the smaller particles.

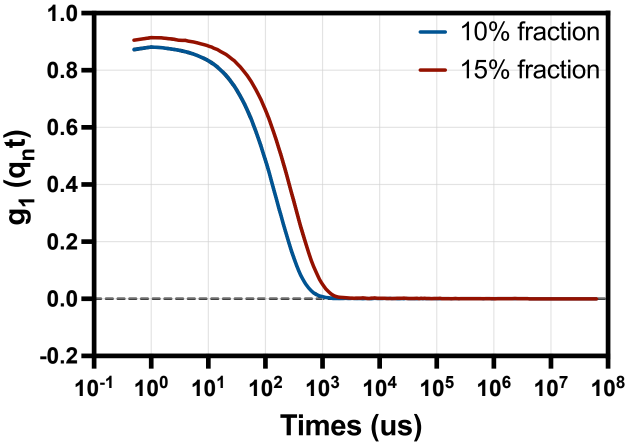

Figure 36. The autocorrelation function obtained by DLS of the 10% (Blue) and 15% (Red) sucrose (w/v) fractions obtained from the density gradient centrifugation purification method.

These results evidence the improvement of the homogeneity of the sample isolated from the 10% fraction which consists mainly of spherical polymersomes. This makes this protocol a suitable protocol for the preparation of PMPC-PDPA polymersomes for chemotactic applications. It is also worth mentioning that the difference between the 10 and 15 % fractions is a great example of the importance of using both DLS correlation function and TEM imaging to assess the quality of the self-assembly. Looking at the DLS data alone would not indicate the presence of tubular structures in the 15 % fraction. However, imaging the sample under TEM clearly shows that the 10% fraction is a far better sample containing spherical polymersomes than the 15 % fraction. Although DLS is a quick method that can be used in routine checks, conjugating it with TEM analysis gives a much more comprehensive view of the sample in question.

4.1.1.1.2 Reproducibility of purification

Having identified a suitable method to prepare a homogeneous sample of spherical polymersomes, I then investigated how reproducible this process is. The reproducibility of this method was evaluated by analysing four replicates, the TEM of the 10% fractions are displayed in Figure 37. All the replicates display vesicular morphologies of polymersomes as shown in the high magnification micrographs. The low magnification TEM images also verify the abundance of spherical polymersomes in all the replicates. The average dry phase diameter of the polymersomes in each replicate is 79.2 ± 17.6, 80.3 ± 20.3, 78.2 ± 23.6 and 75.1 ± 12.2 nm (n=30).

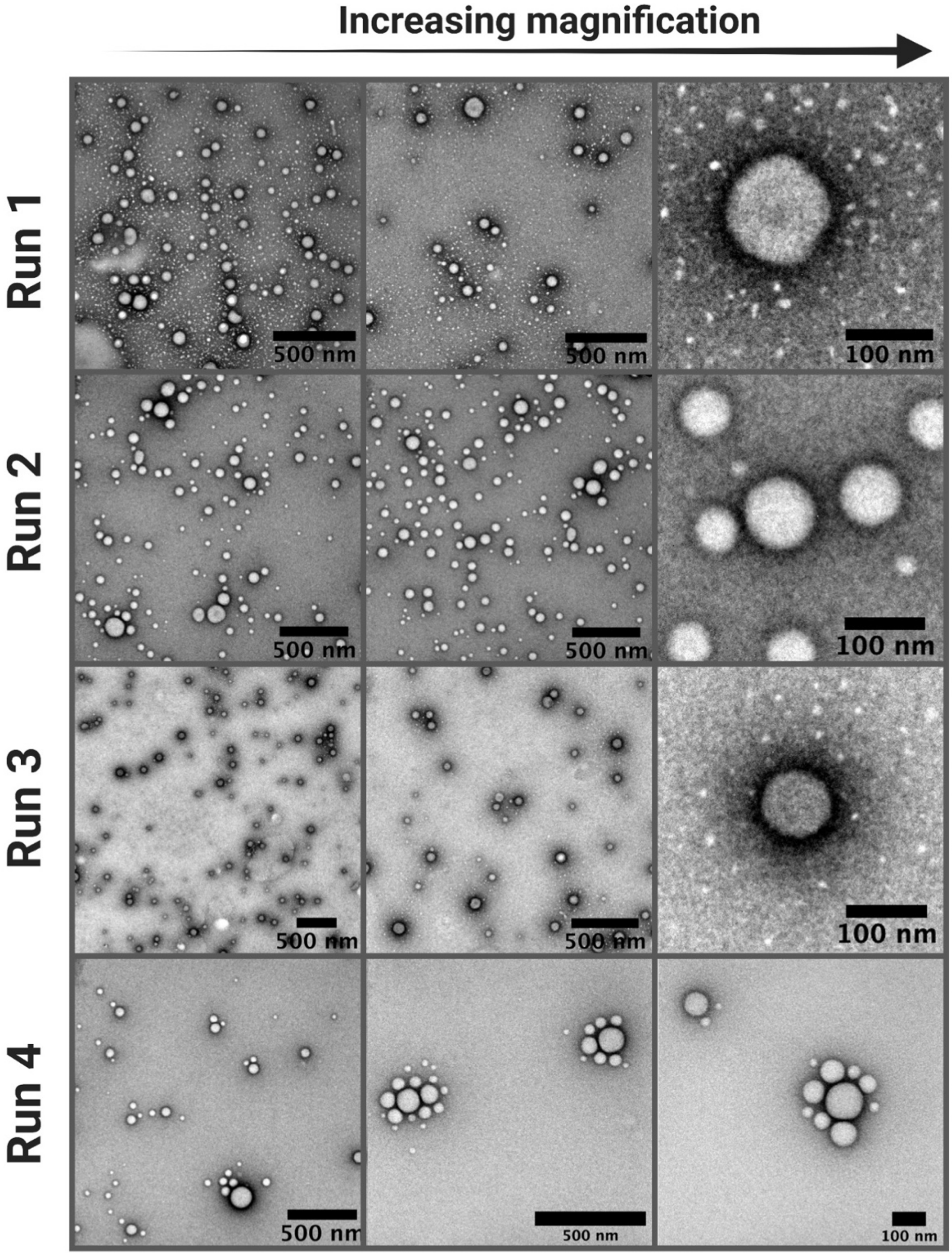

Figure 37. TEM micrographs of pristine PMPC-PDPA samples after density gradient centrifugation purification. Micrographs of four replicates (rows) with increasing magnification from left to right are displayed. The low magnification images (column 1 and 2) show the population of the self-assembled structures in the samples (scale bar of 500 nm). The high magnification images (right column) show the spherical polymersomes formed (scale bar of 100nm).

The DLS data of the 10% fractions are shown in Figure 38. The autocorrelation functions of the 4 replicates are comparable with slightly increased signal-to-noise ratio for run 3, nevertheless, this is still below the optimal value of Y-intercept >0.9. As seen from TEM micrographs, this sample consists mainly of spherical polymersomes, hence DLS analysis can be performed on the autocorrelation function to extract information on polydispersity and size distributions. The PDI values are within the range of 0.053-0.116 with average of 0.092 ± 0.029 between the replicates, the error represents the standard deviation from the replicates, as listed in Table 1. These values indicate that the samples are well dispersed with a poly dispersity index (PDI) of < 0.2.

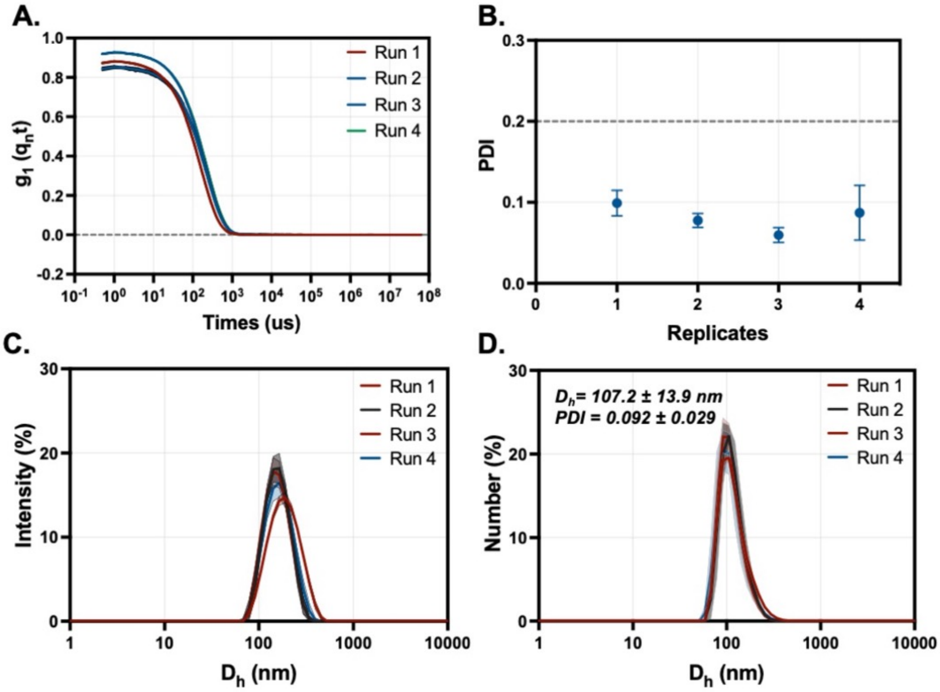

Figure 38. Four replicates of the purified pristine PMPC-PDPA polymersomes obtained by isolating the 10% fraction of the density gradient centrifugation. (A) The autocorrelation functions and (B) PDI of the four runs. (C) The intensity size distribution and (D)the number-weighted size distribution along with the average D_h and the PDI values showing the error as a standard deviation from the replicates.

From the autocorrelation function the intensity size distribution is also obtained and shows a single intensity peak from the size population within the sample, Figure 38. The light scattering intensity is more sensitive to the presence of larger particles, and hence the presence of a single peak below 1000 nm suggests the absence of biproducts in the form of larger aggregates in the sample. Next the number size distribution is analysed which shows a single peak at an average diameter of D_h of 107.2 ± 13.9. This value is in agreement with previously reported data.[74, 161, 162] The evidence proves that this method is a reliable route to the preparation of pristine PMPC-PDPA polymersomes with an enhanced dispersity by film rehydration.

Table 1. Tabulated values of the hydrodynamic diameter (D_h) and the PDI of the pristine PMPC-PDPA polymersomes after (purified) purification by density gradient centrifugation, along with the average and standard deviation from the replicates.

Replicate no.	Purified	
	D_h	PDI
1	123.4	0.116
2	111.0	0.086
3	89.9	0.053
4	106.0	0.111
Average	107.2 ± 13.9	0.092 ± 0.029

4.1.1.2 BI-COMPONENT polymersomes

Now that I have introduced a method to reliably produce a homogenous sample of spherical PMPC-PDPA polymersomes, I next explore the incorporation of PEO-PBO block copolymer into the self-assembly process to obtain a homogenous sample of spherical bicomponent polymersomes. These bicomponent systems are prepared by mixing a small amount (10 mol%) of PEO-PBO to the PMPC-PDPA copolymer during the film rehydration process to ideally yield spherical polymersomes incorporating both the co-polymers within the membrane. These two co-polymers phase separate in time forming a protruding bud of PEO-PBO within a majority PMPC-PDPA matrix, as previously reported by C. LoPresti *et al*. Figure 39, shows the TEM micrographs of the bicomponent polymersomes previously reported and those produced in this work. Due to the preferential staining of PMPC-PDPA compared to PEO-PBO by PTA, PMPC-PDPA appears as the darker domains while the PEO-PBO as the lighter unstained domain. These TEM micrographs verify the formation of the PEO-PBO domain as a bud on the PMPC-PDPA polymersomes in the bicomponent system.

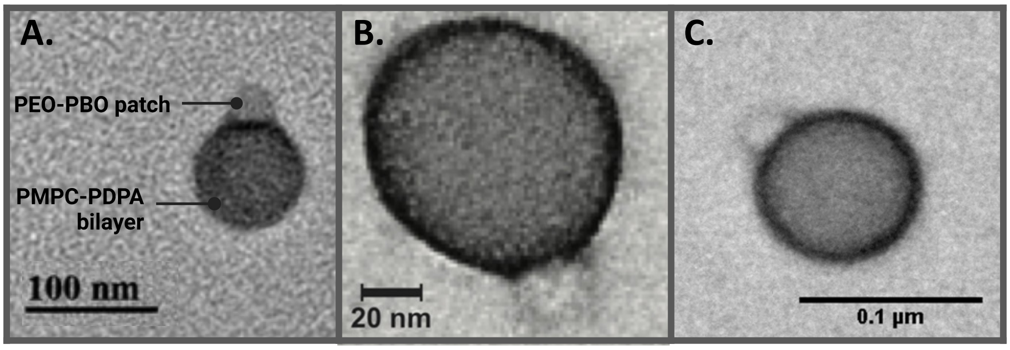

Figure 39. TEM micrographs pf bicomponent polymersomes consisting of a majority PMPC-PDPA bilayer and a minor PEO-PBO patch. Bicomponent polymersomes reported by (A) C. Z. Bueno et al. indicating the PEO-PBO bud protruding from the PMPC-PDPA membrane[162] *and by (B) A. Joseph and C. Contini et al. (C) Shows the high magnification micrograph of the bicomponent polymersome prepared for this thesis.*

The self-assembly was repeated with four replicates to evaluate the robustness of this method. The samples were visualised using TEM to explore the morphologies of the produced nanoparticles and draw comparisons between replicates. Figure 40 displays TEM micrographs in low magnification illustrating the population of the self-assembled structures (column 1 and 2) and high magnification images of the bicomponent polymersomes (column 3). For all the replicates, the micrographs verify the formation of the PEO-PBO domain as a bud on the PMPC-PDPA polymersomes. This is in agreement with previously reported PMPC-PDPA + PEO-PBO system prepared by film rehydration.[8] The average dry-phase diameter (D_D) of the polymersomes is 101.9 ± 63.2 nm (n=30). The membrane thickness of the two copolymer domains within the patchy polymersome is comparable with previously reported membrane thicknesses of 6.4 nm and 2.4 nm for PMPC-PDPA and PEO-PBO membranes respectively.[8,163, 164]

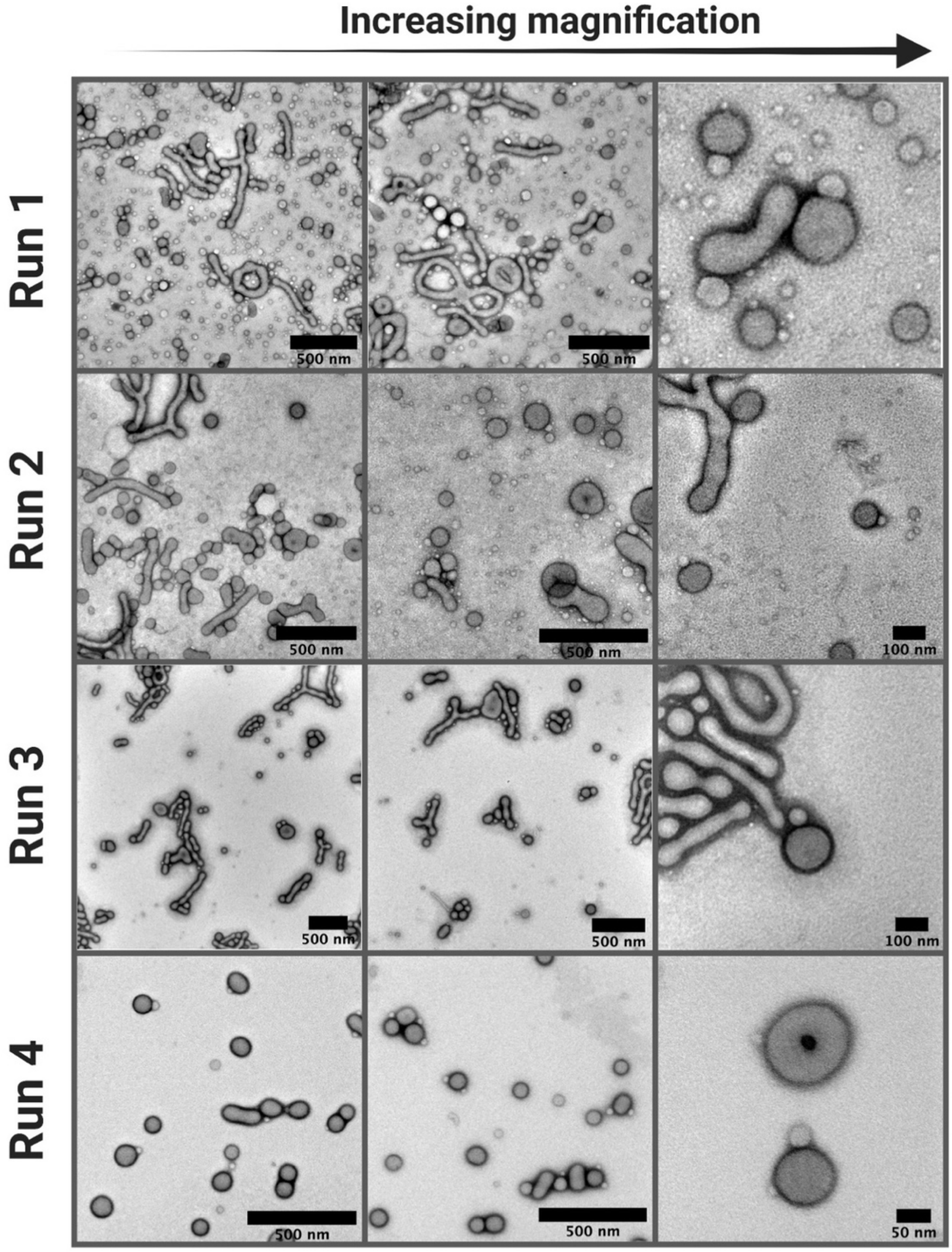

Figure 40. TEM micrographs of bicomponent polymersomes (PMPC-PDPA + PEO-PBO) prepared by film rehydration. The micrographs represent the self-assembled structures of four replicates (rows) with increasing magnification from left to right. The low magnification images (column 1 and 2) show the population of the self-assembled structures in the samples (scale bar of 500 nm). The high magnifications images (right column) show the spherical polymersomes formed.

Although this method yields some asymmetric polymersomes, it forms a variety of different self-assembled structures (small tubes, vesicles, Genus structures) ranging from 100-5000 nm.

Figure 41 shows a low magnification TEM micrograph of the bicomponent PMPC-PDPA + PEO-PBO polymersomes in Run 1. It illustrates the diversity of self-assembled structures produced in this system. Among spherical vesicles (both symmetric or asymmetric polymersomes), tubular structures are observed (such as long tubes or shorter tubular polymersome) and donut-shaped genus vesicles. These results show that the addition of PEO-PBO into the PMPC-PDPA membrane has increased the abundance of larger aggregates in particular tubular structures when compared to the pristine PMPC-PDPA system.

As described previously, tubular structures are intermediate phases. These undergo a process known as pearling in which the membrane pinches towards itself to form spherical polymersomes. This process requires the membrane to bend close together which demands high-energy. The addition of PEO-PBO increases the abundance of tubular morphologies, compared to pristine PMPC-PDPA which suggest that the presence of PEO-PBO stabilises the tubular structures and prevents their transition into spherical polymersomes.

This effect has also been reported when mixing cholesterol (0.05 to 5 w/w %) to PMPC-PDPA membrane.[152] This was also observed when adding cholesterol to the formation of polymersomes by poly(dimethylsiloxane)-block- poly(2-methyloxazoline) (PDMS-b-PMOXA) copolymer.[165] For both of these systems it was found that when added, cholesterol increased the presence of tubular morphologies by stabilising them. From this it can be inferred that the addition of PEO-PBO leads to the stabilisation of the tubular structures and hence a slower transformation into spherical polymersomes.

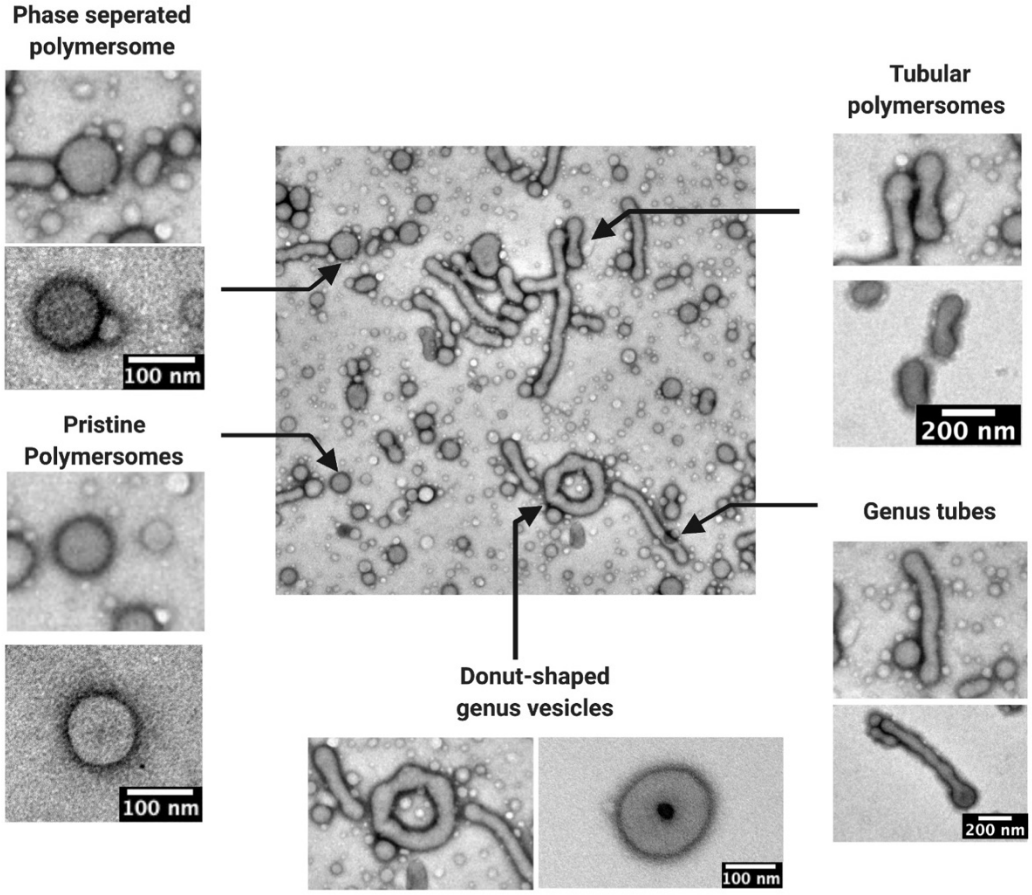

Figure 41. Low magnification TEM micrographs of bicomponent PMPC-PDPA + PEO-PBO sample prepared by film rehydration, illustrating the variety of different aggregates formed.

In addition to tubular structures the self-assembly produced other aggregates that differ in size, stability, structure, etc. Herein I use “aggregates” for any species regardless of its structure. The aggregates formed in these four replicates vary in structure and abundance. This can be seen with respect to the formation of tubes, which not only vary in length within each replicate but also vary in abundance between replicates especially when comparing run 1 and run 4. Additionally, in the case of the spherical polymersomes formed within the same sample, some of which are bicomponent displaying the PEO-PBO bud while others are pristine symmetric PMPC-PDPA polymersomes. On the other hand, between the replicates, the abundance of the bicomponent polymersomes vary. It is clear from the TEM images that the bicomponent systems show worse reproducibility when compared to pristine PMPC-PDPA, making them systems with a repeatability challenge.

Having established a reproducibility challenge in the preparation of the bicomponent systems, possible underlying causes are proposed. The difference between the replicates points towards variation in the aggregation manner upon introducing a second component to the system i.e., PEO-PBO copolymer. This observation may be attributed to the different evaporation temperatures of the chloroform and methanol which are mixed to dissolve both co-polymers. While, when evaporated, these solvents produce identical PMPC-PDPA thin films in the pristine system, the difference in solubility of the two co-polymers in the two solvents could result in different polymeric films at a nanoscopic and even a macroscopic length scale with every replicate. The lack of control on the formed film, in addition to the random aggregation of the two co-polymers in water could also lead to an irreproducibility challenge in producing bicomponent polymersomes and other aggregates.

Nevertheless, the interest in this thesis is the preparation of bicomponent polymersomes for chemotactic applications and hence the spherical polymersomes were separated from these samples by density gradient centrifugation purification, as implemented for the pristine PMPC-PDPA. The 10% w/v sucrose fraction was extracted, concentrated using crossflow and analysed by TEM and DLS.

The TEM micrographs of the four purified samples are presented in Figure 42. The low magnification micrographs display an improvement in the homogeneity of the self-assembled population compared to those pre-purification. The majority of the sample displays vesicular morphologies of polymersomes with the presence of rare elongated tubular polymersomes. This trend is consistent in all the replicates indicating a robust method to purify the spherical polymersomes from other aggregates formed during the self-assembly process. The average D_D and standard deviation for the spherical polymersomes are 94.2 ± 42.7 nm (n=30). Though the purified polymersome fraction contains well defined, spherical homogenously dispersed polymersomes, it consists of both pristine PMPC-PDPA polymersomes with a symmetric topology and the bicomponent PMPC-PDPA + PEO-PBO with visibly protruding PEO-PBO domain, Figure 42. The abundance of both these classes of polymersomes vary between samples, which can also be rationalised by the lack of control over the bicomponent thin film formation.

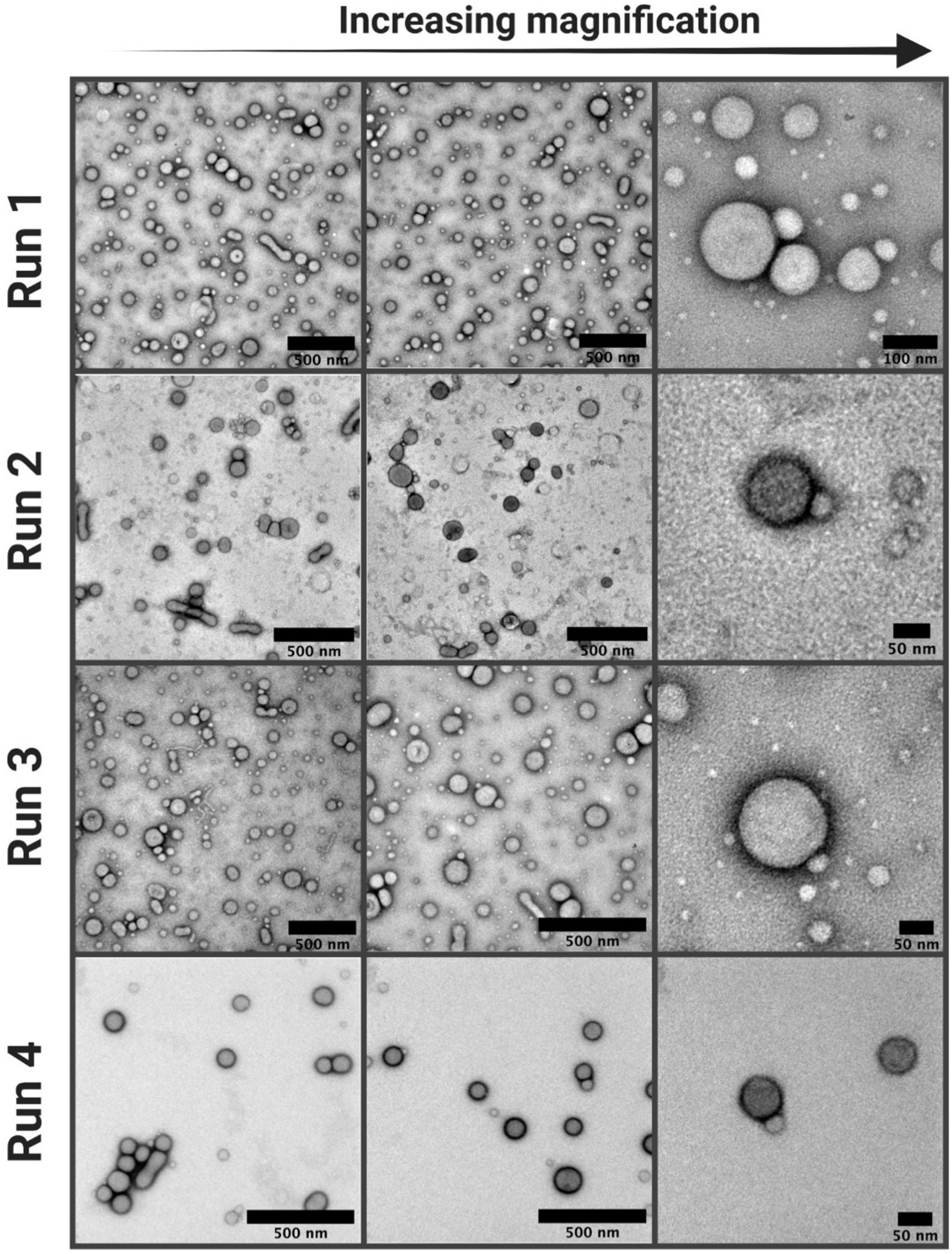

Figure 42. TEM micrographs of bicomponent PMPC-PDPA + PEO-PBO samples after density gradient centrifugation purification. Micrographs of four replicates (rows) with increasing magnification from left to right are displayed. The low magnification images (column 1 and 2) show the population of the self-assembled structures in the samples (scale bar of 500 nm). The high magnification images (right column) show the spherical polymersomes formed (scale bare of 100nm and 50nm).

Autocorrelation functions obtained from DLS are shown in Figure 43. These show a smooth exponential decay with optimal signal-to-noise ratio Y-intercept >0.9 for all the four independent replicates. Both the decay time and the slope are comparable for all the four replicates. The PDI values range from 0.85-0.149 with an average of 0.121 ± 0.026, as listed in Table 2. These values indicate an acceptable dispersity of polymeric nanoparticles (PDI < 0.2).

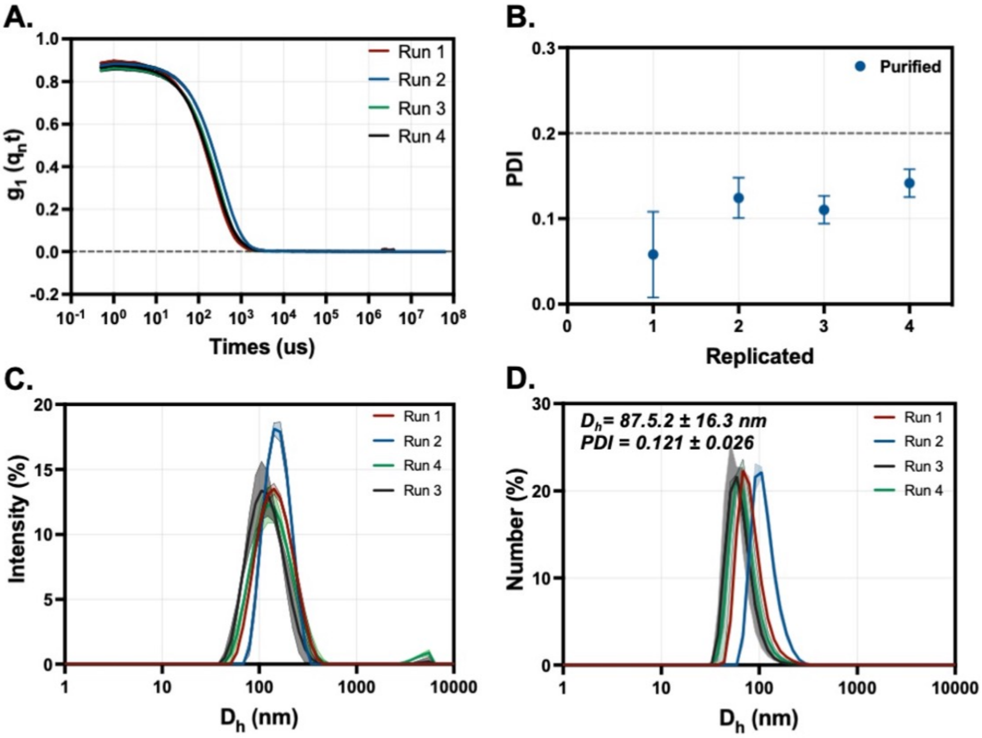

Figure 43. Four replicates of the bicomponent PMPC-PDPA + PEO-PBO polymersomes obtained by isolating the 10% fraction of the density gradient centrifugation. (A) The autocorrelation functions of the four runs. (B) The PDI. The (C) intensity size distribution and (D) number-weighted size distribution along with the average D_h and the PDI values showing the error as a standard deviation from the replicates.

The intensity size distribution shows the presence of a peak at about 100 nm for all the replicates signifying presence of nanosized particles. A second peak larger than 1000 nm in two of the replicates (run 1 and 4) indicates the possible presence of larger aggregates as a biproduct of the preparation, which were not successfully cleared during the purification step. Nevertheless, the absence of these peaks in the number size distribution indicates the scarcity of these biproducts in the sample. The number size distribution, however, shows a single peak around 100 nm in all the replicates which indicates that in all the four replicates the majority of the sample is polymersomes of about 100 nm. The average hydrodynamic diameter of each sample ranges from 72.1-110.4 nm, Table 2. While the average hydrodynamic diameter and standard deviation across 4 batches is a D_h of 87.5 ± 16.3 nm and PDI of 0.121 ± 0.026, showing the errors as standard deviation between the replicates.

Table 2. Listed are the hydrodynamic diameter (D_h) and the PDI values for the bicomponent PMPC-PDPA + PEO-PBO polymersomes after purification by density gradient centrifugation, along with the average and standard deviation from the replicates.

Replicate no.	Purified	
	D_h	PDI
1	110.4	0.085
2	72.1	0.149
3	85.2	0.122
4	82.4	0.130
Average	87.5 ± 16.3	0.121 ± 0.026

HPLC quantification of the PMPC-PDPA copolymer mass revealed a total PMPC-PDPA polymer yield of 18.3 ± 9.2 % for the bicomponent polymersomes within 10% w/v fraction, i.e. the mass of polymer retrieved as spherical polymersomes be pristine or bi-component.[*] The low yield of PMPC-PDPA retrieved as a mono-disperse polymersome sample suggests that a large percentage of the polymer is lost in other forms of self-assembled aggregate. This is not surprising as this method yields a range of aggregates compared to the pristine PMPC-PDPA self-assembly, Figure 40.

These results show that while this method produced polymersomes and more specifically patchy polymersomes, the yield of the spherical bicomponent polymersomes is very low. This is attributed to the noticeable increase in the heterogeneity of the sample due to the formation of a range of aggregates. In addition, this system has shown reduced reproducibility within replicates compared to the pristine single component system. These factors make this not an ideal method for the preparation of a homogenous sample of bicomponent polymersomes for chemotactic studies. Due to the extreme sensitivity of the nanoscale propulsion to the morphologies within the sample, it is necessary to find an alternative, more efficient approach with an improved yield of asymmetric, polymersomes.

---

[*] It is also worth highlighting that due to the random nature of the aggregation process involving these two co-polymers, and the possible variability in polydispersity between batches, the low yield attained could also be attributed to these batches of co-polymers and does not indicate that a higher yield cannot be attained.

4.1.2 Solvent switch preparation

Recently, the underlying mechanism for the bottom-up self-assembly process of PMPC-PDPA has been proposed outlining the evolution of the suspended copolymers to form disk micelles, which further grow to form vesicles and final high-genus vesicles.[73] On the other hand, the top-down method, previously used, involves the breaking down of a larger polymeric film leading to larger aggregates. The aim is to implement the bottom-up route which will limit the formation of larger aggregates such as long tubes and deformed polymersomes, which are the majority of biproducts formed in the bicomponent preparation via film rehydration.

Herein, I present two conditions for the self-assembly of bicomponent PMPC-PDPA + PEO-PBO polymersomes, yielding self-assembled structures of varying sizes, morphologies, and topologies. These are characterised with the aim of identifying spherical, mono-disperse polymersomes with asymmetric PEO-PBO domains within the membrane aimed for chemotactic studies.

4.1.2.1 PMPC-PDPA aggregation by solvent switch

The first condition explored involves solubilising the block co-polymers in an organic solution (3:1: MEOH/THF) and then solvating by the injection of water at a rate of 2 μl/min. The DLS analysis of the pristine PMPC-PDPA polymersomes show a smooth exponentially decaying autocorrelation function, Figure 44. The intensity size distribution displays a single peak at 78.8 nm indicating the presence of a single size class within the sample with no sign of larger aggregates. This is further reinforced by the number size distribution which show that the majority of the sample occupies a single size class with an average hydrodynamic diameter of (D_h) of 39.7nm. The PDI of 0.158 indicates a homogenous sample (PDI<0.2). Nevertheless, the smaller average size of the sample compared to those previously prepared by film rehydration, encourage further investigation as to the morphologies formed.

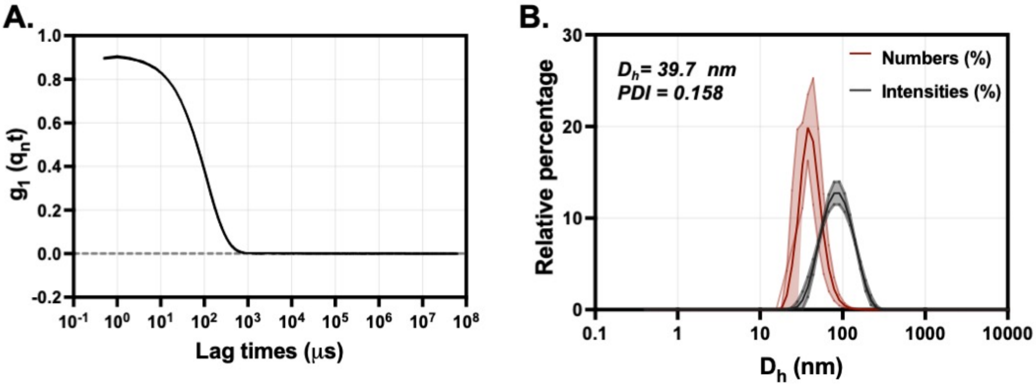

Figure 44. (A) The Autocorrelation function, (B) intensity and number-weighted size distribution along with average D_h and PDI values obtained by DLS for pristine PMPC-PDPA system prepared by solvent switch.

TEM imaging was conducted next, and the micrographs at low and high resolution displayed in Figure 45. The dry-state TEM imaging revealed the formation of highly mono-dispersed aggregates of spherical morphology, with no presence of any tubular or more complex aggregates. The spherical structures are micellar morphologies with a few polymersomes exhibiting vesicular morphologies. Disk micelles are a common product in bottom-up approach and have been reported previously in the literature.[73] [166] The disk-like micelles are identified by the distinct disk-like morphologies (when dried), small diameters (less than 40nm for PMPC-PDPA) and their highly curved edges.

The highly spherical nature of the sample allowed for the utilisation of a computationally aided size distribution analysis of the TEM images. Figure 46, illustrates the detected spherical particles from a micrograph by the developed sizing script as described in Chapter 2. For this sample 10 TEM micrographs were processed to isolate the dry-phase diameter of 1257 particles. The size distribution is shown in Figure 46. The average dry-phase diameter (D_D) is 45.9 ± 15.2 nm (n= 1257 particles) which is comparable to the hydrodynamic diameter (D_h) of 39.7 nm obtained from the DLS.

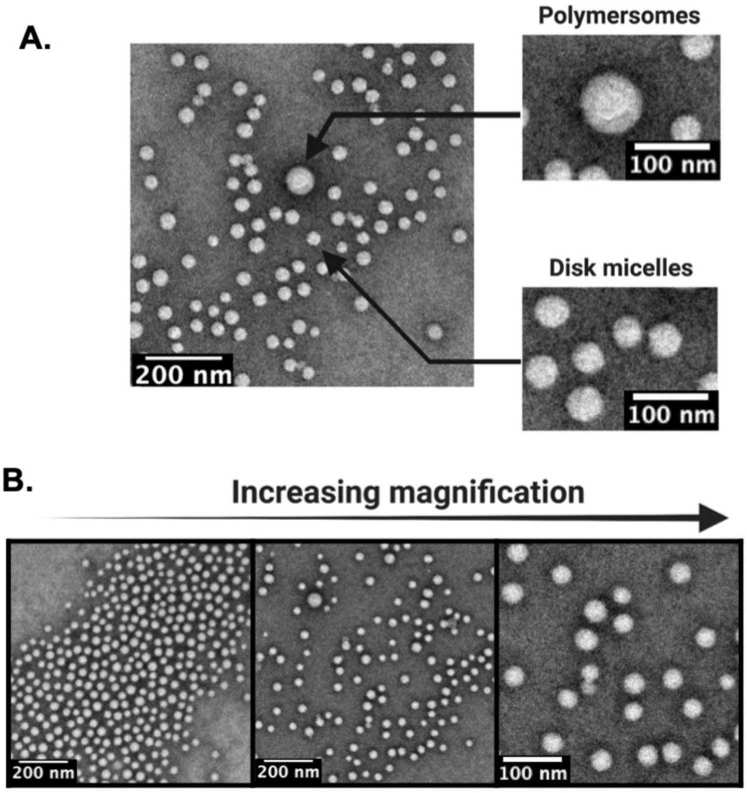

Figure 45. TEM micrographs of pristine PMPC-PDPA micelles formed by solvent switch. (A) low magnification micrograph showing the scarce polymersome and abundant disk micelles formed. (B) TEM micrographs at increasing magnification from left to right, showing the homogenous dispersity of the sample.

These results highlight the strong influence of different self-assembly methods on the aggregation of pristine PMPC-PDPA copolymer. In which the solvent switch method formed a monodisperse system consisting largely of micelles with an average hydrodynamic diameter (D_h) of 39.7 nm while the film rehydration produced a less homogenous sample of spherical and tubular polymersome with an average hydrodynamic diameter of 120 nm respectively. Such a reduction in size and change in morphology can be attributed in part to the bottom-up self-assembly process of the solvent switch method which involves the evolution of the suspended copolymers to form disk micelles, instead of the breaking down of larger polymeric film. [73] This difference is also maintained from the bicomponent system.

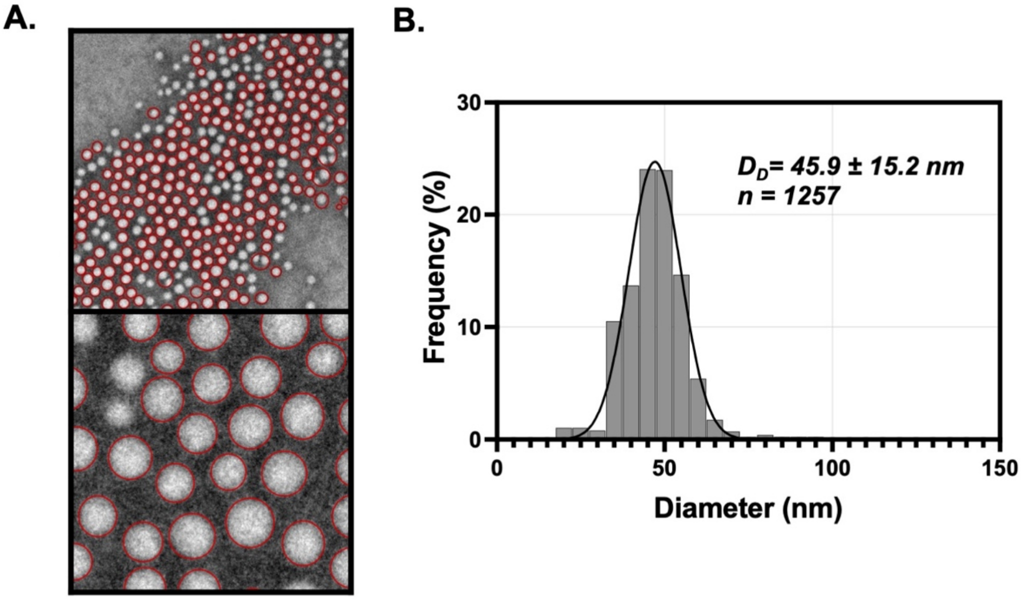

Figure 46. The results of the TEM micrographs analysis using the sizing algorithm. (A) TEM micrographs showing in red circles the round objects identified by the algorithm. (B) Histograms of the size distribution obtained by computing the dry-phase diameter of the detected spherical particles along with the calculated average diameter and the respective number of particles measured.

The DLS analysis of the bicomponent sample presents a single exponentially decaying autocorrelation function with optimal signal-to-noise ratio (Y-intercept >0.9), Figure 47. The PDI value of 0.171 is comparable to the PDI obtained from film rehydration methods of 0.177 ± 0.016. A single intensity peak below 1000 nm suggests the absence of by-products in the form of larger aggregate in the sample. The number size distribution also shows a single peak at an average diameter of 42.2 nm, which suggests that relatively the majority of the sample is within a single size class ranging from 22 nm to 150 nm. The size ranges fall within those for micelles and polymersomes. Nonetheless, this was next verified by TEM imaging of the sample.

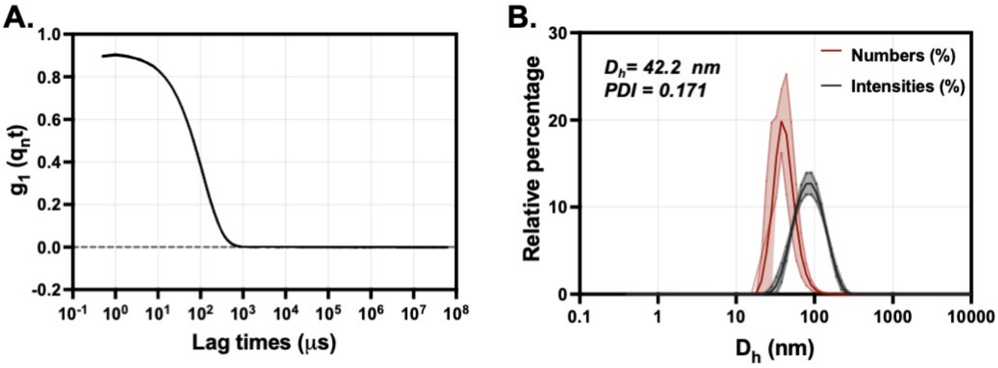

Figure 47. (A) The Autocorrelation function, (B) intensity and number-weighted size distribution along with average D_h and PDI values obtained by DLS for bicomponent PMPC-PDPA + PEO-PBO system prepared by solvent switch.

TEM imaging displayed a monodisperse sample of micelles with rare presence of spherical polymersomes. The dry-phase diameter of the sample was obtained from the TEM micrographs using the developed sizing algorithm. Figure 48B, shows the detected micelles in a TEM micrograph. From the ten processed micrographs, 2794 particles were detected and measured. The average dry-phase diameter (D_D) is 40.4 ± 19.0 nm (n= 2794 particles) which is comparable with the hydrodynamic diameter (D_h) obtained from the DLS. Nevertheless, no phase-separated PEO-PBO domains could be visually identified in the bicomponent micelles. This could be attributed to the small size of the micelles, which would hinder the visualisation of a 10% mol fraction domain on the surface. This could be further assessed by introducing a DOTA chelating a heavy metal on the PEO-PBO which would provide higher contrast on imaging to quantify the presence/absence of the patch.

It is clear from this data that this method improves the homogeneity of both the pristine and bicomponent samples compared to the film rehydration method. Nevertheless, the small size and micellar morphology of the produced sample are inappropriate for enzyme encapsulation which is an essential component in facilitating directional motion of the particles for chemotactic application. In addition, longer circulation time of these smaller particles in the body[167] renders this system not ideal for the purpose of our study and hence further topological characterisation of the micelles was not assessed.

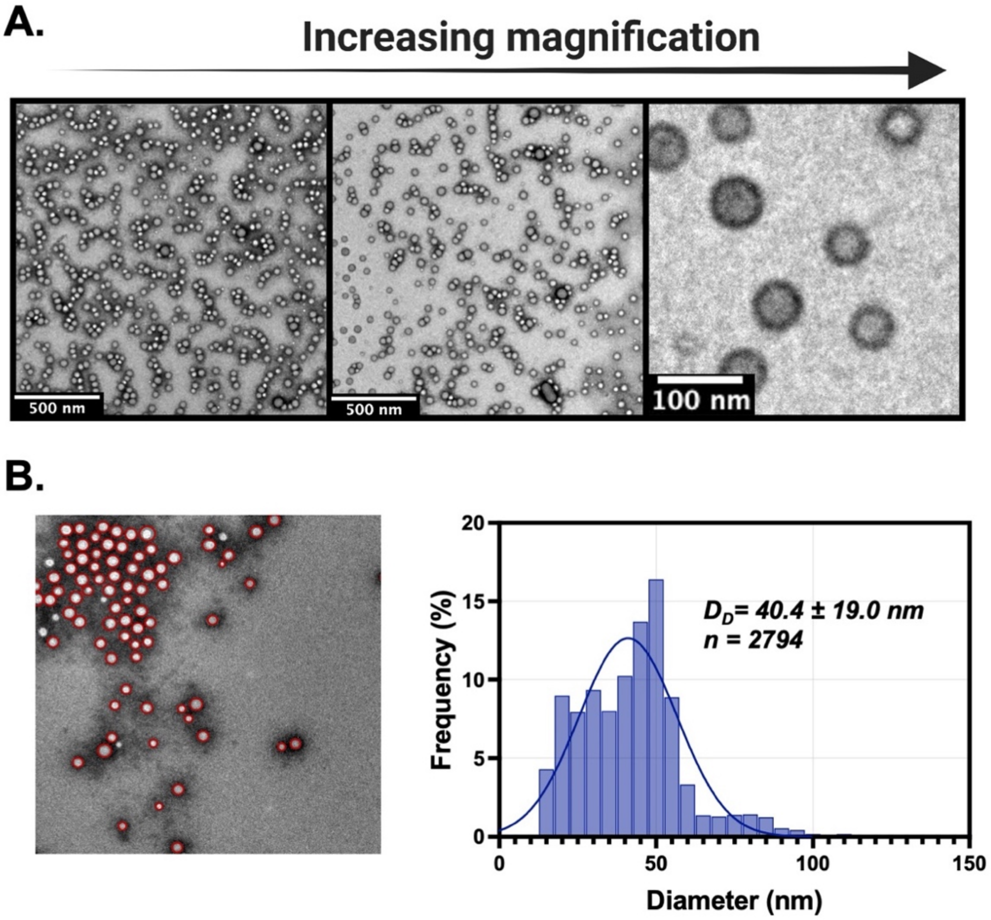

Figure 48. (A) TEM micrographs of bicomponent PMPC-PDPA + PEO-PBO prepared by solvent switch at increased magnification (left to right). (B) TEM micrographs showing in red circles the round objects identified by the algorithm and the histograms of the dry-state size distribution along with the calculated average diameter and the respective number of particles measured by the particle analysis based on TEM images.

4.1.2.2 PRISTINE polymersomes: Slow solvation

As described previously the bottom-up approach involves the evolution of the suspended copolymers to form disk micelles, which further grow to form vesicles and final high-genus vesicles. The kinetics of this process occurs in two stages the fast nucleation which involves the aggregation of the unimers suspended in solution followed by the much slower growth phase which is governed by the insertion of the unimers into the pre-formed assembly.[73] The large presence of the micelles in the PMPC-PDPA sample indicates that the copolymers do not have enough time to perform enough insertion events to allow the micelles to grow into vesicles, suggesting that the kinetics of the self-assembly is highly dominated by the copolymer nucleation. This has also been observed for other bottom-up approaches to assemble PMPC-PDPA such as pH-switch and temperature driven assembly. [73]

As the interest in this project is to attain polymersomes, providing the assembly process longer time could allow for the copolymers to insert into the disk micelles making them grow to a critical radius of about 15 nm at which the membrane begin bending and enclosing on itself to form vesicles. With this in mind, the next condition examined is by solvating the organic polymeric solution (PMPC-PDPA alone or with PEO-PBO dissolved in 3:1 MEOH/THF) at a slower rate to allow for the evolution of the disk micelles to vesicles, via the addition of water at a rate of 1 μl/min. This is then quenched by the addition of water to stop the growth of the present assembled structures. Finally, the remaining organic solvent is removed by dialysis against water for 3 days.

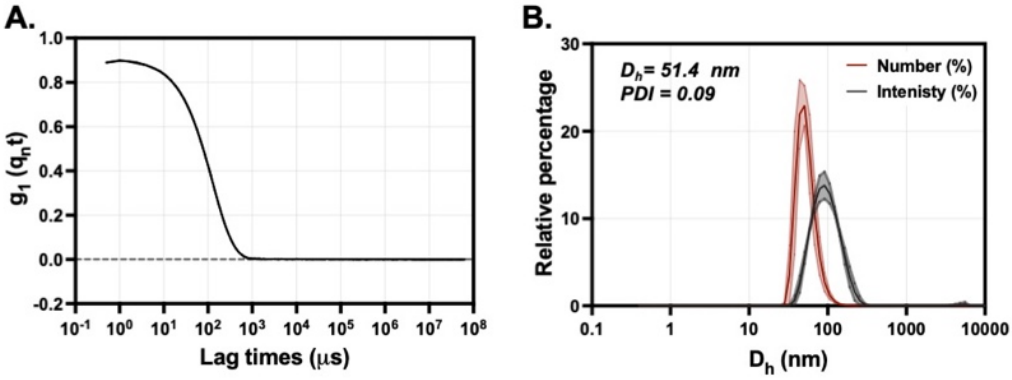

Figure 49. (A) The Autocorrelation function, (B) intensity and number-weighted size distribution along with average D_h and PDI values obtained by DLS for pristine PMPC-PDPA system prepared by the slow solvation of the organic polymers solution during solvent switch self-assembly.

DLS analysis of the PMPC-PDPA system revealed a single exponentially decaying autocorrelation function with ideal signal-to-noise ratio, Figure 49A. The PDI values of the sample is 0.09 indicating a highly stable monodispersed sample. The intensity size distribution shows a single intensity peak from the size population within the sample about 100 nm, Figure 49B. The number size distribution was also obtained and shows a single peak at an average hydrodynamic diameter of 51.4 nm, which suggests that relatively the majority of the sample is within a single size class. This increases the hydrodynamic diameter and reduced PDI value of the sample thus encouraged further investigation as to the morphologies formed.

TEM imaging of the sample using PTA staining, indicates a highly mono-dispersed system of spherical assemblies as shown by the low magnification TEM micrographs in Figure 50. The dry-phase diameter is 54.0 nm (n=300) which is comparable to the hydrodynamic diameter obtained from DLS. These values are within the size range of polymersomes, which in addition to the spherical morphologies conclude the formation of polymersomes in these samples. These also indicate that the polymersomes formed by this method are smaller than polymersomes prepared by the film rehydration which are approximately 80 nm.

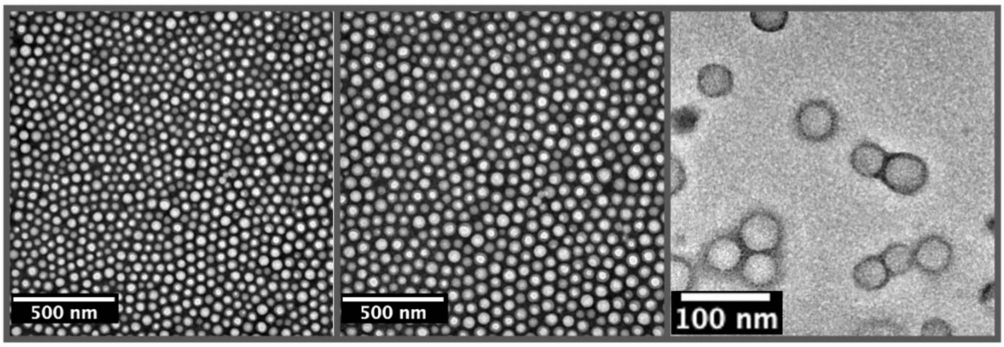

Figure 50. TEM micrographs of pristine PMPC-PDPA prepared by slow solvent switch at increased magnification (left to right).

This encouraging result is next validated for reproducibility between replicates of identical experiments by performing 3 replicates and evaluating the repeatability of the autocorrelation function, PDI, intensity size distribution and average particle size. All the autocorrelation functions show a single exponential decay, with optimal signal-to-noise ratio (Y-intercept >0.9), which lay over each other as shown in

Figure 51. The average PDI values and the corresponding standard deviation between all the replicates is 0.09 ± 0.002 nm, which indicate that the samples are well dispersed, homogenous and the low deviation between the samples indicate the consistency in the dispersity of the repeated samples. [168]

The intensity size distribution shows the presence of a peak about 100 nm for all the replicates signifying the repeatable absence of large aggregates. The presence of a single peak in the number-size distribution for all the replicates indicates that the majority of the sample is polymersomes displaying no statistically significant variations in distribution. The average hydrodynamic diameter and standard deviation of polymersomes formed across three batches is a D_h of 51.4 ± 11.3 nm showing the errors as standard deviation between the replicates.

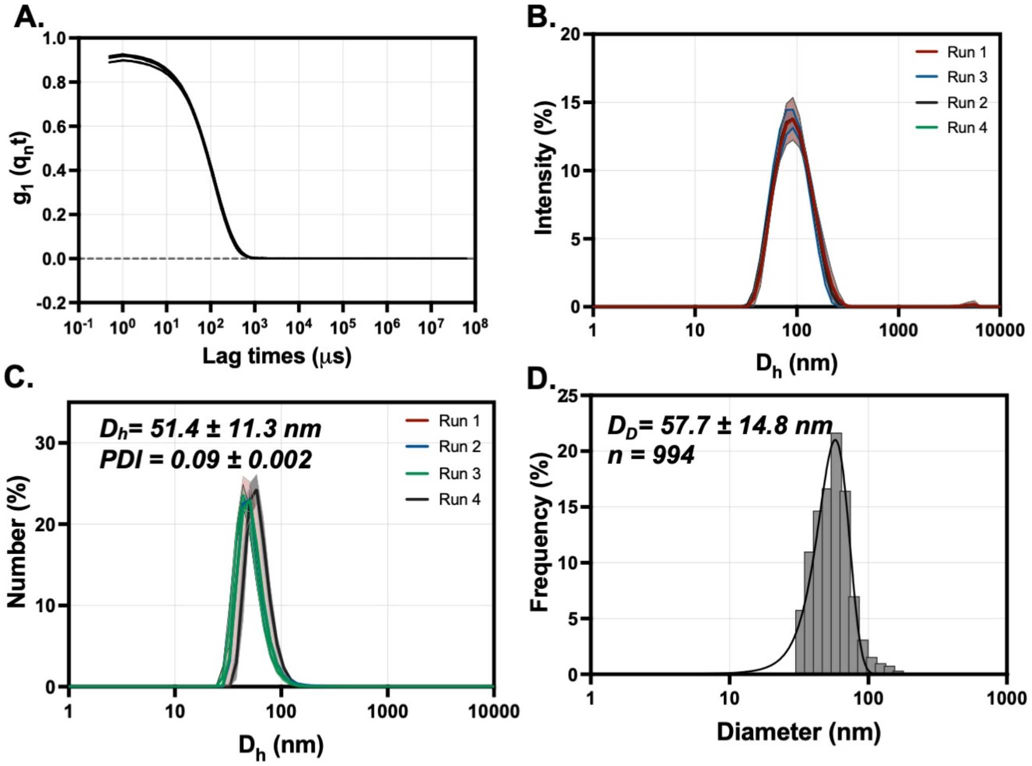

Figure 51. Repeatability of pristine PMPC-PDPA vesicles prepared by slow solvent switch across three replicates of identical experiments (A) Autocorrelation function, (B) intensity size distribution and (C) number-weighted size distribution along with the average D_h and the PDI values showing the error as a standard deviation from the replicates, (D) the histograms of the dry-state size distribution along with the calculated average diameter and the respective number of particles measured by the particle analysis based on TEM images.

The TEM micrographs of the three replicates are presented in Figure 52. These display highly mono-dispersed spherical polymersomes indicated by the spherical stained PMPC-PDPA membrane. The dispersity between samples is comparable with no presence of larger aggregates. This consistency between the samples indicates the reliable formation of polymersomes by this method. The average D_D was next examined by running a total of 10 micrographs of the replicates into the sizing algorithm. The average D_D of each of the three replicates are 56.0 ± 10.3 nm (n= 293), 59.6 ± 17.9 nm (n=347), 57.4 ± 14.6 nm (n=354).

These results point towards the robustness of this method in producing polymersomes across different replicates at an average D_D of 57.7 ± 14.8 nm, for all the 994 particles detected from all the three replicates. Both the DLS and TEM data indicate the robustness of this method in preparing pristine PMPC-PDPA polymersomes at low polydispersity (Highly mono-dispersed samples).

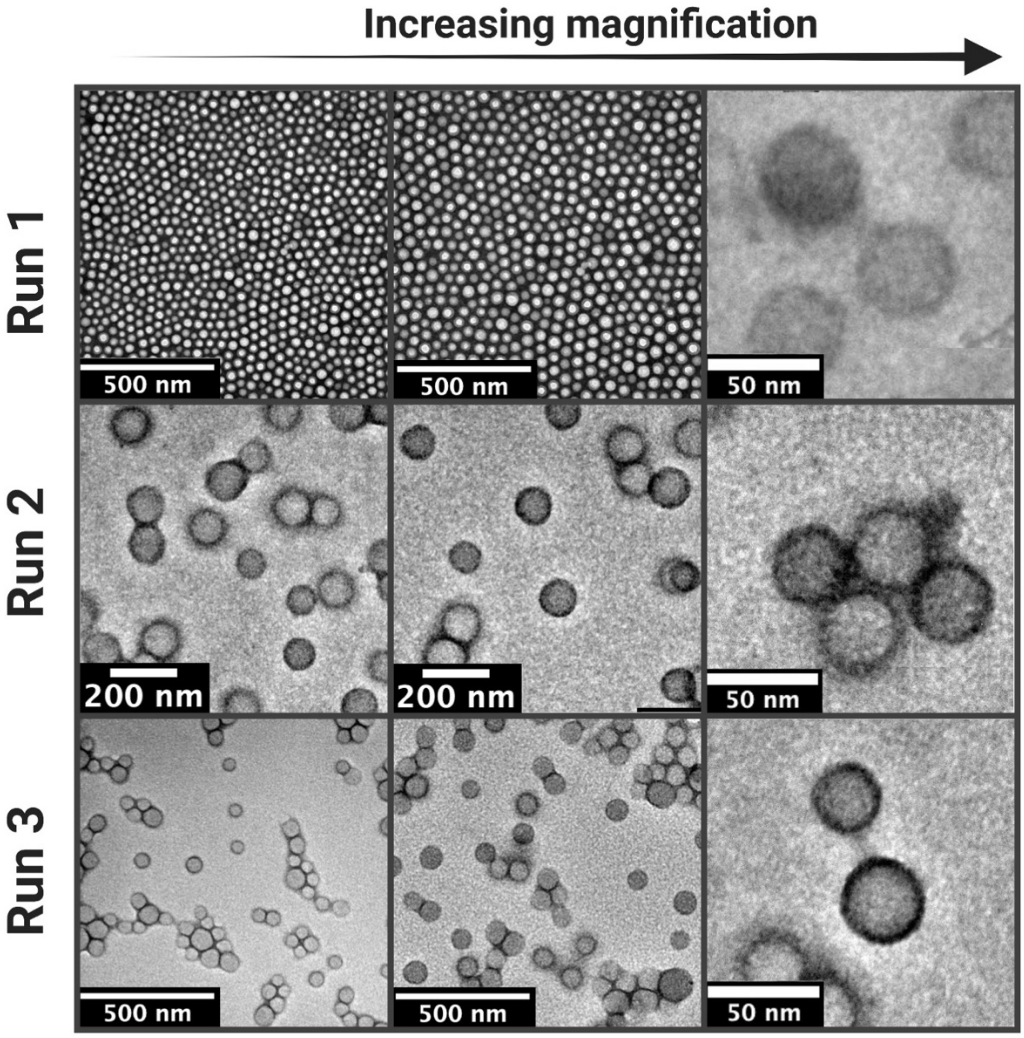

Figure 52. TEM micrographs of pristine PMPC-PDPA polymersome prepared by slow solvent switch. The micrographs represent the self-assembled structures of three replicates (rows) with increasing magnification from left to right. The low magnification images (column 1 and 2) show the population of the self-assembled structures in the samples. The high magnifications images (right column) show the spherical polymersomes formed (scale bar of 50nm).

4.1.2.3 BICOMPONENT polymersomes: Slow solvation

Since the robustness of this method in preparing PMPC-PDPA based polymersomes of about 50 nm has been confirmed, this was next explored for the bicomponent PMPC-PDPA + PEO-PBO. The aim is to attain a mono-dispersed sample of spherical polymersomes with a PEO-PBO domain on the membrane. This was conducted by the slow solvation (1 µl/min) of the organic polymeric solution containing both the co-polymers. Three replicates were also performed to evaluate the repeatability of this method across identical experiments.

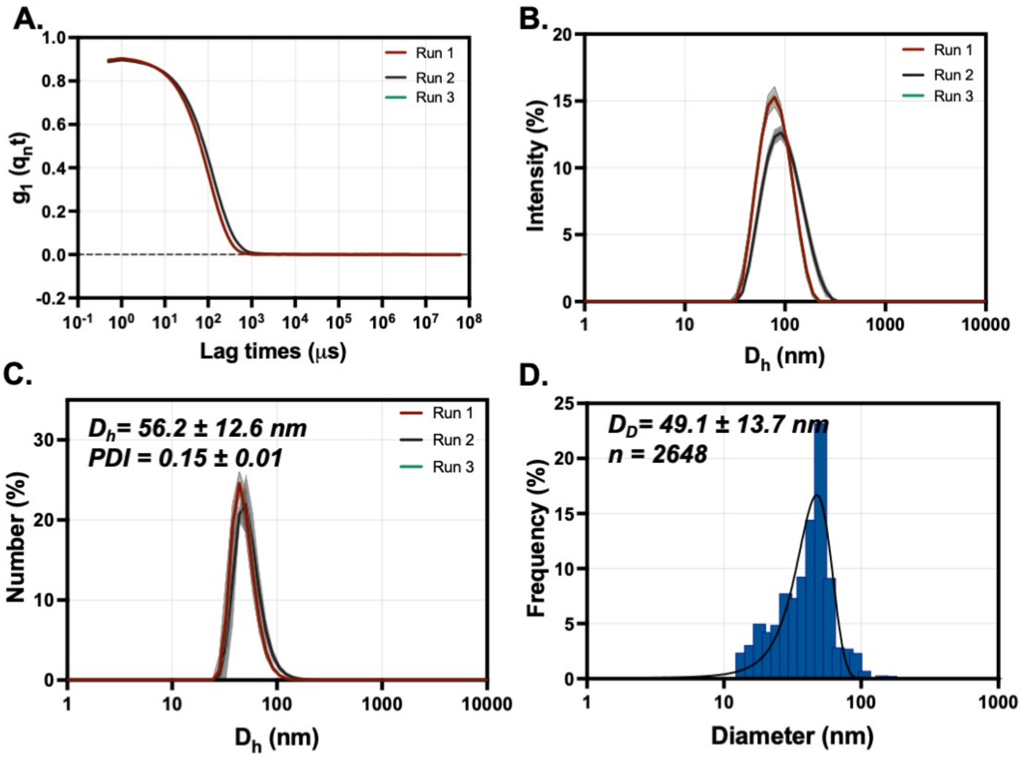

Figure 53. Repeatability of bicomponent PMPC-PDPA + PEO-PBO vesicles prepared by slow solvent switch across three replicates of identical experiments (A) Autocorrelation function, (B) intensity size distribution and (C) number-weighted size distribution along with the average D_h and the PDI values showing the error as a standard deviation from the replicates, (D) the histograms of the dry-state size distribution along with the calculated average diameter and the respective number of particles measured by the particle analysis based on TEM images.

The DLS analysis of the three samples displays single exponentially decaying autocorrelation functions as shown in Figure 53. Run 1 displays a slightly steeper decay at longer lag times compared to the rest of the samples. This can be confirmed by the intensity signal in which all the replicates show a single peak with no evidence of larger aggregates (greater than 1000) produced in this self-assembly. Nevertheless, run 1 displays a slightly narrower size distribution for the signal compared to the remaining runs which indicates that the run 2 and run 3 contain slightly larger structures compared to run 1.

However, this difference is not significant and the number size distribution of all the runs show a single peak at about 50 nm, which suggests that the majority of the sample is within size class for all the replicates. The average hydrodynamic diameter of each of the runs is tabulated in Table 3, with an average hydrodynamic diameter across the replicates of 56.8 ± 3.02 nm and a PDI of 0.15 ± 0.01. Additionally, the polydispersity of all the replicates is within that acceptable for a homogenous polymer nanoparticle system (PDI<0.2). It is also worth noting that the deviation between the dispersity between the sample is within 0.01, which is an indicative of the good degree of the conservation of the polydispersity of the systems prepared by this method. This is contrary to the bicomponent systems prepared previously by film rehydration.

Table 3. Listed are the hydrodynamic diameter (D_h), PDI values and D_D for the single component (pristine) PMPC-PDPA and bicomponent PMPC-PDPA + PEO-PBO polymersomes prepared by solvent switch along with the average and standard deviation from the replicates.

Pristine PMPC-PDPA			Bi component PMPC-PDPA : PEO-PBO		
D_h	PDI	D_D	D_h	PDI	D_D
49.2	0.094	56.0	54.0	0.16	51.4
50.7	0.095	59.6	56.4	0.14	55.1
54.2	0.092	57.4	60.0	0.16	40.8
51.4 ± 2.56	0.09 ± 0.002	57.7 ± 14.8	56.8 ± 3.02	0.15 ± 0.01	49.1 ± 13.7

As expected, the TEM imaging of the bicomponent samples displayed a mono-dispersed sample of spherical polymersomes, Figure 54. The dry-phase diameter of the samples obtained from TEM micrographs are tabulated in Table 3. The average dry-phase diameter across all the replicates (D_D) is 49.1 ± 13.7 nm (n= 2648 particles) which is comparable with the hydrodynamic diameter (D_h) obtained from the DLS. The mono-dispersity is maintained within all the replicates which indicate the repeatability of this method in producing a highly mono-dispersed sample of polymersomes.

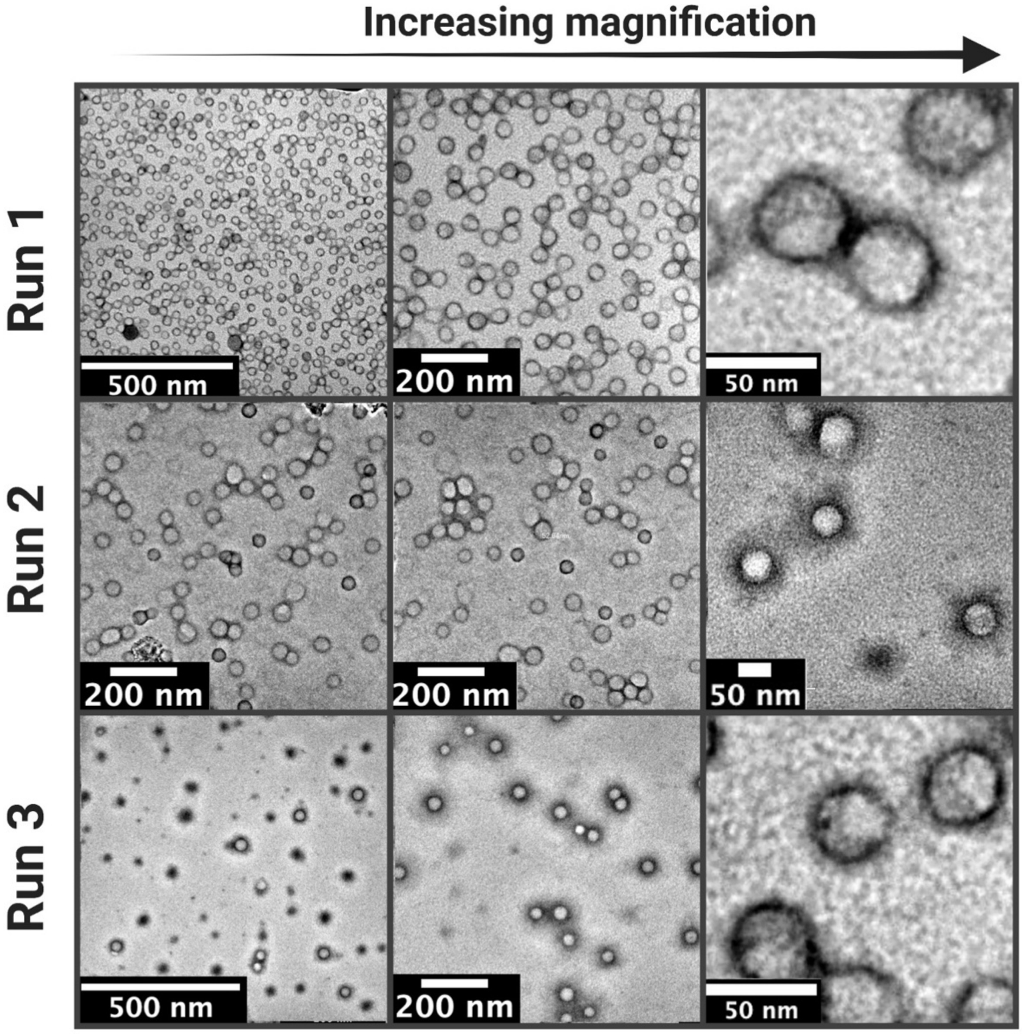

Figure 54. TEM micrographs of bicomponent PMPC-PDPA + PEO-PBO polymersome prepared by slow solvent switch. The micrographs represent the self-assembled structures of three replicates (rows) with increasing magnification from left to right. The low magnification images (column 1 and 2) show the population of the self-assembled structures in the samples. The high magnifications images (right column) show the spherical polymersomes formed (scale bar of 50nm).

The PMPC-PDPA + PEO-PBO polymersomes display discolorations within the membrane indicative of the phase separated PMPC-PDPA (stained), appearing darker, and the unstained PEO-PBO, appearing lighter, Figure 55. These phases separated domains appear in all the samples at varying abundance. The samples also contain a variety of polymersomes showing a single or two separated domains. These phases separated PMPC-PDPA + PEO-PBO polymersomes do not resemble the bicomponent polymersomes prepared by film rehydration. In that, these polymersomes are smaller in size and present a phase separated domain on the surface, unlike the film rehydrated polymersomes which present a protruding bud of PEO-PBO, Figure 39. Nevertheless, this slow solvent switch method produces a highly spherical, mono-dispersity of polymersomes without other self-assembled aggregates of varying morphologies. In addition, the phase-separated PMPC-PDPA + PEO-PBO polymersomes account for the asymmetry (the PEO-PBO domain) aimed to facilitate the directional motion of polymersomes which makes it an ideal system to use for chemotactic studies. It should however be noted that these samples do contain a combination of symmetric (pristine PMPC-PDPA) and asymmetric (phase-separated PMPC-PDPA + PEO-PBO) polymersomes, which to this point no method is known of to separate.

These results have shown a robust self-assembly of mono-dispersed samples of polymersomes of about 50 nm in diameter, with formation of phase-separated PMPC-PDPA-PEO-PBO polymersomes. They have also highlighted a challenge in terms of maintaining the yield of the phase-separated polymersomes within replicates of the same experiment. As this is the first reported PMPC-PDPA + PEO-PBO bicomponent system, no literature values are available to help with evaluating the reproducibility between different polymer batches and investigators. Hence future examinations need to be conducted to evaluate and control the yield of phase separated polymersomes in order to attain more control over the reproducibility of samples.

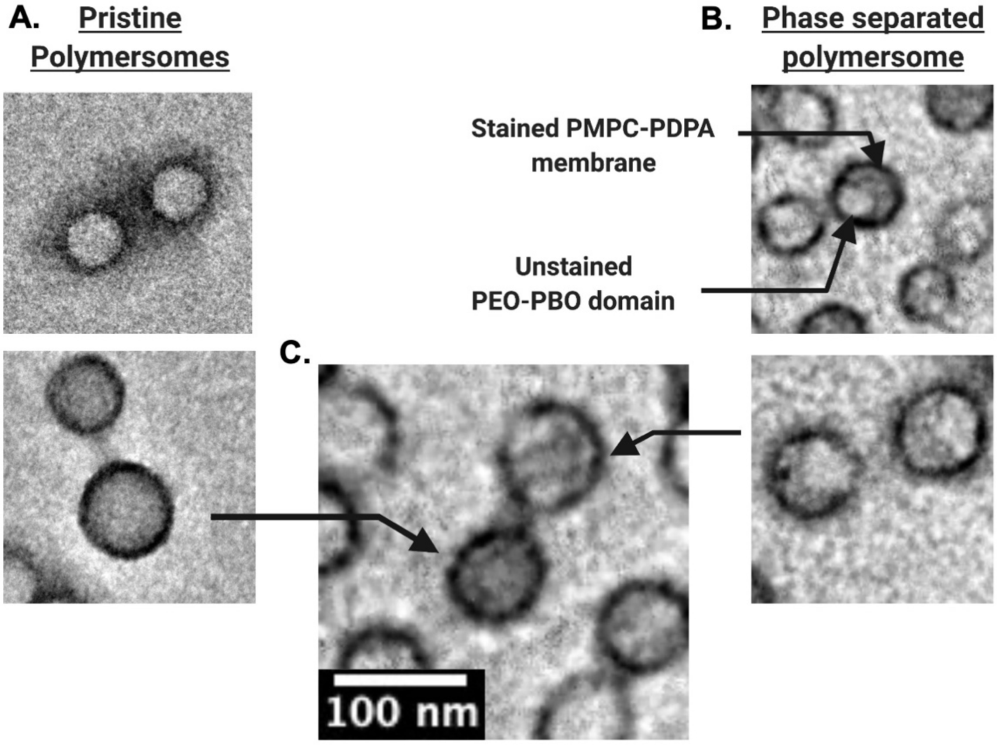

Figure 55. TEM micrographs of bicomponent PMPC-PDPA + PEO-PBO sample prepared by slow solvent switch showing micrographs of the (A) pristine PMPC-PDPA polymersomes and (B) phase separated polymersomes in the (C) sample. (B) The PMPC-PDPA and the PEO-PBO domains within the phase separated polymersomes are also illustrated.

4.2 Liposome

In this section another modified nanovesicle is explored. The 45tt 5ymohmself-assembly of the liposomes and incorporation of a membrane asymmetry is presented. The formed aggregates are characterised as in the previous section using DLS and TEM.

4.2.1 self-assembly and poration introduction

Liposomes are nanoscale compartmentalised objects, able to entrap large and small polar molecules and even enzymes. In the pursuit towards the fabrication of active vesicles, they are sensible candidates able to encapsulate enzymes, including glucose oxidase (GOX), within the aqueous core. Nevertheless, two main issues arise towards an artificial propulsion: (1) the low permeability of the lipid membrane to large and small polar molecules, especially in this case glucose, (the GOX enzyme substrate) and (2) the symmetric topology of liposomes which impedes the possible directionality in motion. In nature the permeability challenge is seen in cellular phospholipid bilayers which are also impermeable to glucose, with an estimated upper limit of the glucose permeability coefficient of 10^{-10} cm/sec.[169] Thus in these systems sugar is moved across the bilayer by membrane carrier proteins that act as transporters. Glucose transporters are a wide group of membrane proteins that span the membrane to allow for the facilitated passive diffusion of glucose across the biological membrane.

Taking inspiration from this, the liposome system is made more permeable here by employing the well-established pore-forming toxin hemolysin, which has been demonstrated to bind to the lipid membrane and assemble to form a heptameric nanopore of 1.4 nm in diameter.[135, 136] This nanopore allows for the passage of molecules smaller than 3 kDa.[137] This molecular mass cut-off range works to keep the encapsulated glucose oxidase enzymes inside while both the reaction substrate (glucose) and product (hydrogen peroxide) can diffuse through the pore. The use of the nanopore not only solves the permeability issue but also introduces asymmetric topology into the design of this vesicle by disturbing the symmetric spherical geometry of the phospholipid bilayer, Figure 56.

In this chapter, I explore the incorporation of membrane asymmetry within spherical liposomes. This modification is achieved by first preparing pristine spherical liposomes, followed by the poration of these liposomes in order to break the symmetry of the spherical phospholipid membrane by α-hemolysin. The formulation and detailed physical characterisation of this system is reported by examining the size distribution, morphology and topology by DLS and TEM.

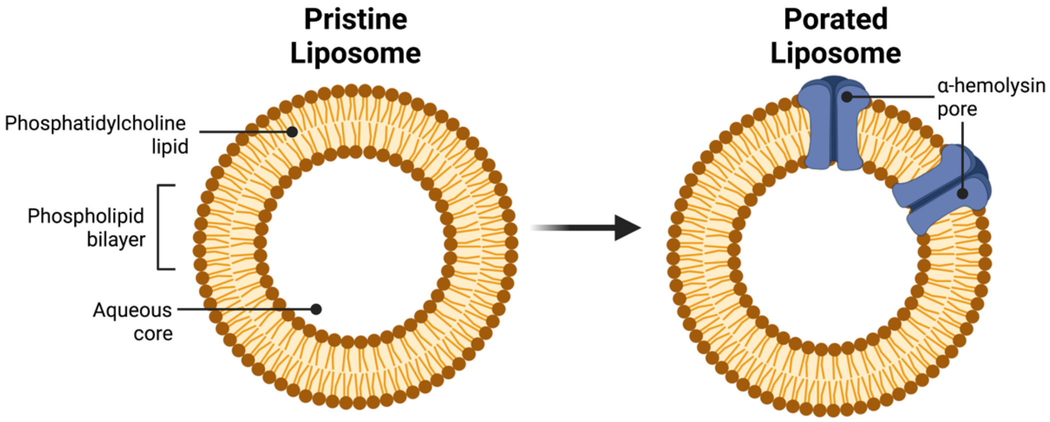

Figure 56. A schematic illustrating the pristine liposome and the modified porated liposome, in which the phospholipid bilayer is porated by a α-hemolysin pore to improve permeability and form an asymmetry within the membrane. The phospholipid head group is in brown and the tail in yellow and the α-hemolysin pore in purple. Drawn in Biorender® with permission to publish.

4.2.2 Pristine liposome preparation

The pristine L-α-phosphatidylcholine liposomes were prepared by film rehydration, as described in section 3.4. Aliquots were taken at the three stages of the process (i) after 1 hour stirring, (ii) after stirring and sonication and (iii) after stirring, sonication and extrusion.

The autocorrelation function of the rehydrated sample after stirring for 1 hour show a distorted exponential decay at long lag times, the sonicated sample shows a smoother exponential decay curve with fluctuations at lag times greater than 10^3 µs. Upon extruding this sample, the autocorrelation function is improved showing a single smooth exponentially decaying curve indicative of a homogenous sample. All the aliquots show an optimal signal-to-noise ratio (Y-intercept >0.9), Figure 57 .

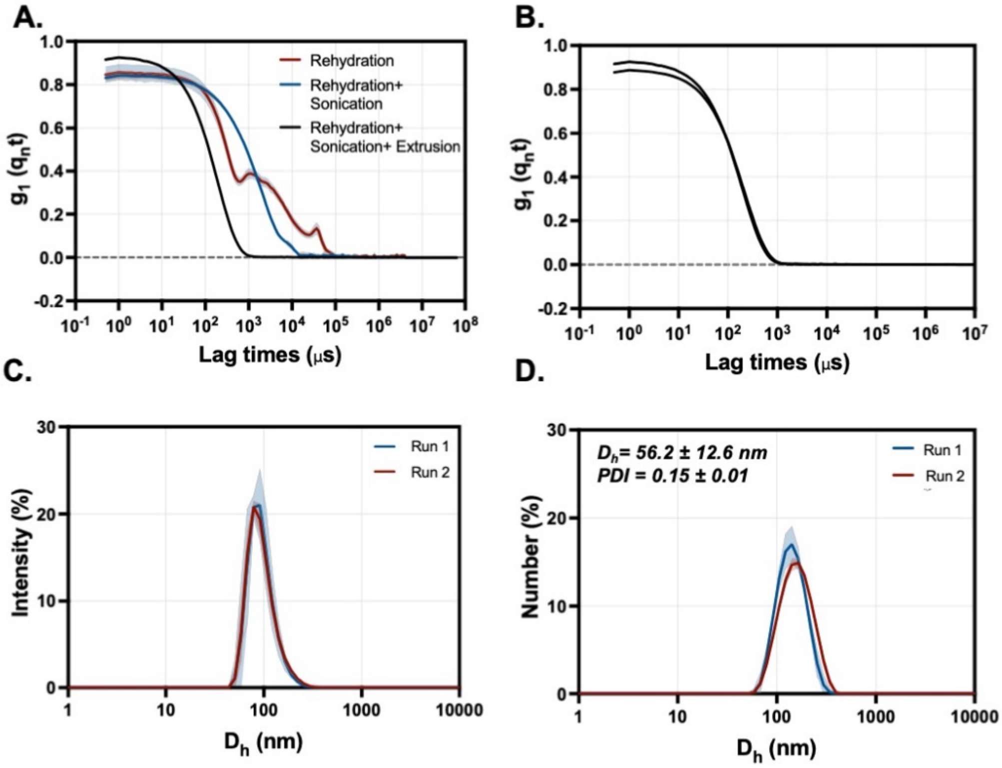

Figure 57. DLS analysis of the L-α-phosphatidylcholine aggregation during rehydration after 1 hour stirring (Red), followed by 10 minutes sonication (Blue) followed by extrusion with 100 nm pore size (Black). The (A) autocorrelation function, (B) intensity size distribution and (C) number-weighted size distribution is shown. (D) The number-weighted size distribution of three replicates of the extruded same along with the average D_h and the PDI values showing the error as a standard deviation from the replicates.

After extruding the sample, the hydrodynamic diameter of the sample is 103.6 nm indicated by a single peak in the intensity and number weighted size distribution, Figure 57C. This was reproduced by preparing two independent extruded sample which show a reasonable degree of reproducibility with an average hydrodynamic diameter between the two replicates of (D_h) of 98.6 and a standard deviation of 25.1 nm. The polydispersity index PDI value is 0.078 ± 0.02 for the replicates, Figure 57D. These results show the effect of the preparation method on the size of the aggregates formed and shows the reduction in both the size and polydispersity of the aggregates after sonication and extrusion. These results are in agreement with those reported in literature. [136]

Transmission electron microscopy (TEM) imaging of the extruded sample was performed by Gabriel Ing. This was done by staining with uranyless for 1 minute. This confirmed the formation of well-defined, L-α- phosphatidylcholine unilamellar vesicles, Figure 58. These liposomes have an average dry-phase diameter of 130.1 ± 69.3 nm (n=15).

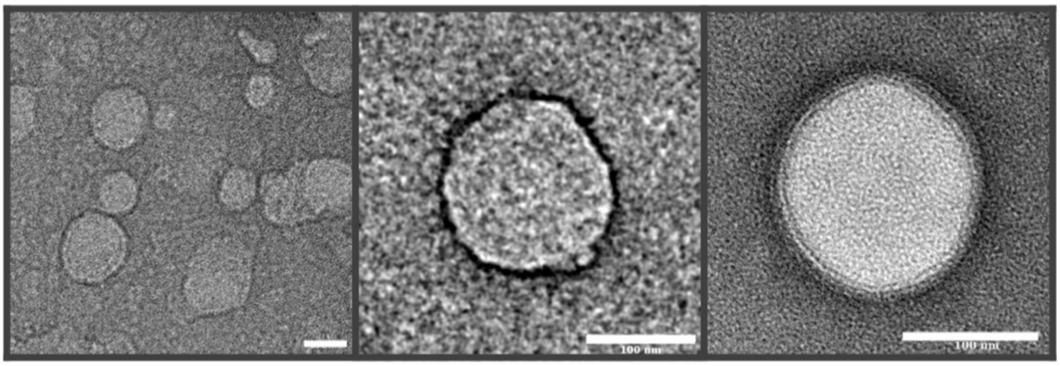

Figure 58. Displays the TEM micrographs of pristine liposomes stained with uranyless for 1 minute. Imaging carried out by Gabriel Ing. The scale bars represent 100 nm.

4.2.3 Porated liposome preparation

The pristine liposomes were incubated with α-Hemolysin monomers to form nanopores, and the poration was confirmed using TEM imaging. Figure 59, displays the TEM micrographs showing the nanopores inserted into the liposome membrane, pointed to by the red arrows. These are in agreement with previously reported α-Hemolysin porated liposomes.[136] The TEM micrographs also indicate the presence of assembled α-Hemolysin pores that do not insert into the liposome membrane, pointed to by the blue arrow, Figure 59. These suggest that the α-Hemolysin does not always successfully insert into the liposome membrane after assembly, which also aligned with previously reported work.[136]

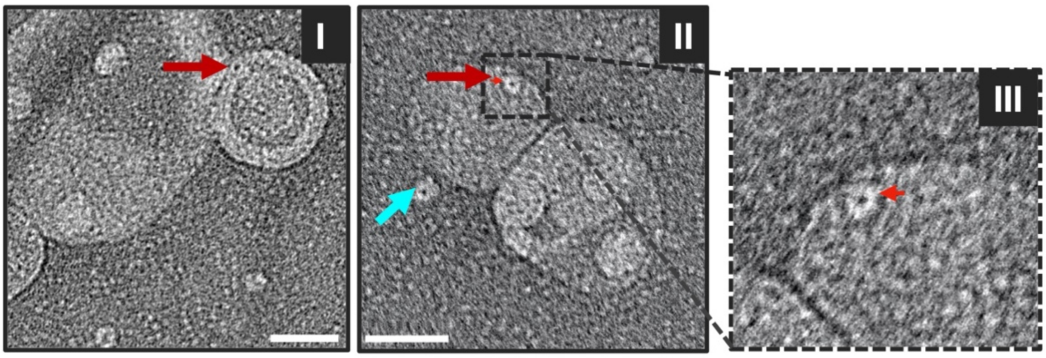

Figure 59. TEM micrographs of liposomes after incubation with α-Hemolysin for one hour, Red arrows point at α-Hemolysin pores inserted and blue point at not inserted into the liposome membrane. Imaging carried out by Gabriel Ing. The scale bars are 50 nm.

The α-Hemolysin monomers assemble to form a mushroom-shaped heptameric complex with an aqueous channel spanning the complex. The average diameter of the complex is measured from TEM micrographs as shown in Figure 60. The liposomes do not appear spherical as previously reported polymersomes, this is owed to the deformation that occurs during the grid preparation, drying of the sample and/or TEM acquisition that tend to be harsh on this soft membrane. This diameter is 12 ± 3.2 nm (n=3) which agrees with previously reported value of 10 nm.[135, 136] The diameter of the aqueous channel within the complex measured is 3 ± 1.7 nm (n=3), which is within the previously reported range between 1.4 and 4.6 nm.[135]

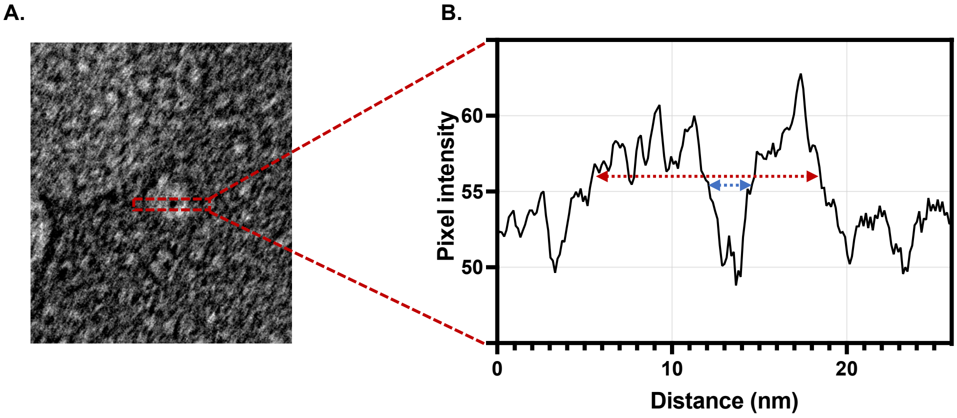

Figure 60. (A)A zoomed in TEM micrographs of a pore in which a portion of the protein (highlighted in dashed red rectangle) is used to compute (B) the respective pixel intensity profile. The red line indicates the diameter of the pore and the blue line the diameter of the aqueous channel. Imaging carried out by Gabriel Ing.

These evidence the preparation of pristine liposomes using the film rehydration method with a hydrodynamic diameter (D_h) of 98.6 ± 25.1. These pristine liposomes were porated by α-Hemolysin. The poration was validated using TEM imaging, and the diameters of the nanopores formed measured (12 ± 3.2 nm).

4.3 PEO-PBO polymersomes

In addition to the modified bicomponent PMPC-PDPA + PEO-PBO and porated liposomes, pristine nanovesicles were also prepared to be used as control sample for chemotactic studies. Both pristine PMPC-PDPA polymersomes and pristine liposomes were prepared in the previous sections. In this section the preparation of pristine PEO-PBO polymersomes is detailed. The PEO-PBO polymersomes were prepared as previously reported in literature.[64] A PEO-PBO film is prepared by film rehydration followed by sonication and extrusion. The physiochemical characterisation of the produced suspension is detailed below.

DLS analysis of the PEO-PBO sample is shown in Figure 61. The autocorrelation function of the rehydrated sample shows a single smooth exponentially decaying curve with an optimal signal-to-noise ratio (Y-intercept >0.9) for all the four replicates. The PDI values range from 0.154 to 0.185 indicative of homogenous samples. Both the intensity and number size distribution display a single peak at around 100 nm for all the four replicates. This signifies the absence of large aggregates of PEO-PBO copolymer and the reproducibility in the preparation of the size distributions. The average hydrodynamic diameter of the polymersomes is 111.9 ± 6.8 nm with a PDI of 0.171 ± 0.019, the error represents the standard deviation across the four replicates.

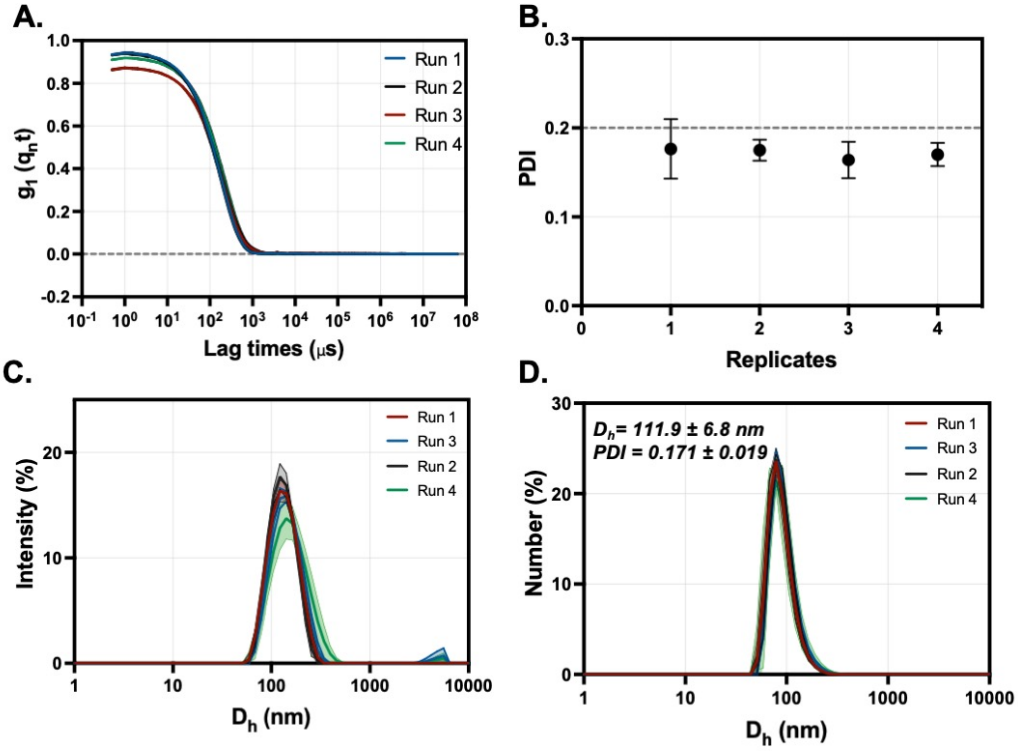

Figure 61. DLS analysis of PEO-PBO vesicles formed by film rehydration showing the (A) autocorrelation function, (B) PDI values (C) intensity size distribution and (D) number-weighted size distribution along with the average D_h and the PDI values showing the error as a standard deviation from the four replicates.

Next, the TEM imaging of the sample is conducted by Uranyl acetate staining which shows the darker PEO-PBO polymersomes with good contrast against the lighter unstained background, Figure 62. The formation of the PEO-PBO polymersomes was also verified by negatively staining the PTA (overstaining). This method was used, as PEO-PBO is not stained by PTA but the over staining of the background provided a reasonable contrast to view the brighter PEO-PBO polymersomes. PEO-PBO vesicles are soft, lower density, flexible membranes which when exposed to the harsh image acquisition or TEM grid preparation, tend to deform more easily than polymersomes. This can be seen in the nonspherical morphology of these PEO-PBO polymersomes compared to the PMPC-PDPA polymersomes. The dry-state diameter. of the PEO-PBO polymersomes is 134.7 ± 40 nm (n = 30). These results point towards the successful formation of pristine PEO-PBO polymersomes with a hydrodynamic diameter of 111.9 ± 6.8 nm.

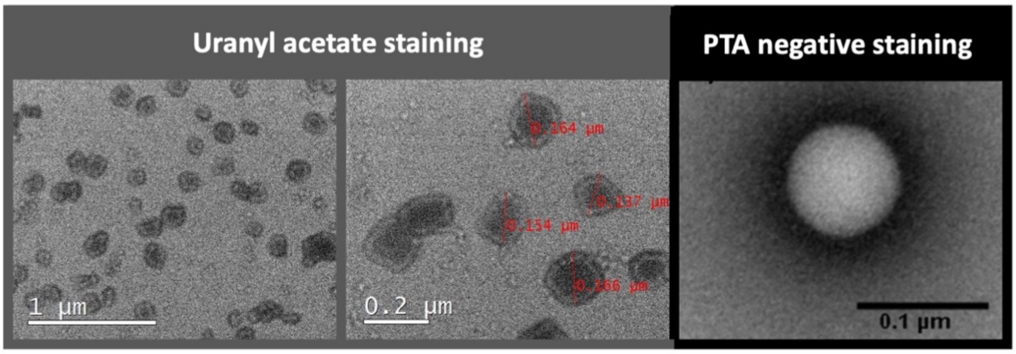

Figure 62. TEM micrographs of Uranyl acetate stained and negative PTA stained PEO-PBO polymersomes.

4.4 Conclusion

The self-assembly of nanovesicles has been studied for pristine and modified polymersomes and liposome systems in this chapter. Firstly, the pristine PMPC-PDPA and bicomponent PMPC-PDPA + PEO-PBO asymmetric polymersomes have been studied. The aim of which is to attain a homogenously dispersed sample of bicomponent spherical polymersomes while incorporating an asymmetric distribution of the two copolymers within the membrane.

4.4.1 The key results

- Pristine PMPC-PDPA prepared by the film rehydration method reproducibly forms homogenous samples of polymersomes around 100 nm.
- The bi-component PMPC-PDPA + PEO-PBO systems, display presence of asymmetric polymersomes in which a protruding bud of PEO-PBO is seen within the PMPC-PDPA membrane.
- During film rehydration, the heterogeneity of the aggregates formed increases as a result of the addition of a second copolymer (PEO-PBO) to the PMPC-PDPA self-assembly.
- The reproducibility between replicates decreases for this bi-component systems (PMPC-PDPA+PEO-PBO) due to the formation of larger aggregates as bi-products.
- Solvent switch method provides monodispersed single component PMPC-PDPA polymersome sample of around 50 nm, with no formation of other larger aggregates (biproducts).
- When using the solvent switch method for the self-assembly of the bicomponent system (PMPC-PDPA +PEO-PBO) the monodispersity of the sample is maintained between replicates.
- In the bi-component system, phase separated polymersomes display domains of PEO-PBO on the membrane. These do not resemble the phase

separated polymersomes prepared by film rehydration in which the polymersomes display a protruding bud of PEO-PBO.

- These phase separated domains appear in all the replicates at varying abundance.
- The samples also contain a variety of polymersomes showing a single or two separated domains.
- This is the first reported bi-component PMPC-PDPA + PEO-PBO system prepared by solvent switch.

The second part of this chapter demonstrated the successful preparation of 100 nm diameter liposomes porated by α-hemolysin, following the method first reported by L. Song *et al.*[135] Finally, the last nanovesicle prepared for the chemotactic studied is the pristine PEO-PBO, to be used as a control vesicle for the bicomponent PMPC-PDPA + PEO-PBO polymersomes in the chemotactic experiments. As such these polymersomes were prepared by film rehydration yielding 111 nm PEO-PBO polymersomes of symmetric membrane geometry.

In the next chapter, all the nanovesicles prepared in this chapter, are loaded with glucose oxidase within the aqueous core of these vesicular structures. This acts as the chemical machinery required to promote motion on the nanoscale by converting chemical energy into mechanical motion.

CHAPTER FIVE

GLUCOSE OXIDASE LOADED NANOVESICLES

After the formulation of both the pristine and membrane modified polymersomes and liposomes, I next explore the encapsulation of glucose oxidase enzyme (GOX) into these nanovesicles. Two methods are used to encapsulate GOX, the first is a post-self-assembly technique known as electroporation, and the second is by self-assembling in presence of GOX followed by extrusion. The second part of this chapter aims to assess the sensitivity of the GOX loaded PMPC-PDPA polymersome system to the presence of glucose in the surrounding environment. This allows for validating the internalisation of the glucose into the polymersome and hence activation of the GOX enzymatic reaction within this nanovesicle.

5.1 Enzyme encapsulation

5.1.1 Introduction

The scope of this work is to create biocompatible synthetic nanovesicles which can be powered in the presence of physiologically abundant biofuel. Therefore, the aim is to combine enzymes with the non-cytotoxic nanovesicles prepared in the previous chapters. Glucose oxidase enzyme is naturally present in the human body and catalyses the oxidation of glucose into d-glucone-δ-lactone and hydrogen peroxide. As a first approach, glucose oxidase is encapsulated alone into the nanovesicles. These loaded nanovesicles will then be used to evaluate autonomous motion in the presence of glucose.

Nanovesicles can encapsulate hydrophilic compounds in their aqueous cores as well as hydrophobic and amphiphilic compounds within their membranes. The most common and well-developed strategy used is encapsulation during vesicle formation. In the case of film rehydration, hydrophilic compounds are loaded by adding an aqueous solution of the component to the thin film. However, hydrophobic components are mixed into the lipid/polymeric organic solution to make the thin film.[50] In the case of liposomes and PEO-PBO polymersomes prepared by film rehydration, GOX is encapsulated by hydrating the film with an aqueous solution and extruded Figure 63. The GOX encapsulated pristine liposomes are then porated by incubation with α-Hemolysin for an hour, as detailed in chapter 4.

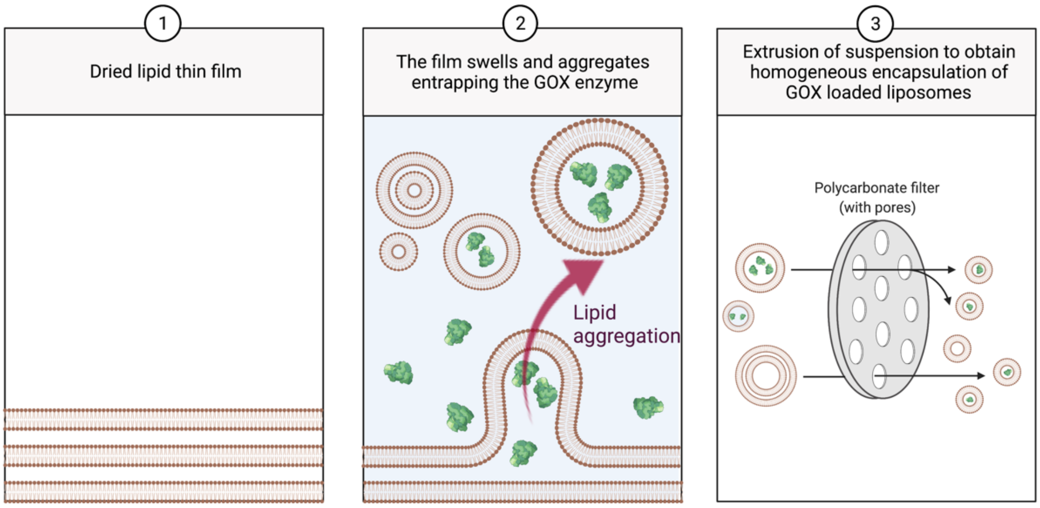

Figure 63. GOX loaded liposomes formed by encapsulation of GOX during the film rehydration process. In which the dry lipid film is hydrated with an aqueous glucose oxidase solution. Upon stirring the film swells and aggregates, entrapping the GOX within the aqueous core of the liposomes. This is followed by extrusion to obtain a homogenous encapsulation of GOX loaded liposomes.

In the case of PMPC-PDPA polymersomes prepared by the solvent switch method, the hydrophilic components can be dissolved in water and injected slowly into the organic polymeric solution, and hydrophobic components can be pre-mixed into the organic polymeric solution.[50] This method of encapsulation has been widely used to encapsulate drugs.[74] However, the addition of the GOX aqueous solution to the organic polymeric mixture denatures the enzyme, rendering this an unfeasible method for the encapsulation of enzymes.[144] Hence an alternative method was adopted, which involves the encapsulation post polymersome formation, known as electroporation. In this method, an external electric field is applied across the polymersome dispersion. The temporary osmotic pressure leads to the rearrangement of the copolymers leading to the formation of hydrophilic membrane pores and hence the diffusion of water and GOX into the aqueous core, Figure 64. I present the encapsulation efficiency of the GOX loading into liposomes and PEO-PBO polymersomes (during self-assembly) and pristine and bicomponent PMPC-PDPA + PEO-PBO polymersomes (post preparation).

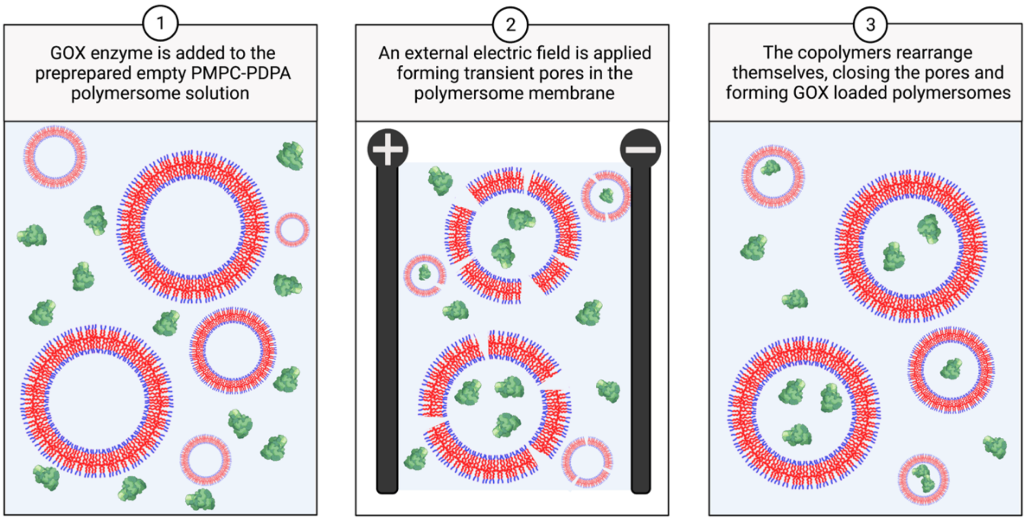

Figure 64. Illustration of loading the PMPC-PDPA polymersomes with glucose oxidase enzyme (GOX) by electroporation. An external electric field is applied to the pre-formed empty PMPC-PDPA polymersomes, which forms transient pores in the polymersome membranes allowing the diffusion of the GOX enzyme into the aqueous core of the polymersomes. In time the copolymers rearrange, the pores close yielding GOX loaded PMPC-PDPA polymersomes.

5.1.2 Efficiency of GOX encapsulation

The loaded nanovesicles are first analysed by BCA assays to quantify the total protein mass, from a known mass of lipid/ copolymer. The loading efficiency is then calculated as the number of proteins per nanovesicles (n/vesicle), as described in section 3.8.3. The encapsulation profiles for all the nanovesicles are presented in Figure 65. These show the loading efficiency coupled with the DLS hydrodynamic diameter distribution of GOX loaded liposomes and PMPC-PDPA and/or PEO-PBO polymersomes.

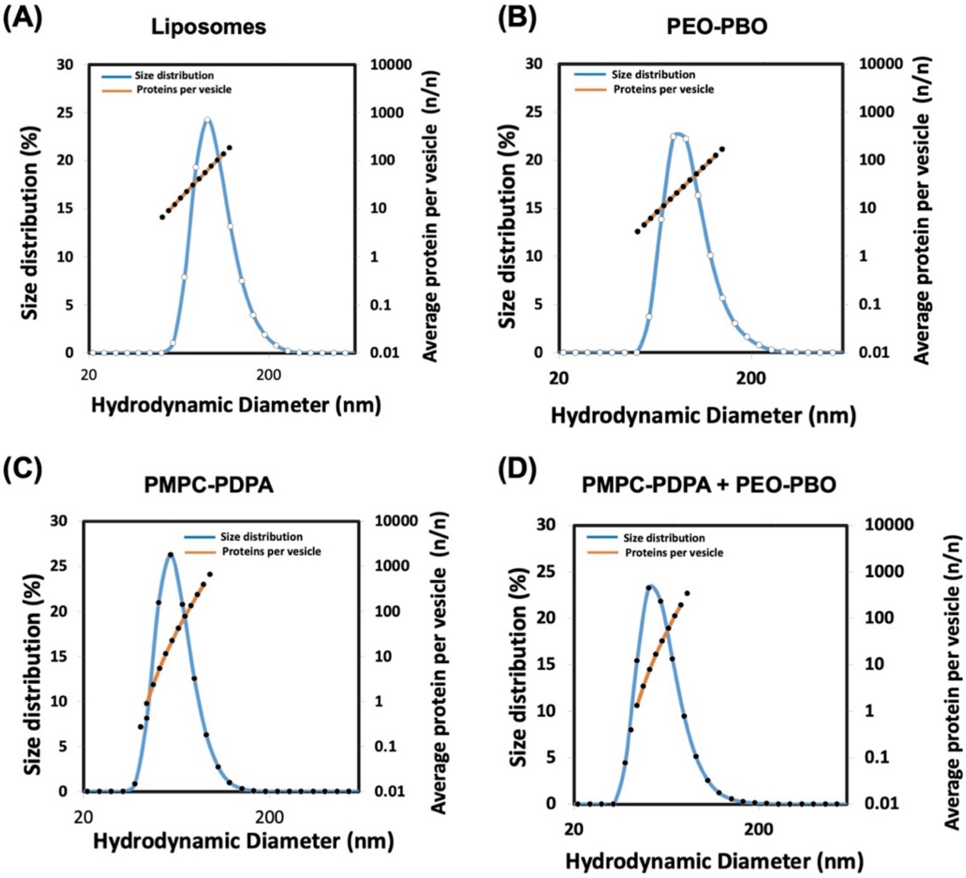

Figure 65. The encapsulation profile presenting the hydrodynamic diameter obtained by DLS versus verses the average number of glucose oxidase enzyme per nanoparticle (loading efficiency) for (A) liposomes, (B) PEO-PBO polymersomes, (C) pristine PMPC-PDPA polymersomes and (D) bicomponent PMPC-PDPA + PEO-PBO polymersomes.

In the case of liposomes, the loading protocol resulted in the encapsulation of an average of 15.9 GOX enzymes per liposome. The average PEO-PBO polymersomes encapsulate 8.6 GOX enzymes per polymersome. The pristine and bicomponent PMPC-PDPA + PEO-PBO polymersomes encapsulate an average of 6.5 and 6.0 GOX enzymes per polymersome.

The reproducibility of this method is evaluated next by conducting three independent replicates for each nanovesicle system. The average loading efficiency (across three replicates) of the GOX enzyme loaded into the nanovesicles is summarised in Figure 66. The average loading efficiencies are 16.0 ± 1.3, 8.0 ± 1.9, 6.3 ± 0.3 and 6.7 ± 0.5 of GOX enzyme in Liposome, PEO-PBO, pristine PMPC-PDPA and bicomponent polymersomes, respectively.

These results indicate an average encapsulation of 16 GOX enzymes per liposome, 8 GOX enzymes per PEO-PO polymersome and 6 GOX enzymes per pristine and bicomponent PMPC-PDPA + PEO-PBO polymersomes.

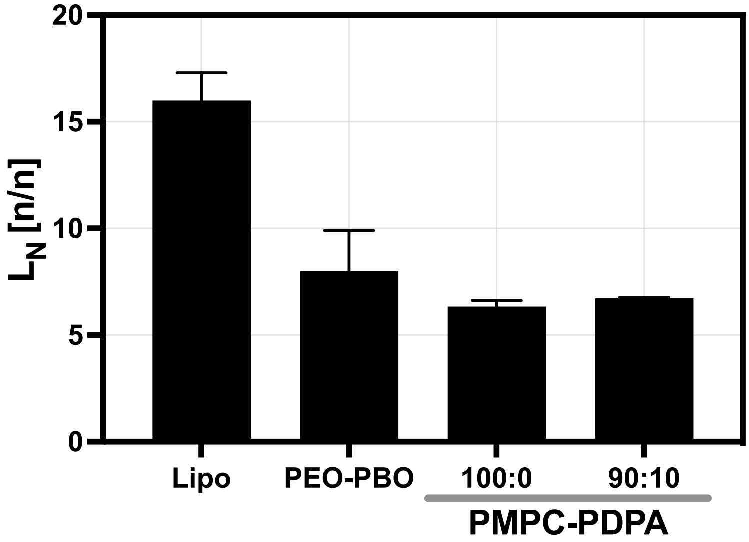

Figure 66. Loading efficiencies L_N for Glucose oxidase within liposomes (Lipo), PEO-PBO polymersomes (EB1), pristine PMPC-PDPA (100:0) and bicomponent PMPC-PDPA + PEO-PBO polymersomes (90:10). The error bars represent the standard deviation across three replicates.

5.2 Enzyme-dependent response to glucose environment

Polymersomes made of the PMPC-PDPA copolymer have the unique ability of disassembling at pH lower than 6.4. This is associated with the protonation of the hydrophobic PDPA block rendering it hydrophilic. Thus, breaking the strong hydrophobic interactions within the membrane which leads to the disassembly of the polymersomes, Figure 20. This pH sensitivity has been shown as a robust drug releasing mechanism such as to trigger disassembly of polymersomes during endosomal intake.[170]

By using this unique property of PMPC-PDPA polymersomes, I next investigate the responsiveness of the polymersomes to the presence of glucose. This was achieved by placing either the empty or the GOX loaded PMPC-PDPA polymersomes within a homogenous glucose environment. Ideally, under these conditions, glucose diffuses through the polymeric membrane. Once internalised into the polymersome and in the presence of GOX within the aqueous core of the polymersomes, the oxidation of glucose into d-glucone-δ-lactone and hydrogen peroxide is catalysed by GOX. In water, the d-glucone-δ-lactone hydrolysis to Gluconic acid lowers the pH of the solution. The pH sensitivity of the PMPC-PDPA polymersomes is triggered by the acidic pH to disassemble the PMPC-PDPA polymersomes. Figure 67, illustrates the pH triggered disassembly of GOX loaded PMPC-PDPA polymersomes in the presence of glucose.

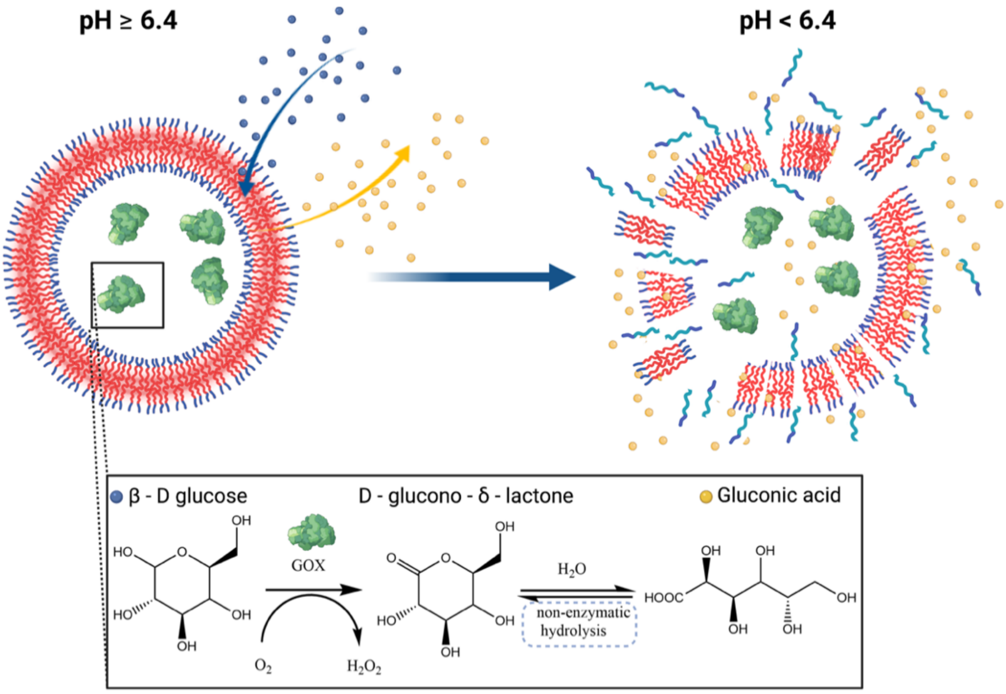

Figure 67. Schematic illustration of the pH triggered disassembly of GOX loaded PMPC-PDPA polymersomes in the presence of glucose. The hydrophilic PMPC (in purple) and hydrophobic PDPA block (red) make up the polymersome membrane at pH > 6.4. The PDPA block (light blue) is protonated in acidic pH < 6.4 leading to the disassembly of the polymersome. The pH triggered disassembly is caused by the GOX (green) catalysed oxidation of glucose (purple circle) into gluconolactone which is hydrolysed in water to gluconic acid (yellow circle). Produced by Biorender® with permission to publish, not drawn to scale.

The experiment is conducted by homogenising the empty or GOX loaded PMPC-PDPA polymersome dispersion in a glucose solution in water (0.2 M). Then the particle size distribution is monitored by DLS at 5, 15, 30, 45 and 60 minutes after the glucose addition. The autocorrelation functions over the 1-hour period follow a smooth exponential decay; these overlay over each other, Figure 68. The PDI values range from 0.1 to 1.5, which suggest no variation in the sample's polydispersity in the presence of glucose.

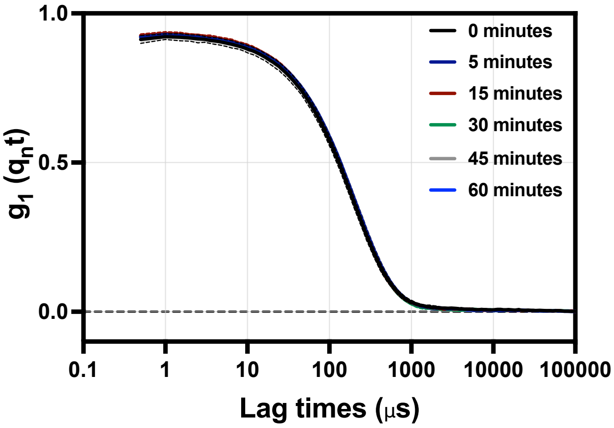

Figure 68. The autocorrelation function of the empty PMPC-PDPA polymersome sample is presented before (0 minutes, black) and 5, 15, 39, 45 and 60 minutes after glucose addition represented by the dark blue, red, green, grey and blue lines respectively.

The intensity and number size distribution shows a single size population with no larger aggregates present in all the time intervals, Figure 69 and Figure 70. The average D_h is around 60 nm between 5 to 60 minutes after the addition of glucose, which is consistent with the D_h before the addition of glucose. As expected, these results show that the presence of glucose does not affect the size of the empty polymersomes, indicated by the consistent hydrodynamic size and PDI.

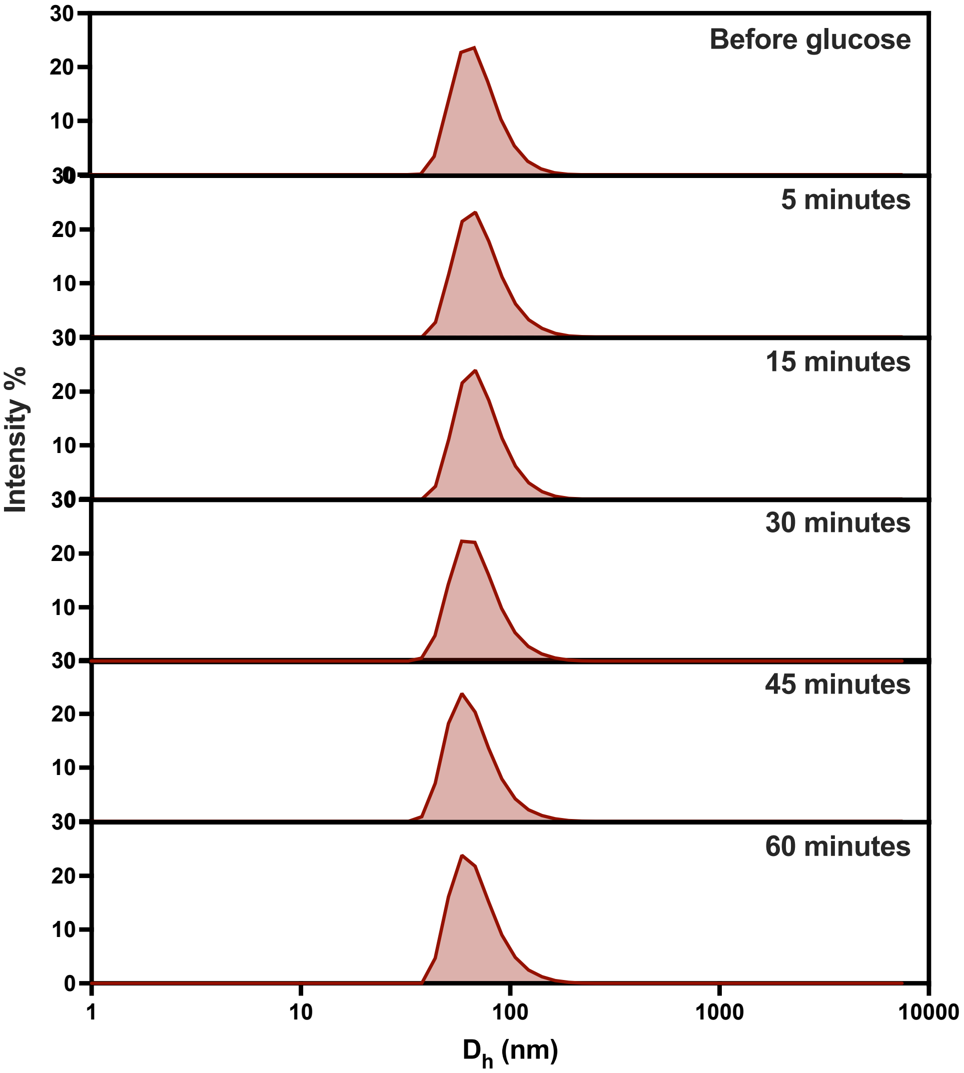

Figure 69. The intensity size distribution of the empty PMPC-PDPA polymersomes in a homogeneous glucose solution at 0 to 60 minutes from glucose addition.

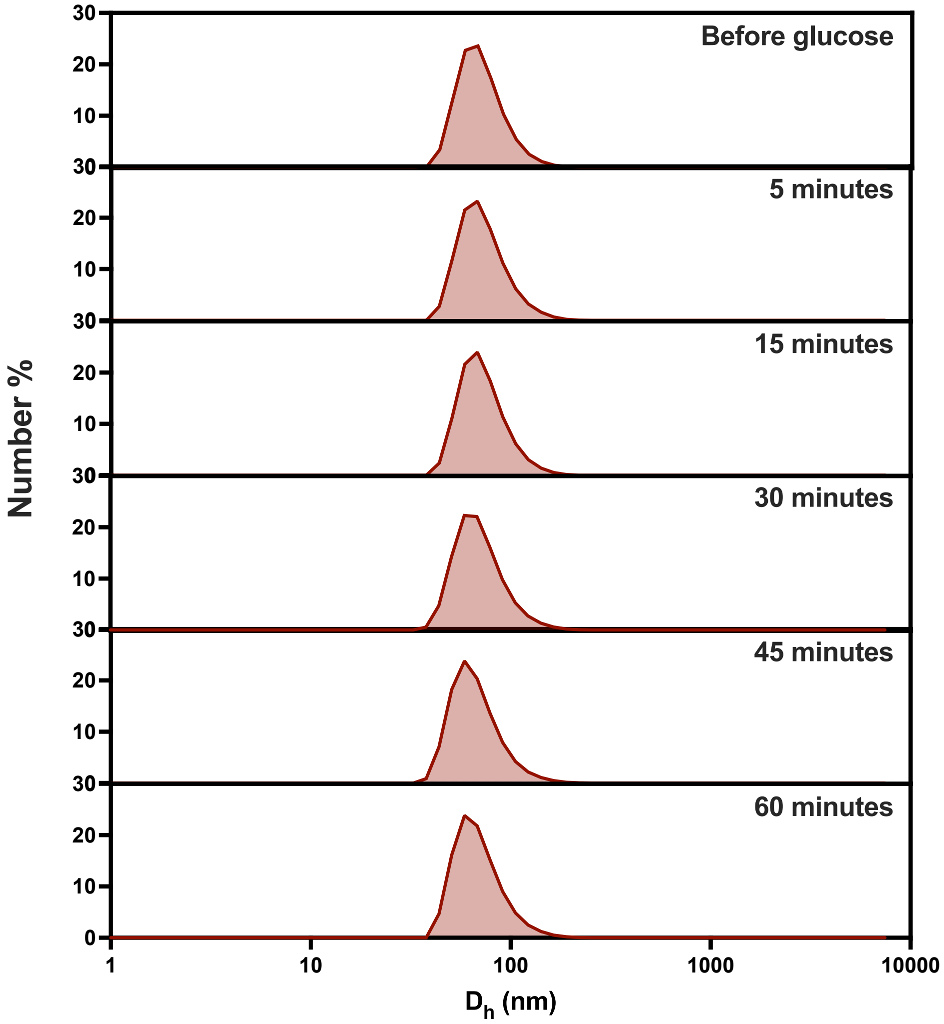

Figure 70. Number-weight size distribution of the empty PMPC-PDPA polymersomes in a homogeneous glucose solution before and 5, 15, 39, 45 and 60 minutes after glucose addition.

For the GOX loaded PMPC-PDPA polymersome in the absence of glucose, the autocorrelation function indicates a single smooth exponential decay with a PDI of 0.15 displayed in Figure 71 by the black line. From the intensity and number size distributions, the average D_h of the sample is 60.2 nm, with no indication of the presence of larger aggregates. Upon the addition of glucose into the polymersome dispersion, the correlation graphs maintain a consistent single exponential decaying curve up to 15 minutes. At 30, 45 and 60 minutes, the autocorrelation functions decay at a shorter time suggesting a decrease in size, Figure 71.

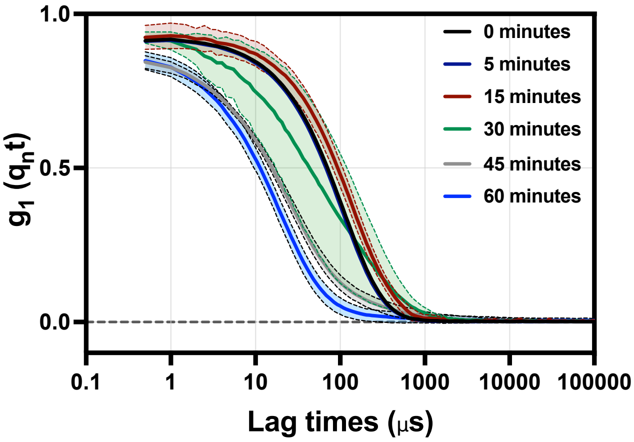

Figure 71. The autocorrelation function of the GOX loaded PMPC-PDPA polymersomes is presented before (0 minutes, black line) and 5, 15, 39, 45 and 60 minutes after glucose addition represented by the dark blue, red, green, grey and blue lines respectively.

The PDI values increase from 0.13 at 5 minutes after glucose addition to 0.38 after 60 minutes. The intensity size distribution shows a single peak corresponding to a hydrodynamic diameter of 58.5 and 60.7 nm for 5 and 15 minutes after the addition of glucose, Figure 72. At 30 minutes, a peak at 13 nm appears which indicates the presence of two populations in the sample. At 45 minutes, the peak at 13 nm increases while that at 50 nm reduces. The 13 nm peak becomes the dominant peak in the sample at 60 minutes after the addition of glucose. This peak is consistent with the size of single copolymer chains and GOX enzymes suspended in water.

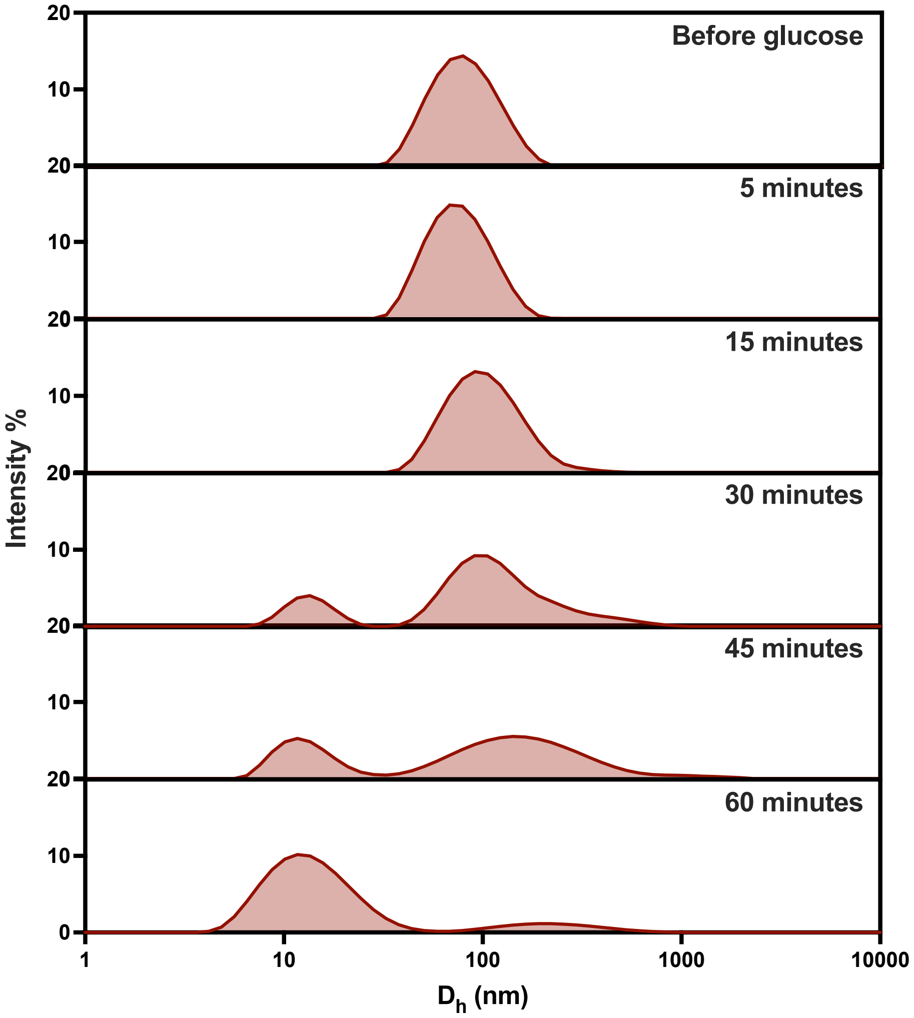

Figure 72. The intensity size distribution of the GOX loaded PMPC-PDPA polymersomes in a homogeneous glucose solution before and 5, 15, 39, 45 and 60 minutes after glucose addition.

These results show the breaking down of GOX loaded polymersomes at 30 minutes from glucose addition. This is attributed to the GOX catalytic oxidation of glucose which, when hydrolysed, lowered the pH activating the disassembly of the polymersomes. Up to 15 minutes, the polymersomes are still the dominant species in the solution, as indicated by the number size distribution, Figure 73. At 30 minutes, the polymersomes start to disassemble (as peak 50 nm starts to diminish). At 30, 45 and 60 minutes, the sample dominantly consists of single copolymer chains and GOX enzymes suspended in water (evident by the 13 nm peak). These results show the breaking down of GOX loaded polymersomes at 30 minutes from glucose addition. This is attributed to the GOX catalytic oxidation of glucose which, when hydrolysed, lowered the pH activating the disassembly of the polymersomes.

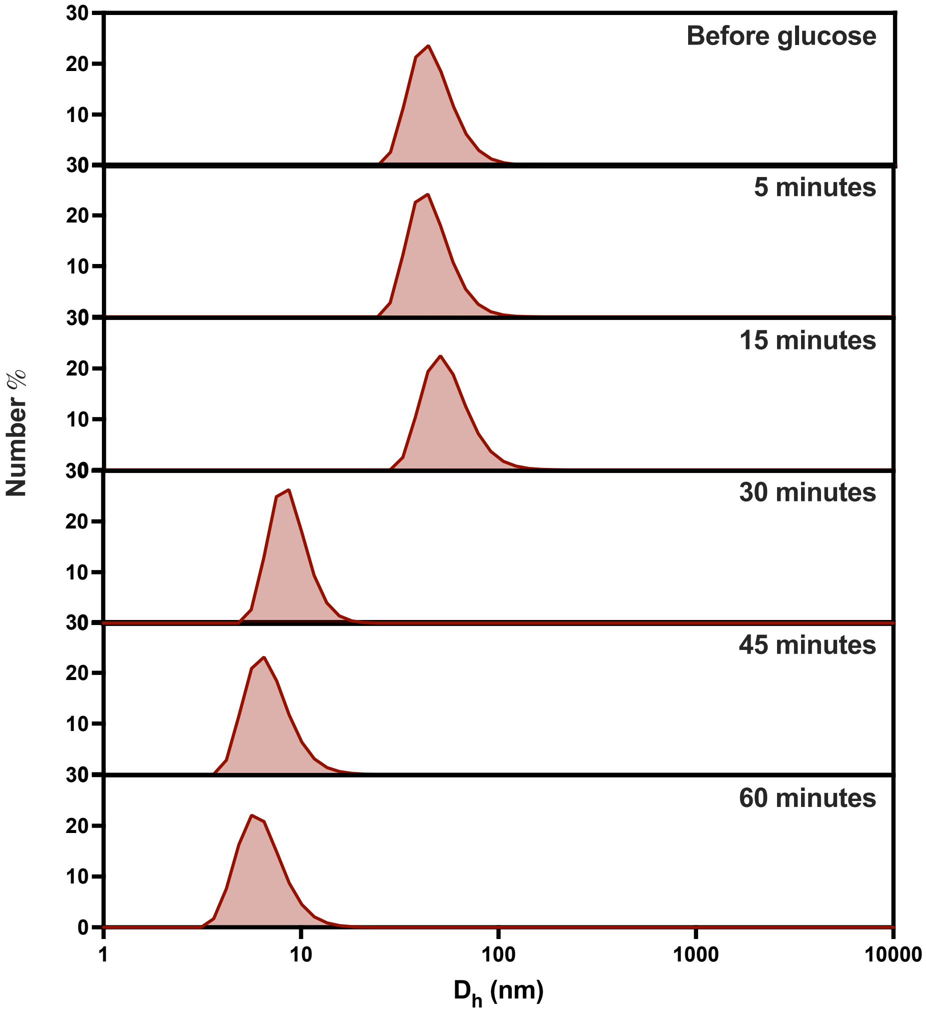

Figure 73. Number-weight size distribution of the GOX loaded PMPC-PDPA polymersomes in a homogeneous glucose solution before and 5, 15, 39, 45 and 60 minutes after glucose addition.

To further confirm this, the pH of the sample was measured before and after the addition of glucose. In the case of the empty polymersomes, the pH was 7.2 ± 0.4 before the glucose addition, which is comparable to the pH after 6.9 ± 0.3. In the case of the GOX loaded polymersomes, the pH reduced from 7.2 ± 0.4 before the addition of glucose to 3.5 ± 0.4 after 60 minutes from the addition of glucose. This not only evidences the successful encapsulation of the GOX enzyme into the polymersomes but also the maintained catalytic activity of the enzyme to glucose within the confined aqueous core of the polymersomes. These results suggest the diffusion of the glucose molecules from the external environment of the polymersomes through the polymeric membrane into the aqueous core.

5.3 Conclusion

The encapsulation of the GOX enzyme into nanovesicles was studied. GOX was successfully encapsulated into the polymersome samples with an average of 6 GOX enzymes per polymersome for the pristine PMPC-PDPA and the bicomponent PMPC-PDPA + PEO-PBO polymersomes encapsulated by electroporation. In addition, encapsulation during self-assembly of PEO-PBO polymersomes yielded an average of 8 enzymes per PEO-PBO polymersome. In the case of liposomes, an average of 16 GOX enzymes are loaded per liposome.

By utilising the pH-sensitive on/off assembly of the PMPC-PDPA polymersomes, the GOX loaded polymersomes were evaluated to assess the responsiveness of these nanovesicles to a glucose environment. The GOX loaded PMPC-PDPA polymersomes were mixed in a homogenous environment of glucose, and the size of the polymersomes was monitored by DLS for 60 minutes. This, in turn, led to the disassembly of the polymersomes after 30 minutes from suspension in glucose.

These results not only evidence the successful encapsulation of the GOX enzyme into the polymersomes but also the maintained catalytic activity of the enzyme to glucose within the confined aqueous core of the polymersomes. They also show the permeability of polymersomes to glucose in which glucose from the surrounding environment is able to access the GOX enzyme entrapped within the polymersome aqueous core. Thus, highlighting the ability of the polymersomes to sense the glucose molecules in the external environment.

Now that the nanovesicles are loaded with GOX and have shown sensitivity/ response to an external homogenous environment of glucose, the next step is to investigate these systems' ability to sense a glucose gradient and move within it, which is the focus of Chapter 6, 7 and 8. For this, the samples are prepared in PBS buffer to prevent the change in pH and the disassembly of the polymersomes due to the production of gluconic acid.

CHAPTER SIX

OVERCOMING DENSITY DRIVEN CONVECTION TO MEASURE CHEMOTAXIS AT THE NANOSCALE

Now that the polymersomes are prepared in PBS buffer and loaded with the GOX enzyme, the Malvern Nanosight device was used to investigate the chemotaxis motion of polymersomes in the way previously described by Joseph *et al.*[8] It was found that convective fluid flow is generated within the sample chamber upon the formation of a glucose gradient, because the sample chamber of the Nanosight is 900 µm deep, hindering the detection of chemotactic migration. Here an investigative approach was taken to assess this flow, focusing on the single and bicomponent PMPC-PDPA polymersomes. This reveals the formation of strong convective flows (up to 50 µm/s) as the glucose gradient is established. The limitations of this method are highlighted and discussed. Addressing these limitations and further expansion of the method makes the basis of chapters 7 and 8.

The NTA technique is based on images captured with a microscope able to record the light scattering patterns of nanovesicles when hit with a laser. The behaviour was investigated by recording the motion of the nanovesicles in both the absence of a chemical gradient (control PBS injections) and the presence of an induced chemical gradient. The nanovesicle trajectories in the recorded videos were tracked using the NTA analysis software and analysed using Matlab® as described in chapter 2. The particle trajectories and the mean square displacement, MSD (a measure of the deviation of the nanovesicle position with respect to the reference position over time) versus time, were used to assess the behaviour.

This method was previously used by Joseph *et al.* to visualise the chemotactic motion of polymersomes.[8] It was reported that when injected with PBS enzymatically loaded symmetric PMPC-PDPA and bi-component PMPC-PDPA+PEO-PBO (asymmetric) polymersomes, show stochastic trajectories and linear MSD characteristic of Brownian motion, Figure 74.a and b. Similar behaviour was observed by the enzyme loaded symmetric polymersomes and the empty asymmetric polymersomes when 1M glucose solution was injected, Figure 74.c and d. However, only by the injection of glucose to the enzymatically loaded bi-component systems (asymmetric) was a directional motion towards the glucose observed by the directional trajectories and ballistic MSD (Figure 74.e).

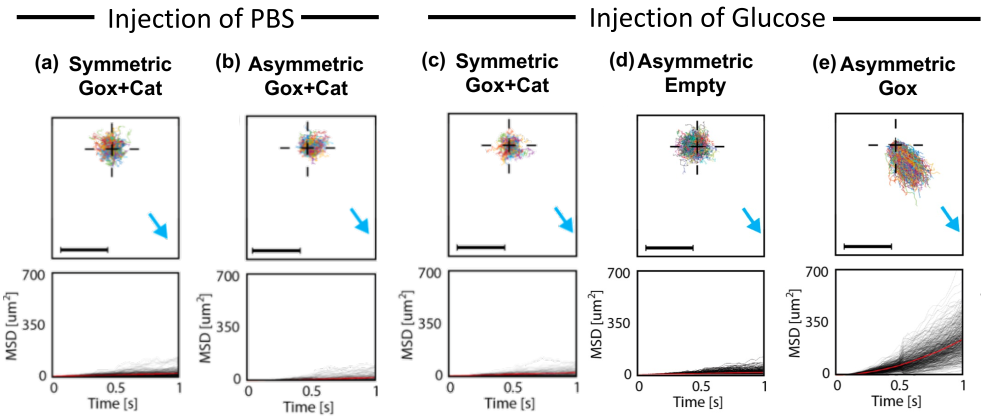

Figure 74. Normalised trajectories and mean square displacement (MSD) plots as a function of time. Blue arrows represent the direction of the chemical gradient. Scale bars=20 μm. Both the (a) pristine and (b) bicomponent polymersomes display Brownian motion (stochastic trajectories and linear MSD) when injected with PBS. When glucose was injected, the (c) enzyme loaded pristine polymersomes, and the (d) empty bicomponent polymersomes also showed Brownian motion. However, the (e) enzyme loaded asymmetric polymersomes display directed movement towards the glucose source as shown by the trajectories and the ballistic MSD. This indicated that directed motion is achieved only by both the enzymatic encapsulation and the membrane asymmetry. Reproduced from ref. 8.

More recently, work by Williams et al. has demonstrated the presence of density-driven convection flow within a 1M glucose gradient. This fluid flow is driven by mass density gradients ρ which increases linearly up the concentration gradient and is a driver of material transport. The slip velocity of this convective flow, assuming that the concentration c varies only along x and subject to gravitational force acting on the fluid and to no-slip boundary conditions $v_x(z=0)=0$ and $v_x(z=H)=0$, in the absence of net flow is given by

$$v_x(z) = v_b\left[\frac{1}{6}\left(\frac{z}{H}\right)^3 - \frac{1}{4}\left(\frac{z}{H}\right)^2 + \frac{1}{12}\left(\frac{z}{H}\right)\right], \tag{13}$$

$$v_b = \left[\frac{(\rho_s \beta g H^3)}{\eta}\right]\left(\frac{dc}{dx}\right). \tag{14}$$

where ρ_s is the solvent density, β is the solute expansion coefficient, η is the viscosity of the fluid, and H is the height of the chamber. The natural convection profile of the fluid is circulating, from high glucose concentration to low concentration at the bottom of the chamber and in the opposite direction at the top of the chamber. The speed of the flow scales linearly to the concentration of the gradient and depends on the third power of the height of the chamber (H).

6.1 Chamber mapping

Therefore, I next explore the circulating density-driven fluid flows in the glucose gradient established within the NTA chamber. To do so, I start by observing the behaviour of the polymersomes at different regions of the chamber. If the motion were induced only by chemotaxis or even diffusiophoresis, the particles would be expected to move towards the glucose source independently of where in the chamber they are observed. If the chamber contains buoyancy driven fluid flows, the motion of the polymersomes will vary at different areas of the channel, suggestive of circulating motion.

The motion of the pristine empty polymersomes was mapped by tracking the trajectories of particles at different regions of the observation area. Firstly, PBS was injected into the polymersomes suspension. Here the polymersomes exhibit stochastic behaviour, the mapping indicated no movement in any of the areas of the chamber, Figure 75. This is consistent with previously reported results by Joseph *et al.,* Figure 74*a and b.*

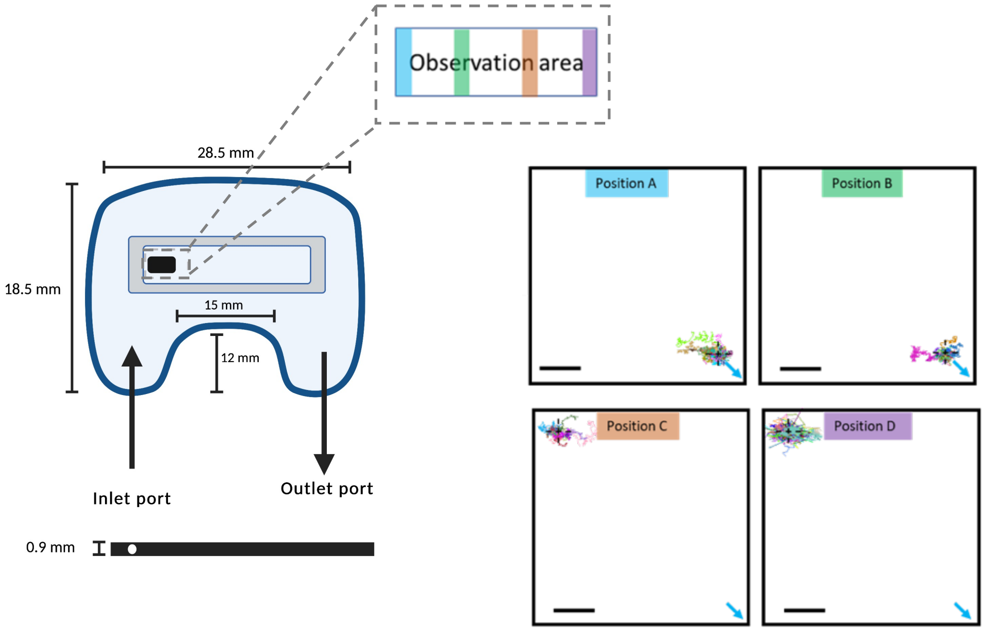

Figure 75. The NTA chamber mapping of the trajectories of empty when injected with PBS to show the similarity in behaviour through the mapped observation area. Blue arrow represents the direction of glucose gradient. Scale bar = 10 μm

However, when glucose is injected pristine polymersomes exhibit directional motion which moved differently at different areas. More specifically, polymersomes observed in regions close to the applied glucose gradient drifted towards it, as in positions D and E in Figure 76. However, in positions A and B, the particles moved in the complete opposite direction. Interestingly, towards the centre, the particles were observed to exhibit two differential non-mixing laminar planes flowing one above the other, as shown in Figure 76.

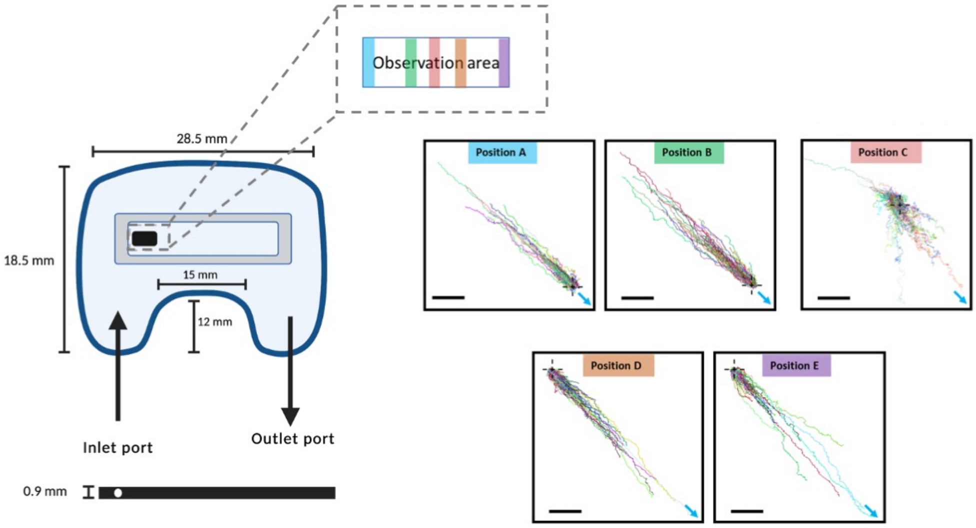

Figure 76. The NTA chamber mapping of the trajectories of polymersomes in the presence of a glucose gradient. Blue arrow represents the direction of glucose gradeint. Scale bar = 10 μm

This is a critical observation that shows that polymersomes move in different directions at different places in the chamber or even different directions in the same place (position C). This is incompatible with chemotactic motion due to the different migration directionality within the chamber and that these polymersomes do not have an asymmetric topology nor are loaded with GOX.

In the NTA, and as shown in Figure 77, the polymersomes are observed by shining a laser beam into the polymersomes suspension, which scatters and hence can be visualised by the microscope on top. This laser beam propagates through the sample at an angle, making imaging at different positions (A to E) equivalent to imaging at different heights. This suggests that the pattern of this motion is circulating around the chamber, in which the bottom of the chamber flows away from the glucose source and the top moves towards it. This also explains the motion seen in position C, which would be equivalent to imaging a section of the channel in which the opposite circulating flows at the bottom and top of the chamber can be seen.

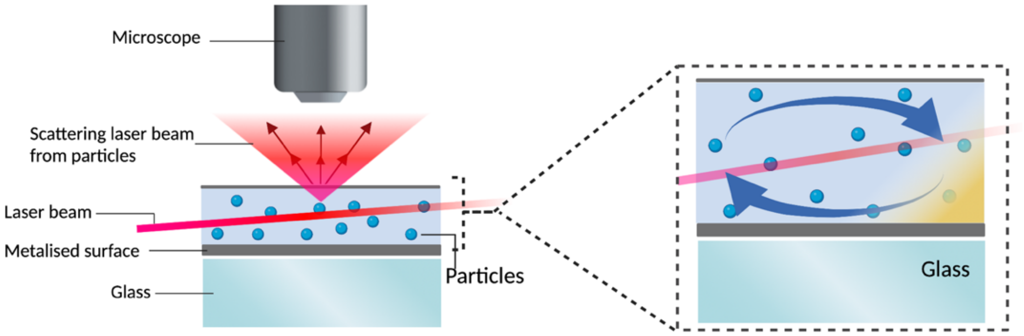

Figure 77. The predicted circulating fluid flow (blue arrows) in the NTA sample chamber is due to the injection of glucose (yellow). (Not drawn to scale)

6.2 Glucose gradient induced fluid flow

Now that we have established that this motion is not chemotactic migration of polymersomes, I next explore the specificity of this glucose-induced circulating flow. Is it a flow exclusive to the motion of polymersomes when glucose is injected or is it a more general motion related to the presence of a glucose gradient (i.e., convection)?

To explore this, latex beads were used as hard spherical colloidal particles with a comparable size of 60 nm and imaged in position A. As a consequence of the PBS injection, the latex beads displayed ideal Fickian diffusion with linear MSDs, whereas the glucose injection demonstrated a ballistic MSD behaviour over time with the normalised trajectories directed away from the applied gradient (position A). The trajectories and the MSD plots are shown in Figure 78.

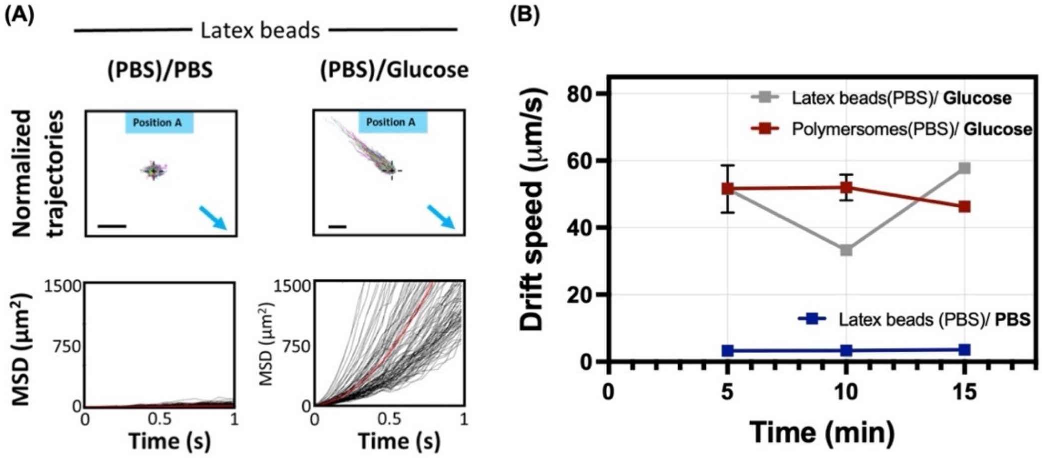

Figure 78. (A) Normalised trajectories and mean square displacement (MSD) plots as a function of time for latex beads suspended in PBS when injected with PBS and 1 M glucose solution (observed at position A). The direction of the injected gradient is denoted by the blue arrows. The scale bars represent 10 μm. The latex beads exhibit a stochastic behaviour when injected with PBS (first column) and a directional particle migration when injected with glucose (second column). (B) The average drift velocities as a function of time after the injection of glucose or PBS. The latex beads and the pristine empty polymersomes display comparable drift velocities in the presence of a glucose gradient, while the beads maintain a constant Brownian motion when PBS is injected.

Further analysis into this superdiffusive response was conducted by examining the drift velocities of the polymersomes as a function of the time after injection of the glucose gradient. Figure 78 shows a similar increase in drift velocities of the pristine empty polymersomes and the latex beads achieved after the injection of glucose with a maximum value of 57.7 ± 1.6 μms^{-1} and 46.2 ± 1.0 μms^{-1} after 15 minutes, respectively. The injection of PBS to the latex beads maintained a lower drift velocity of 3.3 ± 1.0 μms^{-1}, comparable with those previously reported for PBS injection into the empty polymersome suspension. These results suggest that the prompted drift is independent of the polymersome structure (be membrane permeability or hollow structure) and could be related to a fundamental behaviour of nanosized particles in a glucose gradient.

As discussed in chapter 2, particle migration in a fluid can be a result of several contributions. In this system of non-charged particles, in the absence of a chemical gradient, the major contributor to the movement is the Brownian motion, as evidenced by the stochastic trajectories and MSDs. However, upon injection of glucose, the drift velocity increases, and the polymersomes and polystyrene beads demonstrate a directional migration, Figure 78.

These drift velocities are large and comparable, greater than 40 μms^{-1}, for both the polymersomes and beads. Since no enzymes are present in any of these systems, this motion is not driven by chemotaxis. Diffusiophoresis (DP) is another phenomenon that can induce particle migration. Nevertheless, diffusiophoresis relies on the interaction potential between the surface of the particle and the glucose molecules. The surface chemistry of the beads and the polymersomes are different; hence there is no reason to expect both beads and polymersomes to undergo diffusiophoresis at the same speed.

A possible explanation for the observed circulating drifts upon the injection of glucose is convection currents. In this experimental setup, the convection could be thermal or buoyancy. Thermal convection could be induced by the difference in temperature of the injected glucose to the particle solution, where density decreases with increasing temperatures hence creating a density gradient. Buoyancy driven convection could be associated with the density gradient generated due to the injection of a dense glucose solution to the less dense particle solution; density gradient increases linearly with concentration. To further investigate the contribution of each of these parameters, a systematic study was conducted.

The first parameter examined was thermal convection which is caused by variations in temperature within different regions of the fluid. One of the plausible causes could be the slight variations of temperature between the nanoparticle suspension inside the chamber and the injected substrate solution. To examine this, the experimental setup was thermostatised in the best possible way, given the delicate experiment procedure. To visualise these effects, latex beads suspended in PBS were studied by injecting PBS and glucose at varying temperatures, and the trajectories and drift velocities were monitored at 5-minute intervals within a 15-minute period from the injection, Figure 79.

The latex beads behaved stochastically when PBS was injected at the same temperature as the polymersome suspension. This behaviour was maintained when PBS was injected within 10°C difference from the beads suspension. The drift velocities were comparable, demonstrating no significant difference in particle migration velocities, as shown in Figure 79. Similarly, the injection of glucose to a latex bead suspension while maintaining the temperature at 27, 37, or at a 10°C difference, demonstrated the similar directional movement of the nanoparticles away from the injected glucose (viewing through position A) at comparable drift velocities of 47.3 ± 1.1 μms^{-1}, 48.5 ± 0.7 μms^{-1} and 46.3 ± 2.6 μms^{-1} respectively. These velocities are consistent with the previous measurements at position A of polymersomes and beads without careful temperature control. Thus, these results suggest that within the possible thermal fluctuations at room temperature, thermal convection does not contribute to a significant particle migration.

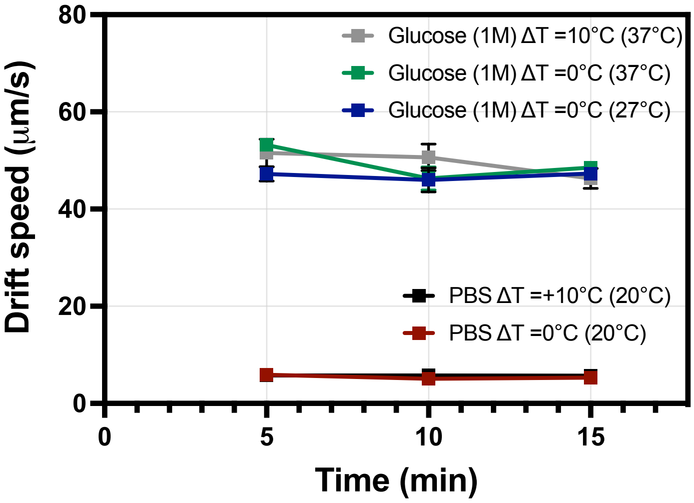

Figure 79. The average drift velocity of the latex beads away from glucose (observed from position A) as a function of the time of a latex bead suspension after the injection of PBS or glucose. Drift velocities typical of Brownian motion of latex beads after injection of PBS at the same temperature (red) or ten degrees higher (black) than the temperature of the latex beads suspension. The glucose injection demonstrated no significant difference in drift velocity between the injection of glucose at the same temperature (blue and green) or ten degrees higher (grey) than the temperature of the latex bead suspension

The second parameter investigated as a potential contributor to particle migration is Buoyancy driven convection (also referred to as density-driven convection in this thesis). To examine this, different concentrations of the glucose solutions, 1 M, 0.5 M and 0.1 M, were used to vary the density of the solution from 1.066, 1.031 and 1.005 gml$^{-1,}$ respectively.[171, 172] As shown in Figure 80, the average drift velocity of the particle migration decreases upon reducing the concentration (and density) of the injected solution from 1 M, 0.5 M and 0.1 M. Hence these results suggest that the migration velocity of the particles is associated with the concentration of the injected glucose, which is linearly related to density. In other words, the velocity of the particle migration decreases with the decrease in the concentration (and hence the density) of injected glucose solution.

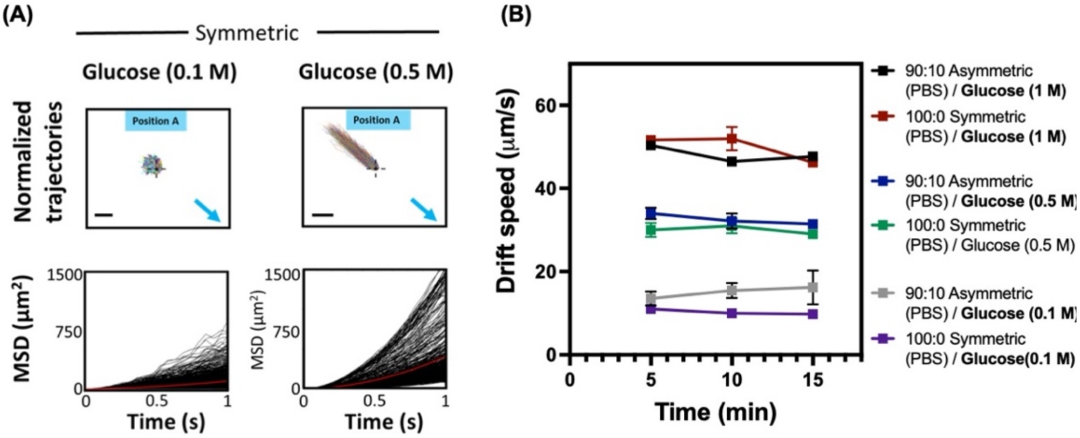

Figure 80. (A) The normalised trajectories and mean square displacement (MSD) plots as a function of time for empty pristine polymersomes suspended in PBS when injected with 0.5 and 0.1 M glucose solution. The direction of the injected gradient is denoted by the blue arrows. The scale bars represent 10 μm. The polymersomes exhibit directional particle migration shown by the trajectories and the ballistic MSD. (B) The average drift velocities as a function of time after the injection of 1 M, 0.5 M and 0.1 M glucose solutions. The polymersomes display a decrease in particle drift velocity with a decrease in substrate concentration.

To further verify the influence of density, fructose was injected instead of the conventional glucose solution into a suspension of polymersomes in PBS, since it is a different chemical compound that provides the same density as glucose at the same concentration, 1M fructose has a density of 1.067 gml^{-1}.[171] As shown in Figure 81, the pristine polymersomes exhibited similar drift velocities when injected with fructose and glucose at the same concentration. Additionally, the radar plotting of the angle of polarisation shows that the particle migration is aligned away, injection at an angle of 60 and drift is exactly towards 240, from the applied gradient in both cases (when imaged at position A, Figure 81) and towards glucose in position E.

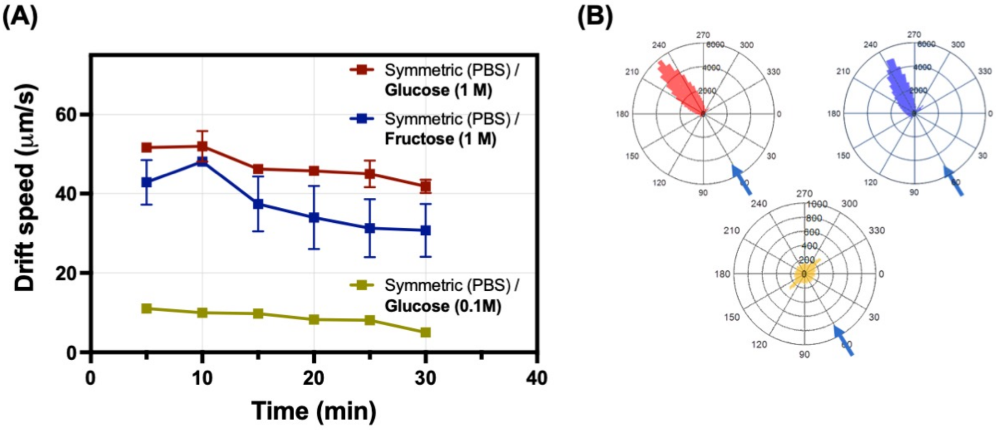

Figure 81. The pristine polymersome (A) average drift velocity as a function of time from injection of 1 M glucose (red), 1 M fructose (blue) and PBS (yellow). (B) The direction of particle displacement is represented by radar plots; the direction of the injection gradient is indicated by the blue arrows.

To confirm the convection fluid flow, the polymersomes were suspended in three different sugar solutions sucrose, fructose and glucose (1 M), while injecting glucose 1 M. The densities of sucrose, fructose, glucose at 1 M are 1.127, 1.067 and 1.066 gml$^{-1,}$ respectively.[172] When the polymersomes were suspended in fructose (1 M) and injected with glucose (1 M), at this concentration, the densities are matched at 1.06 gml^{-1}, and therefore no convection is expected. The tracked particles behaved stochastically with no directional migration of the particles, with a drift velocity of around 5.5 ± 1.2 μms^{-1} after 30 minutes from the injection, Figure 82. This drift velocity is like that observed when the particles were suspended in glucose (1 M) while injecting glucose (1 M). This indicates that on matching the density and the concentration of the solute and the injected solution, the particles do not display any migration and maintain a stochastic behaviour.

When the concentration of the solute and the injected solution is maintained (i.e., injected 1M glucose) while increasing the density by suspending the polymersomes in sucrose (1 M, 1.127 gml^{-1}), the polymersomes were observed to move towards the less dense, injected glucose, indicated in Figure 82 as the blue region. These empty pristine polymersomes exhibit an increase in drift velocity of around 20.8 ± 1.9 μms^{-1} after 30 minutes. Moreover, when suspending the nanoparticles in PBS while injecting glucose (1 M), the particles were observed to migrate away from the higher density glucose and down the glucose concentration gradient, as indicated in, Figure 82 as the red region. However, when the particles were suspended in 1 M glucose, and PBS was injected, the direction of the particle migration was inverted such that the particles were observed to move towards the less dense PBS injection and down the glucose gradient. The drift velocity of polymersomes further increased to 41.8 ± 1.6 μms^{-1}. This could be related to the larger difference in density between PBS and glucose as opposed to sucrose and glucose and the no difference in densities between fructose and glucose.[171]

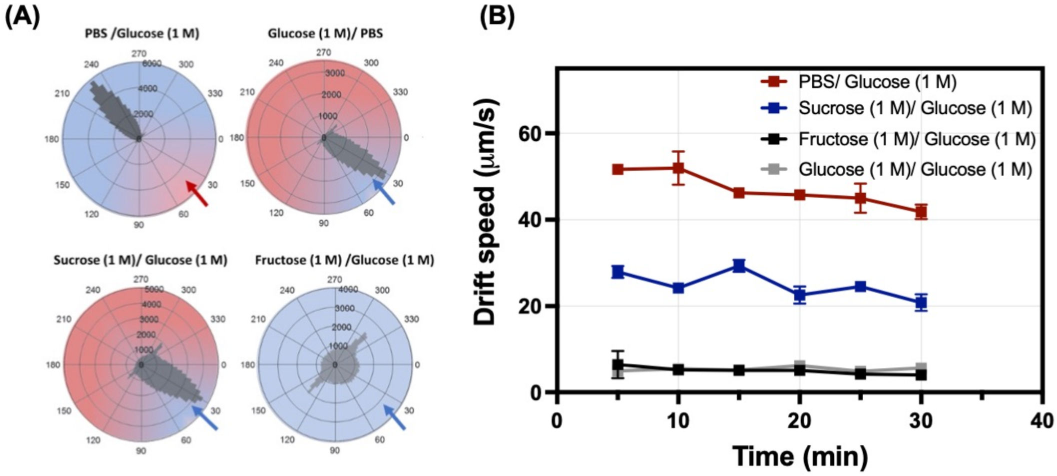

Figure 82. (A) Radar plots displaying the displacement direction of pristine polymersomes upon the introduction of a substrate that has a higher density (red arrow) or lower density (blue arrow) than the polymersomes suspension. The pristine polymersomes suspended in PBS move towards the region of lower density (red) upon the injection of 1 M glucose. The particle displacement direction when the polymersomes are suspended in a dense 1 M glucose (red region) while injected with PBS of a lower density (blue arrow). The particle migration away from the higher density (red region) when polymersomes are suspended in 1 M sucrose and injected with the less dense 1 M glucose solution. Stochastic behaviour is observed when the particles are suspended in 1 M fructose while injecting 1M glucose at the same viscosity. (B) The average drift velocities as a function of time after the injection of 1 M glucose to polymersome suspension in PBS (red), 1 M sucrose (blue), 1 M fructose (black) and 1 M glucose (grey).

These results indicate that this flow is associated with convection fluid flow, which consistently flows towards the less dense solute (and down the concentration gradient) at the bottom of the chamber (position A) and up the density gradient (towards glucose) at the top of the chamber (position E), Figure 77. Illustrating that the major contributor to the motion of the detected nanoparticle is a directional drift velocity associated with the velocity of the underlying fluid flow. These strong convection flows make it challenging to observe possible chemotactic motion of the particles, ie to differentiate between the flow of polymersomes due to the underlying convective flow and the active (chemotactic) migration of the particles themselves.

6.3 Discussion: Limitations of NanoSight in chemotaxis studies

These results highlight fundamental features that need to be considered when performing chemotaxis studies. Firstly, and the most challenging is the density-driven convection that is generated due to a glucose gradient. This is an inherited consequence of the presence of a glucose gradient. Having convection at this large magnitude (approx. 50 μms^{-1}) is not ideal for studying chemotaxis as it would overshadow any possible chemotactic motion making it challenging to detect. The circulating pattern of the convective flows effectively means that imaging the same sample at different regions of the observation area would lead to different results. Thus, making the observation region very critical. Thus, to better understand the propulsion mechanism of the polymersomes and achieve the aims of this project, convection needs to be eliminated.

The speed of the circulating convective fluid flow scales linearly with the concentration gradient and depends on the third power of H, Eqn. (13). Hence the convection is highly affected by the depth of the chamber (third power of H). Therefore, to suppress the convective flows, a thinner sample chamber is necessary. Additionally, the linear correlation with the concentration gradient suggests that on decreasing the concentration gradient, the slower is the convective flows. Thus, in the next chapter, another established chemotaxis setup based on a thinner chamber (the chemotactic ibidi microfluidic chambers) which are imaged using advanced confocal microscopy will be explored.

CHAPTER SEVEN

NANOVESICLE INFLUENCED DIFFUSIOOSMOTIC FLOW IN A GLUCOSE CONCENTRATION GRADIENT

In this chapter, an alternative experimental setup is used to study chemotaxis of the nanovesicles. It was reported by Williams *et al.*[10] that this setup generates weaker convection fluid flows in glucose gradients. This is due to the thinner sample chamber (70 µm), compared to the 900 µm chamber used in the NTA. In the first section of this chapter, the convective and diffusioosmotic (DO) fluid flows in this microfluidic chamber are introduced. This is then used to explore the influence of the nanovesicles on the underlying diffusioosmotic fluid flow in this channel. The results for the different nanovesicles will be reported, focussing in particular on the measurement of the velocity profiles. These results are interpreted by comparing the profiles with theoretical predictions of the ideal diffusioosmotic velocity profile in a glucose gradient within this channel. The following discussion is focused on highlighting the differences in the shape of the velocity profiles and thus inferring the origin of these differences. Henceforth, this allows us to infer for the first time from diffusioosmotic fluid flow the nature of the glucose-nanovesicle interactions. This method proves to be a valuable means to (i) assess the interaction potential of non-electrolytes solutes and surfaces and (ii) control fluid flow in microfluidic devices by in situ alterations of the properties of the walls.

From the previous chapter, we have identified fundamental features of an ideal experimental setup for the study of chemotaxis. These are (a) a linear glucose gradient, (b) no background convective flows and (c) improved imaging resolution. Preventing convective flows is a challenging issue to overcome since the difference in densities is an inherent property of the gradient itself. The speed of convection increases linearly with glucose concentration gradient and decreases to the third power of height.[10] Hence this convection can be suppressed by reducing the glucose concentration gradient and reducing the thickness of the experimental chamber. In the case of the NanoSight, a 1 M glucose gradient in a chamber of thickness 900 μm produced a convective flow of approx. 50 μms^{-1}. Recent work by Williams *et al.* has reported suppressed convective flows in a 1 M/mm glucose gradient to a velocity of about 1 μms^{-1}. This was achieved by reducing the thickness to 70 μm in a linear microchannel. The concentration of the glucose gradient was also reduced to 50 mM/mm, which resulted in a change in fluid flow from convection-driven to diffusioosmotic driven flow at a reduced speed of 0.5 μms^{-1}. For background information on diffusioosmotic flow, refer to section 2.4.

The linear glucose gradient, the dampened convective flows and the improved resolution of the confocal microscopy make this setup ideal for the study of chemotaxis; hence it is explored in this chapter. Here I start by introducing the analytical predictions and replicating the experimental data on the convective and diffusioosmotic fluid flows previously reported by Williams *et al.*[10] By using this setup as the starting point, I expand on this published work by exploring the influence of the nanovesicles on the convective and diffusioosmotic fluid flow. This work is further advanced to use this setup as a method to measure interaction potential between non-electrolyte solutes and nanoparticles.

7.1 Background on the theoretical fluid profile.

Analytical solutions to the flow in different electrolyte or nonelectrolyte gradients have been found for a range of simple flow geometries. For this experimental setup, analytical predictions for velocity profiles in the case of a glucose gradient were presented by Williams *et al.*[10] As shown in Figure 78, I performed experiments in a millimetre-long thin channel (L = 1 mm) of height (H) 70 µm and width (W) 2 mm separating two reservoirs. The gradient is applied along the X-axis of the channel by filling two reservoirs with different solute concentrations, the low concentration reservoir c_0 and the high concentration reservoir at $c_{max} = c_0 + \Delta c$. These reservoirs are sealed; hence the total net fluid volume is preserved, preventing any overall directional fluid flows through the gradient channel. From a mathematical standpoint, the concentrations of the reservoirs are assumed to be fixed. However, in real life, this is not entirely true as the whole system will eventually mix to reach equilibrium. The mathematical assumption is equivalent to having reservoirs of infinite size. This assumption is acceptable as the reservoirs in the real system are large enough that it takes days for this system to reach equilibrium. Thus, the assumption of a uniform and stationary gradient is acceptable on the experimental timescale; hence a gradient of $\Delta c/L$ between the reservoirs is maintained. No gradient is applied in the Y and Z axis; thus, the gradient is assumed to be uniform.

In this setup, as illustrated in 78 and at low Reynolds number (Eqn. 1), the fluid flow can be described by the Stokes equation,

$$-\nabla p + \eta \nabla^2 \vec{u} + \vec{f} = 0 \tag{15}$$

where u is the fluid velocity vector $(\vec{u}_x, \vec{u}_y, \vec{u}_z)$, p is the pressure, η is the viscosity of the fluid and $\vec{f}$ is the body force acting on the fluid. As $H \ll L$ and $H \ll W$ a unidirectional fluid flow is anticipated $\vec{u} = (u_x, 0,0)$, and the incompressibility of the fluid is also assumed $d_x u_x = 0$. Additionally, and for simplicity of analytical predictions, the viscosity is assumed uniform.[10, 173]

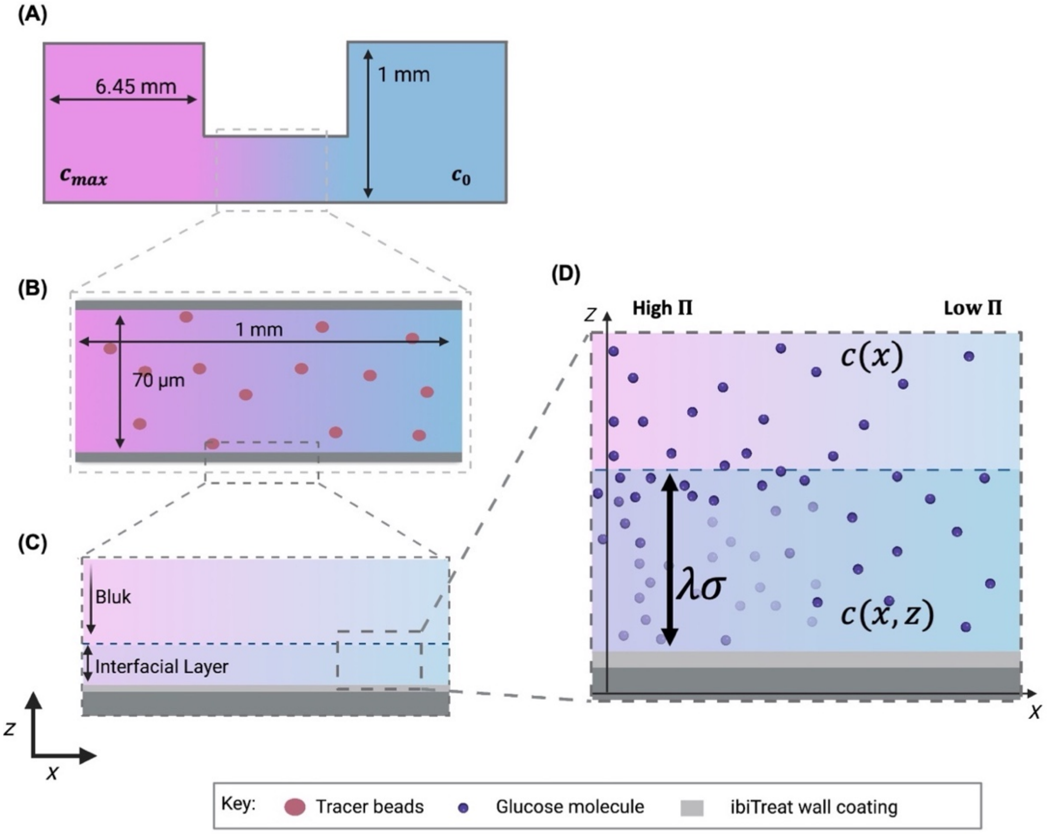

Figure 83. Illustration of the experimental channel (A) consisting of two sealed reservoirs containing c_0 and c_{max}, connected by a thin channel. (B) A glucose gradient is established in the thin channel of height = 70µm and length = 1 mm, in which tracer beads (red circles) are suspended. (C) The microscopic region where the surface-solute interactions affect the solute concentration is shown as the interfacial layer. (D) The surface (dark grey) is coated with an ibiTreat coating (light grey) which attracts the solute (glucose, purple circles) inside the interfacial region of thickness $\lambda\sigma$. The interaction potential experienced by the glucose U vanishes beyond the interfacial layer. The concentration of glucose close to the wall is $c(x, z)$ and that far away from the wall $c(x)$. The osmotic pressure Π increases along the glucose concentration gradient.

In the case of convection, the fluid flow is driven by mass density gradients; as seen in Chapter 6, the velocity profile can be predicted by solving Eqn. (13). The profile solved for by Williams *et al.* is illustrated in Figure 84. The profile displays a circulating flow within the microchannel, at the bottom of the channel, the fluid flows down the concentration gradient (from high to low concentration) and in the opposite direction at the top of the channel. The flow velocity is maximum at $z/H \approx 0.79$ and minimum at $z/H \ \approx 0.21$, both of which have a magnitude $v_b^{max} \approx 8 \times 10^{-3} v_b$. In which the speed scales linearly with the concentration gradient and depends on the third power of the thickness of the channel.

Another type of fluid flow anticipated within these channels is diffusioosmotic flow. Here the flow is driven by the interaction of the external concentration gradient and the solid walls of the channel within the interfacial region, as described in section 2.4. The slip velocity of the generated flow is given by Eqn. (5) and (6).

Williams *et al.* has reported an analytical prediction of the diffusioosmotic flow in a glucose gradient within this microchannel and in the absence of body forces $\vec{f} = 0$. This was done by assuming that slip boundary conditions, $v_x = v_s$ at $z = 0$ and $z = H$, and whilst imposing the condition of zero net flow, $\int_0^H v_x(z)\, dz = 0$. The Stokes equation describing the fluid flow was solved, yielding

$$v_x(z) = v_s \left[6\left(\frac{z}{H}\right)^2 - 6\left(\frac{z}{H}\right) + 1\right]. \tag{16}$$

For an attractive glucose-wall interaction, the slip velocity flow is in the same direction at the top and bottom walls of the channel. Due to the zero net transport condition, a backward flow is observed at the centre of the channel. This flow yields a parabolic flow profile, as shown in 79. Both the convective and diffusioosmotic predicted flows were observed by Williams *et al.* in glucose gradients.

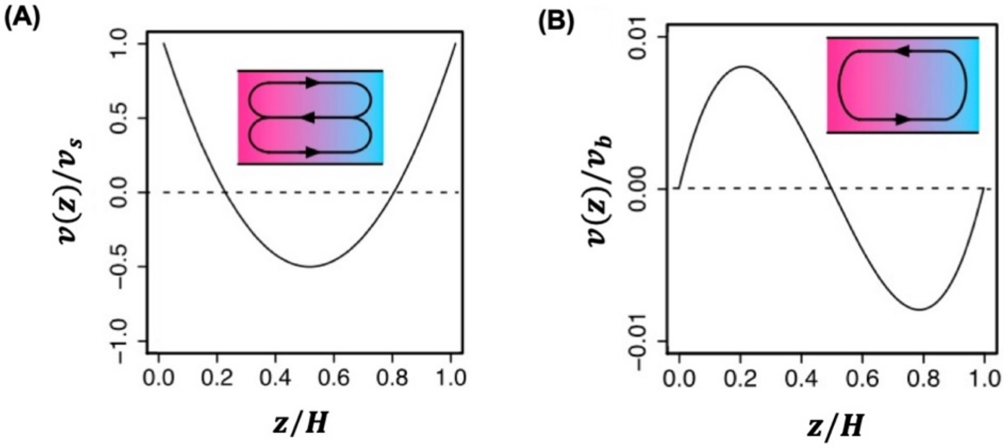

Figure 84. The theoretical predictions of the fluid flow velocity profiles in the thin channel. (A) The diffusioosmotic flow v_s from Eqn. (16). (B) Convection driven flow v_b from Eqn (16). The inserts illustrated the pattern of the circulating flow. Reproduced with permission from Willams et al. ref 10.

7.2 Experimental velocity profiles

Let's now experimentally evaluate the basic fluid behaviour in a 1 M/mm concentration gradient within this thin channel. The obtained experimental profiles are then compared with the theoretically established profiles by Williams *et al.*, Figure 84. This describes the fluid itself in a glucose gradient. To explore this, the fluid motion within the channel was monitored. This was achieved by tracking tracer particles by laser scanning confocal microscopy. These are fluorescently labelled amine-modified polystyrene (PS) spheres, which act as fluid tracers. Two-dimensional (2D) videos are recorded near the middle of the channel along the x and y direction and at different heights in z. The average velocities of the tracers at different heights are used to construct the velocity profile along z axis. Complete details are provided in chapter 2. Six independent replicates of this experiment were conducted, and the obtained velocities were averaged to attain a velocity profile, Figure 85A. The error bars at each velocity represents the standard deviation between the six replicates.

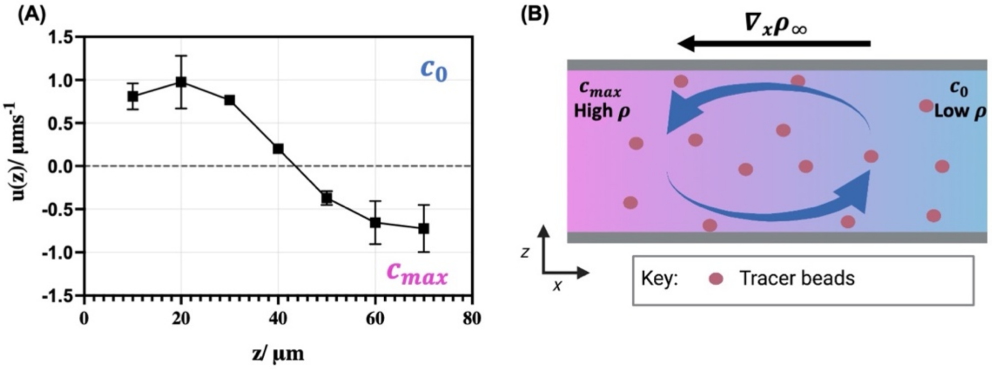

Figure 85. Fluid flow in a high glucose concentration gradient $c_0 = 0\ M$ and $c_{max} = 1\ M$. (A) The velocity profile along the Z direction of the channel shows the average velocity of all the tracked tracer beads (purple circles) over all the experiments. The error bars represent the standard deviation for the tracked tracer beads across six replicates. (B) Illustration of the shape of the fluid flow (blue arrows) along the x-z plane. This circulating flow is characteristic of density (ρ) driven flow.

From this, it is evident that the beads move in different directions at different heights of the channel (along the z- direction). The direction reverses around the centre of the channel. In the bottom half of the channel, the positive velocities indicate that the flow is directed away from the glucose (towards c_0) with a maximum velocity of 1.0 μms^{-1} at the height of 20 μm. At the bottom half of the channel, the beads flow towards the high glucose concentration (c_{max}) at a maximum velocity of 0.8 μms^{-1} at the height of 70 μm. Judging by this similarity of this experimental profile and the analytical predictions reported by Williams *et al*., in Figure 84, we can infer that at this glucose concentration gradient, the motion of the beads traces a flow driven by convection. This fluid flow is driven by the difference in mass density along the glucose gradient, which increases linearly with the concentration of the glucose gradient.[173] This convection-driven circulating flow is illustrated in Figure 85B. These results are in alignment with that previously reported by Williams *et al*., in which fluid flows at high glucose concentration gradient ($\Delta c \gtrsim 100\ mM$) are dominated by convection. [10]

Reducing the thickness of the channel has indeed reduced the speed of convection compared to the NTA experiments from 50 μms^{-1} to 1 μms^{-1}. Another parameter that influences the convection flow is the glucose gradient. Hence let's next look at the influence of reducing the glucose gradient to $\Delta c = 50\, mM$. As previously shown by Williams *et al.*, reducing the concentration gradient completely changes the shape of the velocity profile, as shown in Figure 86A. The beads flow away from the glucose (towards c_0) at the bottom and top walls of the channel. This is expressed by positive velocities with a maximum of about 0.5 μms^{-1}. At the middle of the channel, the velocities reverse in direction and move towards high glucose concentrations with a similar speed of 0.5 μms^{-1}. An illustration of this circulating motion is shown in Figure 86B. The shape of the profile strongly resembles the theoretical predictions of the diffusioosmotic driven fluid flow, Figure 84A.

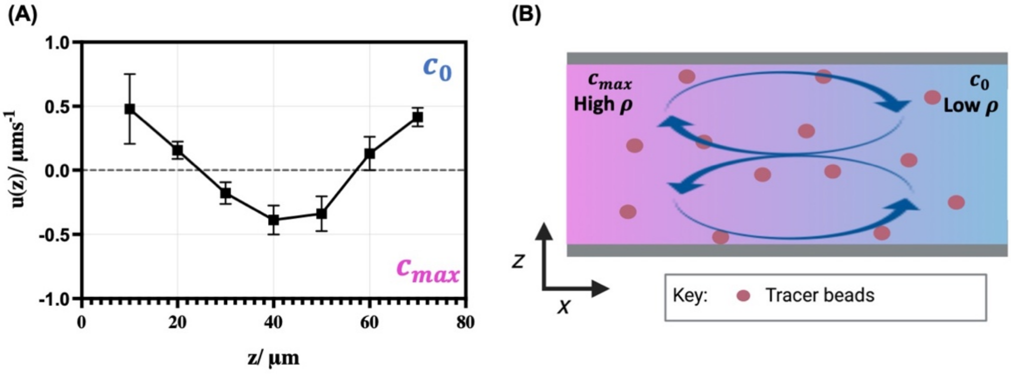

Figure 86. Fluid flow in a low glucose concentration gradient $c_0 = 0\ M$ *and* $c_{max} = 50\ mM$. *(A) The velocity profile along the Z direction of the channel shows the average velocity of all the tracked tracer beads (red circles) over all the experiments. The error bars represent the standard deviation from all six experiments. (B) Illustration of the shape of the fluid flow (blue arrows) along the x-z plane.*

Judging by this similarity, we can deduce that the motion of the beads traces a flow driven by diffusioosmosis. Hence it is reasonable to postulate that the diffusioosmotic flow is a result of the attractive glucose-wall interactions at the interfacial layer. In which the glucose molecules experience a negative potential energy profile, leading to an excess of solute within the interfacial layer, thus a slip coefficient ($\Gamma_{DO} < 0$). The presence of a glucose concentration gradient at the walls induces an osmotic pressure gradient, which is parallel to the glucose concentration. In order to balance the pressure difference fluid is driven, slip velocity (v_s), towards the low glucose concentration, i.e., positive velocity. These results are in agreement with previously reported experimental results by Williams *et al*. In which it was demonstrated that at low glucose concentration ($\Delta c \lesssim 100\ mM$), the fluid flow is dominated by Diffusioosmosis. [10]

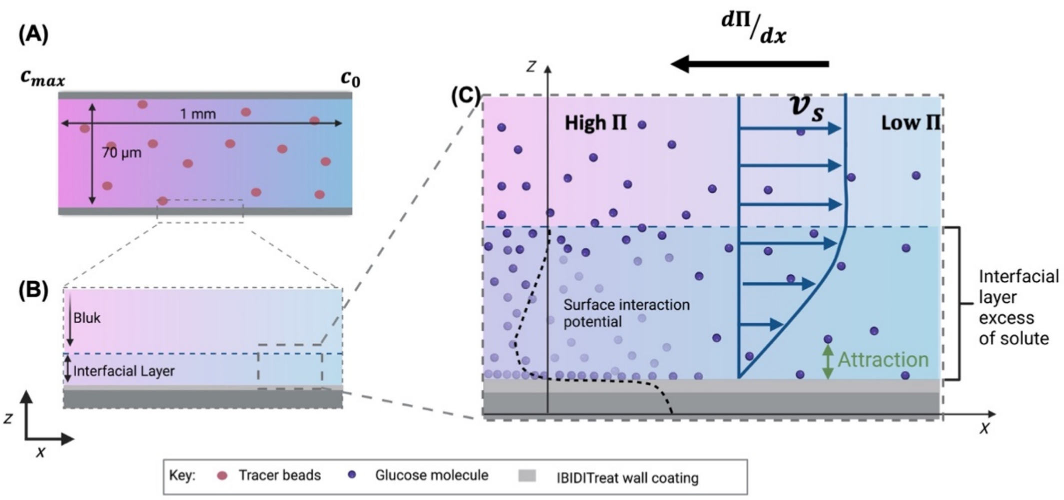

Figure 87. Schematic illustration of the attractive glucose-channel wall interaction facilitating diffusioosmotic fluid flow. (A) The glucose gradient within the thin channel with a maximum concentration ($c_{max} = 50\ mM$, pink region) and minimum concentration of ($c_0 = 0\ M$, blue region). The channel consists of tracer beads (red circles). (B) The interactions between the glucose and the walls happen within the diffusive interfacial layer, which is the region near the walls of the channel. (C) In this region, the glucose (purple) undergoes a negative interaction potential $U(z)$ (The dotted black curve). This potential well attracts the glucose to the walls of the channel leading to an excess of glucose in the interfacial layer. The concentration gradient of glucose at the walls leads to a gradient in osmotic pressure that drives the fluid flow towards low glucose concentrations.

Having seen the influence of diffusioosmosis due to the interactions of glucose and the walls of the channel, let us now have a look at the interactions of glucose and the surfaces of the tracer beads. This interaction would result in the diffusiophoresis of the beads because of the slip-velocity on the surface of the beads. The diffusioosmosis component can be distinguished from the diffusiophoretic component from the velocity profile. Diffusioosmosis acts on the walls of the channel; hence the velocity varies at different heights of the channel (distance away from the walls along z). The diffusioosmotic fluid flow in such a closed channel is circulating, and the net flow over all the heights is zero. Diffusiophoresis, on the other hand, acts on the surface of all the beads in the gradient in the same way. Assuming glucose concentration is constant along z, hence diffusiophoresis is constant overall heights of the channel and can be identified as a vertical offset in the velocity profile.[10] In other words, the sum or integral of the diffusiophoresis velocity over all the heights of the channel is not equal to zero, while the sum or integral of the DO fluid flow sealed channel always equals zero.

In the case of an attractive interaction between glucose and the bead surface, the excess of glucose within the interfacial layer would generate an osmotic pressure, Figure 11. In order to balance out the osmotic pressure, fluid flows towards the low glucose concentration (as seen with diffusioosmosis). This propels the bead in the opposite direction, hence towards the high glucose concentration. It is evident from the velocity profile that the net fluid flow is zero with no evident offset, Figure 86 and Figure 85. This confirms that the beads do not undergo diffusiophoresis within the gradient and only act at fluid tracers.

This difference in slip velocity between glucose and the walls of the channel or the surface of the tracer beads is owed to the difference in surface chemistry. The beads are amine functionalised polystyrene, and the walls of the channel are coated with ibiTreat.[146] While the nature of these interactions is not yet understood, it is evident that the glucose-surface interactions are stronger with the wall of the channel than the surface of the tracer beads.

These results show that the major contributor to the motion of the beads is Brownian motion which is superimposed over a directional drift velocity associated with the velocity of the underlying fluid flow. These outcomes have been previously shown by Williams *et al.*[10]. The linearity of the gradient and the reduced fluid velocities suggest the suitability of this setup for further chemotaxis studies. The weaker the underlying fluid flow, the better it is to evaluate chemotaxis. Thus the 50 mM/mm glucose gradient with a 0.5 μms^{-1} diffusioosmotic fluid flow is the setup chosen to study chemotaxis henceforth. As stated previously, the diffusioosmotic flow is influenced by the interaction potential of the glucose and the surfaces (be walls or beads). Hence, I now build on these findings by exploring the influence of the nanovesicles on the underlying diffusioosmotic flow and hence the interaction potential. It is imperative to quantify the Diffusioosmotic fluid flow for each nanovesicle before assessing any phoresis or taxis of the nanovesicles themselves.

7.3 PMPC-PDPA nanovesicle suppression of diffusioosmotic fluid flow

In this section, I introduce the pristine PMPC-PDPA nanovesicles prepared in chapter 4 to the 50 mM/mm glucose gradient setup, as mentioned in Chapter 3. The tracer beads are tracked, and the velocity profile is developed, Figure 88. Here the velocities slightly fluctuate around zero, with a maximum speed of 9.4 ± 0.4 x 10^{-3} μms^{-1}. The profile does not display any significant velocity shifts along the channel. This does not resemble the previously discussed theoretically predicted or experimentally observed DO flow within a 50 mM/ mm gradient, Figure 84 and Figure 86.

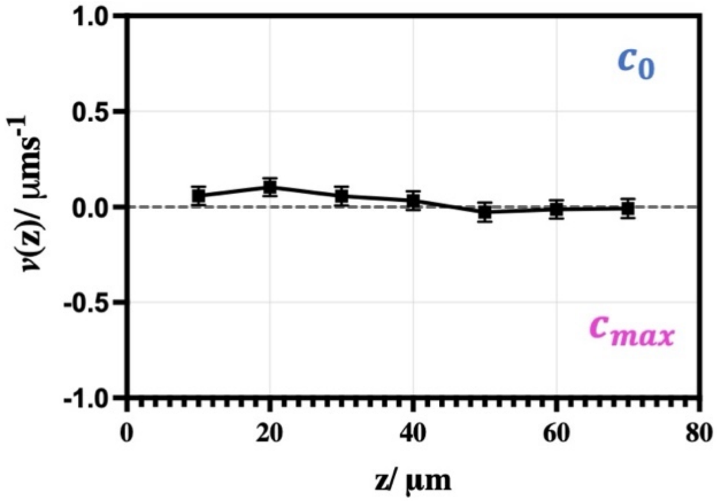

Figure 88. The velocity profile of beads in the presence of PMPC-PDPA polymersomes within a glucose gradient. Error bars indicate standard deviation across six replicates.

Before the addition of PMPC-PDPA vesicles, it was clear that a DO flow of speed 0.5 μms^{-1} is present within the channel, which shed light on the attractive interaction potential between glucose and the ibiTreat coated channel. However, the addition of PMPC-PDPA vesicles has suppressed this DO flow. DO flow is generated to balance out the osmotic pressure resulting from the uneven distribution of solute between the interfacial and bulk layers. In the case that no difference in concentration is present (i.e., no osmotic pressure gradient), flow is not generated. Thus, it is sensible to infer that the PMPC-PDPA influence the interaction with glucose and the wall of the channel. From this, we can deduce that the glucose-wall interactions in the presence of PMPC-PDPA polymersomes are insignificantly small to generate any detectable flow. This could be a result of the adsorption of the PMPC-PDPA vesicles on the walls of the channel. This is illustrated in Figure 89.

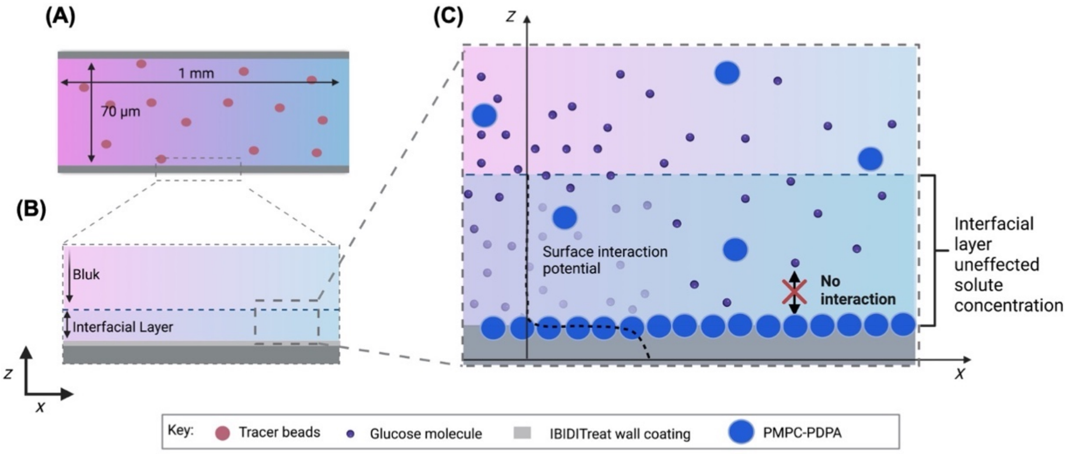

Figure 89. Schematic illustration of the glucose-channel wall interaction influenced by the addition of PMPC-PDPA nanovesicle. (A) The DO fluid flow is suppressed within a glucose gradient with a maximum concentration ($c_{max} = 50\ mM$, pink region) and minimum concentration of ($c_0 = 0\ M$, blue region). The channel consists of tracer beads (red circles). (B) The interactions between the glucose and the walls happen within the diffusive interfacial layer, which is the region near the walls of the channel. (C) In this region, the glucose (purple) undergoes an insignificantly minute interaction potential $U(z)$(The dotted black curve) influenced by the PMPC-PDPA nanovesicles. This potential is not sufficient to generate a difference in glucose concentration between the interfacial and bulk layers; hence no osmotic pressure is generated to drive a fluid flow.

7.4 PEO-PBO nanovesicle induced repulsive diffusioosmotic fluid flow

Having identified the suppression of diffusioosmotic flow due to the addition of PMPC-PDPA nanovesicles, which lead to deducing the nature of the interaction potential between the PMPC-PDPA nanovesicles and the glucose. The next step is to use the same method to investigate the influence of another polymersome which is the PEO-PBO polymersomes. The velocity profile displays a drift towards low glucose at all heights of the channel, with maximum velocity towards the middle of the channel, Figure 90A. The shape of the profile is different than that previously observed diffusioosmotic fluid flow at this glucose concentration Figure 86. To check for experimental artefacts, the directionality of the glucose gradient is reversed by switching the concentrations of glucose in the reservoirs. The same profile shape and directionality is observed in which the tracer beads travel consistently towards low glucose concentrations, Figure 90B.

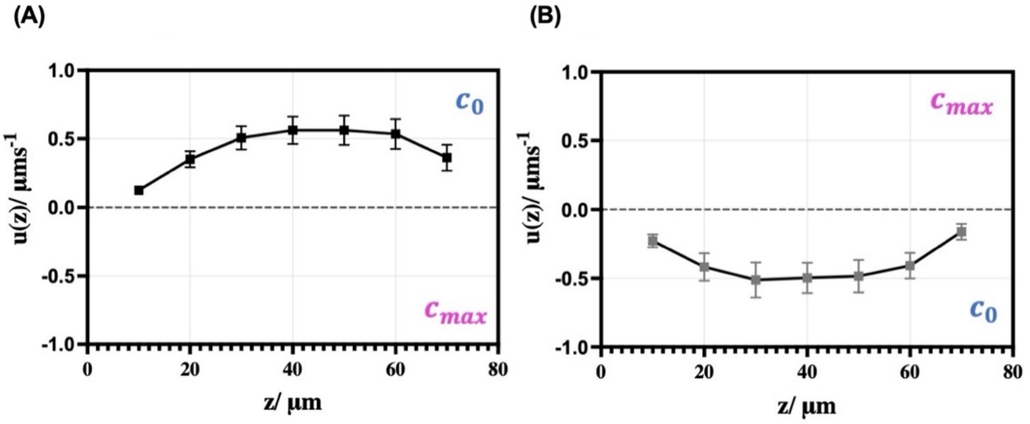

Figure 90. The velocity profiles of tracer beads in a glucose gradient containing PEO-PBO nanovesicles. (A) The gradient is established between two reservoirs of low concentration ($c_0 = 0\ M$) and high concentration ($c_{max} = 50\ mM$). (B) The direction of the gradient is reversed. The velocity profile maintains the same shape with a constant net drift towards the low glucose concentration.

This is interesting as the reservoirs are sealed, so the motion of the beads consistently (at all heights) towards the low glucose concentration cannot be a consequence of a directed fluid flow, i.e., the net overall fluid is conserved (net flow is zero). As mentioned previously, a vertical offset in the velocity profile indicates a migration of the tracers by diffusiophoresis, i.e., the tracers move through the fluid instead of moving with the fluid. As the concentration along the z-direction can be assumed to be relatively consistent, as the gradient is applied only along the x-direction. All the tracer beads along the z direction experience the same concentration gradient, hence the same conditions to facilitate equal migration, and thus an offset in the velocity profile. The offset in the velocity profile can be isolated. Henceforth, the velocity profile can be presented in terms of the bead's migration and the fluid flow component experienced by the tracer beads, Figure 91.

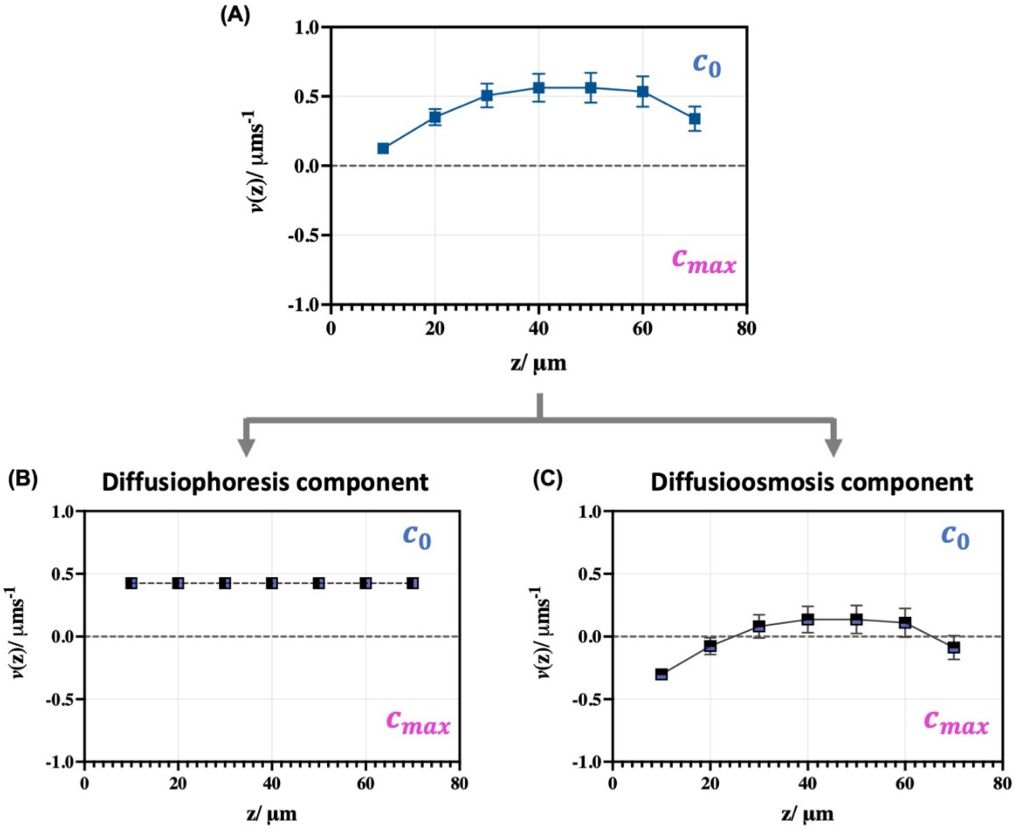

Figure 91. (A) The velocity profile of the tracer beads in the channel of PEO-PBO vesicles and a glucose gradient. From this, both the (B) bead's migration (diffusiophoresis) and (C) fluid flow (diffusioosmosis) velocity profiles are identified.

Let us first consider the fluid flow profile. The velocities are largest and codirectional at the bottom and top walls of the channel and reversed at the centre, shown in Figure 91C. At the walls, the velocity is negative, indicating the flow towards high glucose concentration, while the positive velocities around the middle of the channel indicate flow towards the low glucose concentration. The change in directionality is representative of circulating fluid flow, Figure 8A. The parabolic shape of the profile is analogous with that predicted and observed for the diffusioosmotic driven flow in the case of repulsive glucose-wall interaction, Figure 84 and Figure 86. This suggests that the fluid flow is driven by diffusioosmotic flow. However, the biggest difference between the DO flow induced by attractive glucose-wall interactions and that observed due to PEO-PBO addition is the flipped direction of the velocity profiles, which suggest the reversal in the directionality of the circulating flow. From the change in directionality of flow, it is sensible to deduce that when PEO-PBO is present, the glucose-wall interaction is repulsive, Figure 8A.

In this case, a strong repulsive interaction potential U between the wall and the glucose vanishes beyond the interfacial layer. This leads to the depletion of glucose within the diffusive interfacial layer. The slip coefficient ($\Gamma_{\mathrm{DO}} > 0$) generates an osmotic pressure gradient caused by the difference in glucose concentration, which in turn drives an interfacial fluid flow towards the high glucose concentration, Figure 8.

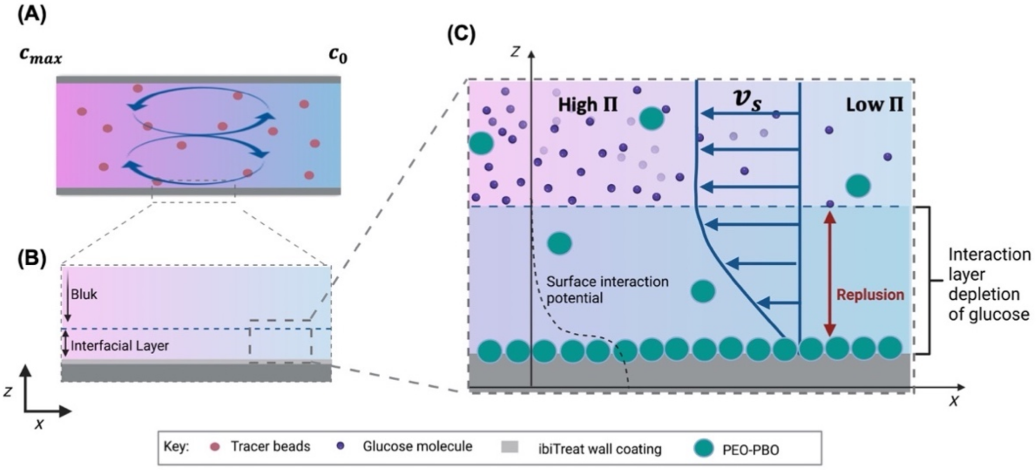

Figure 92. Schematic illustration of the repulsive glucose-channel wall interaction influenced by PEO-PBO nanovesicle addition. (A) The DO circulating fluid flow (blue arrows) within a glucose gradient with a maximum concentration ($c_{max} = 50\,mM$, pink region) and minimum concentration of ($c_0 = 0\ M$, blue region). The channel consists of tracer beads (red circles). (B) The interactions between the glucose and the walls happen within the diffusive interfacial layer, which is the region near the walls of the channel. (C) In this region, the glucose (purple) undergoes a positive interaction potential $U(z)$(The dotted black curve) influenced by the PEO-PBO nanovesicles. This potential repels the glucose leading to the depletion of glucose in the interfacial layer. This in conjugation with the osmotic pressure gradient ($^{d\Pi}/_{dx}$) drives the fluid flow towards high glucose concentrations.

Secondly is the migration component of the beads. The velocity profile of the tracer beads is constant at all heights of the channel at 0.48 μms^{-1} towards the low glucose concentration. It is evident that the addition of the PEO-PBO nanovesicles has induced migration of the tracer beads, which was not present beforehand. Within a glucose gradient, the most plausible migration of the beads would be facilitated by diffusiophoresis. Unlike diffusioosmosis, in diffusiophoresis the motion of the fluid around the surface of the bead leads to propulsion, or recoiling of the bead in the opposite direction. Hence the migration of the beads towards the low glucose concentration is characteristic of a fluid flow towards the high glucose concentration. As for diffusioosmosis, it is sensible to infer from this flow that the interaction between the bead and the glucose is repulsive.

In this case, the repulsion results in the depletion of glucose within the interaction layer (analogues to the interfacial layer at the walls of the channel) due to the repulsive interaction potential, Figure 93B. This generates a larger net repulsion on the high concentration side. An osmotic pressure gradient is generated, which leads to a positive slip coefficient and a resulting flow of the fluid towards higher glucose concentration (negative slip velocity). This flow arises to balance the pressure difference, which propels the particle in the opposite direction (towards low glucose concentration). Figure 93C illustrates the fluid flow from the reference frame of the particle, i.e. how the particle “sees” the fluid motion around it.

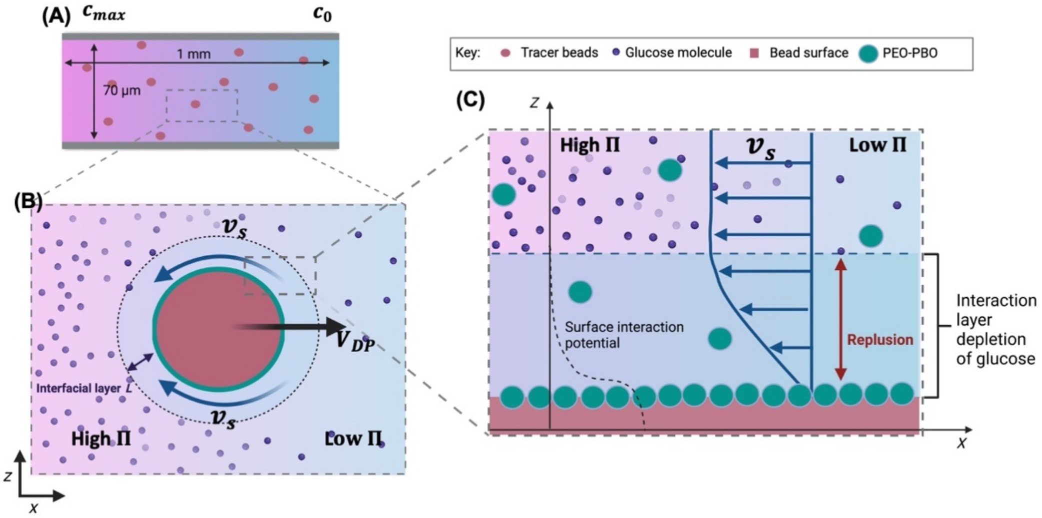

Figure 93. Illustration of diffusiophoretic motion of (A) tracer beads in the presence of PEO-PBO. within a glucose gradient. (B) The surface of the beads is coated with PEO-PBO nanovesicles which in turn induce a repulsive interaction potential with glucose (purple circles). (C) This leads to a depletion of glucose concentration at the interaction layer close to the surface of the beads. To balance the osmotic pressure, fluid flows towards the high glucose concentration (a slip velocity, v_s), forcing the tracer bead to move in the opposite direction (towards low glucose concentration) at a velocity V_{DP}.

Both the DO and DP phenomena are essentially owed to the interaction of the solute and the surface (either the walls of the channel or the surface of the beads). Changes in the slip velocity (in DP and DO) could be attributed to changes in osmotic pressure in the interfacial layer due to surface interactions, Eqn. **(5)**. Since the glucose concentration gradient is maintained throughout these experiments, no change in the externally applied osmotic pressure contribution is expected ($\frac{d\Pi}{dx}$). Hence changes in slip velocity are a result of the influence of the PEO-PBO on the surface's interaction with the glucose. This could be due to the adsorption of the PEO-PBO vesicles on both the surfaces (walls of the channel and beads surface). In this case, both the channel wall and the surface of the beads correspond to the repulsive interaction of glucose with PEO-PBO.

These results are interesting as measurements of diffusioosmotic flow are inevitably measurements of the interaction potential. In the case of electrolytes, interaction potential with charged surfaces is essentially an electrostatic interaction potential that can effectively be measured by the zeta potential (such as by DLS).[174] However, interaction potentials of nonelectrolyte solutes and uncharged surfaces are typically a challenging task to measure. Hence this method is a means to measure interaction potentials of nonelectrolyte solutes.

7.5 Liposome interaction potential with glucose.

The final type of nanovesicle to investigate are the liposomes. The experimentally extracted velocity profiles are plotted along the heights of the channel, Figure 94A. The slip velocity displays a drift towards low glucose at all heights of the channel, with a maximum velocity of 1.0 μms^{-1} at around the middle of the channel. The shape of the profile is different than that previously observed diffusioosmotic fluid flow at this glucose concentration Figure 86. However, it is similar to that obtained due to the addition of PEO-PBO nanovesicles, Figure 91. From this, both the diffusioosmotic and diffusiophoresis components velocity profiles are isolated.

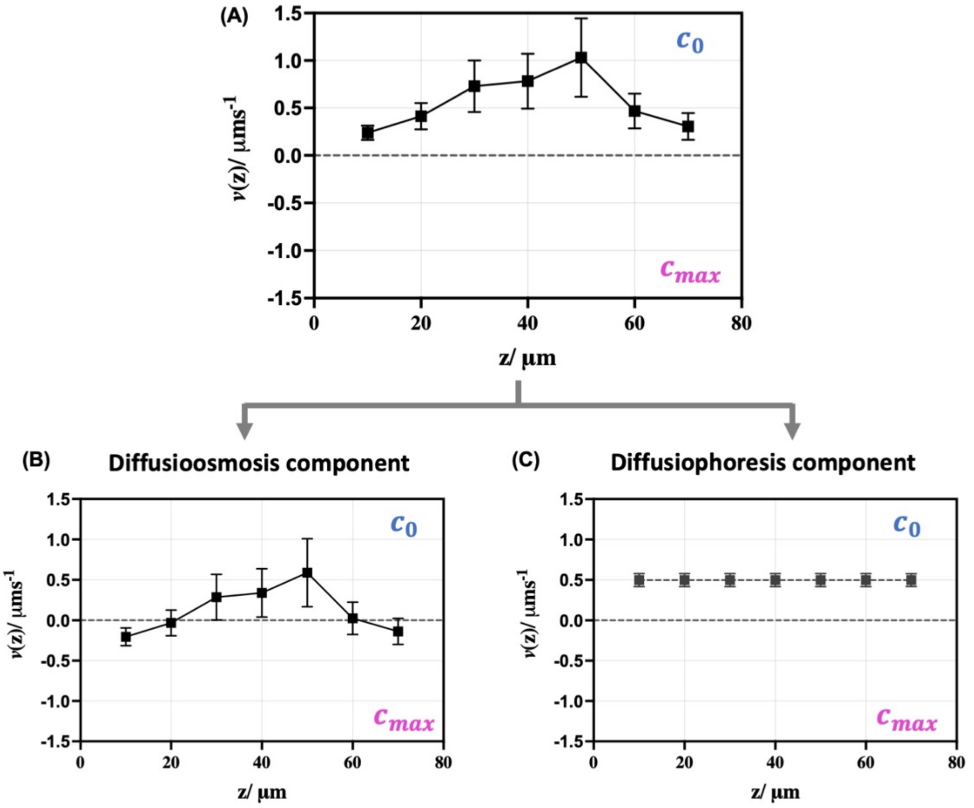

Figure 94. (A) The velocity profile of the tracer beads in the presence of liposomes within a 50mM/mm glucose gradient. From this, both the (B) fluid flow (diffusioosmosis) and (C) bead's migration (diffusiophoresis) velocity profiles are isolated.

This is also similar in shape and directionality to the flow profile due to the addition of PEO-PBO nanovesicles, Figure 91. The shape suggests that the fluid flow is driven by diffusioosmotic flow. From the change in directionality of flow when compared to the theoretically predicted profile, it is possible to infer that glucose-liposome interaction is repulsive. The velocities of the profile are comparable to that obtained for the PEO-PBO system, with a maximum speed of 0.5 µms^{-1}. This repulsive interaction can also be inferred from the diffusiophoresis of the beads, which migrate towards the low glucose concentration, as a direct result of the induced fluid flow towards the high glucose. Without the presence of any nanovesicles, the beads do not display any diffusiophoresis indicating a weak interaction potential of the amine modified surface with glucose. When liposomes are added, the surface-solute interaction is altered, which is most likely a result of the adsorption to the wall. However, no independent methods have been performed to verify the adsorption.

The diffusiophoresis velocity is 0.4 μms^{-1}, which is comparable to the velocity of beads due to the PEO-PBO addition. We can infer from both the diffusioosmotic flow and the diffusiophoresis migration of the beads that the interactions of both the PEO-PBO polymersomes and the liposomes are repulsive to glucose, and it also seems from the velocities that the magnitude of the repulsive interaction is similar.

7.6 Conclusion

In the attempt of reducing the speed of convective flows produced by the glucose gradient, the flow shifts from being convection dominated to diffusioosmosis dominated. This is in agreement with previous results.[10] While the diffusioosmotic fluid flow is slower than that previously reported by convection, its introduced its own challenges towards chemotactic characterisation. This work has evidenced that the mere addition of nanovesicles affects the diffusioosmotic fluid behaviour. Hence further investigation was conducted to evaluate the effect of the different types of nanovesicles on it. It has been shown that the PMPC-PDPA nanovesicles suppress the diffusioosmotic fluid flow completely, while the addition of PEO-PBO or liposomes completely reverses the direction of the flow. Moreover, the addition of the nanovesicles affected the DP migration of PS beads. The difference in the slip velocity of the flow is summarised in Table 4. I hypothesis that due to the addition of the nanovesicles to this system, their adsorption at the walls of the microfluid channel and the tracer beads surface results in the modification of the glucose-surface interactions and thus the diffusioosmotic fluid flow and diffusiophoretic motion.

The DO flow is a consequence of the surface-solute interactions. Hence it can be used as a sensitive tool to quantify these interactions. This is a powerful concept as it is difficult to predict the interaction potential between a combination of non-electrolyte solutes and a surface, let alone estimate the DO speed. The use of this observable property (DO and DP) to estimate the interaction strength between surface-solute has been employed to measure zeta potential between electrolyte and charged surfaces.[174] To the best of our knowledge, this is the first characterisation of the nonelectrolyte glucose interaction potential with nanovesicle through DO, and DP measurements, the nature of the interaction potentials are summarised in Table 4.

Table 4. A summary of the slip velocity of the Diffusioosmotic driven flow due to the interaction of glucose with ibTreat coating, PS beads, PMPC-PDPA polymersomes, PEO-PBO polymersomes or Liposomes. The directionality of the slip velocity provides insight into the nature of interaction potential between them, positive being away from the glucose and negative being towards the glucose.

Interaction of glucose	Slip velocity	Nature of interaction potential
ibTreat coating	0.5 μms^{-1}	Attractive
PS beads (1μm)	0 μms^{-1}	No interaction
PMPC-PDPA	0 μms^{-1}	No interaction
PEO-PBO	-0.5 μms^{-1}	Repulsive
Liposomes	-0.4 μms^{-1}	Repulsive

To account for these DO fluid flows when studying chemotaxis, the velocity profiles attained for each type of nanovesicle will be used in the next chapter to access the movement of the nanovesicles themselves within this background DO flow.

CHAPTER EIGHT

CHEMOTAXIS & DIFFUSIOPHORESIS OF VESICLES AT THE NANOSCALE

8.1 Diffusiophoretic behaviour of polymersomes in a glucose gradient.

To investigate the motility of polymersomes, their behaviour within a 50 mM/mm concentration gradient was observed. Here the experiments are conducted in the absence of tracer beads and the nanovesicles are imaged and tracked, for further information, refer to chapter 2. Due to the nano-size of these vesicles, they were much more difficult to image compared to the larger micron-sized PS beads. The focus of this section is to evaluate the behaviour of the empty polymersome systems; pristine PEO-PBO, pristine PMPC-PDPA and bi-component PMPC-PDPA+PEO-PBO. Six independent replicates of the experiment were performed for each sample, to develop a velocity profile to evaluate the polymersome behaviour.

Firstly, let's consider the pristine empty PEO-PBO polymersomes. Based on the findings in chapter 7, I hypothesised that the glucose-PEO-PBO interaction is repulsive, therefore I expect that PEO-PBO polymersomes themselves would undergo diffusiophoresis migration towards low glucose. The experimentally tracked polymersomes were used to develop a velocity profile within the channel shown in Figure 95.A. Due to the limited working distance of the 63x magnification lens used to image these nano-sized vesicles, the polymersomes could only be imaged up to halfway into the chamber. Hence velocity profiles are constructed from a height of 10 to 30 μm into the chamber. The experimentally observed average velocities from 10 to 30 μm are -0.14 ± 0.03, 0.13 ± 0.09 and 0.12 ± 0.02 μms^{-1} in which the error bars represent the standard deviation across six replicates.

From the previous analysis of the background fluid flow, a diffusioosmotic driven flow due to the repulsive interaction of the adsorbed PEO-PBO and glucose was identified, Figure 91C. To isolate the motion of the polymersomes themselves, the background fluid flow is subtracted from the experimentally observed movement of the polymersomes at each height in the velocity profile. This reveals the velocity profile of the diffusiophoretic motion of the PEO-PBO polymersomes, Figure 95B. The velocities are 0.15 ± 0.16, 0.21 ± 0.17, 0.05 ± 0.19 μms^{-1} from 10 to 30 μm respectively. This indicates a diffusiophoresis of the empty PEO-PBO polymersomes towards low glucose concentration. This is the expected motion induced by the repulsive interaction of the PEO-PBO and glucose. When analysing such nanovesicles caution needs to be taken during analysis not to confuse this diffusiophoretic motion with chemotaxis. In fact, due to the high water permeability of PEO-PBO, osmophoresis could be another contributor to this motion, however, we also expect PBO to be more permeable to glucose.[175] Osmophoresis is the movement of particles in a concentration gradient due to the difference in osmotic pressure inside and outside a vesicle with a semipermeable membrane.[176] Like diffusiophoresis, osmophoresis is driven by an externally applied gradient. At this point, it is not possible to distinguish whether this motion is solely diffusiophoresis or includes an osmophoresis component. Nevertheless, for what concerns this project, the emphasis is on trying to identify chemotaxis, which this motion is not.

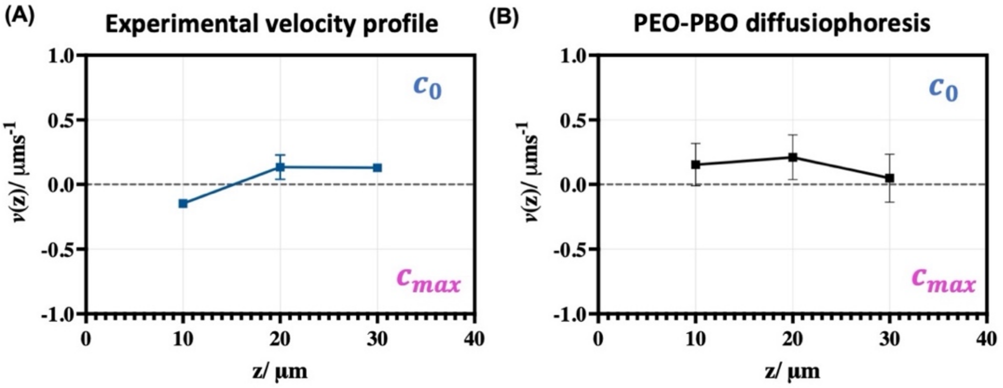

Figure 95. (A) The raw velocity profile obtained experimentally of the empty PEO-PBO polymersomes within a glucose gradient. From this, the background diffusioosmotic fluid flow is subtracted to obtain a (B) profile of the diffusiophoresis of the polymersome itself.

The previous chapter suggests that the glucose and PMPC-PDPA interaction is very weak, so I anticipate no motion for the PMPC-PDPA polymersome. The velocity profile of the experimentally tracked pristine PMPC-PDPA polymersomes, is displayed in Figure A. 2. This is the raw profile obtained experimentally which displays average velocities of 0.032 ± 0.001, 0.041 ± 0.001, 0.032 ± 0.004, 0.062 ± 0.004 μms^{-1} from 10 to 40 μm respectively. These velocities fluctuate about zero underlying an ideal nondirectional Brownian motion of the polymersomes. As seen before, the presence of PMPC-PDPA in the channel suppresses any diffusioosmotic fluid flow, Figure 88D. Subtracting this negligible background flow leaves us with a diffusiophoretic velocity profile of the PMPC-PDPA polymersomes,

Figure 96. The PMPC-PDPA does not undergo any diffusiophoresis behaviour within this glucose gradient.

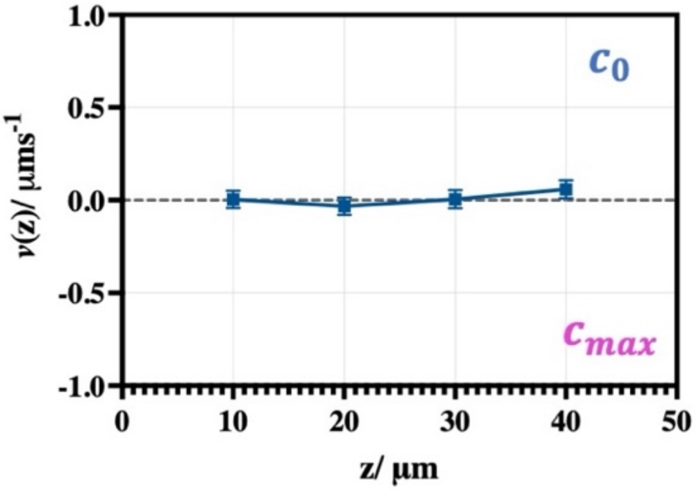

Figure 96. The diffusiophoretic velocity profile of the pristine PMPC-PDPA within a 50 mM/mm glucose gradient.

These findings show the difference in slip velocity of the PMPC-PDPA and PEO-PBO in the glucose gradient (indicated by the DO and DP), which suggest that the combination of these two copolymers on the surface of a single polymersome (i.e., the bicomponent system) would be advantageous in breaking the random directionless motion of the polymersome, by introducing an asymmetric distribution of slip velocity within the polymersomes surface. Hence further supporting the choice of these copolymers to achieve chemotactic motion.

Next let's investigate the behaviour of the empty bicomponent PMPC-PDPA+PEO-PBO polymersomes in 50 mM/mm glucose gradient. In this case, both the experimentally observed velocity profile and the DP (diffusiophoretic) profile of the bicomponent polymersomes fluctuate about zero, Figure 97, Figure A. 3. Despite the presence of the PEO-PBO domain on the membrane, these polymersomes maintain a negligible net slip velocity within a 50 mM/mm glucose gradient. The absence of the underlying fluid flow or diffusiophoresis of the empty polymersome itself is an advantageous property of the PMPC-PDPA based polymersomes which will allow for better evaluation of any chemotactic motion. These profiles lay the fundamental control observations of the empty polymersomes, in the next section I compare these profiles with those obtained from the glucose oxidase encapsulated polymersomes.

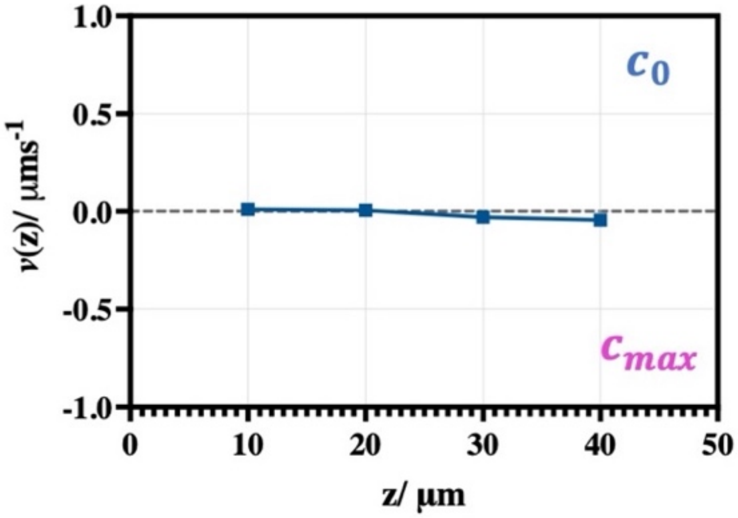

Figure 97. The diffusiophoretic velocity profile of the pristine PMPC-PDPA+PEO-PBO within a 50 mM/mm glucose gradient.

8.2 Chemotactic motion of polymersomes in glucose gradient

Now that we have established the diffusiophoretic motion of the polymersomes in a glucose gradient, solely on the glucose-copolymer interactions. This section focuses on exploring the motion of the enzyme loaded polymersome prepared in Chapter 5. The first polymersome to look at is the glucose oxidase loaded PEO-PBO polymersomes. The experimentally obtained velocity profile is displayed in Figure A. 4. This displays an increase in the velocity of the polymersomes from 0.053 ± 0.006 µms^{-1} at 10 µm to 0.365 ± 0.011 µms^{-1} at 30 µm. When subtracting the underlying diffusioosmotic fluid drift at these heights the revealed migration velocities of the GOX loaded are 0.354 ± 0.164 µms^{-1} and 0.284 ± 0.184 µms^{-1}, as shown in Figure 98. This identifies a consistent migration of GOX loaded PEO-PBO polymersomes towards low glucose at a velocity ranging from 0.18 to 0.35 μms^{-1}.

When compared with the diffusiophoretic motion of the empty PEO-PBO polymersomes, the encapsulation of the GOX enzyme seems to slightly increase the velocity of the polymersomes towards the low glucose concentration. While the difference between the two velocities is low, the consistent increase along the heights of the channel could suggest a chemotactic influence. Nevertheless, the difference between the data is within error bars, with no statistically significant difference, which could suggest that the incorporation of GOX does not change the migration velocity of the PEO-PBO polymersomes. This directionality could be largely attributed to the repulsive interaction of the glucose and the PEO-PBO polymersomes themselves. However, further investigation into the significance and nature of this propulsion needs to be conducted.

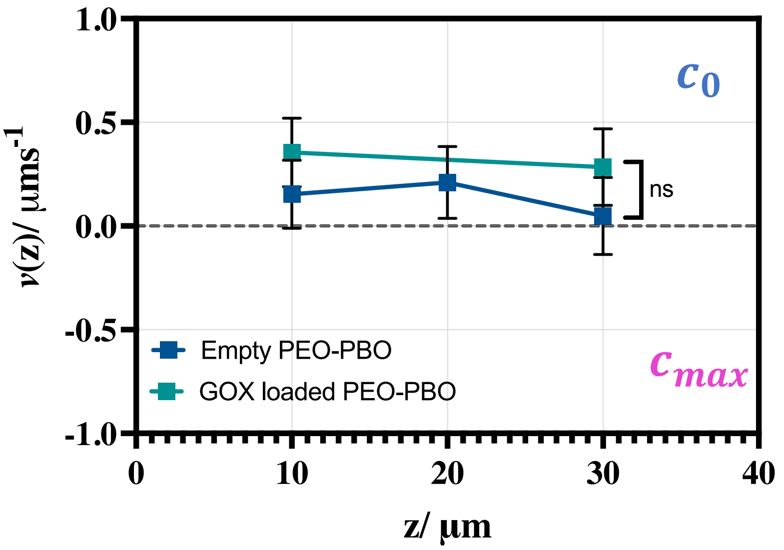

Figure 98. The velocity profile of the GOX loaded PEO-PBO polymersomes (Teal green) within a 50 mM/mm glucose gradient compared to the empty PMPC-PDPA (Blue).

Next, let’s explore the behaviour of the GOX loaded pristine PMPC-PDPA polymersomes, Figure 99. The experimentally observed profile displays a minimal fluctuation of velocity around zero with a minimum velocity of -0.02 ± 0.002 μms^{-1} and a maximum velocity of 0.08 ± 0.004 μms^{-1}, Figure A. 5. Subtracting the background fluid flow exposes the motion of the polymersomes, Figure 99. These polymersomes display typical directionless Brownian motion, which is comparable to that of the empty PMPC-PDPA polymersomes and effectively zero. From chapter 5, we have demonstrated that in a homogenous environment of glucose the GOX loaded pristine PMPC-PDPA system is capable of sensing the surrounding glucose. However, the lack of directed motion in a glucose gradient indicates that the encapsulation of the GOX enzyme alone is not sufficient to facilitate chemotaxis motion.

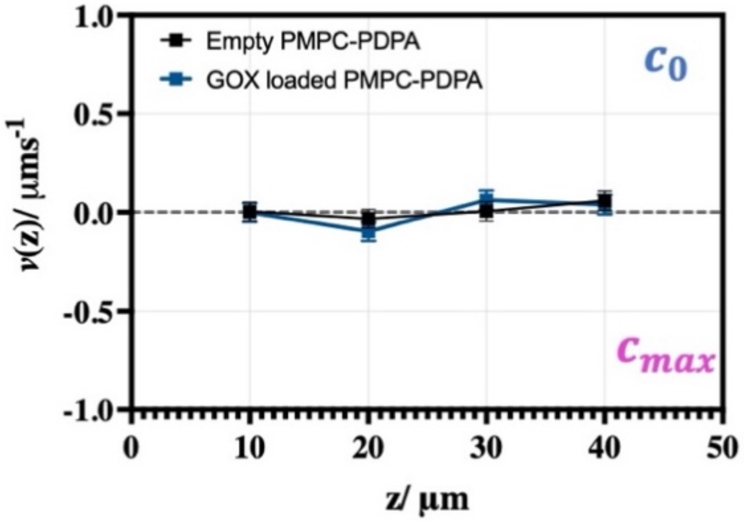

Figure 99. The diffusiophoretic velocity profile of the GOX loaded PMPC-PDPA polymersomes (Blue) within a 50 mM/mm glucose gradient compared to the empty PMPC-PDPA (Black).

The final polymersome system is the bicomponent system. The experimentally obtained velocity profiles display migration of the polymersomes towards the glucose with increasing speeds deeper into the channel, Figure A. 6. The minimum velocity is -0.14 ± 0.003 μms^{-1} at 10 μm and a maximum velocity of -0.341 ± 0.002 μms^{-1} at 40 μm. Since these polymersomes generate a minute background fluid flow, the migration velocity profile of these polymersomes remains consistently migrating towards the high glucose concentration, Figure 100. Compared to the velocity profile of the empty bicomponent (PMPC-PDOA+PEO-PBO) the directional motion of the GOX loaded bicomponent (PMPC-PDPA+PEO-PBO) is obvious, and statically significant ($p<0.001$). This shows that the glucose oxidase enzyme encapsulation is a facilitator of this motion. In addition, from comparison to the velocity profile of the GOX loaded pristine PMPC-PDPA, the change from a random Brownian motion to a directional motion is clear and statically significant ($p<0.001$). This data also highlights that in order to observe directional motion of a polymersome towards glucose, the polymersome needs to have an asymmetric surface and it must encapsulate the enzyme.

This data shows a chemotactic propulsion of the polymersomes at a speed of 0.35 μms^{-1} towards glucose. While this value seems small compared to the convection speeds we have come across, it is imperative to appreciate that these nanoscopic polymersomes (about 50 nm in diameter) are propelling at a speed that is about 6 times per second their size.

These findings also emphasise the important aspects associated with characterising chemotaxis: the isolating of the underlying fluid flow and the isolation of the diffusiophoretic migration of the nanoparticle themselves. This is of extreme importance as a chemotactic migration of about 0.35 μms^{-1} can be overshadowed by strong convective flows (for instance 40 μms^{-1} in the NTA) or diffusiophoretic migration due to the attractive or repulsive interaction of the nanoparticle to the gradient itself (the repulsive diffusiophoresis of PEO-PBO).

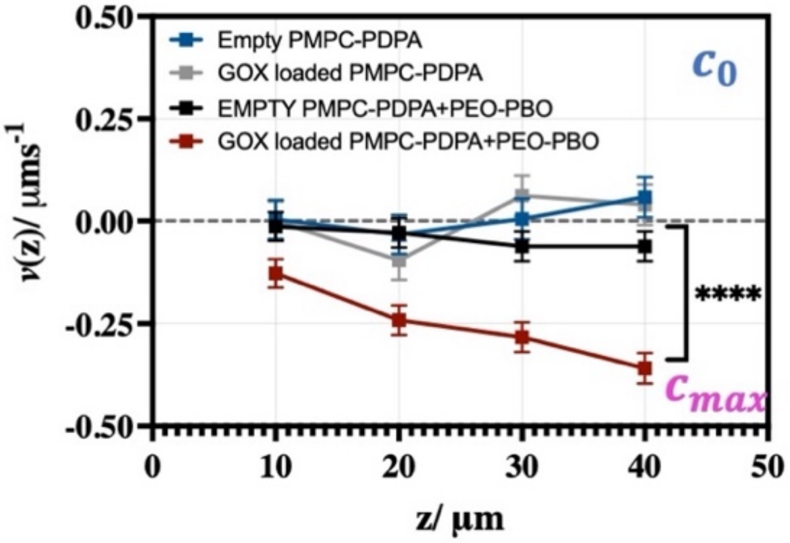

Figure 100. The extracted migration velocity profile of the GOX loaded PMPC-PDPA+PEO-PBO polymersome (Red) which is compared to the empty PMPC-PDPA+PEO-PBO (Black), empty PMPC-PDPA (Blue) and GOX loaded PMPC-PDPA (Grey) within a 50 mM/mm glucose gradient.

8.3 Liposomes

From the polymersome findings, we can recognise that the chemotaxis at the nanoscale could be as small as 0.3 μms^{-1} and that, unlike the PMPC-PDPA polymersome system, the liposomes produced an inherent diffusioosmotic fluid flow that can be as strong as 1 μms^{-1}, Figure 94. This DO flow is not only strong but changes in magnitude and direction at different heights of the channel. Hence, this experiment was conducted differently, in which a specific height within the channel was chosen and monitored over time. At 35 μm within the channel, the diffusioosmotic fluid flow was recorded from 5 minutes to 20 minutes after establishing the glucose gradient, over 5-minute intervals.

To commence, the change in DO and DP as a function of time was investigated, Figure 101. This was achieved by tracking bead tracers at a height of 35 μm for 30 minutes at 5-minute intervals. What we observe is an increase in the velocity of the beads from 0.290 ± 0.03 to 0.645 ± 0.047 μms^{-1} from 5 to 15 minutes, after that the velocity is constant at around 0.6 μms^{-1} up to 30 minutes. From previous velocity profiles it was evident that the beads experience both a diffusioosmotic fluid drift and a diffusiophoretic migration. The diffusioosmotic fluid flows towards the high glucose concentration at the walls of the channel and away from glucose at the middle of the channel. The beads diffusiophoresis towards the low glucose concentration at a constant velocity of 0.4 μms^{-1}. In addition to these two phenomena affecting the migration of the beads within the heights of the channel Figure 101, shows a time dependent component affecting the movement at the short time scale (between 5 to 10 minutes). This could be the time delay due to the adsorption of the liposomes onto the surface of the channel and the beads.

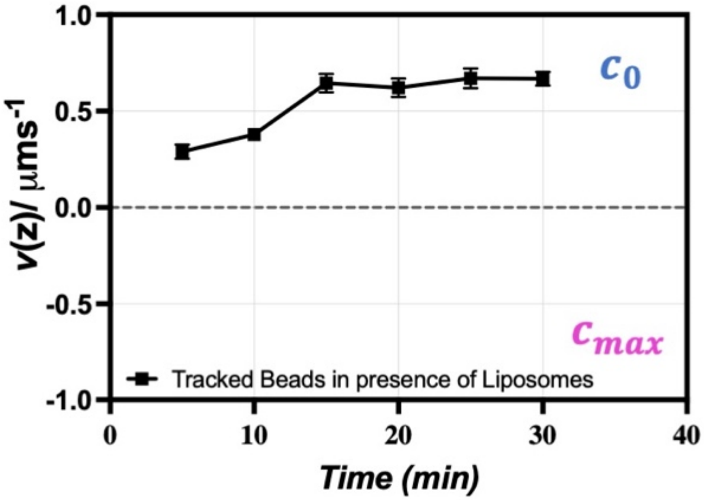

Figure 101. Velocity as a function of real time (minutes) plots of the tracked beads in the presence of liposomes within a 50 mM/mm glucose. The profile is measured at a height of 35 μm from the bottom of the channel. The error bars represent the standard deviation across six independent replicates.

Owing to the threefold complexity of the liposome system, chemotaxis was investigated as the difference in migration velocities of the modified liposomes to the pristine empty liposome system. Figure 102A, shows the experimentally obtained velocity vs time plots of each of the four liposome systems. All the liposomes systems follow the general trend of increase in velocity away from glucose with experimental time reaching a maximum velocity of 0.60 ± 0.007 μms^{-1}, 0.45 ± 0.03 μms^{-1}, 0.42 ± 0.014 μms^{-1} and 0.22 ± 0.01 μms^{-1} at 20 minutes for the empty pristine liposomes, empty porated liposomes, GOX loaded pristine liposomes, GOX loaded porated liposomes respectively. This consistent movement away from glucose is a direct result of the diffusioosmotic flow generated within the channel due to the glucose-liposome interaction potential, Figure 94. From Figure 102A, it can be seen that the empty porated and GOX loaded pristine liposomes show a slight distinction compared to the empty liposome plot. However, a larger, more obvious reduction in velocity can be seen for the GOX loaded porated liposome which is consistent at all time points after 10 minutes. This is an indication of a reduced migration of the liposomes away from the glucose.

To better evaluate the distinctions in behaviour of the liposomes systems, the difference in velocities between the empty pristine liposome and each of the three modified liposome systems are calculated, Figure 102B. These show a consistent increase in the velocity of the GOX loaded porated liposome towards glucose, with a maximum of 0.38 ± 0.014 μms^{-1} at 20 minutes after the gradient is established (red plot). The difference between the empty pristine liposomes and the empty porated liposomes (grey plot) is statistically significant ($p<0.0001$). The velocities fluctuate around zero, that could indicate a possible influence of the poration on the migration of the liposomes. This could be an influence due to changes in the generated diffusioosmotic flow, diffusiophoretic or even osmophoric migration of the liposomes. In either case, this difference is not chemotaxis as no enzyme is encapsulated and further investigation is needed to be conducted to explore the significance and nature of this difference.

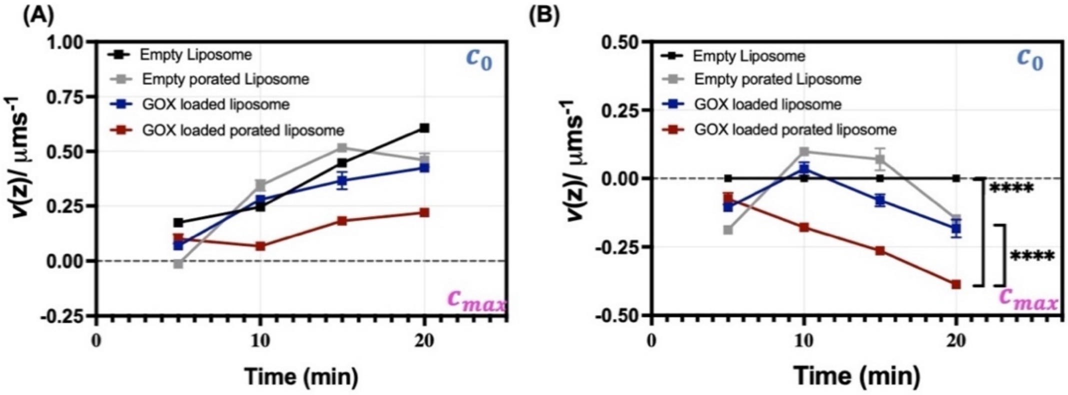

Figure 102. (A) The experimentally obtained velocity vs time plots at 35 μm from 5 to 20 minutes of empty pristine liposomes (Black), empty porated liposome (grey), GOX loaded pristine liposomes (blue) and the GOX loaded porated liposomes (red). (B) The difference in velocity of the empty pristine liposome to each of the porated liposome, GOX loaded pristine and GOX loaded porated liposome. The error bars represent the standard deviation of the six replicates.

In the case of the GOX loaded pristine liposomes (blue), the difference in velocities is very similar to that observed for the empty porated liposomes. In fact, there is no statistically significant difference between these two velocity profiles. However, it is only by combining both the poration and the GOX encapsulation that a large distinctive difference in velocities is observed. These polymersomes display a consistent reduction in velocity (i.e. moving more towards glucose) that shows a statically significant difference from all the other three velocity profiles (p<0.0001). This difference can be attributed to the chemotactically facilitated motion of these liposomes up the concentration gradient and in this case against the diffusioosmotic fluid flow. However, it should be noted that this conclusion is weaker than that drawn for polymersomes because the evidence is not so clear. This is most probably influenced by an inherent diffusioosmotic flow that is generated in the liposome system which is not present for the PMPC-PDPA based polymersome.

These findings are the first step towards accurate measurements of chemotactic motion in synthetic nanovesicles, by separating this motion from other nanoparticle induced motion (be phoresis of the nanovesicles or the fluid flow). Further investigations and experiments, in particular into the physical theory of chemotactic propulsion mechanism, will led to more inclusive understanding of this work.

8.4 Conclusion

The results discussed in this chapter demonstrate the possibility to create self-propelling systems that can chemotactically propel as a result of the encapsulation of enzymes and using asymmetric nanovesicle surfaces. The careful isolation of this chemotactic motion from other phenomenon led to an accurate and rigorous measurement of this chemotactic motion at the nanoscale. In particular, DP migration which can be confused for chemotactic motion of nanovesicles, this was observed in the case of PEO-PBO or liposomes and isolating it is imperative. Fluid flows are another factor that needs to be isolated before drawing conclusions on chemotactic motion such as convective or diffusioosmotic flow which can overshadow or alter measurements of chemotactic motion at the nanoscale. In addition, the small size of the vesicles made confocal imaging a very challenging task due to the quick diffusion of the vesicles out of plane.

This work makes for the first measurement of chemotactic motion of nanovesicles in the world. Effectively proving that for both polymersomes and liposomes combining surface asymmetry and an encapsulated enzyme can result in a new component of motion which is directed motion towards glucose sources, thus achieving chemotaxis.

CHAPTER NINE

CONCLUSIONS AND FUTURE WORK

This chapter summarises the key findings of this thesis. The findings from each chapter are discussed in turn and future research areas inspired by this work are proposed.

9.1 Self-assembly of modified nanovesicles

In this thesis, ten nanovesicles systems are synthesised and modified by applying the minimal criteria from active matter research to attain self-propelling nanovesicles. The two modified systems are PMPC-PDPA polymersomes and liposomes. The modifications involve the incorporation of an asymmetry within the membrane of the nanovesicle followed by the encapsulation of an enzyme.

9.1.1 Membrane asymmetry

Introducing membrane asymmetry in the PMPC-PDPA polymersomes was achieved by incorporating a PEO-PBO copolymer on the bilayer membrane which would phase separate to form a PEO-PBO domain within a majority-PMPC-PDPA matrix. In chapter 4, the preparation method of these bicomponent polymersomes was optimised and their physicochemical properties studied by DLS and TEM. The sample was prepared using the solvent switch method to attain a monodisperse sample of 50 nm-diameter polymer vesicles. The bicomponent system shows phase separation of the co-polymers on the surface yielding a PEO-PBO domain on the membrane. In addition to the asymmetric polymersomes, PMPC-PDPA symmetric polymersomes were also formed. The second system is the liposome. The asymmetry was achieved by porating 100 nm diameter liposomes by α-hemolysin, following the method first reported by L. Song *et al.* [135]

9.1.2 *Enzymatic encapsulation*

Glucose oxidase was encapsulated into the bicomponent polymersomes using electroporation. The encapsulation resulted in the loading of around 6 enzymes per polymersome. In addition to the bi-component polymersomes, pristine single-component PMPC-PDPA polymersomes and PEO-PBO polymersomes were prepared as controls. The encapsulation yielded an average of 6 glucose oxidase enzymes per PMPC-PDPA polymersome and 8 glucose oxidase enzymes per PEO-PBO polymersome. Finally, 16 glucose oxidase enzymes are loaded per liposome.

9.1.3 *Future work I: Reproducibility of self-assembly*

One of the biggest hurdles in nanomedicines is reproducibility, and the bicomponent polymersomes are no exception. Despite the low polydispersity of the prepared sample, it contains both asymmetric (phase-separated PMPC-PDPA + PEO-PBO) polymersomes and symmetric (PMPC-PDPA) polymersomes. Within the same sample the phase-separated PMPC-PDPA + PEO-PBO can exhibit one or two PEO-PBO domains. The results have demonstrated that the abundance of these polymersome classes vary between different replicates.

As this is the first reported PMPC-PDPA + PEO-PBO bicomponent system prepared by solvent switch, further evaluation as to the reproducibility between different polymer batches and investigators is essential. This would provide insight into the control of the yield of phase separated polymersomes. This highlight areas of future research into phase separation of copolymers within a nanosized membrane.

This reproducibility issue can be approached by implementing automated nanoparticle production methods driven by robotic platforms that have been shown to reliably optimise conditions to produce a variety of nanoparticles.[177] Coupling automated sample production with automated image acquisition and morphology detection would provide the ability to screen large number of self-assembly methods and copolymer batches for the desired particle size and morphology.[178]

Another possible approach is to purify the asymmetric from the symmetric polymersomes prepared during the self-assembly of the bicomponent polymersomes. An idea for achieving this is by increasing the amount of PEO-PBO copolymer to attain a larger PEO-PBO domain. By exploiting the possible variations in diffusiophoretic migration between the Brownian single component PMPC-PDPA polymersomes and the phoretic bi-component system within a glucose gradient, the bi-component polymersomes can be isolated due to their migration towards or away from glucose.

9.2 Phoresis characterisation

The first step to evaluating the sensitivity of the modified systems was by investigating their behaviour in a homogenous glucose environment. This was done by using the pH sensitive on/off assembly of the PMPC-PDPA polymersomes. The results show the disassembly of the glucose oxidase loaded polymersomes in response to the surrounding glucose environment as a consequence of the production of Gluconic acid, a by-product of the catalysis of glucose by glucose oxidase inside the polymersomes. This evidences the successful encapsulation of glucose oxidase enzymes into the polymersomes, the crossing of glucose from outside the polymersomes to inside the aqueous core where the enzymes are located and the maintained catalytic activity of the enzyme within the confined aqueous core of the polymersomes.

The next step is to investigate the ability of the system to sense and move within a glucose gradient. This led to uncovering and quantifying a variety of phenomena that can cause motion of the nanovesicles within this gradient. The first and the biggest challenge is the inherent convection flow driven by the glucose gradient itself. This motion of the fluid results in the drifting of the nanovesicles along with it. The convective flows have been quantified in the case of the NTA chambers to be as large as 50 μms^{-1} (and even potentially larger as a velocity profile in the NTA is unattainable) and as small as 1 μms^{-1} within the available ibidi μslide chemotaxis chambers. On further attempting to reduce the impact of the flow, i.e., reducing the speed of the moving fluid, the fluid flow shifted from being dominated by convection to dominated by diffusioosmosis. This flow had a maximum speed of 0.5 μms^{-1}. These flows are in agreement with previously reported work.[10] This was used as the basis of the work henceforth.

One of the key findings in this thesis is identifying that the mere addition of the nanovesicles to this glucose gradient changes the diffusioosmotic fluid flow. By exploring the influence of each nanovesicle on the diffusioosmotic fluid flow, it was seen that the empty PMPC-PDPA polymersome completely suppresses the flow while empty PEO-PBO polymersomes and liposomes reverse the directionality of the flow.

The diffusioosmotic fluid flow is a measurable consequence of the glucose-surface interaction. This gives insight into the nature of the interaction potential between the nonelectrolyte glucose and the nanovesicles. From the velocity profiles, it was possible to infer that the glucose interaction with PEO-PBO and the liposomes was repulsive while its interaction with the ibiTreat coating of the ibidi μslide chemotaxis chambers was attractive. The PMPC-PDPA polymersomes on the other hand, exhibited complete suppression of the diffusioosmotic fluid flow suggestive of negligible interaction potential between it and glucose.

9.2.1.1 Future work II: Interaction potential measurements of nonelectrolytes

Using a sensitive property like flow to quantify potential interactions is a very powerful concept. This is especially relevant in the case of non-electrolytes as it is difficult to predict the interaction potential between a combination of non-electrolyte solutes and a surface, let alone estimate the diffusioosmotic speed.[174] From a single measurement lasting less about 30 seconds the nature of the interaction potential can be identified (i.e., whether it is attractive, repulsive or weak). Future work can be conducted to allow for more reasonable deductions about the complete interaction potential. The applications of this extend from surface potential characterisation of small charged (like proteins) and noncharged particles (neutral nanoparticles), to routine analysis of stability of emulsions and even assessing dynamics of protein corona. [122, 179]

9.2.1.2 Future work III: Suppression of underlying fluid flow

An ideal chemotactic experimental setup for measuring any nanoparticle phoresis will not involve any background fluid flow. The convective fluid flow can be suppressed by using thinner fabricated microfluidic or even nanofluidic channels.[180] The fabrication of microfluidic channels can also allow for flexibility in the choice of surface chemistry which can be altered to reduce the interaction potential with the solute gradient of interest, hence supressing the diffusioosmotic flow.[181]

9.3 Chemotactic nanovesicles

After establishing the underlying fluid flow for each of the nanovesicles of interest, the last part of this thesis focused on evaluating the behaviour of the particles within this flow. This was achieved by subtracting the fluid drift from the tracked nanovesicle motion. In the case of empty pristine PMPC-PDPA, empty bi-component and glucose oxidase (GOX)-loaded pristine PMPC-PDPA, subtracting the drift displayed stochastic motion of these polymersomes. This indicated that the main contributor to the motion is Brownian motion, which is superimposed over a directed fluid drift. The results showed that the GOX loaded bicomponent (PMPC-PDPA+PEO-PEO) exhibited chemotactic motion towards high glucose gradient. This data clearly suggests that the combination of both the enzyme and the asymmetry are essential in facilitating chemotactic motion.

The final modified system investigated is the liposome system, in this case a strong diffusioosmotic fluid flow and diffusiophoretic migration of the liposomes was observed away from the glucose. In the case of the empty pristine, empty porated and GOX loaded pristine liposomes, the diffusional behaviour of the particles is comparable indicating no significant changes in migration. However, the glucose oxidase loaded, porated liposomes displayed a reduction in the velocity away from the glucose. This corresponded to a difference of 0.3 $\mu ms^{-1.}$ towards the high glucose concentration. These results show the chemotactic behaviour in both the polymersome and liposome system, although results for polymersomes are stronger.

9.3.1 Future work IV: Translation to delivery systems

This work has demonstrated the minimal requirements to attaining a chemotactically driven nanovesicle. Due to the polymersomes' and liposomes' versatility, a variety of different enzymes, or combinations of enzymes, can be explored in future work to allow for chemotactic response to different substrates. This could have great future applications in targeted drug delivery or in diagnostics.[120] The chemical versatility of these nanovesicles can be used to attach targeting moieties on their surface such as protein ligands to increase the specificity of drug delivery.[182]

Transforming the demonstrated chemotactic motion into an *in-vivo* delivery system opens doors to a large array of potential future work. The biggest of which, highlighted by the data from this thesis, is the influence the presence of copolymers or nanovesicles have on the diffusiophoretic migration and surrounding diffusioosmotic fluid flow. This brings to light the challenges that protein corona within the blood, in which proteins adsorbed onto the nanoparticles surface[122], would have on the phoresis of these particles. This could be investigated by analysis of the movement of the nanovesicles in complex environments such as gels and blood plasma. Another necessary area of investigation is to towards a better understanding the self-propelled mechanism of chemotactic nanovesicles and collective motion within crowded environments.[183]

9.4 Conclusion

The novelty of this project is twofold, the first is in identifying and isolating chemotactic motion from other phenomena that govern motion of nanovesicles within a glucose gradient. The second is in identifying the importance of surface-solute interactions, in particular is how the surfaces can be modified in multi-component mixtures to lead to an unexpected behaviour such as the reversal or suppression of diffusioosmosis flow when polymersomes are added. It starts by showing that it is possible to create bio-compatible, non-immunogenic and nanosized nanovesicles capable of self-phoresis using enzymes, asymmetry, and presence of a gradient (active particles). This work was then able to identify the convective flows created by the glucose gradient which overshadow and lead to overestimation of chemotactic velocities if not carefully isolated. In fact, these results have shown a variety of other phenomena that can affect the motion of nanovesicles in a microfluidic chamber: diffusioosmotic fluid flows and diffusiophoretic migration of particles. This was the case for PEO-PBO polymersomes and liposomes which displayed a diffusiophoretic behaviour in the glucose gradient solely based on the interaction of the nanovesicle surface and the glucose gradient.

This is significant as Brownian motion is widely used to describe the diffusive movement of particles in physical, chemical, and biological sciences. However, these findings show that Brownian motion alone cannot describe the motion of these particles when out-of-equilibrium, such as by the presence of chemical gradients. Chemical interactions in the gradient would lead to local fluid flows which induce movement in the passive particles. In fact, biological systems are far away from equilibrium, with a variety of physiological gradients created which are consistently varying and commonly present simultaneously. These generate huge possible out of equilibrium fluid flows, hence large deviation of movement not only by colloids but also proteins, viruses, and DNA. This not only sheds light on the non-equilibrium motion of passive particles but also reveals more generally how delicate the behaviour of these particles is and how they can be controlled.

Finally, a successful quantification of the magnitude of chemotactic motion of nanovesicles about 0.4 μms^{-1} within a 50 mM/mm glucose gradient was identified. This speed corresponds to moving a distance of 3-6 nanovesicle diameters per second. Additionally, the phoresis and fluid flow measurements inspire a whole range of future work, developments and possibilities for the use of flow measurements to identify non-electrolyte interaction potentials.

9.4.1 Outlook

While Einstein's theory of Brownian motion describes the movement of particles in a static fluid (or in equilibrium), in real-life the fluid moves and contain other particles and chemicals. This out-of-equilibrium state influences the movement of the particles. A passive particle is dragged by fluid movement and the interaction with chemicals can generate local fluid flows leading to the migration of the particles themselves. Both have been shown in this thesis for nanovesicles and polystyrene beads in a glucose gradient. However, this is only a very simple adaptation of a chemical gradient. In biology, a variety of physiological gradients are created and mostly present simultaneously. This would lead to the generation of huge possible local fluid flows and hence large diversity of the movement of passive particles. These findings are merely scratching the surface to potentially understanding the behaviour of passive particles like nutrients, DNA or viruses in real-life physical and biological environments.

APPENDIX

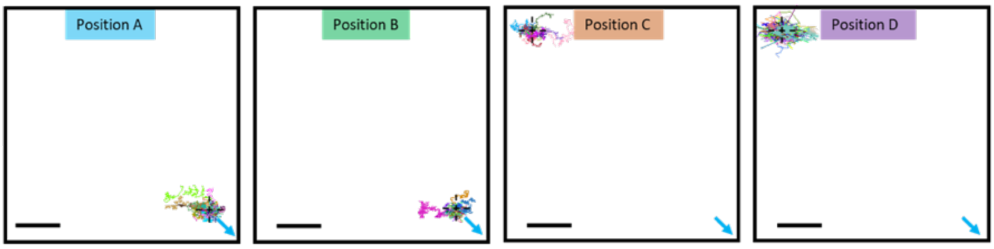

Figure A. 1. The NTA chamber mapping of the trajectories of empty when injected with PBS to show the similarity in behaviour through the mapped observation area.

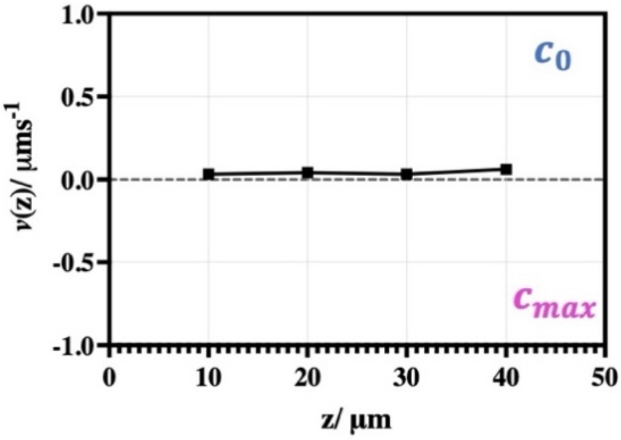

Figure A. 2. The experimentally obtained velocity profile of the pristine PMPC-PDPA within a 50 mM/mm glucose gradient.

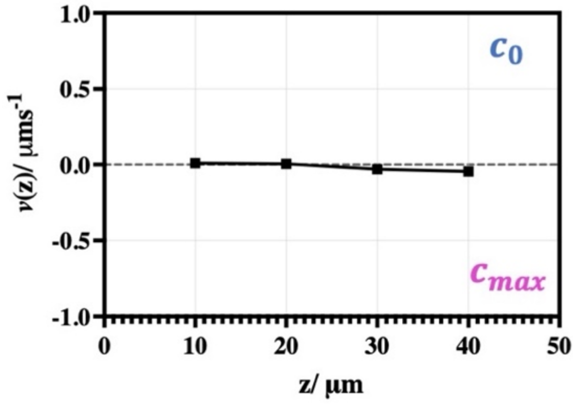

Figure A. 3. The experimentally observed velocity profile of the pristine PMPC-PDPA+PEO-PBO within a 50 mM/mm glucose gradient.

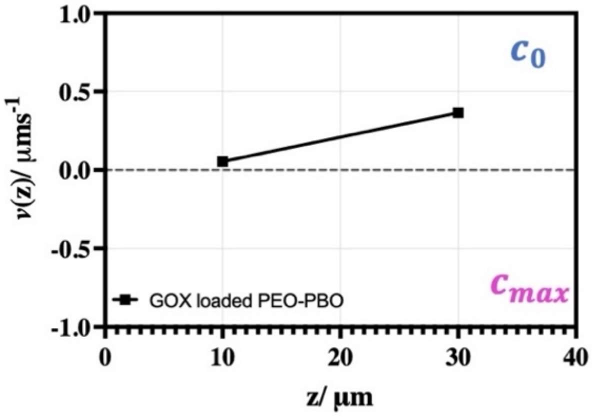

Figure A. 4. The experimentally obtained velocity profile of the GOX loaded PEO-PBO polymersomes within a 50 mM/mm glucose gradient.

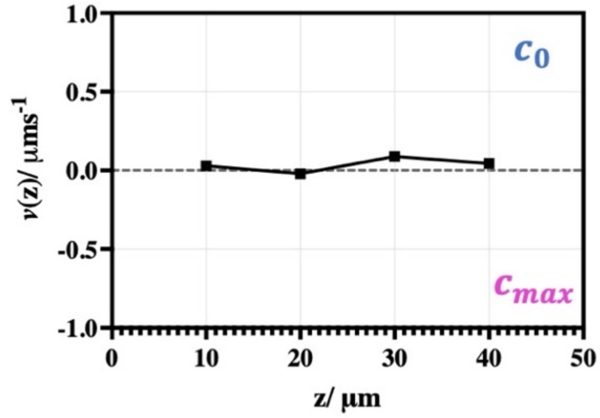

Figure A. 5. The experimentally obtained velocity profile of the GOX loaded PMPC-PDPA polymersomes within a 50 mM/mm glucose gradient

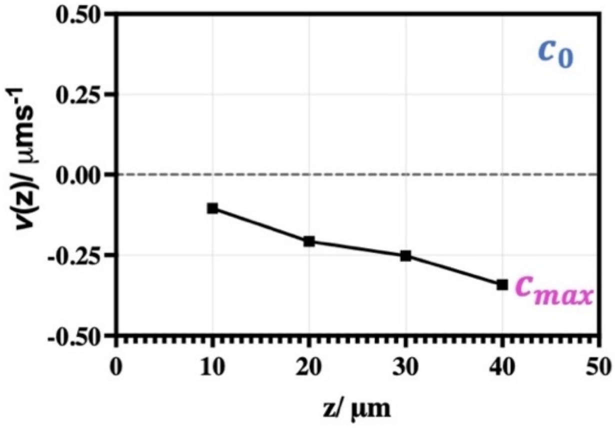

Figure A. 6. The experimentally observed velocity profile of the GOX loaded PMPC-PDPA+PEO-PBO within a 50 mM/mm glucose gradient.

BIBLIOGRAPHY

1. A. Kesselheim, T. Hwang and J. Franklin, *Nat Rev Drug Discov*, 2015, **14**, 815–816.
2. D. H. Wasserman, *Am J Physiol Endocrinol Metab.*, 2009, **296**.
3. C. W. Kuzawa, H. T. Chugani and L. I. Grossman, *Proc Natl Acad Sci.*, 2014, **111**, 13010–13015.
4. D. J. Begley and M. W. Brightman, *Prog. Drug Res.*, 2003, **61**, 40–78.
5. H. Koepsell, *Pflugers Arch – Eur J Physiol*, 2020, **472**, 1299–1343.
6. S. G. Patching, *Mol Neurobiol.*, 2017, **54,**, 1046–1077.
7. T. Patiño, X. Arqué, R. Mestre, L. Palacios and S. Sánchez, *Acc. Chem. Res.*, 2018, **51**, 2662–2671.
8. A. Joseph, C. Contini, D. Cecchin, S. Nyberg, L. Ruiz–Perez, J. Gaitzsch, G. Fullstone, X. Tian, J. Azizi, J. Preston, G. Volpe and G. Battaglia, *Science Advances*, 2017, **3**.
9. M. Riaz, *Pak J Pharm Sci.*, 1996, **9**, 65–77.
10. I. Williams, S. Lee, A. Apriceno, R. P. Sear and G. Battaglia, *PNAS*, 2020, **117**, 25263–25271.
11. V. L. Feigin and T. Vos, *Neuroepidemiology*, 2019, **52**, 1–2.
12. https://www.who.int/publications/i/item/9789241563369, Neurological Disorders: Public Health Challenges, (accessed 15/01/2021, 2021).
13. CDC, *National Center for Health Statistics. Health, United Sates*, 2015.
14. Alzheimer'sAssociation, *Alzheimers & Dementia*, 2013, **9**, 208–245.
15. J. A. Driver, G. Logroscino, J. M. Gaziano and T. Kurth, *Neurology.*, 2009, **72**, 432–438.
16. F. O. Walker, *Lancet*, 2007, **367**, 218–228.
17. S. V. Ramagopalan, R. Dobson, U. C. Meier and G. Giovannoni, *Lancet Neurol*, 2010, **9**, 727–739.
18. X. A. Behin, A.F. Carpentier, J.Y. Delattre, *Lancet*, 2003, **361**, 323–331.
19. S. Agnihotri, K. E. Burrell and A. W. e. al, *Arch. Immunol. Ther. Exp.*, 2013, **61**, 25–41.
20. P. S. A. Béduneau, J. Benoit, *Biomaterials*, 2007, **28**, 4947–4967.

21. R. K. Jain, *Adv Drug Deliv Rev.* , 2001, **1**, 149–168.
22. R. Stupp, W.P. Mason, M. J. v. d. Bent, M. Weller, B. Fisher and e. a. M.J. Taphoorn, *New Engl. J. Med.*, 2005, **352**, 987–996.
23. S. Senapati, A. K. Mahanta and S. Kumar, *Sig Transduct Target Ther* 2018, **3**.
24. N.J Abbott, A. A. K. Patabendige, D. E. M. Dolman, S. R. Yusof and D. J. Begley, *Neurobiol. Dis*, 2010, **37**, 13–25.
25. N. Abbott, L. Rönnbäck and E. Hansson, *Nat Rev Neurosci*, 2006, **7**, 41–53.
26. C. P. Profaci, R. N. Munji, R. S. Pulido and R. Daneman, *J Exp Med* 2020, **217**, 1–16.
27. L. N. Nguyen, D. Ma, G. Shui, P. Wong, A. Cazenave–Gassiot, X. Zhang, M. R. Wenk and a. D. L. S. E.L. Goh, *Nature*, 2014, **509**, 503–506.
28. S. W. Zhang., *Rev. Neurosci.*, 2010, **21**, 29–53.
29. W. M. Pardridge, *Mol. Interv.* , 2013, **3**, 90–105.
30. M. Aryal, N. Vykhodtseva, Y.Z Zhang and N. McDannold, *J. Control. Release* 2015, **204**, 60–69.
31. G. Manich, I. Cabezon, V.J Del, J. Duran–Vilaregut, A. Camins and e. a. M. Pallas, *Eur. J. Pharm. Sci.*, 2013, **49**, 556–564.
32. J. Gillet and M. M. Gottesman, in *Multi–Drug Resistance in Cance*, ed. Z. J., Humana Press. , 2009, vol. 569.
33. S. H. Jang, M. G. Wientjes and J. L. Au, *Pharm Res.*, 2003, **9**, 1337–1350.
34. B.Bahrami, M. Hojjat–Farsangi, H. Mohammadi, E. Anvari, G. Ghalamfarsa, M. Yousefi and F. Jadidi–Niaragh, *Immunology Letters*, 2017, **190**, 64–83.
35. X. Gao, *Brain Targeted Drug Delivery Systems: A Focus on Nanotechnology and Nanoparticulates.*, Netherlands: Elsevier Science, 2018.
36. G. F. Gensini, A. A. Conti and D. Lippi, *J Infect.*, 2007, **54**, 221–224.
37. K. Strebhardt, Ullrich, A. , *Nat Rev Cancer*, 2008, **8**, 473–480.
38. L. R. F. Bosch, *Pharmacology.*, 2008, **82**, 171–179.
39. R. P. Feynman, *Eng Sci*, 1960, **23**, 22–36.
40. I. Lagzi, *Cent. Eur. J. Med.*, 2012, **8**, 377–382.
41. M. Barz, *Nanomedicine (Lond).* , 2015, **10**, 3093–3097. .
42. T. J. Webster, *Int J Nanomed*, 2006, **1**, 115–116.
43. M. Liong, J. Lu, M. Kovochich, T. Xia, S. G. Ruehm, A. E. Nel, F. Tamanoi and J. I. Zink, *ACS Nano*, 2008, **2**, 889–896.
44. I. I. Slowing, B. G. Trewyn and V. S. Y. Lin, *Journal of the American Chemical Society*, 2007, **129**, 8845–8849.

45. Y. F. Huang, D. Shangguan, H. Liu, A. Phillips Joseph, X. Zhang, Y. Chen and W. Tan, *ChemBioChem*, 2009, **10**, 862–868.

46. A. D. Bangham, *Chemistry and Physics of Lipids*, 1993, **64**, 275–285.

47. G. Pasut and F. M. Veronese, *Progress in Polymer Science*, 2007, **32**, 933–961.

48. E. M. Pelegri O'Day, E.W. Lin and H. D. Maynard, *Journal of the American Chemical Society*, 2014, **136**, 14323–14332.

49. R. Duncan and R. Gaspar, *Molecular Pharmaceutics*, 2011, **8**, 2101–2141.

50. L. Messager, J. Gaitzsch, L. Chierico and G. Battaglia, *Current Opinion in Pharmacology*, 2014, **18**, 104–111.

51. Y. Barenholz, *Journal of Controlled Release*, 2012, **160**, 117–134.

52. I. A. Bakker–Woudenberg, *Int J Antimicrob Agents.*, 2002, **19**, 299–311.

53. P. Nakhaei, R. Margiana, D. O. Bokov, W. K. Abdelbasset, M. A. Jadidi Kouhbanani, R. S. Varma, F. Marofi, M. Jarahian and N. Beheshtkhoo, *Front. Bioeng. Biotechnol*, 2021, **9**, 705886.

54. H. Bermudez, A. K. Brannan, D. A. Hammer, F. S. Bates and D. E. Discher, *Macromolecules*, 2002, **35**, 8203–8208.

55. C. LoPresti, H. Lomas, M. Massignani, T. Smart and G. Battaglia, *Journal of Materials Chemistry*, 2009, **19**, 3576–3590.

56. H. B. K. Letchford, *Eur J Pharm Biopharm*, 2007, **65**, 259–269.

57. D. E. Discher and A. Eisenberg, *Science*, 2002, **297**, 967.

58. W. Chen, F. Meng, R. Cheng and Z. Zhong, *Journal of Controlled Release*, 2010, **142**, 40–46.

59. M. A. Pangburn, B. Waybrant, M.M. Adil, E. Kokkoli, *J. Biomech. Eng. Trans. ASME*, 2009, **131**, 1–20.

60. I. C. Lomas, S. MacNeil, J. Du, S.P. Armes, A.J. Ryan, A.L. Lewis, G. Battaglia, *Adv. Mater.*, 2007, **19**, 4238–4243.

61. D. A. Christian, S. Cai, D. M. Bowen, Y. Kim, J. D. Pajerowski and D. E. Discher, *European Journal of Pharmaceutics and Biopharmaceutics*, 2009, **71**, 463–474.

62. B. Sola–Barrado, D. M. Leite, E. Scarpa, A. Duro–Castano and G. Battaglia, *Mol Pharm.*, 2020, **17**, 4709–4714.

63. B. Priya, P. Viness, E. C. Yahya and C. d. T. Lisa, *Biomedical Materials*, 2009, **4**, 022001.

64. S. E. Dunn, S. S. Brindley A Fau – Davis, M. C. Davis Ss Fau – Davies, L. Davies Mc Fau – Illum and L. Illum.

65. A. Z. Mirza and F. A. Siddiqui, *International Nano Letters*, 2014, **4**, 94.
66. J. J. Mulvihill, E. M. Cunnane, A. M. Ross, J. T. Duskey, G. Tosi and A. M. Grabrucker, *Nanomedicine (Lond).* 2020, **15**, 205–214.
67. X. Wu, H. Yang, W. Yang, X. Chen, J. Gao, X. Gong, H. Wang, Y. Duan, D. Wei and J. Chang, *J Mater Chem B.*, 2019, **7**, 4734–4750.
68. B. Ruozi, D. Belletti, F. Pederzoli, P. Veratti, F. Forni, M. A. Vandelli and G. Tosi, *Curr Med Chem.*, 2014, **21**, 4169–4185.
69. X. Tian, D. M. Leite, E. Scarpa, S. Nyberg, G. Fullstone, J. Forth, D. Matias, A. Apriceno, A. Poma, A. Duro–Castano, M. Vuyyuru, L. Harker–Kirschneck, A. Šarić, Z. Zhang, P. Xiang, B. Fang, Y. Tian, L. Luo, L. Rizzello and G. Battaglia, *Science Advances*, 2020, **6**.
70. C. He, Zhang, Z., Ding, Y. *et al.* , *J Nanobiotechnol*, 2021, **19**.
71. P. J. Photos, L. Bacakova, B. Discher, F. S. Bates and D. E. Discher, *J Control Release*, 2003, **90**, 323–334.
72. S. I. Jeon and J. D. Andrade, *J Colloid Interface Sci*, 1991, **1**, 159–166.
73. C. Contini, R. Pearson, L. Wang, L. Messager, J. Gaitzsch, L. Rizzello, L. Ruiz–Perez and G. Battaglia, *iScience*, 2018, **7**, 132–144.
74. V. M. Gouveia, L. Rizzello, C. Nunes, A. Poma, L. Ruiz–Perez, A. Oliveira, S. Reis and G. Battaglia, *Pharmaceutics*, 2019, **11**.
75. A. Tewabe, A. Abate, M. Tamrie, A. Seyfu and E. T. A. Siraj, *J Multidiscip Healthc.*, **14**, 1711–1724.
76. Y. H. Bae and K. Park, *J Control Release.*, **153**, 198–205.
77. D. B. Dusenbery, *Proceedings of the National Academy of Sciences of the United States of America*, 1997, **94**, 10949–10954.
78. S. L. Porter, G. H. Wadhams and J. P. Armitage, *Nature Reviews Microbiology*, 2011, **9**, 153.
79. F. Peruani, *J. Phys.: Condens. Matter*, 2020, **32**, 8–10.
80. G. Gompper and R. G. Winkle, *J. Phys.: Condens. Matter* 2020, **32**.
81. M. Ripoll, *J. Phys.: Condens. Matter*, 2020, **32**, 37–39.
82. G. I. Taylor, *Proc. R. Soc. A.*, 1951, **209**, 447–461.
83. E. Purcell, *Am. J. Phys.*, 1977, **45**, 3–11.
84. A. C. Tsang, E. Demir, Y. Ding and O. S. O.S. Pak, *Adv. Intell. Syst.*, 2020, **2**, 1900137.
85. T. Qiu, T. C. Lee and e. a. A. Mark, *Nat Commun*, 2014, **5**, 5119.
86. B. A. Lodish H, Zipursky SL, et al. , in *Molecular Cell Biology*, ed. N. Y. W. H. Freeman, 2000, vol. 4th edition, ch. Section 19.4.

87. H. R. Bourne and O. Weiner, *Nature*, 2002, **419**, 21.
88. S. Nain and N. N. Sharma, *Frontiers in Life Science*, 2015, **8**, 2–17.
89. W. D. W. Wang, S. Ahmed, T. E. Mallouk, A. Sen, *Nano Today*, 2014, **8**, 531–554.
90. M. A. Fischbach, J. A. Bluestone and W. A. Lim, *Sci Transl Med.*, 2013, **3**, 179.
91. D. Prieve, Anderson, J., Ebel, J., & Lowell, M., *Journal of Fluid Mechanics*, 1984, **148**, 247–269.
92. F. F. Reuss, *Mémoires de la Société Impériale des Naturalistes de Moscou*, 1809, **2**, 327–337.
93. A. Tiselius, *Trans. Faraday Soc.*, 1937, **33**, 542–531.
94. H. J. Keh, *Langmuir* 2001, **17**, 1437–1447.
95. J. P. Ebel, and D. C. Prieve, *Langmuir*, 1988, **4**, 396–406.
96. D. C. Prieve, *Separation and Purification Methods*, 1984, **13**, 67–103.
97. W. C. Ludwig, *Math.–Nat. Wiss. Kl.*, 1856, **20**, 539.
98. J. K. Platten and P. Costesèque, *Eur Phys J E Soft Matter.*, 2004, **5**, 235–239.
99. J. L. Anderson, *Annual Review of Fluid Mechanics*, 1989, **21**, 61–99.
100. S. Wiegand, *J. Phys.: Condens. Matter*, 2019, **31**, 503003.
101. J. D. Posner, *Annual Review of Fluid Mechanics*, 2017, **49**, 511–540.
102. J. L. Anderson, *Annu. Rev. Fluid Mech.*, 1989, **21**, 61–99.
103. S. Shin, *Physics of Fluids*, 2020, **32**, 101302.
104. M. A. Mozaffari, J. Koplik, et al., *Phys. Fluids*, 2016, **28**, 053107.
105. J. Anderson, M. Lowell, D. Prieve, *Journal of Fluid Mechanics*, 1982, **117**, 107–121.
106. E. C. L. Bocquet, *Chem. Soc. Rev.*, 2010, **39**, 1073–1095.
107. H. Y. S. Marbach, L. Bocquet,, *J. Chem. Phys.*, 2017, **146**, 194701.
108. J. K. N. Sharifi–Mood, and C. Maldarelli, *Physics of Fluids*, 2013, **25**, 012001.
109. A. R. Golestanian, *Physical review letters*, 2005, **94**, 220801.
110. P. Schattling, B. Thingholm and B. Städler, *Chemistry of Materials*, 2015, **27**, 7412–7418.
111. G. L. Hazelbauer, *Annual review of microbiology*, 2012, **66**, 285–303.
112. M. McCutcheon, *Physiological Reviews*, 1946, **26**, 319–336.
113. W. Poon., *arXiv preprint arXiv:1306.4799*.
114. J. R. Howse, *Soft Matter*, 2010, **6**, 726–738.
115. A. C. Hortelao, A. Miguel–Lopez and S. Sańchez, *J. Am. Chem. Soc.*, 2016, **138**, 13782—13785.

116. X. MA, A. Jannasch, U. Albrecht, K. Hahn, A. Miguel–Loṕez, E. Schaffer and S. Sańchez, *Nano Lett.*, 2015, **15**, 7043−7050.

117. S. Sanchez, A. Alexander Y. Mei, Yongfeng and O. G. Schmidt, *J. Am. Chem. Soc.*, 2010, **132**, 13144–13145.

118. K. K. Dey, X. Zhao, B. M. Tansi, W. J. Méndez–Ortiz, U. M. Córdova–Figueroa, R. Golestanian and A. Sen, *Nano Letters*, 2015, **15**, 8311–8315.

119. X. Ma, X. Wang, K. Hahn and S. Sańchez, *ACS Nano*, 2016, **10**, 3597−3605.

120. A. C. Hortelaõ, T. Patiño, A. Perez–Jimeńez, A. Blanco and S. Sańchez, *Adv. Funct. Mater.*, 2018, **28**, 1705086.

121. L. Baraban, S. Sanchez, O. G. Schmidt, *Angewandte Chemie*, 22013, **52**, 5552–5556.

122. L. Marichal, G. Klein and J. A. e. al., *Nanomaterials (Basel)*, 2020, **10**, 240.

123. A. Abdelmohsen, M. Nijemeisland, G. M. Pawar, G.–J. A. Janssen, R. J. M. Nolte, J. C. M. van Hest and D. A. Wilson, *ACS Nano*, 2016, **10**, 2652–2660.

124. Britannica, The Editors of Encyclopaedia. "capillary". Encyclopedia Britannica, (accessed Accessed 11 February 2022., DOI: https://www.britannica.com/science/capillary.).

125. A. V. Kabanov, P. Lemieux, S. Vinogradov and V. Alakhov, *Adv Drug Deliv Rev.*, 2002, **54**, 223–233.

126. P. Mergenthaler, U. Lindauer, G. A. Dienel and A. Meisel, *Trends in neurosciences*, 2013, **36**, 587–597.

127. M. Wong, B. A. Horri and B. Salamatinia, ed. V. K. Thakur, Elsevier, 2018, ch. Chapter 8 – Grafted Copolymerized Chitosan and Its Applications as a Green Biopolymer, pp. 285–333.

128. H. Lomas, J. Du, I. Canton, J. Madsen, N. Warren, S. P. Armes, A. L. Lewis and G. Battaglia, *Macromol.* , 2010, **10**, 513–530.

129. A.L. Lewis, L. A. Tolhurst and P. W. Stratford, *Biomaterials*, 2002, **23**.

130. K. L. Robinson, J. V. M. Weaver, S. P. Armes, E. D. Marti and F. C. Meldrum, *Journal of Materials Chemistry*, 2002, **12**, 890–896.

131. C. LoPresti, H. Lomas, M. Massignani, T. Smart and G. Battaglia, *J. Mater. Chem.*, 2009, **19**, 3576–3590.

132. M. Lee James C-, H. Bermudez, M. Discher Bohdana, A. Sheehan Maureen, Y. Y. Won, S. Bates Frank and E. Discher Dennis, *Biotechnology and Bioengineering*, 2001, **73**, 135–145.

133. J. D. Robertson, L. Rizzello, M. Avila–Olias, J. Gaitzsch, C. Contini, M. S. Magoń, S. A. Renshaw and G. Battaglia, *Scientific Reports*, 2016, **6**, 27494.

134. H. R. Marsden, L. Gabrielli and A. Kros, *Polym. Chem.*, 2010, **1**, 1512–1518.
135. L. Song, C. Hobaugh Mr Fau – Shustak, S. Shustak C Fau – Cheley, H. Cheley S Fau – Bayley, J. E. Bayley H Fau – Gouaux and J. E. Gouaux, *Science*, 1996, **274**, 1859–1866.
136. S. Fujii, T. Matsuura T Fau – Sunami, Y. Sunami T Fau – Kazuta, T. Kazuta Y Fau – Yomo and T. Yomo, *Proc Natl Acad Sci U S A*, 2013, **110**, 16796–16801.
137. V. Noireaux and A. Libchaber, *Proceedings of the National Academy of Sciences of the United States of America*, 2004, **101**, 17669.
138. M. I. Worldwide, *Journal*, 2011, 1–6.
139. Dynamic light scattering, (accessed 09/2021, DOI: https://www.malvernpanalytical.com/en/learn/knowledge-center/whitepapers/WP111214DLSTermsDefined).
140. C. LoPresti, M. Massignani, C. Fernyhough, A. Blanazs, A. J Ryan, J. Madsen, N. J. Warren, S. P. Armes, A. L. Lewis and S. Chirasatitsin, *ACS Nano*, 2011, **5**, 1775–1784.
141. U. W. Gedde, *Polymer Phycisc*, Chapman & Hall, London, 1995.
142. K. Zuiderveld, *Graphics Gems IV*, 1994, 474–485.
143. N. Otsu, *IEEE Transactions on Systems, Man, and Cybernetics*, 1979, **9**, 62–66.
144. L. Wang, L. Chierico, D. Little, N. Patikarnmonthon, Z. Yang, M. Azzouz, J. Madsen, P. Armes Steven and G. Battaglia, *Angewandte Chemie International Edition*, 2012, **51**, 11122–11125.
145. G. Volpe, S. Gigan and G. Volpe, *Am. J. Phys.*, 2014, **82**, 659–664.
146. https://ibidi.com, The Surfaces and Coatings of the ibidi Chambers, (accessed 21/12, 2021).
147. J. C. Crocker and D. G. Grier, *J. Colloid Interface Sci.*, 1996, **179**, 298–310.
148. L. Luo and A. Eisenberg, *Journal of the American Chemical Society*, 2001, **123**, 1012–1013.
149. K. Bryskhe, J. Jansson, D. Topgaard, K. Schillén and U. Olsson, *J. Phys. Chem. B*, 2004, **108**, 9710–9719.
150. D. R. Arifin and A. F. Palmer, *Biomacromolecules*, 2005, **6**, 2172–2181.
151. G. Battaglia and A. J. Ryan, *Angew Chem Int Ed Engl.*, 2006, **45**, 1433–7851.
152. J. D. Robertson, G. Yealland, M. Avila-Olias, L. Chierico, O. Bandmann, S. A. Renshaw and G. Battaglia, *ACS Nano*, 2014, **8**, 4650–4661.

153. G. Battaglia and A. J. Ryan, *The Journal of Physical Chemistry B*, 2006, **110**, 10272–10279.
154. G. Battaglia and A. J. Ryan, *Angew. Chem.*, 2006, **45**, 2052–2056.
155. P. F. Green and R. Limary, *Adv. Colloid Interface Sci.*, 2001, **94**, 53–81.
156. Y. Mai and A. Eisenberg, *Chem. Soc. Rev*, 2012, **41**, 5969–5985
157. F. Olson, C. A. Hunt , F. C. Szoka, W. J. Vail and D. Papahadjopoulos, *Biochim Biophys Acta.*, 1975, **557**, 9–23.
158. S. Cerritelli, A. Fontana, D. Velluto, M. Adrian, J. Dubochet, P. De Maria and J. A. Hubbell, *Macromolecules*, 2005, **38**, 7845–7851.
159. M. Discher Bohdana, Y. Won, S. Ege David, C. M. Lee James, S. Bates Frank, E. Discher Dennis and A. Hammer Daniel, *Science*, 1999, **284**, 1143–1146.
160. J. Robertson, L. Rizzello and e. a. M. Avila–Olias, *Sci Rep*, 2016, **6**.
161. C. Pegoraro, D. Cecchin, L.S. Gracia, N. Warren, J. Madsen, S.P. Armes, A. Lewis, S. Macneil and G. Battaglia, *Cancer Lett.*, 2013, **334**, 328–337.
162. C. Z. Bueno, A. C. Apolinário, A. Duro–Castano, A. Poma, A. Pessoa, C. O. Rangel–Yagui and G. Battaglia, *ACS Macro Letters*, 2020, **9**, 1471–1477.
163. G. Battaglia and J. A. Ryan, *Journal of the American Chemical Society*, 2005, **127**, 8757–8764.
164. G. Battaglia, Degree of Doctor in Philosophy, University of Sheffield, 2006.
165. S. Winzen, M. Bernhardt, D. Schaeffel, A. Koch, M. Kappl, K. Koynov, K. Landfester and A. Kroeger, *Soft Matter*, 2013, **9**, 5883–5890.
166. T. Smart, H. Lomas, M. Massignani, M. V. Flores–Merino, L. Ruiz Perez and G. Battaglia, *Nano Today*, 2008, **3**, 38–46.
167. D. V. Devine, K. Wong, K. Serrano, A. Chonn and P. R. Cullis, *Biochimica et Biophysica Acta (BBA) – Biomembranes*, 1994, **1191**, 43–51.
168. S. Clarke, Dublin City University, 2013.
169. R. E. Wood, F. P. Wirth and H. E. Morgan, *Biochimica et Biophysica Acta (BBA) – Biomembranes*, 1968, **163**, 171–178.
170. I. Canton and G. Battaglia, *Chem. Soc. Rev*, 2012, 2718–2739.
171. M. Hennemeyer, B. Stefan and R. Stark, *Cantilever Micro–rheometer for the Characterization of Sugar Solutions*, 2008.
172. T. Houpt., Density of Sugar Solutions, (accessed 15/02/2022, DOI: https://wiki.houptlab.org/wiki/Density_of_Sugar_Solutions).
173. J. R. Rumble, ed. e. CRC Press, 2019, p. 100.
174. M. K. Rasmussen, J.N Pedersen, R. Marie, *Nat Commun*, 2020, **11**, 2337.
175. D. S. Shin, and Ji. Feng, *Phys. Rev. Applied*, 2019, **12**, 024014.

176. J. L. Anderson, *The Physics of Fluids*, 1983, **26**, 2871.

177. D. Salley, Keenan, G., Grizou, J. et al., *Nat Commun*, 2020, **11**.

178. M. A. Touve, D. B. Wright, H. S. C. Mu, C. Park and N. C. Gianneschi, *Macromolecules*, 2019, **52**, 5529–5537.

179. R. Rampado, P. Caliceti, S. Pucciarelli and M. Agostini, *Front. Bioeng. Biotechnol.*, 2020, **8**, 166.

180. N. T. Nguyen, *Analytical Chemistry*, 2008, **80**, 2326–2341.

181. Z. Ali, *Micromachines (Basel)*, 2021, **12**, 319.

182. E. Gullotti and Y. Yeo, *Mol Pharm.*, 2009, **6**, 1041–1051.

183. C. Bechinger, H. Löwen, C. Reichhardt, G. Volpe, G. Volpe, *Rev. Mod. Phys.*, 2016, **88**, 045006.